Fire and ice

Infrared spectroscopy as a probe of ice and gas in star forming regions

PROEFSCHRIFT

ter verkrijging van
de graad van Doctor aan de Universiteit Leiden,
op gezag van de Rector Magnificus Dr. D.D. Breimer,
hoogleraar in de faculteit der Wiskunde en
Natuurwetenschappen en die der Geneeskunde,
volgens besluit van het College voor Promoties
te verdedigen op donderdag 14 oktober 2004
klokke 14.15 uur

door

Klaus Martin Pontoppidan
geboren te Esbjerg, Denemarken
in 1977

PROMOTIECOMMISSIE

Promotor :   Prof. dr. E. F. van Dishoeck

Referent :   Prof. dr. Th. Henning (Max Planck Institut für Astronomie,
                  Germany)

Overige leden :   Prof. dr. G. A. Blake (California Institute of Technology, USA)
                  Prof. dr. P. Ehrenfreund
                  Dr. L. d'Hendecourt (Université Paris d'Orsay, France)
                  Dr. S. Schlemmer
                  Prof. dr. A. G. G. M. Tielens (Rijksuniversiteit Groningen)
                  Prof. dr. P. T. de Zeeuw

Til Zita og Teddy

Contents

Contents

Chapter 1

Introduction

...a great part of our time was spent discussing the problem of interstellar matter, on which we held different views - though I cannot remember what they were.

Sir A. S. Eddington, 1937, on a meeting between him and Rosseland in November 1923.

It is exactly 100 years since the interstellar medium was discovered by Hartmann (1904) in an article published in the Astrophysical Journal on the spectroscopic binary δ Orionis. In that spectrum a narrow line due to calcium ions was detected, which did not change its wavelength as the stars revolved around eachother. The presence of a stationary line came as a considerable surprise. As in many other occasions in astrophysics, the discovery was driven by technological advances in high resolution spectroscopy, in which Hartmann was an expert. Regardless, no-one realised the significance of the discovery until decades later, and although Hartmann correctly conjectured that the calcium must reside in an intervening cloud, the astronomical community at the time insisted that the line must be due to some peculiarity of the δ Ori system itself. The confirmation of the presence of interstellar atomic gas came through similar spectroscopic observations of larger samples of stars.

Thus, a few narrow lines in a few stellar spectra marked the beginning of the unravelling of a great astronomical mystery, namely the nature of interstellar matter. Eddington wrote a an article on the subject in 1937 at a time when articles were permitted to contain just a short presentation of a few stray ideas (Eddington, 1937). The article is remarkable because, apart from containing some memorable comments on the chemistry of the interstellar medium, it also contains the first identifiable reference to interstellar water ice. Clearly, Eddington must have been a man with considerable theoretical intuition, considering that the article was written just before the first interstellar molecules were identified (McKellar, 1940; Merrill, 1934; Swings & Rosenfeld, 1937).

Eddington was led to the conjecture of the presence of abundant water ice in the interstellar medium through arguments which probably would not be accepted by a modern referee. Nevertheless, it is intriguing to follow the simple argumentation. Eddington notes that ionising photons will be extinguished by ionisation events and that neutral species therefore must exist at some distance from ionising sources. He then proceeds to suggest that someone should work out the details, which happened two years later in the famous work on HII regions of Strömgren (1939). Since ion-neutral reactions were known at the time to proceed without reaction barriers, Eddington concludes that molecules must exist in the interstellar

1

medium and continues that water ice is a good candidate for interstellar dust due to its high boiling point.

However, Eddington discloses his real reasons at the end of the article:

"Perhaps my inclination to a 'water theory' is influenced by the feeling that, inasmuch as the gas responsible for the mysterious light of the nebulæ has turned out to be just *common air*, it is fitting that the mysterious dark obscuring masses in the Galaxy should turn out to be just *common clouds*" (Eddington's emphasis).

The foresight contained here is quite amazing because the analogy is of considerable use today in the study of interstellar ices, both in the way it is right and wrong. Today many similarities can be drawn between physical chemistry of atmospheric ices and interstellar ices, and although water is now known to chemically form on the surfaces of icy dust grains rather than accrete from the gas phase, other atomic and molecular species do freeze out in the dense clouds of the interstellar medium, much like in atmospheric cirrus clouds. The formation of water ice and other saturated molecules on the surfaces of dust grains was later postulated by van de Hulst (1946), who reasoned that atomic hydrogen could react with the most abundant elements in the solid phase. In this picture, hydrogen reacts with other hydrogen atoms and with oxygen, nitrogen and carbon to form H_2, H_2O, NH_3 and CH_4. Based on the elemental abundances, iron and silicon species were thought to be a minor component of interstellar dust. In fact, the prevailing hypothesis in the 50s seems to have been that interstellar dust mostly consisted of water ice (Kahn, 1952). That idea was later largely forgotten, but has received increasing attention in the last decade, as observations have shown ices to play a major role in the chemical evolution of dense clouds. Significant parts of this thesis deal with Eddington's interstellar snow.

1.1 The birth of infrared astronomy

The need for opening the infrared wavelength regions for astronomical observations in the 1940s was born out of the early realisation that infrared photons penetrate sub-micron sized dust much easier than do visible photons. This was something which could prove the dusty nature of the dark spots cluttering the plane of the Milky Way, and disprove that they were simply holes in the stellar distribution. A second major incentive for infrared astronomy was the possibility for observing the vibrational bands of molecules (Swings, 1944), which had been studied at resolving powers of $\lambda/\Delta\lambda \sim 1000$ in the laboratories of the 1920s (e.g. Cooley, 1925; Sleator & Phelps, 1925). It was not until the late 1960s that it was realised that the sky is full of bright infrared sources (Neugebauer et al., 1965).

Although infrared detectors sensitive above $1.3\,\mu$m can be traced back to the 19th century, the beginning of the evolution which led to the infrared detector technology of the 21st century is generally ascribed to R. J. Cashman, who was hired by the U.S. defense department in 1941 to develop a detector for military purposes. He produced the first PbS (lead sulfide) infrared detector cell, which

was sensitive to wavelengths up to 3.5 μm. Astronomers were quick to see the potential of observing in the infrared and some of the first results were spectroscopic observations of molecular absorption bands in the solar spectrum (e.g. Adel, 1938). It was rapidly recognised that most of the absorption lines found at wavelengths between 1 and 20 μm were due to molecules in the Earth's atmosphere, and it was shown that large parts of the infrared spectrum were completely inaccessible because of strong absorption by atmospheric, or telluric, molecules. A great deal of effort was spent identifying the telluric lines in the infrared spectrum, and in that process several important trace constituents of the Earth's atmosphere were discovered, such as NH_3 and CH_4 (McMath et al., 1948; Migeotte, 1948). However, it came as a considerable surprise when carbon monoxide (CO) was discovered in the atmosphere of the Sun by using the bandhead lines at $\sim 2.3\,\mu$m as well as the fundamental band at $\sim 4.7\,\mu$m (Pierce et al., 1952). As today, the extra-terrestial lines were distinguished from the telluric lines using the Doppler shift of the source; the lines were observed in the solar limb.

1.2 Interstellar dust grains

Today, the dust grains of the interstellar medium are known to take a range of different appearances depending on the environment in which they are found. Although the detailed molecular structure of interstellar dust is presently a very active area of debate, some properties can be settled. Dust grains are generally small; from 0.01-1 μm, but larger grains are known to exist primarily in planet-forming disks surrounding young stars. Extinction and scattering properties of dust in the diffuse interstellar medium are commonly fitted by a power law size distribution: $n(a) \propto a^{-3.5}$ (Mathis et al., 1977). Elements such as iron, silicon and magnesium are heavily depleted from the gas phase, and are believed to reside in the dust in the form of silicates and iron compounds. A significant secondary dust component is composed of some form of amorphous carbon. It is not clear if the carbon dust represents a grain population separate from the silicate grains, or if the carbon and the silicates are part of the same grains, possibly in a layered structure. The silicate and amorphous carbon components of the interstellar dust are usually called, somewhat misleadingly, refractory dust, a label referring to their high sublimation temperatures. These types of dust are formed primarily in supernova remnants (Dunne et al., 2004) and in the winds of asymptotic giant branch stars (Habing, 1996). In terms of the most abundant heavy elements, oxygen, nitrogen and carbon, the refractory dust grains account for about 1/3 by number in the solar neighbourhood. The relative mass of silicate and carbonaceous dust is currently believed to be 70%/30%, albeit with some uncertainty (Draine, 2003).

The remaining C, N and O is found in the gas phase in the diffuse interstellar medium. However, in dense and cold regions, these elements can condense on dust grains as well. It is now known that the conversion of these elements through surface reactions into a volatile molecular mantle, consisting of the saturated species postulated by van de Hulst as well as CO_2 and a number of molecular ions, is extremely effective. These solid-state volatiles are in general called

'ices'. One volatile molecule, namely CO, distinguishes itself from all the other known ice species by being formed by gas phase chemistry and only subsequently condensing onto grains.

In terms of numbers, ice is the second-largest molecular reservoir in dense cores after H_2, accounting for up to 50% of the available gas-phase oxygen (see Chapter 4). Carbonaceous dust including polycyclic aromatic hydrocarbons (PAH) and silicate dust are however close contestants. CO gas is a significant reservoir, while all other gas-phase molecules are found in trace amounts. Typical molecular abundances in dense clouds are given in Table 1.1.

A classic problem is the question whether all the basic elements have been accounted for in dense clouds. Table 1.1 illustrates some of the challenges facing astrochemistry in the near future. For instance, it is seen that the reservoirs of all carbon atoms are known, within the uncertainties. The same holds for the oxygen, where everything which is not bound in dust or CO seems to be in the form of atomic oxygen, although the exact amount is uncertain (Caux et al., 1999; Poglitsch et al., 1996). It seems that very little oxygen is in the form of O_2 gas or ice, in conflict with some chemical models, but consistent with observations (Goldsmith et al., 2000; Vandenbussche et al., 1999). Conversely, the nitrogen is still largely unaccounted for. The location of the nitrogen represents one of the long-standing problems in the study on dark cloud chemistry. Models have long suggested that the nitrogen is bound in N_2, either as gas or ice. N_2 has only weak bands in infrared, indirect searches searches have failed to find it in the solid phase (Chapter 3). Observations of the N_2H^+ ion in the gas phase provide indirect evidence that the abundance of N_2 gas is high in dense molecular clouds (Womack et al., 1992).

Historically, gas-phase and solid-state chemistry are often discussed separately, but the distinction is becoming increasingly blurred. A wealth of information on the chemistry in dark clouds has been obtained through observations of rotational emission lines from molecules in the millimetre wavelength regime. These observations are extremely sensitive and can trace molecules with abundances as small as 10^{-12}. Therefore, a large number of molecular species have been identified in the gas-phase which can be compared to chemical models. Yet, gas-phase molecules besides H_2 and CO account for only a miniscule part of the chemistry taking place in dense clouds, the rest being surface reactions on dust grains. It has become clear that a significant interaction takes place between the gas and solid phase, but although many attempts have been made to model the grain component in chemical networks, insufficient observational constraints on ices have hampered the progress. The main reason is that observations of ices are challenging. Ice bands are often severely blended, absorption lines studies are only sensitive to abundances greater than 10^{-6} and many ice bands can only be observed from space. Gas-phase and solid-state observations are therefore highly complementary.

The shape and structure of interstellar dust is, perhaps unsurprisingly, not well known. However, it is well established that they are not round, even though almost all dust models assume this for practical purposes. Polarisation measurements have clearly shown grains to be elongated and oriented by magnetic fields,

Table 1.1: *Known molecular reservoirs in cold dense clouds in order of abundance*

	abundance $[H_2^{-1}]$	% of O	% of C	% of N
H_2	1	–	–	–
He	0.12	–	–	–
Atomic oxygen[1]	$3 - 6 \times 10^{-4}$	30-50%	–	
Oxygen-bearing ice[2]	4×10^{-4}	29%	20%	–
Carbon dust[3]	3.3×10^{-4}	–	50%	–
Silicates[4]	2.6×10^{-4}	23%	–	–
Gas-phase CO[5]	1×10^{-4}	9%	15%	–
Nitrogen-bearing ice[6]	3×10^{-5}	$< 1\%$	$< 1\%$	18%
PAHs[7]	–	–	10%	–
Other gas-phase molecules[8]	$10^{-7} - 10^{-6}$	$< 1\%$	$< 1\%$	$< 1\%$
Total[9]		100%	95%	18%

[1] An uncertain, but large, abundance of atomic oxygen is present in dense clouds (e.g. Caux et al., 1999)

[2] H_2O, CO, CO_2, CH_3OH and H_2CO (See Chapter 4).

[3] Includes amorphous carbon and/or graphite (Zubko et al., 2004).

[4] Assuming $(Mg + Fe) : Si = 3 : 1$ (Howk et al., 1999) and that the grains consist of $MgSiO_3$ (enstatite) and FeO.

[5] Gas-phase CO may be heavily depleted.

[6] The presence of a nitrogen-bearing ice component is highly debated. The numbers are the highest possible abundances of OCN^-, NH_3 and NH_4^+.

[7] From Zubko et al. (2004) for the diffuse ISM.

[8] Although this figure is somewhat uncertain, gas-phase abundances do not become higher until significant parts of the ice mantles have evaporated at $T \sim 100$ K.

[9] Elemental abundances: $O/H = 5.5 \times 10^{-4}$, $C/H = 3.5 \times 10^{-4}$ and $N/H = 0.85 \times 10^{-4}$ (Frisch & Slavin, 2003).

while theoretical dust growth models suggest a fluffy, almost fractal structure. In recent years, spectroscopy of solid state absorption bands in the mid-infrared has shown that the grains are likely to have highly irregular shapes (see e.g. Hony, 2002 and Chapter 3). Furthermore, there are clear indications that most of the dust components are not well-mixed, but rather reside on or in the grains as layers or discrete inclusions, testifying to a complex formation history.

1.3 Observing molecules in the thermal infrared

Molecules have vibrational frequencies which are typically located in the thermal infrared wavelength region, defined as 2-30 μm. A gas-phase molecule has a large number of transitions between vibrational levels in which the rotational quantum number also changes. These transitions give rise to rotational-vibrational lines. The lines can be divided into bands containing all the rotational transitions

within a given vibrational transition. Fig. 1.1 shows examples of observations of the fundamental band (v=1–0) of CO toward three young, embedded stars. In the solid phase, the molecules can no longer rotate, but they can still vibrate. This collapses the ro-vibrational band into a single, broad resonance. The broad absorption lines seen at 4.67 μm in Fig. 1.1 are caused by solid CO. Due to the presence of neighbouring molecules, the vibrational frequency of a solid-state molecule is perturbed, thus changing the shape and center position of the resonance. This effect can be used to infer properties of the molecular structure of the solid.
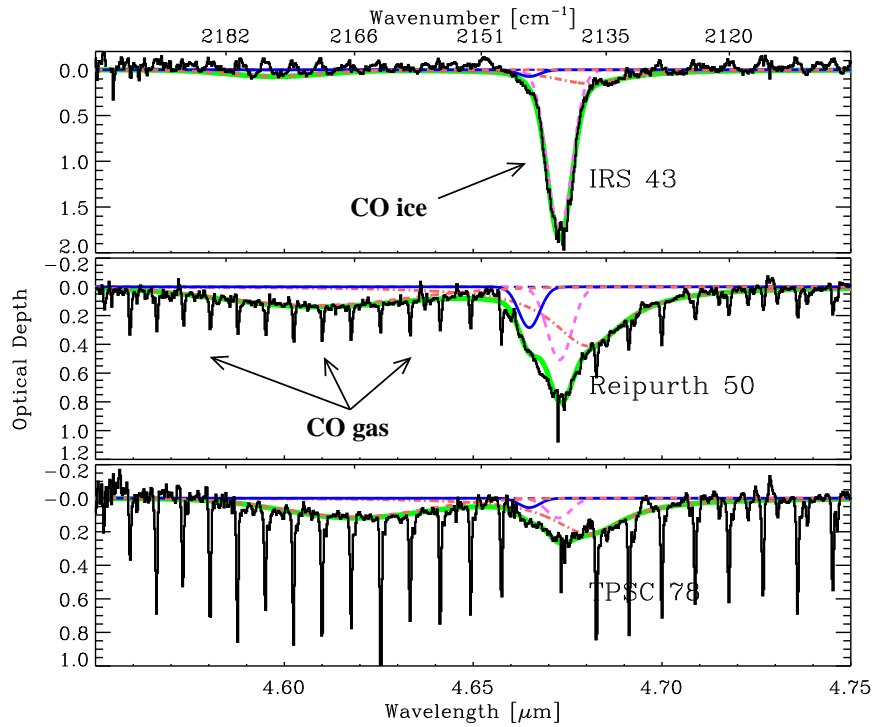
Figure 1.1: *VLT-ISAAC spectra taken in the direction of three young stars. The spectra show the presence of both gas-phase and solid carbon monoxide (CO) and illustrate how pure CO ice evaporates but leaves significant amounts trapped in water ice (see Chapter 3).*

If the molecular gas is hot enough, the ro-vibrational band may be seen in emission. This typically happens for temperatures of $\sim 500\,$K or above. Ro-vibrational transitions may also be pumped in the presence of a strong radiation field or continuum photons can be scattered resonantly in the ro-vibrational transitions. For all other configurations, molecular lines can only be observed in absorption. This is practically always true for ice bands, because the evaporation temperatures of volatiles are much lower than the temperatures required to excite them. This means that a bright continuum source is needed in order to observe interstellar

ice, and only the ice located directly in front of the source can be observed. Some ice bands exist beyond $40\,\mu$m, which are excited by lower temperatures, and are therefore seen in emission, such as the $45\,\mu$m band of crystalline water ice (Malfait et al., 1999).

Because of the rich molecular composition of the Earth's atmosphere, most infrared wavelengths are not accessible to ground-based telescopes. This causes, for instance, CO_2 ice to be unobservable from the ground. The windows in the infrared spectrum which are observable from the ground are strongly affected by a large number of atmospheric lines. This causes considerable technical difficulties, especially if accurate measurements on narrow gas-phase lines are to be performed. Fortunately, several infrared observatories equipped with spectrometers have been launched into space in the last decade, most notably the Infrared Space Observatory (1995-1998) and the Spitzer Space Telescope (2003–). The instrumentation used to obtain the data presented in this thesis is given in Table 1.2.

Table 1.2: *Infrared spectroscopy used in this thesis*

Instrument	Wavelengths [μm]	$\lambda/\Delta\lambda^1$	Sensitivity [Jy]^2	Molecules
ISO-SWS	2.5–20	2000	10	all
ISOCAM-CVF	5.2–17	50	0.5	H_2O, 6.85, CO_2
Spitzer-IRS (SL)	5.2–14.5	100	0.005	H_2O, 6.85, CH_4
Spitzer-IRS (SH)	9.9-19.6	600	0.1	CO_2
VLT-ISAAC	2.85-4.2	1000	0.1	H_2O, CH_3OH
VLT-ISAAC	4.55-4.9	10 000	0.2	CO, OCN^-

[1] Average spectral resolving power for typically used instrumental settings.

[2] Average source flux producing a signal-to-noise of $\sim$100 on the continuum for typical integration times.

1.4 Interstellar ice as a tracer of physical cloud conditions

Like gas-phase molecules, interstellar ices vary in abundance in different regions of molecular clouds. Therefore, it follows that the ice traces the physical conditions under which it formed and developed. However, contrary to gas-phase molecules, solid state molecules carry additional spectroscopic information related to the molecular structure of the ice matrix. Interactions on the molecular level in the ice and due to scattering properties of the grain on large scales change the shape of specific ice bands. This can in principle be used to determine whether that particular ice species is crystalline or amorphous, whether it is mixed with other molecular species or pure, on which type of surface the ice is bound, whether the ice species is evenly distributed on a grain or located as inclusions, and whether the ice is compact or porous. Evidence such as this provides not simply a snapshot of the current chemical state, but also a 'geological' record of the

physical evolution of the cloud. For instance, there is now clear observational evidence that not all ice species form at the same time or under the same conditions. Water and CO_2 ice seem to form at the same time early in the evolution of a dense cloud and at fairly low densities, while CO only freezes out later at higher densities. This is supported by the fact that line profiles indicate that water and CO_2 ice are mixed, while CO is largely pure. It is therefore of considerable importance to study the physical chemistry of ices in order to isolate the observational tracers of past cloud conditions.

One extremely important method to study the molecular physics governing the structure and behaviour of ice is via laboratory experiments coupled with quantum chemical modelling. Models and experiments of specific reactions or molecular dynamics processes have provided many invaluable insights in the physics of interstellar ice (Al-Halabi et al., 2004; Collings et al., 2003; Hornekaer et al., 2003; Watanabe et al., 2003). However, due to the long evolutionary time scales, low pressures and poorly known boundary conditions of ice-forming dense clouds, one cannot hope to create a meaningful and complete interstellar ice analogue in a laboratory setting, at least in the foreseeable future. Fortunately, nature provides such a laboratory in abundance in real dense clouds. The information is however subject to certain observational limitations. Ever since ice was first discovered in dense clouds, it has only been possible to observe it toward a small number of bright, isolated infrared sources, simply because of sensitivity constraints. This means that correlating the observed ice features to physical cloud conditions has been notoriously difficult. This reliance on extreme objects have made interpretations vague. However, new instrumentation such as ground-based 8m-class telescopes equipped with sensitive infrared spectrometers and the Spitzer Space Telescope have now reached sensitivities where, in principle, hundreds or even thousands of lines of sight can effectively be probed by mid-infrared spectroscopy. In particular, new instrumentation allows the mapping of ices toward background stars with a spatial resolution approaching that of current single dish millimetre molecular line maps. Indeed, this thesis contains the first spatial map of the abundance distribution of ice in a protostellar envelope with a spatial resolution of less than $10''$ (see Chapter 4).

1.5 Where do the molecules go?

One of the principal motivations for studying the bulk chemistry in dense clouds and star forming regions is to follow the material from its formation until it presumably has some role in determining the composition of a forming planetary system. A central question is whether the cometary ices of our Solar System were originally formed as ice mantles in the dense cloud out of which the Sun and the planets were formed. The path of the volatile solids of a dense cloud into a circumstellar disk is presently not clear. Observations of stars located behind dense clouds have established the presence of abundant water ice prior to the formation of stars, indicating that ices form very early in the life of a molecular cloud (Smith et al., 2002; Whittet et al., 2001). The early formation of other ice species is less well
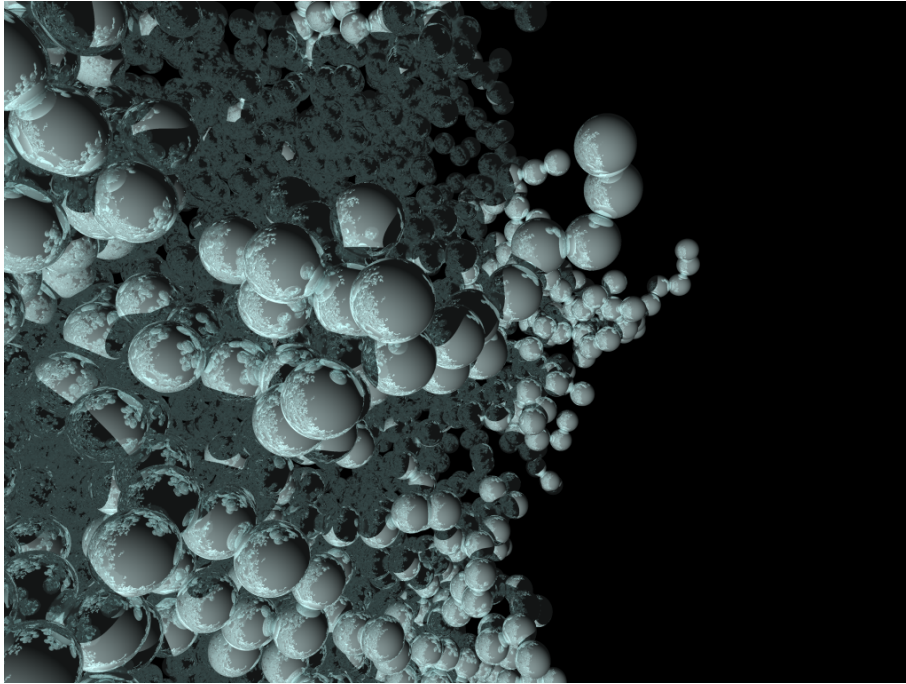
Figure 1.2: *The porous structure of an amorphous ice surface simulated by a simple ballistic deposition. This reproduces the density of amorphous solid water of $0.6\,g\,cm^{-3}$. A more realistic approach will require input from a full molecular dynamics model.*

established with the possible exception of solid methanol, the abundance of which only has strict upper limits in quiescent dense clouds. However, in general the observational statistics for most ices are poor and not well understood, implying that many surprises are likely to be hidden in unobserved regions. The primary reason for this is that background stars are very faint in the mid-infrared, and the technology necessary for achieving the high sensitivity needed has only recently been developed. The best studied regions in terms of ices are the remnant envelopes surrounding young newly-formed stars. In these regions, a complete inventory of ice species has been assembled, especially in the case of massive young stars (Gibb et al., 2004). During the intervening step, the pre- and protostellar stages, the ice content of the material is almost completely unexplored due to the near total lack of infrared sources bright enough to penetrate the dense envelope.

Once the ices become part of a protostellar envelope, they are subjected to conditions which are different from those of the quiescent medium. This includes densities many orders of magnitude higher than typical dense cloud material as well as increasing temperatures. Additionally, the ices may encounter shocks from outflows produced by the central star. Irradiation by ultra-violet photons produced by the central object are unlikely to affect more than a very small fraction

of the ice during this stage. The main reason for this is that the UV photons are extinct after passing 1/100 of the total column density of dust. The dust grains closest to the central object, which do see the UV photons are typically heated above the 100 K necessary to evaporate ice. The main source of UV photons capable of affecting the ices seems to be photons produced by interactions between cosmic rays and the hydrogen of the cloud. All these effects are often called 'processing' of the ice and have been a lively subject of discussion. The heating of the ices or 'thermal processing' is fairly well established observationally. Evidence includes the presence of crystalline water and CO_2 ice (Gibb et al., 2004), evaporation of solid CO (chapter 3) and the emergence of a rich gas-phase chemistry in compact regions surrounding young stars, the so-called 'hot cores' (Cazaux et al., 2003; Gibb et al., 2000). Shocks from outflows are rich in methanol and ethanol gas, which is often interpreted as evaporation of ice mantles (Garay et al., 2002; Martín-Pintado et al., 2001). No unambiguous evidence has been found for UV-processing of ices, which is however not proof of the opposite.

A completely unexplored process is the transport of molecular material from a protostellar envelope into a circumstellar disk. The presence of energetic shocks produced when accreting onto a circumstellar disk may significantly alter the chemistry of any material involved (Bergin et al., 1999). Chapter 6 presents evidence that dissociative accretion shocks may be present in the disks of embedded young low mass stars. Direct observations of ices in circumstellar disks are therefore important in order to determine whether the ices are transported to planet-forming regions in an untouched state or whether the chemistry is reset or significantly altered by shocks. Chapter 5 presents Spitzer spectroscopic observations and axisymmetric Monte Carlo radiative transfer models of the edge-on disk CRBR 2422.8-3423 in order to address this question.

1.6 Outline of the thesis

The work presented in this thesis has been largely driven by observations in the infrared wavelengths regions of nearby low-mass star-forming regions. The primary instrumentation used is summarised in Table 1.2. The bulk of the data presented was obtained using the long wavelength mode of the Infrared Spectrometer and Array Camera (ISAAC) mounted on UT1-Antu of the Very Large Telescope (VLT) at Paranal, Chile from 2000 to 2004. The spectra cover the L- and M-band atmospheric windows from 2.85-4.2 μm and 4.55-4.90 μm, respectively. Most of the ISAAC spectra were obtained as part of a large ESO programme to survey ices in nearby low-mass star-forming regions, although several smaller observing programmes added to the total database. In total, high-quality ice spectra were obtained for $\sim$ 60 lines of sight, primarily toward low-mass young stars with luminosities less than 50 $L_\odot$. The ISAAC sample was designed to have a large overlap with the sources currently being observed from 5.2-37.2 μm by the InfraRed Spectrograph on the Spitzer Space Telescope as part of the Legacy Programme 'From Molecular Cores to Protoplanetary Disks' (c2d). This combination provides almost complete spectral coverage of the mid-infrared, with the unfortunate omis-

sion of the 4.2-4.5 μm region, containing the stretching modes of solid $^{12}CO_2$ and $^{13}CO_2$. The first results from the combined ISAAC-Spitzer spectra are presented in Chapter 5, Boogert et al. (2004) and Noriega-Crespo et al. (2004). Additionally, significant archival data from the ISO archive have been used.

The principal conclusions of this thesis can be summarised as follows:

- The large increase in sensitivity of infrared spectrometers achieved in the last five years has made it possible to explore the spectroscopic diagnostics of the circumstellar environments of 'average' low-mass young stars. Increased sensitivity means that fainter sources as well as a larger sample can be observed in a reasonable time. The large spectroscopic survey in the 3–5 μm range has been used to show that interstellar ices have a very similar spectroscopic signature everywhere in nearby dense clouds. Relative abundances of molecular species may vary slightly with a few notable exceptions, but the basic formation processes are similar. Specifically, this means that little 'processing' has been detected apart from effects due to moderate heating, which seems to be common.

- Chapters 2 and 4 present the first detections of solid methanol in low-mass star forming regions using the 3.54 μm CH-stretch band. The previous conclusion that large abundances of solid methanol are uncommon in low-mass star forming regions is confirmed, and it is shown that the abundance of methanol may suddenly increase from $< 5\%$ to $> 25\%$ relative to water ice in localised regions. In the most extreme case, 2/3 of the CO removed from the gas-phase by freeze-out has been converted to CO_2, CH_3OH and H_2CO.

- The thesis has added to the understanding of the path of molecules from dense clouds to planet-forming disks in two epochs of the evolution of interstellar ices. First, observations presented in Chapter 4 present the first direct measurement of ices in the envelope of a deeply embedded class 0 protostar. This bridges the gap between ices observed in quiescent dense clouds along lines of sight toward extinct background stars and ices observed in the remnant envelopes of class I objects. Second, Chapter 6 describes how dissociative accretion shocks may be observed in disks of more evolved class I objects, directly probing how molecular material is incorporated in disks.

- Spatial mapping of ices at high angular resolution has been introduced as a powerful tracer of surface chemistry as well as the thermal history of dense clouds and protostellar envelopes. In Chapter 4, a specific example has been given for the case of a protostellar envelope, which demonstrates how unique observational constraints on the spatial distribution of the most abundant ice species can be obtained with currently available instrumentation. Specifically, maps of ices can now reach the same spatial resolution of gas-phase observations ($\sim 10''$). In the example studied, 50% of the available oxygen is frozen out as ices in the densest part of the cloud.

- In Chapter 5, it is shown that detailed 2D Monte Carlo radiative transfer modeling coupled with 3–5 μm ground-based and 5.2–37.2 μm Spitzer-IRS

spectroscopy and high resolution near-infrared imaging can constrain the location of ices in edge-on circumstellar disks. The edge-on disk CRBR 2422.8-3423 is used to illustrate the method. In general, ices observed in disks must be warm rather than cold because the optically thick mid-plane cannot be probed by absorption line observations.

- Finally, the 2D radiative transfer model setup developed for CRBR 2422.8-3423 is used in Chapter 7 to show that circumstellar disks may cast large shadows on reflection nebulosity illuminated by the central star. A range of different morphologies of the shadows, mainly dependent on the structure of the surrounding material, is envisioned. Two well-known bipolar reflection nebulae have been modelled as disk shadows using both spectroscopic and imaging data. The conspicuous shadows may be used to identify edge-on disks suited for ice absorption observations.

Bibliography

Adel, A. 1938, ApJ, 88, 186

Al-Halabi, A., Fraser, H. J., Kroes, G. J., & van Dishoeck, E. F. 2004, A&A, 422, 777

Bergin, E. A., Neufeld, D. A., & Melnick, G. J. 1999, ApJL, 510, L145

Boogert, A., Pontoppidan, K., Lahuis, F., et al. 2004, ApJS, 154, 359

Caux, E., Ceccarelli, C., Castets, A., et al. 1999, A&A, 347, L1

Cazaux, S., Tielens, A. G. G. M., Ceccarelli, C., et al. 2003, ApJL, 593, L51

Collings, M. P., Dever, J. W., Fraser, H. J., McCoustra, M. R. S., & Williams, D. A. 2003, ApJ, 583, 1058

Cooley, J. P. 1925, ApJ, 62, 73

Draine, B. T. 2003, ARA&A, 41, 241

Dunne, L., Morgan, H., Eales, S., Ivison, R., & Edmunds, M. 2004, New Astronomy Review, 48, 611

Eddington, A. S. 1937, The Observatory, 60, 99

Frisch, P. C. & Slavin, J. D. 2003, ApJ, 594, 844

Garay, G., Mardones, D., Rodríguez, L. F., Caselli, P., & Bourke, T. L. 2002, ApJ, 567, 980

Gibb, E., Nummelin, A., Irvine, W. M., Whittet, D. C. B., & Bergman, P. 2000, ApJ, 545, 309

Gibb, E. L., Whittet, D. C. B., Boogert, A. C. A., & Tielens, A. G. G. M. 2004, ApJS, 151, 35

Goldsmith, P. F., Melnick, G. J., Bergin, E. A., et al. 2000, ApJL, 539, L123

Habing, H. J. 1996, A&A Rev., 7, 97

Hartmann, J. 1904, ApJ, 19, 268

Hony, S. 2002, Ph.D. Thesis

Hornekaer, L., Baurichter, A., Petrunin, V. V., Field, D., & Luntz, A. C. 2003, science, 302, 1943

Howk, J. C., Savage, B. D., & Fabian, D. 1999, ApJ, 525, 253

Kahn, F. D. 1952, MNRAS, 112, 518

Malfait, K., Waelkens, C., Bouwman, J., de Koter, A., & Waters, L. B. F. M. 1999, A&A, 345, 181

Martín-Pintado, J., Rizzo, J. R., de Vicente, P., Rodríguez-Fernández, N. J., & Fuente, A. 2001, ApJL, 548, L65

Mathis, J. S., Rumpl, W., & Nordsieck, K. H. 1977, ApJ, 217, 425

McKellar, A. 1940, PASP, 52, 187

McMath, R. R., Mohler, O. C., & Goldberg, L. 1948, AJ, 54, 44

Merrill, P. W. 1934, PASP, 46, 206

Migeotte, M. V. 1948, Phys. Rev., 73, 519

Neugebauer, G., Martz, D. E., & Leighton, R. B. 1965, ApJ, 142, 399

Noriega-Crespo, A., Morris, P., Marleau, F. R., et al. 2004, ApJS, 154, 352

Pierce, A. K., Goldberg, L., McMath, R. R., & Mohler, O. C. 1952, Physical Review, 85, 140

Poglitsch, A., Herrmann, F., Genzel, R., et al. 1996, ApJL, 462, L43+

Sleator, W. W. & Phelps, E. R. 1925, ApJ, 62, 28

Smith, R. G., Blum, R. D., Quinn, D. E., Sellgren, K., & Whittet, D. C. B. 2002, MNRAS, 330, 837

Strömgren, B. 1939, ApJ, 89, 526

Swings, P. 1944, PASP, 56, 220

Swings, P. & Rosenfeld, L. 1937, ApJ, 86, 483

van de Hulst, H. C. 1946, Recherches Astronomiques de l'Observatoire d'Utrecht, 11, 2

Vandenbussche, B., Ehrenfreund, P., Boogert, A. C. A., et al. 1999, A&A, 346, L57

Watanabe, N., Shiraki, T., & Kouchi, A. 2003, ApJL, 588, L121

Whittet, D. C. B., Gerakines, P. A., Hough, J. H., & Shenoy, S. S. 2001, ApJ, 547, 872

Womack, M., Ziurys, L. M., & Wyckoff, S. 1992, ApJ, 393, 188

Zubko, V., Dwek, E., & Arendt, R. G. 2004, ApJS, 152, 211

Chapter 2

Detection of abundant solid methanol toward young low mass stars

Abstract

We present detections of the absorption band at 3.53 μm due to solid methanol toward three low-mass young stellar objects located in the Serpens and Chamaeleon molecular cloud complexes. The sources were observed as part of a large spectroscopic survey of $\approx$40 protostars. This is the first detection of solid methanol in the vicinity of low mass ($M \lesssim 1\ M_\odot$) young stars and shows that the formation of methanol does not depend on the proximity of massive young stars. The abundances of solid methanol compared to water ice for the three sources are in the range 15-25% which is comparable to those for the most methanol-rich massive sources known. The presence of abundant methanol in the circumstellar environment of some low mass young stars has important consequences for the formation scenarios of methanol and more complex organic species near young solar-type stars. [1]

2.1 Introduction

The presence and origin of complex organic molecules in protostellar regions and their possible incorporation in protoplanetary disks is an active topic of research, both observationally and through laboratory simulations. Large organic molecules such as CH_3OCH_3 and CH_2CH_3CN have been detected with enhanced abundances in so-called 'hot cores' around massive young stars (e.g. Gibb, 2001; Hatchell et al., 1998). In the laboratory, UV photolysis of ice mixtures of species prepared with interstellar abundances followed by thermal warm-up to 300 K is known to lead to a wealth of complex species such as carboxylic acids and esters (Briggs et al., 1992), hexamethylene-tetramine (Bernstein et al., 1995) and prebiotic molecules including amino acids (Bernstein et al., 2002; Munõz Caro et al., 2002). In the ice experiments, methanol is thought to be a key molecule in the production of these complex molecules. Understanding the methanol content of interstellar ice mantles and its variation in different circumstellar environments is therefore

---

[1] K. M. Pontoppidan, E. Dartois, E. F. van Dishoeck et al. 2003, A&A, 404, L17

essential to test the validity of the basic assumptions that enter the chemical models and experimental approach.

So far, solid methanol has only been detected along lines of sight associated with intermediate- to high-mass protostars, with abundances ranging from 5% up to 30% with respect to the dominant ice mantle component, H_2O (Dartois et al., 1999). Extensive searches toward low-mass protostars have resulted in typical upper limits of a few % (Brooke et al., 1999; Chiar et al., 1996). In contrast, gas-phase methanol has been found toward both high- and low-mass YSOs with evidence for abundance jumps of factors of 100–1000 in the inner part of the envelope, consistent with ice evaporation (e.g. Bachiller et al., 1995; Schöier et al., 2002; van der Tak et al., 2000). Still, the observed gas-phase column densities of methanol are usually $10 - 10^4$ times less than those observed in the solid phase (e.g. Schöier et al., 2002). In hot cores, a rapid high-temperature gas-phase chemistry is triggered by the evaporation of methanol-rich ices, which forms high abundances of large organic molecules for a period of $10^4 - 10^5$ yr (e.g. Charnley et al., 1992; Rodgers & Charnley, 2001). Understanding the origin of solid CH_3OH and its variation from source to source is a key ingredient for these models.

As part of a large VLT-ISAAC 3–5 μm spectral survey toward young low mass stars we have detected an absorption feature at 3.53 μm towards at least three icy sources out of $\approx$40, which is attributed to solid methanol. Two of the sources are part of the dense cluster of young low-mass stars, SVS 4, located in the Serpens cloud core (Eiroa & Casali, 1989). The third source is a more isolated low-mass class I source in the Chamaeleon I cloud known as Cha INa 2 (Persi et al., 1999). The spectra presented here represent the first detections of solid methanol toward low mass YSOs. The observations and analysis are reported in §2, whereas the implications for the chemical evolution of circumstellar matter are discussed in §3.

2.2 Observations

2.2.1 The L-band spectra

The observations were performed using the Infrared Spectrometer and Array Camera (ISAAC) mounted on the Very Large Telescope UT1-Antu of the European Southern Observatory at Cerro Paranal. L-band spectra were obtained using the low resolution mode and the $0\rlap{.}''3$ slit resulting in resolving powers of $\lambda/\Delta\lambda = 1200$. SVS 4-5 and SVS 4-9 were observed simultaneously on May 5, 2002. Cha INa 2 was observed on May 6, 2002. All spectra were recorded during good weather conditions. The data were reduced using our own IDL routines, which are described in Pontoppidan et al. (2003). Correction for telluric absorption features was done using the early-type standard stars BS 4773 (B5V) and BS 7348 (B8V) for Cha INa 2 and the SVS 4 sources, respectively. The wavelength calibration was obtained using the telluric absorption features with an estimated accuracy of 0.001 μm. The spectra were flux calibrated using the standard stars with an estimated uncertainty of 15%, mainly due to uncertainties in slit losses.
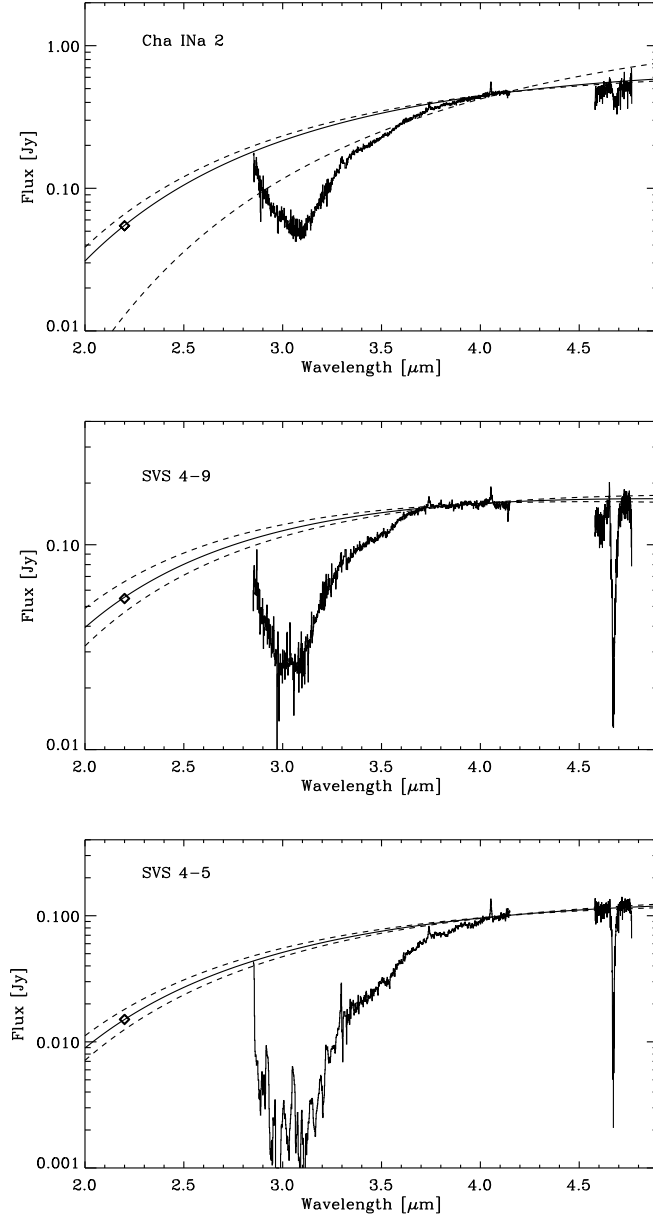
Figure 2.1: *Adopted blackbody continua for estimating water band optical depths (solid curves). The K-band magnitudes (diamonds) for the Serpens sources are taken from Giovannetti et al. (1998). The adopted K-band magnitude for Cha INa 2 is discussed in the text. Dashed curves indicate continua calculated using a conservative estimate for the uncertainties on the (sometimes variable) K-band fluxes. The spectrum of SVS 4-5 has been smoothed to a resolution of $R = 120$ between 2.8 and 3.3 μm.*
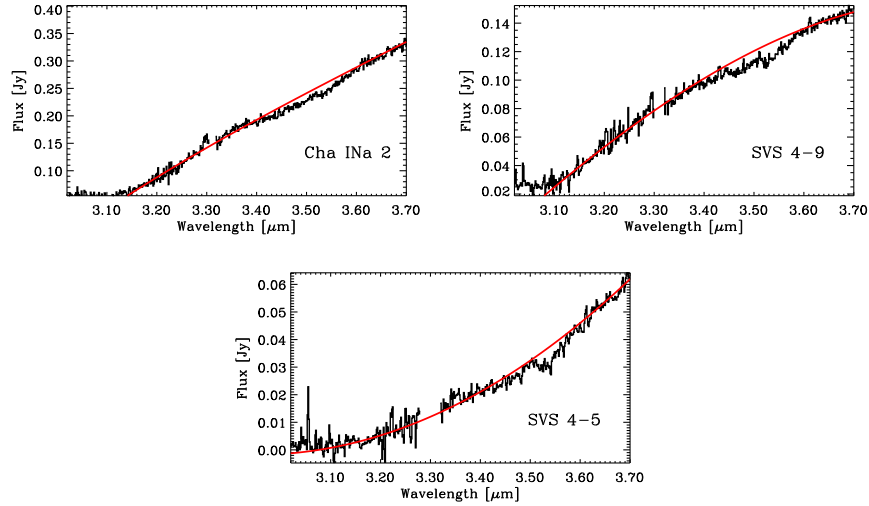
Figure 2.2: *Local third order polynomial continua for extracting the methanol band profiles.*

2.2.2 Derivation of methanol abundances

The water band profile was obtained by adopting a blackbody continuum fitted to a K-band photometric point from the literature and the observed L-band spectrum from 4.0 to 4.15 μm as well as the M-band spectra, which are discussed in detail in Pontoppidan et al. (2003). The 2.8–4.8 μm spectra are shown in Fig. 2.1. The accuracy of the K-band points are crucial for estimating the column density of the water ice bands. However, the K-band fluxes have considerable uncertainties since many young stellar objects are known to be highly variable and the sources may have changed their flux level since the photometric measurement. Indeed, Cha INa 2 is known to vary significantly in the K-band (Carpenter et al., 2002) and has apparently continuously brightened with 1.7 mag between March 1996 and April 2000 (Carpenter et al., 2002; Kenyon & Gómez, 2001; Persi et al., 1999) to $K = 11.044$. It is found that at least $K = 10.2$ is necessary to fit the continuum defined by the ISAAC L and M-band spectra, consistent with the assumption that the source has continued to brighten until May 2002 with the same rate. The continua used for deriving the optical depths of the water bands are shown in Fig. 2.1 along with continua fitted using extreme K-band fluxes. For the Serpens sources a conservative estimate of the K-band variability is 0.2 mag when comparing with the photometry of Eiroa & Casali (1992). For Cha INa 2 continua using $K = 10$ and $K = 12.75$ are also shown.

A local third order polynomial was used to estimate the continuum around the methanol feature (see Fig. 2.2). The polynomial was fitted to the points between 3.1 μm and 3.2 μm, and the region between 3.63 μm and 3.70 μm. The confidence in the local continuum for extraction of the methanol profiles is high, partly due to
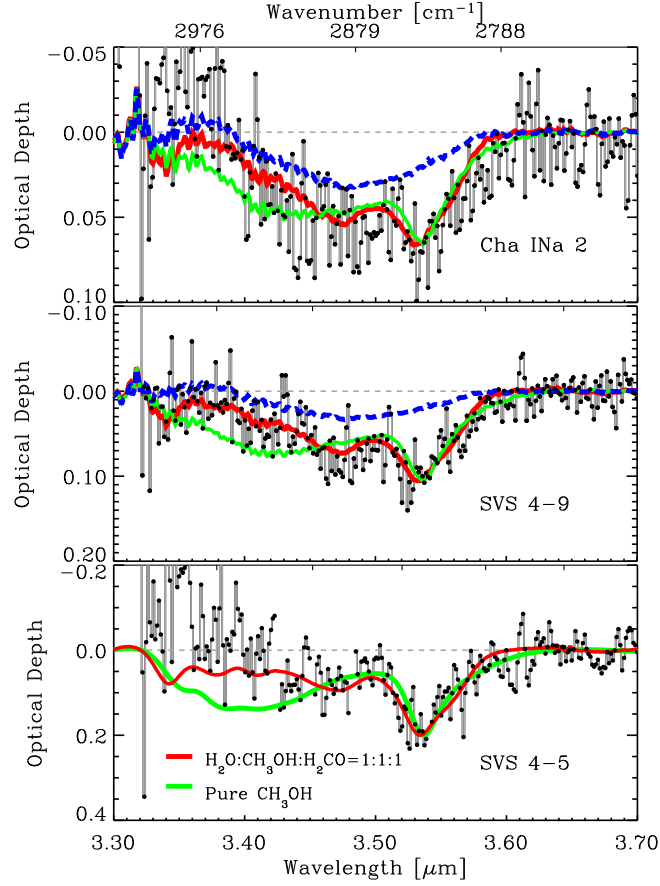
Figure 2.3: *The detected methanol bands on an optical depth scale. The dashed curve shows the 3.47 μm feature from the intermediate mass YSO Reipurth 50. The solid curves show the sum of laboratory spectra of methanol-rich ice mixtures at 10 K and the 3.47 μm feature from Reipurth 50. There is no contribution from a 3.47 μm feature in SVS 4-5. The contents of the laboratory mixtures are indicated in the lower panel.*

the low order of the polynomial and partly due to the low curvature required for the three spectra. The uncertainty in the derived abundances is thus dominated by the main water band continuum. The measured water ice abundances are presented in Table 2.1. The values were derived by fitting a laboratory spectrum of pure amorphous water ice at 50 K to the observed water bands and integrating the scaled laboratory spectrum from 2.5 to 3.7 μm. None of the observed water bands are saturated. However, due to the low S/N ratio in SVS 4-5, the fit in this source relies on the wings in the water band. The adopted band strength is 2.0×10^{-16} cm molec^{-1} (Gerakines et al., 1995). Note that laboratory measure-

ments of solid state band strengths may in general only be accurate within 30%.

The final absorption profiles in the 3.3–3.7 μm region are shown in Fig. 2.3 on an optical depth scale. Common to the profiles of SVS 4-9 and Cha INa 2 is a broad feature centered at 3.47 μm along with a narrow feature at 3.53 μm seen in all three sources. The former is most likely the same feature seen in this wavelength region toward many other young stars, generally known as the '3.47 μm feature' and thought to be due to diamonds or an ammonia hydrate. The 3.53 μm feature is seen toward much fewer objects and is assigned to the ν_3 CH-stretching vibration band of solid methanol.

To estimate the true depth of the methanol band, it is necessary to remove the contribution from the 3.47 μm feature. A first-order approximation is to use a high signal-to-noise profile observed toward another YSO. We chose here the feature observed toward the intermediate mass YSO Reipurth 50 described in Dartois et al. (2003). The feature has a center position of 3.478 μm and a $FWHM$ of 0.12 μm. 3.47 μm features from other sources give similar results (Brooke et al., 1999). The 3.47 μm band from Reipurth 50 was fitted to the observed spectra simultaneously with a laboratory methanol band.

It is well-known that the 3.53 μm methanol band is sensitive to the structure and composition of the ice (Ehrenfreund et al., 1999). Laboratory spectra are compared to the observed methanol bands in Fig. 2.3. A laboratory spectrum of pure methanol does not give a perfect fit of the exact profile to any of the observed spectra, mainly due to the relative weakness of the secondary band of solid methanol at 3.40 μm in the observed spectra. It is interesting to note that the ratio of the 3.40 μm and the 3.53 μm methanol features in low-mass sources are similar to that of the high-mass sources of Dartois et al. (1999). A laboratory spectrum rich in water and formaldehyde (H_2CO) can reproduce the spectra. However, the H_2CO identification was found to be inconsistent for the massive stars W 33A and RAFGL 7009S (Dartois et al., 1999) due to the absence of bands at 5.8 and 6.69 μm. Other mechanisms of reducing the strength of the 3.40 μm band cannot be ruled out. For example, irradiated pure methanol spectra annealed to temperatures higher than 60 K also gives good matches. For the estimate of the CH_3OH column densities it is assumed that H_2CO does not contribute to the 3.53 μm band. The adopted band strength of the CH-stretching mode at 3.53 μm is 5.3×10^{-18} cm molec^{-1}. This value is not found to vary significantly depending on the ice mixture (Kerkhof et al., 1999). The derived abundances are summarized in Table 2.1.

Brooke et al. (1999) and Chiar et al. (1996) find in general upper limits on the methanol abundance in the solid phase of a few % with respect to water. We find consistent results for the rest of our observed sample, i.e. methanol with an abundance of more than 5% is found toward only 3 out of a sample of $\approx$40 low mass YSOs.

Table 2.1: *Column densities of solid methanol and water*

Source	$\tau(H_2O)$	$N_{H_2O}^a$ 10^{18} cm^{-2}	$N_{CH_3OH}^a$ 10^{18} cm^{-2}	N_{CH_3OH}/N_{H_2O}
SVS 4-5	4 ± 1	7 ± 2	1.5 ± 0.1	0.21 ± 0.05
SVS 4-9	1.6 ± 0.1	2.5 ± 0.2	0.62 ± 0.05	0.25 ± 0.03
Cha INa2	1.5 ± 0.1	2.2 ± 0.2	0.3 ± 0.05	0.14 ± 0.03

[a] Statistical 1σ errors. Uncertain laboratory estimates of band strengths may introduce a systematic error of up to 30%.

2.3 Chemical implications

The methanol can be produced in space and in laboratory experiments through several different pathways. Gas-phase chemistry produces only low abundances of CH_3OH, of order 10^{-9} with respect to H_2, so that simple freeze-out of gas-phase CH_3OH cannot reproduce the observed solid state abundances of $\sim 10^{-5}$. A possible route is therefore thought to be grain surface hydrogenation reactions of solid CO with atomic H, leading to H_2CO and eventually CH_3OH (Tielens & Hagen 1982, Charnley et al. 1997). Experimental results on this reaction scheme at low temperatures are still controversial. Watanabe & Kouchi (2002) find efficient formation of H_2CO and CH_3OH by warm (≈ 300 K) hydrogen addition to CO in an H_2O-CO ice mixture, but the temperature of the hydrogen is not relevant for quiescent dark clouds. Other authors find yields which show that the formation of methanol directly via hydrogenation of CO is inefficient in dark clouds in the 10–25 K regime (Hiraoka et al., 2002). Further experiments are needed to solve this discrepancy.

Theoretical models of grain surface chemistry indicate that the fraction of CH_3OH ice with respect to H_2O ice, as well as the H_2CO/CH_3OH ratio, depend on the ratio of H accretion to CO accretion on the grains and thus on the density of the cloud (e.g., Charnley et al. 1997, Keane et al. 2002). In the framework of these models, solid CH_3OH abundances of 15–30% with respect to H_2O ice such as found here can only be produced at low densities, $n \approx 10^4$ cm^{-3}. Moreover, the region needs to be cold, $T_{dust} < 20$ K, to retain sufficient CO on the grain surfaces. The models thus suggest that solid CH_3OH formation occurs primarily in the cold pre-stellar phase. However, this fails to explain the large range of methanol abundances observed along lines of sight toward low mass YSOs in the same star forming cloud, unless the duration of the pre-stellar phase varies strongly from source to source. As discussed by van der Tak et al. (2000), comparison of solid CH_3OH with solid CO_2 can further constrain the H/O ratio of the accreting gas and thus the density and duration of the pre-stellar phase. For low-mass YSOs, data on solid CO_2 are not yet available, but will be possible with the *Space Infrared Telescope Facility* (SIRTF) via the 15.2 μm CO_2 bending mode.

An alternative formation route of solid CH_3OH may be through ultraviolet processing (Schutte, 1988) or proton irradiation of ices (Hudson & Moore, 1999).

However, as shown by van der Tak et al. (2000), the CH_3OH production rates in these experiments are orders of magnitude lower than those through grain surface formation. The fact that some low-mass sources show similarly high solid CH_3OH abundances as many massive sources argues further against ultraviolet radiation playing a significant role.

It is clear that any formation scheme of solid CH_3OH must be able to explain local ice mantle abundances of at least 15–30% compared to H_2O ice, regardless of the potential differences in density, temperature and ultraviolet radiation field between high- and low-mass YSO environments. At the same time, such models need to explain the large variations in solid CH_3OH abundances from object to object, with abundances of less than 3–5% found for both low- and high-mass YSOs (Brooke et al., 1999; Chiar et al., 1996). In this context, it is interesting that abundant solid methanol is now detected toward two sources which are members of the same dense cluster, SVS 4-5 and 4-9, while other nearby sources in Serpens such as CK 1 show solid methanol abundances of less that a few % . This suggests that the ice mantle chemistry may differ significantly between different regions even in the same star-forming clouds or that the formation and subsequent presence of methanol on grain surfaces is a transient phenomenon related to strong heating of the ices. In the last scheme the methanol may not exist for long in the solid phase before being desorbed by the continuous heating of the ice. Finally shock processing may produce a different ice chemistry (Bergin et al., 1998). Making a survey of the SVS 4 cluster lines of sight may help to decipher the relation of the methanol ice to the environmental differences between 'quiescent' environments as opposed to the massive and complex star-forming environments probed so far.

Acknowledgements

Bibliography

Bachiller, R., Liechti, S., Walmsley, C. M., & Colomer, F. 1995, A&A, 295, L51

Bergin, E. A., Neufeld, D. A., & Melnick, G. J. 1998, ApJ, 499, 777

Bernstein, M. P., Dworkin, J. P., Sandford, S. A., Cooper, G. W., & Allamandola, L. J. 2002, Nature, 416, 401

Bernstein, M. P., Sandford, S. A., Allamandola, L. J., Chang, S., & Scharberg, M. A. 1995, ApJ, 454, 327

Briggs, R., Ertem, G., Ferris, J. P., et al. 1992, Origins of Life Evol. Biosphere, 22, 287

Brooke, T. Y., Sellgren, K., & Geballe, T. R. 1999, ApJ, 517, 883

Carpenter, J. A., Hillenbrand, L. A., Skrutskie, M. F., & Meyer, M. R. 2002, AJ, 124, 1001

Charnley, S. B., Tielens, A. G. G. M., & Millar, T. J. 1992, ApJ, 399, L71

Chiar, J. E., Adamson, A. J., & Whittet, D. C. B. 1996, ApJ, 472, 665

Dartois, E., Schutte, W., Geballe, T. R., et al. 1999, A&A, 342, L32

Dartois, E., Thi, W.-F., Pontoppidan, K. M., et al. 2003, A&A, submitted

Ehrenfreund, P., Kerkhof, O., Schutte, W. A., et al. 1999, A&A, 350, 240

Eiroa, C. & Casali, M. M. 1989, A&A, 223, L17

—. 1992, A&A, 262, 468

Gerakines, P. A., Schutte, W. A., Greenberg, J. M., & van Dishoeck, E. F. 1995, A&A, 296, 810

Gibb, E. L. 2001, PhD thesis, Rensselaer Polytechnic Institute

Giovannetti, P., Caux, E., Nadeau, D., & Monin, J.-L. 1998, A&A, 330, 990

Hatchell, J., Thompson, M. A., Millar, T. J., & Macdonald, G. H. 1998, A&AS, 133, 29

Hiraoka, K., Tesuya, S., Sato, S., et al. 2002, ApJ, 577, 265

Hudson, R. L. & Moore, M. H. 1999, Icarus, 140, 451

Kenyon, S. J. & Gómez, M. 2001, AJ, 121, 2673

Kerkhof, O., Schutte, W. A., & Ehrenfreund, P. 1999, A&A, 346, 990

Munõz Caro, G. M., Meierheinrich, U. J., Schutte, W. A., et al. 2002, Nature, 416, 403

Persi, P., Marenzi, A. R., Kaas, A. A., et al. 1999, AJ, 117, 439

Pontoppidan, K. M., Fraser, H., Dartois, E., et al. 2003, A&A, submitted

Rodgers, S. D. & Charnley, S. B. 2001, ApJ, 546, 324

Schöier, F. L., Jørgensen, J. K., van Dishoeck, E. F., & Blake, G. A. 2002, A&A, 390, 1001

Schutte, W. A. 1988, PhD thesis, Leiden University

van der Tak, F. F. S., van Dishoeck, E. F., & Caselli, P. 2000, A&A, 361, 327

Bibliography

Watanabe, N. & Kouchi, A. 2002, ApJ, 571, L173

Chapter 3

A 3–5 μm spectroscopic survey of young low mass stars I

Structure of the CO ice

Abstract

Medium resolution ($\lambda/\Delta\lambda = 5\,000 - 10\,000$) VLT-ISAAC M-band spectra are presented of 39 young stellar objects in nearby low-mass star forming clouds showing the 4.67 μm stretching vibration mode of solid CO. By taking advantage of the unprecedentedly large sample, high S/N ratio and high spectral resolution, similarities in the ice profiles from source to source are identified. It is found that excellent fits to all the spectra can be obtained using a phenomenological decomposition of the CO stretching vibration profile at 4.67 μm into 3 components, centered on 2143.7 cm^{-1}, 2139.9 cm^{-1} and 2136.5 cm^{-1} with fixed widths of 3.0, 3.5 and 10.6 cm^{-1}, respectively. All observed interstellar CO profiles can thus be uniquely described by a model depending on only 3 linear fit parameters, indicating that a maximum of 3 specific molecular environments of solid CO exist under astrophysical conditions. A simple physical model of the CO ice is presented, which shows that the 2139.9 cm^{-1} component is indistinguishable from pure CO ice. It is concluded, that in the majority of the observed lines of sight, 60-90% of the CO is in a nearly pure form. In the same model the 2143.7 cm^{-1} component can possibly be explained by the longitudinal optical (LO) component of the vibrational transition in pure crystalline CO ice which appears when the background source is linearly polarised. The model therefore predicts the polarisation fraction at 4.67 μm, which can be confirmed by imaging polarimetry. The 2152 cm^{-1} feature characteristic of CO on or in an unprocessed water matrix is not detected toward any source and stringent upper limits are given. When this is taken into account, the 2136.5 cm^{-1} component is not consistent with the available water-rich laboratory mixtures and we suggest that the carrier is not yet fully understood. A shallow absorption band centered between 2165 cm^{-1} and 2180 cm^{-1} is detected towards 30 sources. For low-mass stars, this band is correlated with the CO component at 2136.5 cm^{-1}, suggesting the presence of a carrier different from XCN at 2175 cm^{-1}. Furthermore the absorption band from solid ^{13}CO at 2092 cm^{-1} is detected towards IRS 51 in the ρ Ophiuchi cloud complex and an isotopic ratio of ^{12}CO/^{13}CO$= 68 \pm 10$ is derived. It is shown that all the observed solid ^{12}CO profiles, along with the solid ^{13}CO profile, are consistent with grains

with an irregularly shaped CO ice mantle simulated by a Continuous Distribution of Ellipsoids (CDE), but inconsistent with the commonly used models of spherical grains in the Rayleigh limit. [1] [2]

3.1 Introduction

Solid interstellar CO was first reported by Soifer et al. (1979) who observed a strong absorption band at 4.61 μm in a spectrum from the Kuiper Airborne Observatory (KAO) along the line of sight towards the massive young stellar object (YSO) W 33A. Although the absorption band later turned out to be dominated by a CN-stretching carrier, this was the first observational indication that the ice mantles on dust grains in dense clouds carry a rich chemistry, as indicated by early chemical models (e.g. Tielens & Hagen, 1982, and references therein). Until this time the early ideas about "dirty ice" were mostly supported by observations of the 3.08 μm water band and the extended red wing of this band, which was suggested to be due to NH_3-H_2O complexes and CH_3OH (e.g. Gillett & Forrest, 1973; Willner et al., 1982). The presence of both solid CO and XCN towards massive young stars was confirmed by Lacy et al. (1984). The identification and subsequent study of the ices in general, and of the CO stretching mode at 4.67 μm in particular, was aided by laboratory spectroscopy of ices intended to simulate interstellar ices, such as those presented in e.g. Hagen et al. (1979); Sandford et al. (1988); Schmitt et al. (1989) and more recently by Ehrenfreund et al. (1997); Elsila et al. (1997) and Baratta & Palumbo (1998). The typical spectral resolution of these studies was $\lambda/\Delta\lambda \sim 1\,000 - 2\,000$ ($1.0 - 2.0$ cm^{-1}). However, at this resolving power the ^{12}CO stretching mode as well as the ^{13}CO stretching mode at 2092 cm^{-1} are in general not fully resolved. This problem has caused difficulties when interpreting both interstellar and laboratory spectra.

The laboratory studies have shown that some band profiles, and in particular that of the CO stretching vibration mode, are sensitive to the presence of secondary species in the ice as well as to thermal and energetic processing of the ices, and attempts have been made to quantify some of these effects. For instance, the 4.67 μm CO stretching vibration profile has been used in attempts to constrain the concentration of species like CO_2, O_2, N_2 and the degree to which the CO is mixed with the water component (Chiar et al., 1994, 1995, 1998; Tielens et al., 1991). This information is otherwise hard or impossible to extract from observations (Vandenbussche et al., 1999). It has also been suggested that the CO profile may be used as an indicator of the degree to which the ice has been thermally processed if different components of the profile correspond to CO ices in environments of different volatility. For instance, pure CO may be expected to desorb at lower temperatures than CO mixed with water (Collings et al., 2003; Sandford & Allamandola, 1988). The laboratory simulations have been used for comparisons with a large number of spectra from both high and low mass young stars and quiescent

---

[1] K. M. Pontoppidan, H. J. Fraser, E. Dartois et al. 2003, A&A, 408, 981

[2] Based on observations obtained at the European Southern Observatory, Paranal, Chile, within the observing programs 164.I-0605 and 69.C-0441.

cloud lines of sight probed towards background late-type giant stars, to constrain the ice mantle composition for a wide range of different cloud conditions. Often these studies employ the full range of available laboratory spectra in order to find the best-fitting combination of ice mixtures to each source (Chiar et al., 1994, 1995, 1998; Kerr et al., 1993; Teixeira et al., 1998; Tielens et al., 1991). This approach is known to suffer from serious degeneracies and is further complicated by the fact that profiles from ice mixtures with a high concentration of CO are significantly affected by the shape of the grains (Tielens et al., 1991). Consequently, the detailed environment of solid CO in interstellar grain mantles and its role in the solid state chemistry is not strongly constrained by observations. Clearly, a large, consistent sample of lines of sight is necessary to obtain further information on the "typical" structure of ices in space.

Recent results from medium to high resolution ($R = 5\,000 - 25\,000$) spectrometers mounted on 8 m class telescopes are beginning to cast new light on the 3-5 μm region of protostellar and interstellar spectra. In particular, new insights have been gained through careful studies of the resolved CO ice band structure and its relation to gas phase CO (Boogert et al., 2002b), using the higher sensitivity to probe new environments (Thi et al., 2002) and using the ^{13}CO band to constrain both composition and grain shape corrections (Boogert et al., 2002a).

Here we present medium resolution ($R = 5\,000 - 10\,000$, $\Delta\tilde{\nu} = 0.4 - 0.2\ \mathrm{cm}^{-1}$) M-band spectra of 39 low mass young stellar objects obtained with the Infrared Spectrometer And Array Camera (ISAAC) mounted on the Very Large Telescope (VLT) ANTU telescope of the European Southern Observatory at Cerro Paranal. These spectra have allowed us to obtain meaningful statistics on the general shape of the CO ice profile for the first time. In this work, we show that statistically there is enormous advantage in using a large sample of fully resolved spectra from a well-defined set of young stellar objects. By using the highest possible spectral resolution, we are able to cast new light on the underlying ice structure from a detailed analysis of the CO stretching vibration profile. The L-band spectra and the analysis of the gas phase CO lines seen in the M-band spectra will be presented in later articles.

This chapter is organised as follows. In Sec. 3.2 the sample of sources is described including the adopted selection criteria, observational procedures and main features in the spectra. Sec. 3.3 presents a phenomenological decomposition of the CO ice band and the observational results of the decompositions are then discussed. A simple physical model is described in Sec. 3.4, which can partly explain the success of the phenomenological decomposition. The results from the observations and the modeling are discussed in Sec. 3.5 and the astrophysical implications are outlined. Finally, Sec. 3.6 presents the conclusions and suggests further observations and laboratory experiments which can be used to test the results presented in this work. Appendix 3.1 reviews the simplest mechanisms governing solid state line shapes and Appendix 3.2 gives comments on individual sources in the sample.

3.2 The sample

3.2.1 Source selection

The primary objective was to perform a broad survey of the dominant ice components on grains surrounding low-mass embedded objects in the nearest ($D <$ 500 pc) star forming clouds in the southern sky. Emphasis was put on obtaining good S/N ratios at the highest possible spectral resolution in order to study not just the main H_2O and CO features but also the fainter ice species, probe substructure in the ice features, and obtain a census of gas-phase ro-vibrational emission and absorption towards low mass young stars. The observed sample was primarily extracted from the list of sources to be observed with the Space Infrared Telescope Facility (SIRTF) as part of the Legacy project *From Molecular Cores to Planets* (Evans, 2003), but was supplemented with additional sources. The majority of sources have luminosities of $L_{bol} < 10$ L$_\odot$, with only a few brighter sources being included for comparison. Embedded sources are selected from their published Lada classes if no other information is available indicating youth. The sample includes class I sources as well as flat spectrum sources defined by having a vanishing spectral index between 2.5 and 15 μm (Bontemps et al., 2001). In addition, the background star CK 2 in Serpens was observed to probe the quiescent cloud material.

A number of the sources have published M-band spectra, albeit at lower spectral resolution, coverage and S/N ratio and were re-observed in order to get a consistent sample. The list of observed sources and relevant observational parameters is given in Table 3.1.

3.2.2 Observations and data reduction

The ISAAC spectrometer is equipped with a 1024×1024 Aladdin array, which is sensitive in the 1-5 μm region. The pixel scale is $0.148''$ pixel^{-1} when using the spectroscopic objective. The telescope was operated using a standard chop-nod scheme with typical chop-throws of 10-20$''$. Both L and M-band spectra of each source were obtained. The medium resolution grating was used for the 4.53-4.90 μm region, resulting in resolving powers of $\lambda/\Delta\lambda = 5\,000 - 10\,000$ ($0.4 - 0.2$ cm^{-1}). Here a single setting covering 4.53 to 4.77 μm was always observed and a second setting extending to 4.85-4.90 μm was obtained if necessary, e.g. because of the presence of strong gas phase lines in the first setting. Often, it was possible to place a secondary source in the slit by rotating the camera. In this way spectra of both components of all binaries with separations of more than $\sim 1''$ were obtained.

The data were reduced using our own IDL routines. The individual frames were corrected for the non-linearity of the Aladdin detector, distortion corrected using a startrace map, and bad pixels and cosmic ray hits were removed before co-adding. Both positive and negative spectral traces were extracted and added before division by the standard star spectrum. An optimal small shift and exponential airmass correction between the source and the standard were applied by requiring that the pixel-to-pixel noise on the continuum of the final spectrum is

minimized. Before an exponential airmass correction is applied, the detector and filter response curve has to be removed in order to obtain a spectrum of the true atmospheric absorption. The combined filter and detector response curve was obtained by fitting an envelope to both the standard star spectrum and a spectrum of the approximate atmospheric transmission and taking the ratio of the two envelopes.

The spectra were flux calibrated relative to the standard and wavelength calibrated relative to telluric absorption lines in the standard star spectrum. The uncertainty in the flux calibration is estimated to be better than 30% for most sources and the wavelength calibration is accurate to ~ 5 km s^{-1}. The high accuracy in wavelength calibration is due to the large number of well-defined and separated telluric lines present in a medium resolution M-band spectrum. For some of the weaker sources, the wavelength calibration becomes considerably more inaccurate because of difficulties in determining the small shift always present between the standard star spectrum and the source spectrum.

Finally, optical depth spectra were derived by fitting a blackbody continuum to the regions where no features are expected to appear, namely around 4.52-4.55 μm and around 4.76-4.80 μm. In every case care was taken not to include gas phase lines and regions affected by strong telluric residual in the fit. In cases of doubt the fit was compared to the continuum in the 4.0-4.2 μm region and adjusted accordingly. However, normally the L-band spectra were not used for the continuum fit, due to uncertainties in the relative flux calibrations between the two spectra.

3.2.3 Features in the M band spectra

The most prominent features in the 4.5-5.0 μm region of low mass young stellar objects are the absorptions from the stretching mode of solid CO around 4.67 μm and the multitude of lines from the ro-vibrational fundamental band of gas-phase CO extending across the entire M-band. In addition the region covers the CN stretching band around 4.61 μm as well as the bright Pfβ hydrogen recombination line at 4.65 μm and the S(9) line from molecular hydrogen at 4.687 μm. The VLT spectra in general show the presence of all these features, although the shape and strength of each feature varies greatly from source to source. For example, the ro-vibrational lines of CO are seen as both broad and narrow absorption lines and as broad and narrow emission lines. The broad absorption lines are often asymmetric indicating the presence of outflows and infall. The broad emission lines show a higher degree of symmetry and are clearly caused by hot gas as indicated by the presence of CO molecules excited to the second and even third vibrational levels. One source showing narrow emission lines (GSS 30 IRS 1) is treated in detail in Pontoppidan et al. (2002). All the gas-phase CO lines will be analysed in a later paper (Pontoppidan et al., in prep). At a resolving power of $\lambda/\Delta\lambda = 10\,000$ (30 km s^{-1} = 0.2 cm^{-1}) all solid state features are completely resolved, including the central parts of the main CO feature and the very narrow ^{13}CO feature. This is generally not the case for previously obtained astronomical and laboratory spectra at resolutions of $\lambda/\Delta\lambda = 1\,000 - 2\,000\,(1 - 2\ \text{cm}^{-1})$.

The individual M-band spectra with detected CO ice are shown in Figs. 3.1–3.7

on an optical depth scale. IRS 46, IRS 54, LLN 39 and LLN 47 have no or only marginally detected CO ice bands and are not shown. The spectrum of GSS 30 IRS 1 is presented in Pontoppidan et al. (2002) and shows the presence of a very shallow CO ice band. The spectrum of CRBR 2422.8-3423 is shown in Thi et al. (2002) and the spectrum of LLN 17=IRAS 08448-4343 is shown in Thi (2002).

3.2.4 New detection of solid ^{13}CO

The $2092 \, \text{cm}^{-1}$ band of solid ^{13}CO has been detected in one source in the sample, namely IRS 51 in the ρ Ophiuchi cloud. The source is a transitional Class I-II object and shows a very deep ($\tau \sim 5$) ^{12}CO ice band. The ^{13}CO band has an optical depth of 0.12 and a width of $1.2 \, \text{cm}^{-1}$. The detection is analysed in Sec. 3.4.4. This is only the second ^{13}CO feature reported in the literature after NGC 7538 IRS 9 (Boogert et al., 2002a) and the first towards a low mass source.

3.3 Analytical fits

3.3.1 A phenomenological approach

One approach to the analysis of interstellar ice bands, especially in the case of the CO stretching vibration, is via a mix-and-match scheme, whereby laboratory spectra of differing chemical composition, relative concentrations, temperature and degree of processing are compared to astronomical spectra to find the best fits (e.g. Chiar et al., 1994, 1995, 1998; Teixeira et al., 1998). While the presence of solid CO can be unambiguously identified using the laboratory data, the mix-and-match approach is seriously affected by the degeneracy introduced by the dependancy of the CO vibration profile on many experimental parameters. In Sec. 3.5.3 we will return to this point and discuss the best strategies for comparing laboratory data to interstellar spectra.

Due to the degeneracy encountered when attempting to match CO ice bands in space with a database of interstellar ice simulations, a more phenomenological approach is attempted here. Results from laboratory work can then be applied subsequently to explain the general trends identified using a phenomenological method of analysis. Similar approaches to the analysis of ice bands were used by Keane et al. (2001) for the 6.85 μm band, Boogert et al. (2002a) for the CO band and Thi (2002) for the 3.08 μm water band, although for smaller samples or for individual sources.

The motivation is to drastically reduce the number of free model parameters and at the same time break the degeneracy by requiring the ice profiles of the entire sample to be described by a single model. The literature suggests that 3 distinct components are fundamental to the CO stretching vibration profile. It is well known that the CO band can be decomposed into a narrow component centered around $2140 \, \text{cm}^{-1}$ and a broader red-shifted component situated somewhere in the region $2130 - 2138 \, \text{cm}^{-1}$ (Tielens et al., 1991). Furthermore, Boogert et al. (2002b) detected the presence of a third narrow blue component at $2143 \, \text{cm}^{-1}$
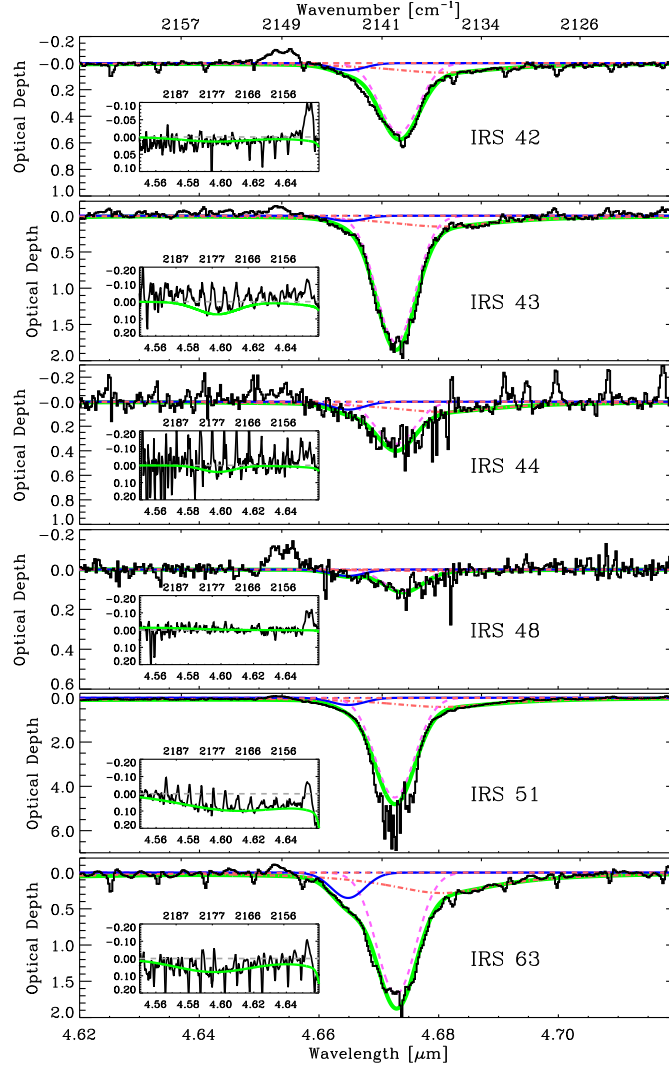
Figure 3.1: *VLT-ISAAC M-band spectra of sources in the ρ Ophiuchi cloud. The spectra have been put on an optical depth scale by fitting a blackbody continuum to parts of the spectrum free of intrinsic features as well as deep telluric lines. In general, the continuum points are taken in the region 4.52-4.55 μm and between 4.76-4.80 μm. The thick solid curve shows the total phenomenological model fit to the spectrum and the thin solid, dashed and dot-dashed curves show the individual components (blue, middle and red, respectively). The inset figures show the fit in the region of the 2175 cm⁻¹ feature.*
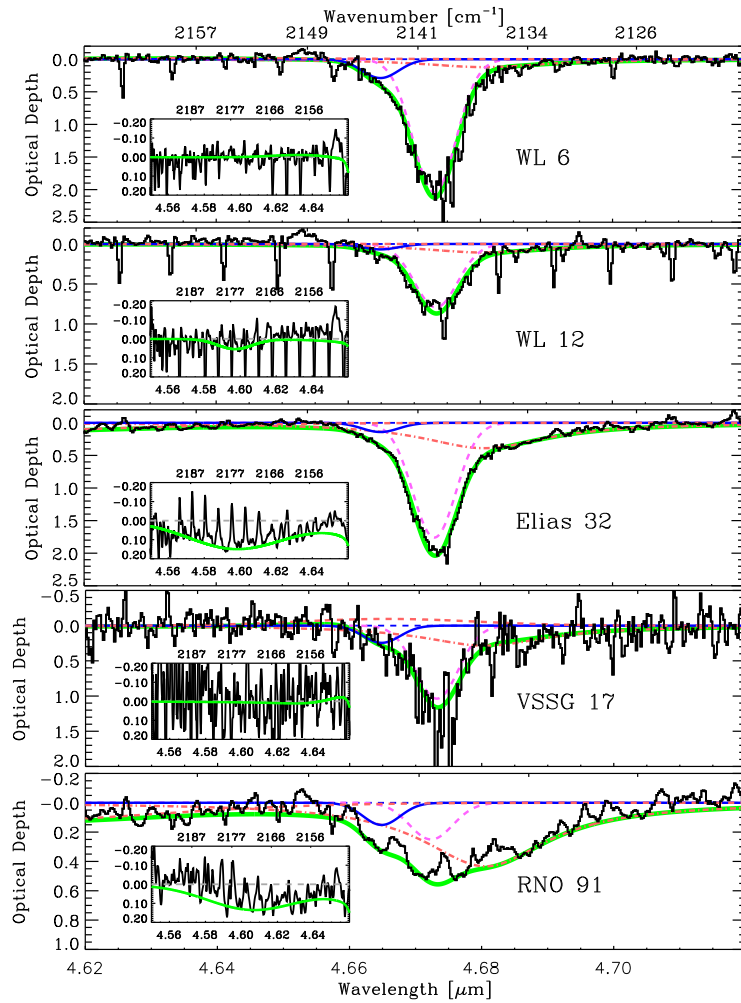
Figure 3.2: *ρ Ophiuchi sources, cont. Legend as in Fig. 3.1*
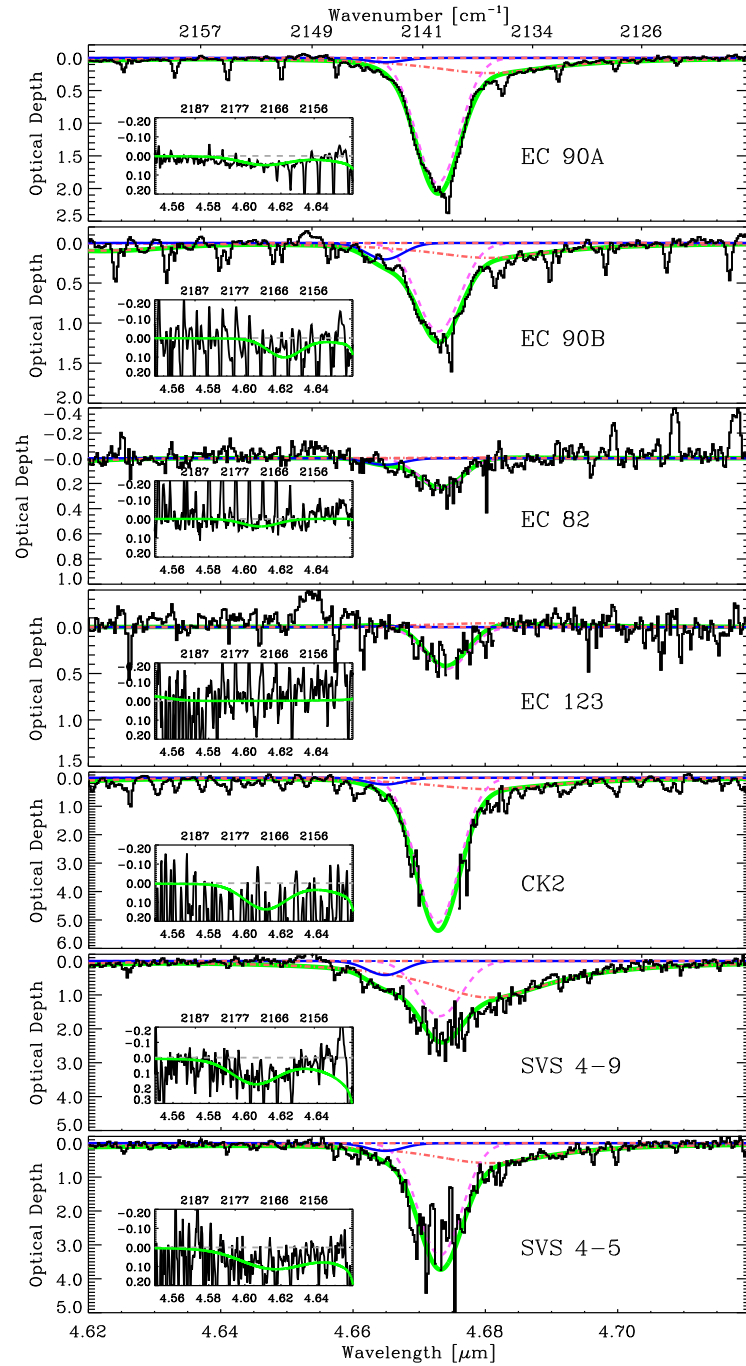
Figure 3.3: *Sources in the Serpens cloud. Legend as in Fig. 3.1*

Table 3.1: *Parameters of the M-band observations*

Source	Lada class	Bolom. lum. [L$_\odot$]	M-band resolution	Date of observation	Standard star	Int. time [min]	Simbad name
ρ Ophiuchus							
IRS 42	I-II	5.6ᵃ	5000	13/8/2001	BS6084	20	BKLT J162721-244142
IRS 43	I	6.7ᵃ	10000	1/5/2002	BS6175	25	BKLT J162726-244051
IRS 44	I	8.7ᵃ	10000	1/5/2002	BS6175	15	BBRCG 49
IRS 46	I	0.62ᵃ	10000	1/5/2002	BS6084	15	BBRCG 52
IRS 48	I	7.4ᵃ	10000	4/5/2002	BS6084	20	BKLT J162737-243035
IRS 51	I-II	1.1ᵃ	5000	19/8/2001	BS6084	20	BKLT J162739-244316
IRS 54	I-II	6.6ᵃ	10000	4/5/2002	BS6175	10	BKLT J162751-243145
IRS 63	I-II	4.2ᵇ	5000	19/8/2001	BS6084	20	GWAYL 4
WL 6	I	1.7ᵃ	10000	4/5/2002	BS6084	30	BBRCG 38
WL 12	I	2.6ᵃ	10000	6/5/2002	BS6084	25	BBRCG 4
GSS30 IRS1	I	21ᵃ	5000	3/9/2001	BS6378	20	BKLT J162621-242306
CRBR 2422.8	I-II	0.36ᵃ	10000	5/5/2002	BS6378	35	CRBR 2422.8-3423
Elias 32	II	1.1ᵃ	10000	1/5/2002	BS6084	25	[B96] Oph B2 5
VSSG 17	I	3.7ᵃ	10000	1/5/2002	BS6084	35	[B96] Oph B2 6
RNO 91	II	4.7ᵇ	5000	20/8/2001	BS6147	10	HBC 650
Serpens							
EC 90A	I	35ᵈ	10000	1/5/2002	BS6084	16	[B96] Serpens 7
EC 90B	I	20ᵈ	10000	1/5/2002	BS6084	16	[B96] Serpens 7
EC 82	II	9.7ᵈ	10000	1/5/2002	BS6084	25	CK 3
EC 123	II	1ᵈ	10000	6/5/2002	BS6378	20	[EC92] 123
CK 2	Background	?	10000	6/5/2002	BS6378	20	CK 2
SVS 4-9	I	1.5ᵈ	10000	6/5/2002	BS7121	21	–
SVS 4-5	I	1.2ᵈ	10000	6/5/2002	BS7121	21	–

Table 3.1: *Parameters of the M-band observations, cont'd.*

Source	Lada class	Bolom. lum. [L☉]	M-band resolution	Date of observation	Standard star	Int. time [min]	Simbad name
Orion							
TPSC 78	I	~ 30[d]	10000	14/11/2001	BS1790	20	TPSC 78
TPSC 1	I	~ 20[d]	10000	14/11/2001	BS1790	20	TPSC 1
Reipurth 50	I	70[j]	10000	12/11/2001	BS3468	20	HBC 494
Corona Australis							
HH 100 IRS	I	14[h]	10000	2/5/2002	BS7121	10	V* V710 CrA
RCrA IRS7A	I	3[i]	10000	2/4/2002	BS6084	30	–
RCrA IRS7B	I	3[i]	10000	2/4/2002	BS6084	30	–
RCrA IRS5A	I	0.6[e]	10000	2/5/2002	BS7348	20	[B87] 7
RCrA IRS5B	I	0.4[e]	10000	2/5/2002	BS7348	20	[B87] 7
Chameleon							
Cha INa 2	I	0.6[f]	10000	6/5/2002	BS4844	25	[PMK99] IR Cha INa2
Cha IRN	I	15[e]	10000	7/5/2002	BS3485	30	[AWW90] Ced 111 IRS 5
Cha IRS 6A	I	6[g]	10000	7/5/2002	BS3468	30	[PCW91] Ced 110 IRS 6A
Vela							
LLN 17	I	3100[l]	800	11/1/2001	BS3185	10	IRAS 08448-4343
LLN 20	I	344[l]	10000	14/11/2001	BS3468	8	[LLN92] 20
LLN 33	I	91[l]	10000	14/11/2001	BS3468	12	[LLN92] 33
LLN 39	I	807[l]	10000	14/11/2001	BS1790	20	[LLN92] 39
LLN 47	I	21[l]	10000	12/11/2001	BS3468	20	[LLN92] 47
Taurus							
LDN 1489 IRS	I	3.7[k]	5000	19/9/2001	BS1543	20	NAME LDN 1489 IR

References [a]Bontemps et al. (2001), [b] Chen et al. (1995), [c] Chen et al. (1997), [d] Rough estimate, this work, [e] Chen et al. (1997), [f] Persi et al. (1999), [g] Persi et al. (2001), [h] Wilking et al. (1989), [i] Wilking et al. (1986), [j] Dartois et al. (2003), [k] Kenyon et al. (1993), [l] Liseau et al. (1992)
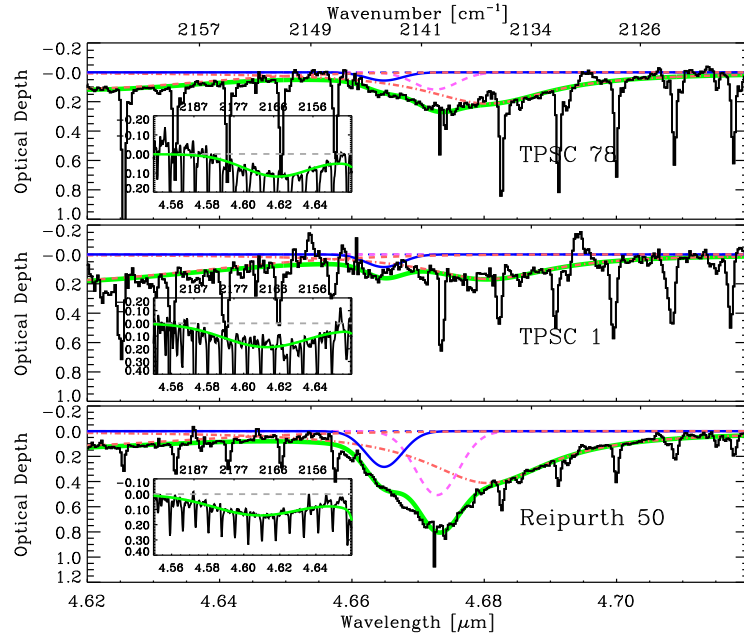
Figure 3.4: *Sources in the Orion molecular cloud complex. Legend as in Fig. 3.1*

in the spectrum of the low mass young star L1489 in Taurus. We will in the remainder of the text refer to the $2134 \, \mathrm{cm}^{-1}$ feature as the red component (rc), the $2140 \, \mathrm{cm}^{-1}$ feature as the middle component (mc) and the $2143 \, \mathrm{cm}^{-1}$ feature as the blue component (bc).

The qualitative identification proposed in the literature of the three components is as follows: The red component is traditionally identified as CO ice in a mixture with hydrogenated molecules such as H_2O or NH_3, while the middle component is thought to be connected with pure CO or CO in a non-hydrogenated mixture containing species such as O_2, N_2 or CO_2. The physical difference between the two components is that hydrogen-bearing species form pseudo-chemical bonds between the hydrogen and the CO molecules, while the non-hydrogenated mixture only interacts via weak van der Waals forces. Traditionally, in the astronomical literature the two components are referred to as "polar" and "apolar". However, while it is true that the traditional mixtures used to reproduce the red component are dominated by polar molecules, the chemical mechanism governing the profile of this component are bonds with the hydrogen atoms of the surrounding H_2O, CH_3OH and NH_3 molecules. Therefore, in the astronomically relevant case, the presence of hydrogenated species is what physically distinguishes the red component from the other two components and not their polarity. Incidentally, the presence of hydrogen bindings in the red component also determines a number of known characteristics such as lower volatility, ability to trap CO molecules
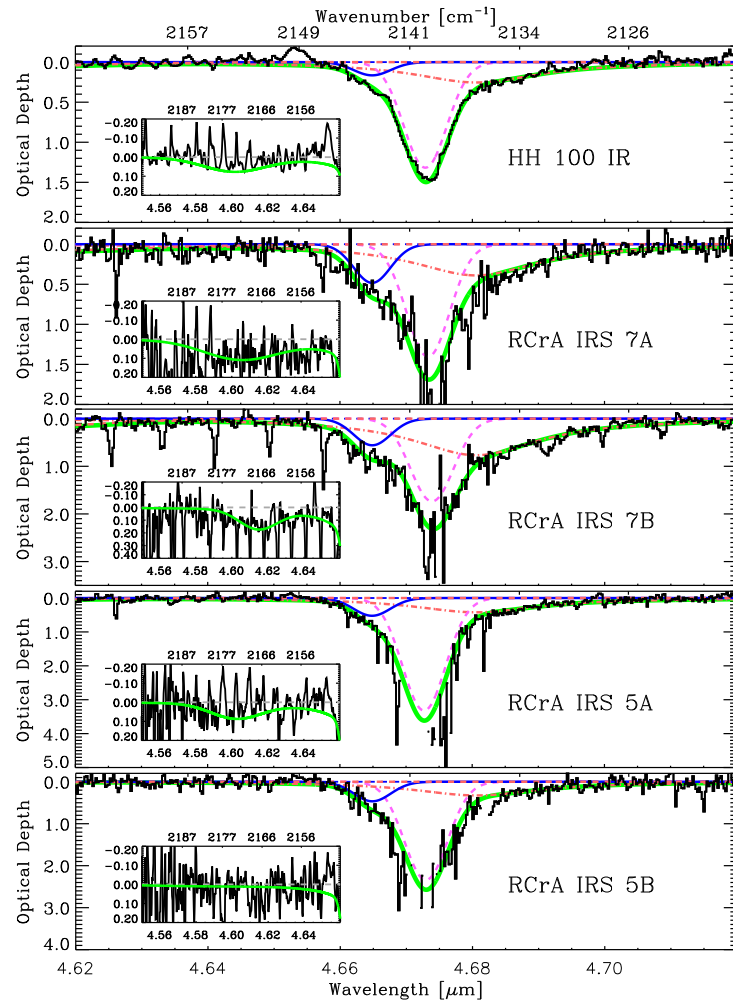
Figure 3.5: *Sources in the Corona Australis cloud. Legend as in Fig. 3.1*
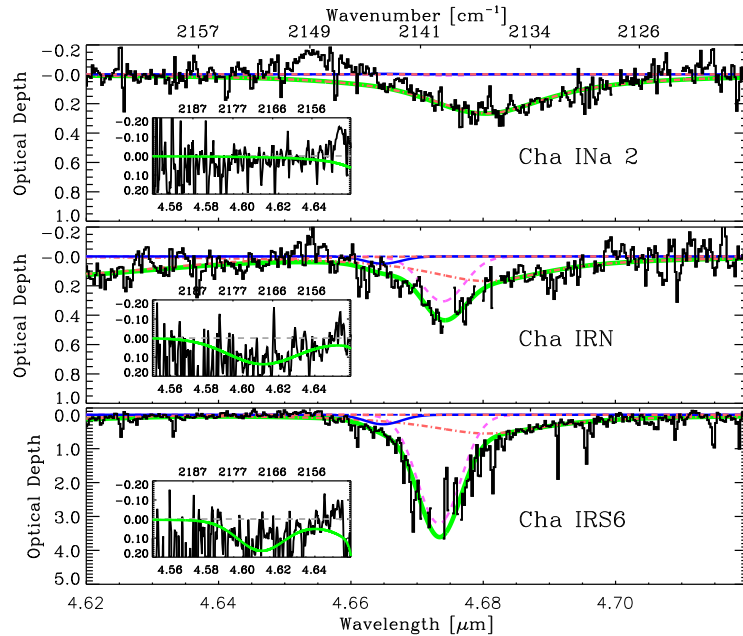
Figure 3.6: *Sources in the Chameleon clouds. Legend as in Fig. 3.1*

in micropores etc. Henceforth in this chapter we will refer to the two components as hydrogen-bonding and van der Waals-bonding components, which more accurately describes the chemical and physical structures in the ice mantles.

A simple way of treating different components of the CO ice band, is to postulate that the entire band is fundamentally a superposition of contributions from CO stretching vibrations where the CO is situated on or in a discrete number of environments. The term environment is defined in the broadest sense and refers to an average configuration of nearest molecular neighbours to a CO molecule for a given ice. The environment depends on the abundance of other species as well as the structure of the ice, such as phase, density, porosity etc. Each environment should give rise to a certain spectral line with a center frequency and a width determined by the average interaction between a CO molecule and its nearest neighbours. A detailed discussion and justification is given in Sec. 3.5 along with implications for the interpretation of the spectra presented in this chapter.

3.3.2 The analytical model

To test the simple postulate on the large sample of YSO's observed here, every CO ice band is assumed to be decomposed into the three components mentioned in the literature. Since the presence of discrete components suggests that only a small number of environments are fundamental to ice on interstellar grains, it is
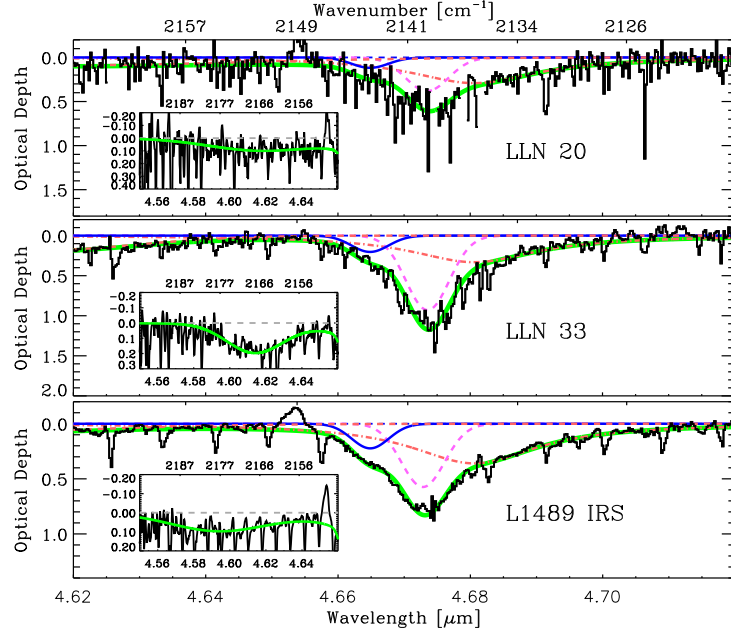
Figure 3.7: *Sources in Vela and the Taurus molecular clouds. Legend as in Fig. 3.1*

also required that *each of the three components has a constant central position and width such that only the relative intensities are allowed to vary from source to source.* In practice the position (but not the width) of the middle component is allowed to vary freely because it is the most sensitive to grain shape effects. The derived center position may then serve to test the degeneracy of the problem. It is essential to note, that if the fitted center positions of the middle component for the entire sample vary by more than is allowed by the statistical uncertainty of the data, then either the fit is degenerate or our assumptions are incorrect.

Since there are sources in our sample where only one component in the CO ice dominates, it is straightforward to determine the best centers and widths for each component. In this way TPSC 78, SVS 4-9, Cha INa 2 and RCrA IRS 7A are used to determine the position and width of the red component, while L1489, Reipurth 50, IRS 63 and Elias 32 fix the parameters of the blue component.

The fundamental analytical shapes which can be chosen for each component are Gaussian and Lorentzian profiles. If three Lorentz curves are used in the fit, it quickly becomes clear that the blue side of the CO band fits very poorly in all cases. This is due to the steepness of the blue wing in the astronomical spectra. Since a Lorentz profile has a very broad wing, it is not appropriate for the middle and the blue component and consequently a Gaussian is adopted for these two components. At the same time, use of a Lorentz curve for the red component gives significantly better results than using a Gaussian for all three components.
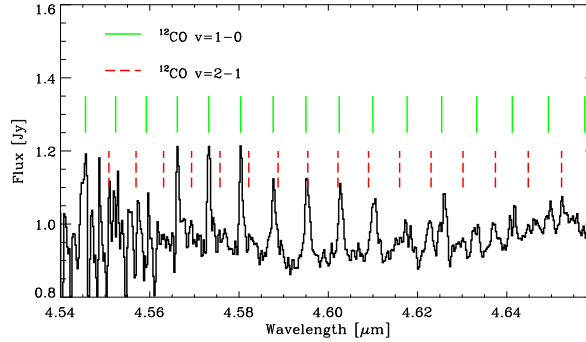
Figure 3.8: *Example of the identification of gas phase CO emission lines. Shown is the spectrum of Elias 32. In this case all the lines are resolved. A weak and broad underlying 4.61 μm feature is seen.*

Consequently, two Gaussians and a Lorentzian were used for the blue, middle and red component, respectively. Physical reasons for this choice are given in detail in Sec. 3.4.2.

In addition to the three components used for the CO ice band, a Gaussian is placed at about 4.61 μm to account for possible absorption by OCN$^-$. In this case our choice of a Gaussian is not as significant as for the blue and the middle component. A Gaussian gives in most cases a better fit than a Lorentzian, but due to the weakness of the feature other types of profile cannot be ruled out. This last component does not overlap with the CO band, and has rarely any influence on the three component fit and thus both center and width of this component are allowed to vary.

Before attempting to fit the decomposition to the data a correction for the systemic velocity was applied to the model. The motion of the Earth in addition to the LSR velocity of the sources can shift the spectrum by up to ± 40 km s^{-1} corresponding to ± 0.29 cm^{-1}. The fits improve significantly when a proper velocity correction is applied. Finally, the model spectra are convolved with a Gaussian to match the spectral resolution of the ISAAC spectra. Even at $R = 5\,000$ (~ 0.4 cm^{-1}) this correction must be done to obtain consistent results.

The common presence of CO gas phase lines requires that care is taken when fitting a Gaussian to the 4.61 μm band. Especially when broad emission lines are present, a careful selection of unaffected parts of the spectrum for the ice fit must be made. This is evident in e.g. IRS 43, Elias 32 and HH 100 IR, and indeed in most of the sources to some extent. In general the CO gas-phase lines were identified and small areas between the lines were picked by eye for the fitting. In Fig. 3.8 an example is shown of the line identification. This also prompts a concern in the case of spectra of low signal-to-noise, which may contain a significant filling-in of the 4.61 μm region from gas phase emission lines, which individually may remain undetected. This may be the case in SVS 4-5, Cha IRN, Cha IRS 6, RCrA IRS 7B and RCrA IRS 5B.

40

Only the points on the spectrum which are not affected by CO gas-phase lines are used in the fit of the phenomenological ice band. In cases where broad emission lines with a complex structure are present, it is especially difficult to determine which points to use for the fit. This is in a few cases reflected in a reduced χ^2 value significantly greater than unity. However, since most of the broad gas lines are very weak compared to the main ice features, the final fitting parameters are not expected to be severely affected. Note that the broad lines are fully resolved and the selection of points will not improve with higher spectral resolution.

3.3.3 The CO ice band structure

The common parameters adopted for the decomposition are shown in Table 3.2. The best fit parameters are given in Tables 3.3 and 3.4 and the decompositions are shown overlaid on the spectra in Figs. 3.1–3.7. The uncertainties on optical depths are given as statistical 3σ errors. Due to the systematic errors introduced by the continuum fit, the presence of gas-phase CO lines and the phenomenological decomposition we estimate that the statistical uncertainties on the optical depths of the red, middle and blue components are underestimates of the total error when the features are strong. However, since the fitting parameters for the 4.61 μm feature are left free and the feature is not blended with other components, the statistical 1σ error on $\tau(2175 \mathrm{~cm}^{-1})$ is probably a good estimate of the total error. For consistency reasons the errors on this quantity are also given as 3σ errors in Table 3.4.

The empirical fits are in general excellent, as is seen from the reduced χ^2 values in Table 3.3 and by visual inspection. The distribution of fitted positions of the middle component is shown in Fig. 3.14. It is found to vary between 2139.7 cm^{-1} and 2140.1 cm^{-1} which corresponds to a standard deviation of 0.16 cm^{-1}. Since the mean uncertainty of the positions is 0.12 cm^{-1}, the scatter in the fitted center positions is to a large extent caused by statistical uncertainties in the fitting and not necessarily by a real effect. An additional scatter may be introduced from uncertainties in the velocity correction of the model. The accuracy of the velocity correction is illustrated by the differences between the velocity shift of the CO gas-phase lines and the calculated velocity shift. If no velocity correction is applied, the spread in center positions of the middle component increases significantly to a standard deviation of 0.20 cm^{-1}. The parameters for the blue and the red component are slightly more uncertain, since they are both shallower and the red one significantly broader than the middle component.

In view of the large number of lines of sight probed, the large range of source parameters and the great variety in CO ice profiles, this result is highly surprising. In simple terms, it is seen that *all CO bands towards both YSOs and background stars can be well fitted with an empirical model depending on only 3 linear parameters.* Therefore our original postulate from Sec. 3.3.1 that the CO stretching vibration mode can be decomposed into a small number of unique components holds. This strongly suggests that there is more physics contained in the decomposition than previously assumed. The approach of fitting the same simple structure to every astronomical spectrum has thus provided three fundamental, identical line com-

Table 3.2: *Best fitting CO ice profile decomposition*

Component	Center $[\mathrm{cm}^{-1}]$	FWHM[a] $[\mathrm{cm}^{-1}]$
red	2136.5 ± 0.3	10.6
middle	2139.9 ± 0.16	3.5
blue	2143.7 ± 0.3	3.0

[a] FWHM of Lorentzian profile for the red component and of Gaussian profile for the middle and blue components.

ponents that are common to all the lines-of-sight observed, and which must be taken into account in subsequent experimental and theoretical modeling of interstellar ice mantles.

3.3.4 The 4.61 μm band

A weak absorption band between $2200 \, \mathrm{cm}^{-1}$ (4.55 μm) and $2150 \, \mathrm{cm}^{-1}$ (4.650 μm) is detected towards 30 of the 39 sources. Absorption in this spectral region can be attributed to the stretching mode of CN bonds. The most likely species to contain the CN bond around young stars is the OCN^- ion (Novozamsky et al., 2001; Pendleton et al., 1999; Schutte & Greenberg, 1997). The derived band parameters along with upper limits are given in Table 3.4. The widths and center positions of the band seem to vary significantly. In particular, many of the bands are centered closer to $2175 \, \mathrm{cm}^{-1}$ than to the $\sim 2165 \, \mathrm{cm}^{-1}$ found for the bands discovered previously, mostly towards high-mass sources. Also laboratory spectra give center positions of the OCN^- band and for the CN-stretch, which in general are located red-ward of many of the observed center positions. For example Hudson et al. (2001) and van Broekhuizen et al. (2003) find that the centers of the CN-stretch in interstellar ice analogs vary between 2158 and $2170 \, \mathrm{cm}^{-1}$. Most of the fitted centers in our sample are placed between 2170 and $2180 \, \mathrm{cm}^{-1}$. There is a clear tendency that the higher mass stars have redder 4.61 μm band centers than lower mass stars. The average position for the intermediate mass stars Reipurth 50, LLN 20, LLN 33 together with the low mass stars TPSC 1 and TPSC 78, which are located only $30''$ from the trapezium OB association in Orion, is $2167 \pm 2 \, \mathrm{cm}^{-1}$. The rest of the detected bands have an average position of $2173 \pm 4 \, \mathrm{cm}^{-1}$. For simplicity the band will hereafter be referred to as the $2175 \, \mathrm{cm}^{-1}$ band.

3.3.5 Correlations

Correlation plots for the derived optical depths of the components of the decomposition are shown in Figs. 3.9–3.13. Possible interpretations of the correlations, non-correlations and exclusion regions are given in Sec. 3.3.6. All correlations except Fig. 3.13 only show points with firm detections of the relevant CO components. A decomposition of the CO ice band taken from ISO-SWS ($\lambda/\Delta\lambda \sim 2000$)

Table 3.3: *Best fits to the CO ice band*

Cloud	Source	center(mc) cm^{-1}	τ(rc)^{a,c}	τ(mc)^{b,c}	τ(bc)^c	Vel. corr.^{d} km s^{-1}	CO gas vel.^{e} km s^{-1}	χ^2
ρ Oph	IRS 42	2139.78 ± 0.02	0.072 ± 0.006	0.53 ± 0.02	0.05 ± 0.01	+22	+20	0.82
	IRS 43	2140.01 ± 0.01	0.15 ± 0.02	1.75 ± 0.02	0.07 ± 0.02	-20	–	1.76
	IRS 44	2140.08 ± 0.08	0.08 ± 0.03	0.34 ± 0.05	0.07 ± 0.03	-20	-12	0.85
	IRS 46	2140.24 ± 0.43	0.09 ± 0.03	0.11 ± 0.06	0.08 ± 0.06	-20	–	1.81
	IRS 48	2139.47 ± 0.07	0.01 ± 0.01	0.11 ± 0.02	0.03 ± 0.01	-20	–	2.36
	IRS 51	2140.12 ± 0.01	0.42 ± 0.02	4.54 ± 0.15	0.33 ± 0.03	+23	–	2.30
	IRS 54	–	< 0.06	< 0.12	< 0.06	-20	–	1.89
	IRS 63	2140.01 ± 0.01	0.28 ± 0.02	1.69 ± 0.03	0.35 ± 0.02	+23	+18	2.84
	WL 6	2139.94 ± 0.03	0.12 ± 0.01	2.04 ± 0.12	0.29 ± 0.05	-20	–	1.45
	WL 12	2139.82 ± 0.03	0.11 ± 0.02	0.79 ± 0.04	0.07 ± 0.04	-20	-9	2.10
	GSS30 IRS1	2139.22 ± 0.32	0.06 ± 0.02	0.07 ± 0.06	< 0.04	+23	+20	0.57
	CRBR 2422.8	2139.89 ± 0.04	0.47 ± 0.03	4.38 ± 0.60^h	0.13 ± 0.07	-17	-9	2.35
	Elias 32	2139.95 ± 0.01	0.39 ± 0.02	1.76 ± 0.05	0.14 ± 0.03	-24	–	1.04
	VSSG 17	2139.86 ± 0.13	0.28 ± 0.30	1.04 ± 0.36	0.25 ± 0.32	+22	+20	0.30
	RNO 91	2140.25 ± 0.27	0.43 ± 0.02	0.25 ± 0.02	0.15 ± 0.04	-19	–	2.85
Serpens	EC 90A	2140.07 ± 0.01	0.24 ± 0.01	2.09 ± 0.03	0.06 ± 0.02	-23	-35	9.84
	EC 90B	2140.00 ± 0.01	0.19 ± 0.02	1.11 ± 0.02	0.21 ± 0.03	-23	-35/-120	5.12*
	EC 82	2139.82 ± 0.12	< 0.03	0.24 ± 0.05	0.05 ± 0.05	-22	-18	0.72
	EC 123	2139.50 ± 0.50	< 0.12	0.45 ± 0.15	< 0.09	–	–	0.47
	CK 2	2140.06 ± 0.05	0.40 ± 0.07	5.11 ± 0.60	0.23 ± 0.12	–	–	0.73
	SVS 4-9	2139.93 ± 0.16	1.07 ± 0.10	1.63 ± 0.30	0.42 ± 0.14	-22	–	0.52
	SVS 4-5	2139.89 ± 0.07	0.59 ± 0.09	3.32 ± 0.71	0.23 ± 0.14	-22	–	0.60

Table 3.3: Best fits to the CO ice band, cont'd.

Cloud	Source	center(mc) cm^{-1}	τ(rc)^{a,c}	τ(mc)^{b,c}	τ(bc)^c	Vel. corr.^{d} km s^{-1}	CO gas vel.^{e} km s^{-1}	χ^2
Orion	TPSC 78	2140.13 ± 0.04	0.21 ± 0.01	0.12 ± 0.01	0.06 ± 0.01	+8	+8	5.98
	TPSC 1	2140.60 ± 0.88	0.17 ± 0.03	0.06 ± 0.01	0.09 ± 0.06	+8	+8	0.74
	Reipurth 50	2140.02 ± 0.01	0.412 ± 0.003	0.51 ± 0.01	0.28 ± 0.003	+7	+10	12.1
CrA	HH 100 IRS	2140.01 ± 0.01	0.25 ± 0.01	1.32 ± 0.01	0.17 ± 0.01	-23	—	82.5*
	RCrA IRS7A	2139.82 ± 0.06	0.39 ± 0.04	1.41 ± 0.17	0.48 ± 0.11	-24	-24	1.14
	RCrA IRS7B	2139.55 ± 0.07	0.77 ± 0.06	1.74 ± 0.27	0.56 ± 0.10	-24	-24	0.75
	RCrA IRS5A	2140.08 ± 0.02	0.42 ± 0.02	3.33 ± 0.18	0.53 ± 0.04	-22	—	3.40
	RCrA IRS5B	2139.98 ± 0.10	0.33 ± 0.06	2.34 ± 0.57	0.47 ± 0.17	-22	—	0.77
Cha	Cha INa 2	—	0.27 ± 0.02	< 0.03	< 0.06	+3	0	0.43
	Cha IRN	2139.54 ± 0.16	0.17 ± 0.05	0.31 ± 0.10	0.05 ± 0.07	+3	—	0.42
	Cha IRS 6A	2139.82 ± 0.05	0.55 ± 0.06	3.22 ± 0.47	0.28 ± 0.11	+3	—	0.36
Vela	LLN 17	2140.30 ± 0.13	0.32 ± 0.02	0.19 ± 0.03	0.14 ± 0.04	-15	—	1.00
	LLN 20	2139.74 ± 0.13	0.29 ± 0.04	0.38 ± 0.08	0.12 ± 0.07	-10	—	2.05
	LLN 33	2139.70 ± 0.06	0.33 ± 0.03	0.94 ± 0.09	0.21 ± 0.05	-10	—	1.04
	LLN 39	2139.97 ± 0.10	0.03 ± 0.01	0.02 ± 0.01	0.004 ± 0.003	-10	—	7.72
	LLN 47	2138.78 ± 0.43	< 0.01	< 0.02	< 0.06	-10	—	3.24
Taurus	LDN 1489 IRS	2140.04 ± 0.04	0.36 ± 0.02	0.58 ± 0.03	0.23 ± 0.04	-11	-10	0.99
Add. sources	GL 2136^f	2139.50 ± 0.06	0.17 ± 0.01	0.15 ± 0.02	0.02 ± 0.02	—	—	0.96
	NGC 7538 IRS1^f	2140.04 ± 0.03	0.10 ± 0.01	0.19 ± 0.01	0.10 ± 0.01	—	—	2.09
	RAFGL 7009S^f	2140.19 ± 0.04	0.89 ± 0.02	0.66 ± 0.06	0.19 ± 0.03	—	—	3.82
	W33A^f	2140.90 ± 0.08	0.75 ± 0.05	0.59 ± 0.10	< 0.05	—	—	1.01
	RAFGL 989^f	2139.90 ± 0.30	0.18 ± 0.03	0.44 ± 0.10	0.14 ± 0.03	—	—	0.98

a Solid CO column densities of the red component can be calculated using eq. 3.4.
b Solid CO column densities of the middle component can be calculated using eq. 3.3.
c Uncertainties are 3σ.
d Calculated absolute velocity shift of the spectra, including Earth motion and LSR velocity of the parent molecular cloud.
e Measured absolute velocity shift of CO ro-vibrational gas phase lines, where available.
f ISO-SWS archive data.
* The optical depth given for the (saturated) CO band of CRBR 2422 is different from that of Thi et al. (2002) since a laboratory profile was used rather than the emperical profile presented here.
h The goodness-of-fit estimate for this source is affected by broad CO gas phase emission lines.

Table 3.4: *Best fits to the* $2175\ \mathrm{cm}^{-1}$ *band*

Source	center	FWHM	$\tau(2175\ \mathrm{cm}^{-1})$[a]
ρ Ophiuchus			
IRS 42	2175.7 ± 2.5	23 ± 6	0.012 ± 0.006
IRS 43	2175.0 ± 1.2	14 ± 3	0.07 ± 0.03
IRS 44	2174.8 ± 2.5	11 ± 6	0.04 ± 0.05
IRS 46	2165.0 ± 3.2	24 ± 8	0.06 ± 0.03
IRS 48	2194.3 ± 8.6	29 ± 11	0.013 ± 0.015
IRS 51	2170.2 ± 1.2	36 ± 4	0.089 ± 0.006
IRS 54	–	–	< 0.1
IRS 63	2176.2 ± 0.8	26 ± 2	0.073 ± 0.009
WL 6	–	–	< 0.06
WL 12	2175.2 ± 1.3	11 ± 3	0.05 ± 0.04
GSS30 IRS1	–	–	< 0.075
CRBR 2422.8	2175.2 ± 1.1	9 ± 2	0.09 ± 0.05
Elias 32	2175.1 ± 0.8	29 ± 2	0.14 ± 0.03
VSSG 17	–	–	< 0.2
RNO 91	2171.2 ± 0.4	28 ± 1	0.125 ± 0.009
Serpens			
EC 90A	2170.5 ± 0.7	17 ± 2	0.073 ± 0.009
EC 90B	2163.6 ± 0.4	10 ± 1	0.10 ± 0.02
EC 82	–	–	< 0.06
EC 123	–	–	< 0.3
CK 2	–	–	< 0.15
SVS 4-9	2171.3 ± 1.9	14 ± 4	0.15 ± 0.10
SVS 4-5	2166.6 ± 3.4	19 ± 8	0.10 ± 0.10
Orion			
TPSC 78	2165.3 ± 0.2	20 ± 1	0.111 ± 0.006
TPSC 1	2167.9 ± 0.7	26 ± 2	0.18 ± 0.03
Reipurth 50	2170.2 ± 0.1	27 ± 1	0.129 ± 0.003
Corona Australis			
HH100 IRS	2173.2 ± 0.2	19 ± 1	0.072 ± 0.006
RCrA IRS7A	2171.5 ± 2.2	23 ± 5	0.10 ± 0.06
RCrA IRS7B	2167.0 ± 1.2	12 ± 2	0.15 ± 0.08
RCrA IRS5A	2172.7 ± 0.9	16 ± 2	0.08 ± 0.02
RCrA IRS5B	–	–	< 0.09
Chameleon			
Cha INa 2	–	–	< 0.09
Cha IRN	2168.6 ± 3.0	22 ± 6	0.13 ± 0.07
Cha IRS 6A	2169.1 ± 2.1	14 ± 4	0.15 ± 0.14
Vela			
LLN 17	2169.2 ± 0.3	27 ± 1	0.13 ± 0.01
LLN 20	2166.2 ± 2.6	31 ± 9	0.09 ± 0.04
LLN 33	2167.4 ± 0.7	17 ± 2	0.19 ± 0.04
LLN 39	2173.4 ± 1.3	24 ± 3	0.010 ± 0.003
LLN 47	–	–	< 0.03
Taurus			
LDN 1489 IRS	2176.9 ± 1.2	29 ± 3	0.09 ± 0.02
Additional sources			
GL 2136[b]	2164.4 ± 0.2	24 ± 2	0.13 ± 0.01
NGC 7538 IRS1[b]	–	–	< 0.03
RAFGL 7009S[b]	2168.2 ± 0.2	25 ± 1	0.47 ± 0.02
W33A[b]	2165.7 ± 0.1	26 ± 1	1.19 ± 0.03
RAFGL 989[b]	2169.7 ± 1.2	23 ± 3	0.04 ± 0.01

[a] 3σ errors are given.

[b] ISO-SWS archive data.

archival spectra of the high-mass stars W 33A, GL 989, GL 2136, NGC7538 IRS 1 and RAFGL 7009S have been added to the sample for comparison. The parameters derived for these sources are included in Table 3.3 and 3.4. The error bars in the correlation plots are $\pm 1\sigma$.

No correlation is found between the red and the middle component (see Fig. 3.9). Sources exist where virtually only the red component is visible, such as TPSC 78, TPSC 1 and Cha INa 2, while other sources are dominated by the middle component. However, no source with a deep middle component has been found where the red component is altogether absent. This effect is seen in the figure as an exclusion region in the upper left corner where no points are located. The region is indicated by a solid line.

In Fig. 3.10 the red component optical depth is plotted against the ratio of the middle and red component optical depths. Evidently no direct correlation is seen. However, the region in the upper right corner of the figure is excluded, which means that a deep red component results in a low strength of the middle component relative to the red component. This plot has been included to investigate if the ratio between the two components can be used as a processing indicator.

The plot of the red and the blue component shown in Fig. 3.11 also shows that certain regions in parameter space are excluded as indicated by solid lines. However, it should be noted that the blue component is the most susceptible to systematic effects created by the artificial decomposition due to the dominating presence of the nearby middle component. Thus caution should be exercised when interpreting this correlation plot in areas where the blue component is weak. In essence, a strong blue component is excluded if the red component is weak as seen by the absence of sources in the upper left corner of the figure. The absence of sources in the lower right corner indicates that a deep red component excludes a weak blue component

Fig. 3.12 shows the depth of the middle component plotted against the blue component. The curves indicate constant polarisation fractions of the background source as required if the blue component is assumed to be due to the LO-TO splitting of crystalline CO as discussed in Sec. 3.4.7.

Finally, a trend between the red component and the 2175 cm^{-1} component is evident in Fig. 3.13. In this correlation plot the sources have been divided into low-mass and high-mass stars to search for evidence for enhanced OCN$^-$ abundances around high-mass stars. High-mass stars have been defined as stars more luminous than 50 L$_\odot$ (bolometric). This definition is flawed by the fact that the luminosity of a young star is dependent on age as well as inclination, but due to the inherent difficulties in determining spectral classes of embedded stars no better definition was found. Roughly, the definition will divide bona fide embedded sources into young stars lighter and heavier than ~ 2 M$_\odot$, respectively. The low-mass stars exhibit a nearly linear relation between the red component optical depth and the 2175 cm^{-1} feature for $\tau(\mathrm{rc})$ up to 0.6 after which the relation apparently saturates and flattens out. However, the flattening in the relation only depends on a few points and should thus be interpreted with caution. Some of the high-mass stars follow the same relation, but many show a dramatic excess absorption around 2175 cm^{-1}. When including the massive young stars W 33A
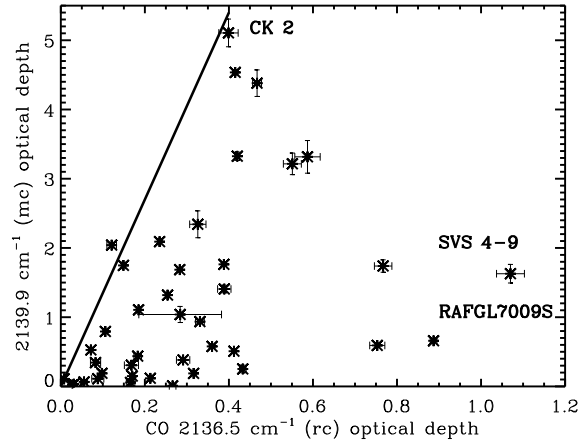
Figure 3.9: *Red component optical depth against middle component optical depth. The solid line corresponds to 16% of the total amount of CO present in a hydrogen-bonding environment under the assumption that the red component is carried by a water-rich mixture. The percentage can be calculated using Eqs. 3.3 and 3.4.*

and RAFGL 7009S a rough correlation can also be seen for the high-mass stars, although much steeper than for the low-mass stars. No sources are found significantly under the best-fitting line and no 2175 cm^{-1} absorption bands are detected for sources without CO ice bands. Within our detection limits, there seems to be an almost one-to-one relationship between the presence of a 2175 cm^{-1} feature and the red component of the CO ice.

3.3.6 Possible interpretation of correlations

In Sec. 3.3.5 the optical depths of the four separate solid state components identified in the spectra have been plotted against each other. The regions of the parameter space covered by the observed sources and especially the regions where no sources fall may provide clues to the nature and evolution of the components.

If the middle component is ascribed to pure CO and the red component to CO in a water-rich environment, one relevant question is how the volatile, pure CO interacts with the water-rich CO when the ice is thermally processed. If processing causes the evaporation of some of the carrier of the middle component while the rest migrates into a porous water ice believed to be located below, such as has been suggested by Collings et al. (2003), an increase in red component optical depth would be expected when the ratio of middle to red component decreases. Due to different absolute column densities along different lines of sight, this effect may be hard to detect without comparing to an independent ice temperature indicator, such as the 3.08 μm water band. However, the exclusion regions seen in Figs. 3.9 and 3.10 still provide useful constraints. The fact that the sources with the deepest
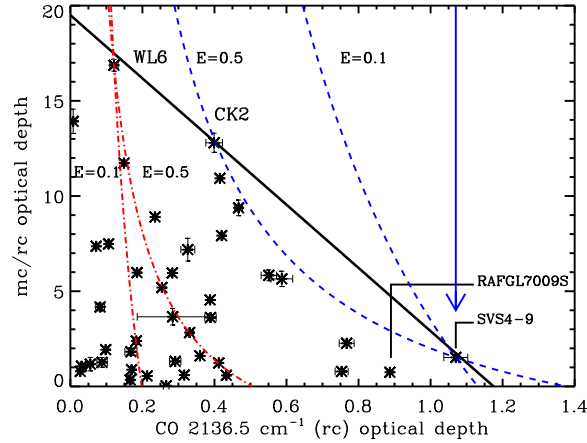
Figure 3.10: *Red component optical depth against the ratio of the middle component optical depth and the red component optical depth. The solid arrow indicates the possible evolutionary track of a source if the pure CO does not migrate into a porous water ice during warm-up. The solid line indicates the excluded region. The dashed curves indicate evolutionary tracks for SVS 4-9 assuming that migration does occur with efficiencies of 0.1 and 0.5. The dot-dashed curves are evolutionary tracks for WL 6 with migration (see Sec. 3.3.6).*

red components seem to have the smallest middle components compared to the red as shown with a solid line in Fig. 3.10 indicates that this redistribution of CO may take place. If this holds then Fig. 3.9 would indicate that some redistribution of CO has taken place for all sources, since the red component is always present with a minimum depth relative to the middle component. This is indicated in Fig. 3.9 with a solid line, corresponding to 16% of the total amount of CO embedded in water. The interpretation is then that the least processed CO profiles are those closest to the solid line, and for some reason the minimum fraction of CO in water along any line of sight is 16%.

Sketches of possible evolutionary tracks with or without migration of the CO ice into the water ice during warm-up have been drawn in Fig. 3.10. The solid track shows the middle component evaporating independent of the red component at temperatures below 90 K for SVS 4-9. This scenario of no CO migration raises the question of why no "progenitors" have been found of the sources in the lower right corner of Fig 3.10, such as SVS 4-9, RCrA IRS 7B and the massive YSOs W 33A and RAFGL 7009S. According to the simple evolutionary track without migration, these progenitors should be found in the upper right corner of the plot. If migration does occur, i.e. if the CO of the middle component is deposited on a layer of porous water ice, the first part of the evolutionary track changes due to a growth of the red component simultaneously with the evaporation of the middle component. For a constant efficiency, E, of migration, such that $dN_{rc} = -E dN_{mc}$,
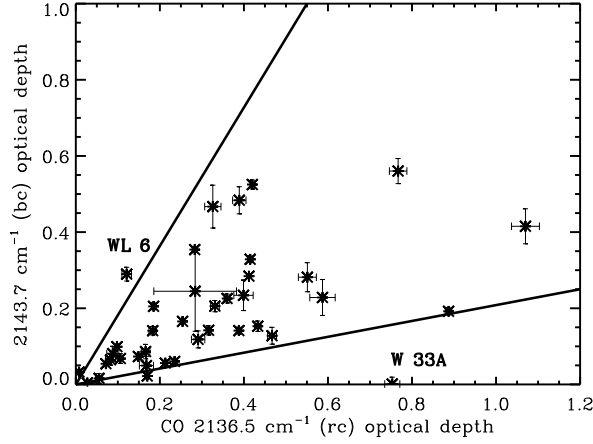
Figure 3.11: *Red component optical depth against blue component optical depth. The solid lines indicate excluded regions.*

the evolutionary track is:

$$\frac{N_{\mathrm{mc}}}{N_{\mathrm{rc}}} = \frac{1}{E}\frac{(N_{\mathrm{rc},0} - N_{\mathrm{rc}}) + N_{\mathrm{mc},0}}{N_{\mathrm{rc}}}, \qquad (3.1)$$

where N_{mc} and N_{rc} are the column densities of the middle and red components, respectively, while $N_{\mathrm{mc},0}$ and $N_{\mathrm{rc},0}$ are the observed column densities. In Fig. 3.10, evolutionary tracks for migration efficiencies of 0.1 and 0.5 have been drawn through the extreme sources WL 6 and SVS 4-9. It is seen that the CO profile of SVS 4-9 can be explained by evolution from a quiescent line of sight, such as that probed by the background source CK 2, if the migration efficiency is large. This is consistent with the lack of sources above the solid line in the diagram. The tracks through WL 6 show how this source can evolve into sources in the lower left part of the diagram. The distribution of sources in Fig. 3.10 can thus be taken as evidence that migration of CO molecules into a porous water ice does occur upon warm-up of the circumstellar grains (but see Sec. 3.4.5).

Amorphous water ice only becomes porous when it is deposited at low temperatures (10–20 K). The migration efficiency drops with increasing deposition temperature and if the ice is deposited at temperatures higher than 70 K, the pores do not form at all (Collings et al., 2003). If the distribution of sources in Fig. 3.10 is interpreted as a result of migration, an ice structure created at a low deposition temperature is favoured. Since water is thought to be formed on interstellar grain mantles rather than being deposited, this may put constraints on the formation of H_2O, since a similar porous structure must then be formed as the water is chemically assembled on the grain surfaces.

The trend between the red component and the 2175 cm^{-1} band has not previously been observed, probably because earlier samples contained a large fraction of intermediate and high mass stars. The observation that high-mass stars exhibit
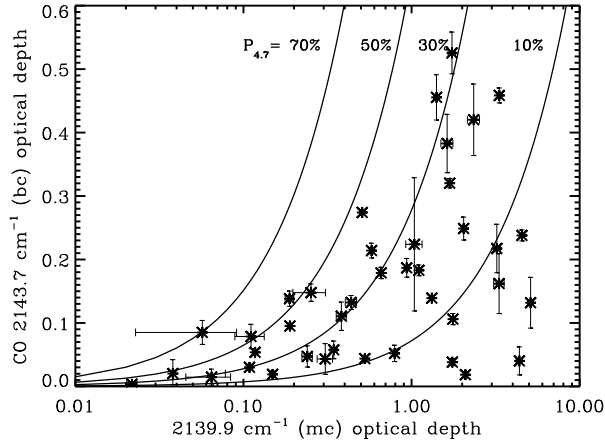
Figure 3.12: *Middle component optical depth against blue component optical depth. The solid lines are curves of constant polarisation fraction calculated using Eq. 3.5. The blue component optical depths have been slightly corrected by using a Lorentz oscillator model for the middle component rather than a Gaussian. See Secs. 3.4.2 and 3.4.7.*

a radically different correlation suggests that two different components contribute to the absorption between 2155 and 2185 cm^{-1}. Since the 2175 cm^{-1} profiles towards the low mass stars also tend to be centered redder than laboratory experiments allow for the CN-stretch, we propose that a second weak absorber is present with a center at $2170 - 2180$ cm^{-1} and a FWHM of $15 - 25$ cm^{-1} and that, based on the correlation with the red component, a likely carrier is CO in a presently unidentified binding site. One significant implication of the proposed correlation is that no absorption at 2136.5 cm^{-1} is expected for any source if the 2175 cm^{-1} band is not present. This is supported by the sensitive upper limits given in Fig. 3.13 for a number of sources which contain abundant water ice.

The excess seen in some high mass stars is then an indication of the formation of OCN^{-} by thermal, UV or other forms of processing not present in low mass stars. The OCN^{-} band in these sources floods the weaker underlying band and the correlation disappears.

A number of alternative explanations may be explored. For example, it is known that a libration band of water ice creates a broad band centered on 2200 cm^{-1}. This libration mode could create an excess absorption, which when requiring the continuum to fit the blue edge of the spectra, may mimic the observed 2175 cm^{-1} band. This is a valid objection, since the depth of the feature depends on the assumption that the blue edge of the spectrum can be used as continuum. However, the water libration band has a FWHM of about 300 cm^{-1} and the total depth is only $\sim 2.5\%$ of the 3.08 μm main water band. This means that the expected excess optical depth from the water combination mode when using a continuum fixed at 2100 and 2200 cm^{-1} is at most $\tau \sim 0.01$ for a $\tau \sim 5$ main water band.

Figure 3.13: *Optical depth at* $2175\ cm^{-1}$ *against optical depth of the red component. Stars indicate low-mass young stars defined by having* $L_{bol} < 50\ L_\odot$*. Diamonds indicate intermediate to high-mass stars with* $L_{bol} > 50\ L_\odot$*. Small arrows indicate upper limits on the* $2175\ cm^{-1}$ *optical depth. The points of the high-mass stars W 33 A and RAFGL 7009 S lie outside the plotting range and are indicated by large arrows. Although TPSC 1 and TPSC 78 are low-mass stars, they are marked as high-mass stars due to their location in the high-mass star forming Orion core. The marked region indicates the possible range of the correlation for low mass stars.*

3.4 Physical modeling of the solid CO band

3.4.1 The middle component

Having identified a simple and well-defined decomposition of the astronomical CO ice band, a unique basis is provided, which can be tested against models of interstellar CO ice. Since the shape of the middle component is the best constrained, it is instructive to compare it to laboratory spectra of van-der-Waals interacting ice mixtures corrected for different grain shapes. Such a comparison is not intended to provide unique constraints on the composition of the CO ice responsible for the middle component, but illustrates well how narrow the observed range of profiles is, compared to the possible range of shapes depending on ice composition and grain shape corrections. For this purpose the optical constants from the laboratory database of non-hydrogenated mixtures by Ehrenfreund et al. (1997) (hereafter E97) are used. The laboratory spectra are corrected for grain shape effects using the standard four particle shapes almost exclusively used in the literature, namely spheres, coated spheres, a continuous distribution of ellipsoids (CDE) and an MRN (Mathis et al., 1977) size distribution of coated spheres. The parameters for the grain shape correction from E97 have been adopted. For details the reader is referred to Bohren & Huffman (1983); Ehrenfreund et al. (1997); Tielens et al.
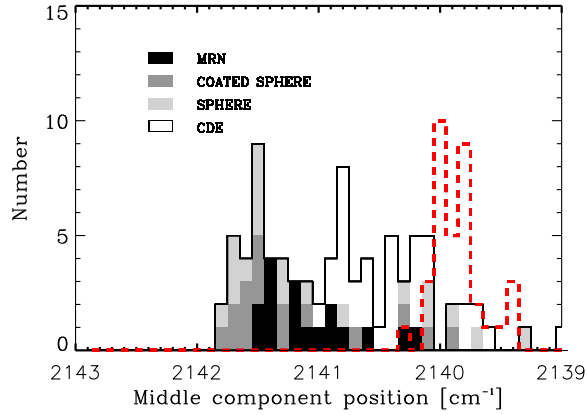
Figure 3.14: *Distribution of fitted middle component positions. The thick, dashed curve shows the distribution derived from the astronomical spectra and corrected for the systemic velocities of the sources. Only middle component positions with 1σ errors of less than 0.15 cm^{-1} have been included. The thin curve shows the distribution of the center positions of the non-hydrogenated ices from the ice analog database by E97. Only ice analogs with FWHM between 3 and 4 cm^{-1} have been included in the distribution. All the laboratory ices are corrected for grain shapes as indicated in the figure.*

(1991). In general, the grain shape corrections are independent of grain size as long as the grains are small, i.e. $2\pi a/\lambda \ll 1$, and the Rayleigh approximation is valid. Clearly, the requirement is only marginally satisfied at 5 μm and breaks down for grains larger than 0.1 μm. This may be a serious concern in the vicinity of protostars, where grain growth is expected to occur. Strictly, grain shape corrections for wavelengths shortwards of 10 μm should be applied using a full numerical solution of the field interactions with the particle. Nonetheless, we assume in the following that the Rayleigh condition holds given the limited constraints on the detailed grain size distributions in the observed lines of sight. In essence it is assumed that the extinction is dominated by small grains. This also implies that the effects of scattering out of the line of sight are ignored. For small particles, the ratio of average absorption to scattering cross sections can be approximated with $\sim (18\pi/3) \times \hat{\nu}^{-3} V^{-1}$, where $\hat{\nu}$ is the wave number and V is the particle volume, which only becomes less than unity for $a \gtrsim 10$ μm at a frequency of 2140 cm^{-1}. For the CO band it is a good approximation to ignore scattering effects, while they become important for bands at higher frequencies, such as for the water band at 3 μm. Scattering effects on the CO band may become observable in regions with grain growth, such as in circumstellar disks.

The coated sphere model was calculated using identical volumes of core and mantle, while the MRN model was calculated using a constant mantle thickness of 0.01 μm; models with thicker mantles approximate the results for solid ice spheres.

For these models, a constant baseline was subtracted from the absorption cross sections to remove the absorption from the silicate core.

A Gaussian was fitted to the CO band to determine the peak position and FWHM of the laboratory ice absorption. Shape corrected laboratory ices with FWHM larger than 4 cm^{-1} and smaller than 3 cm^{-1} were discarded since they are inconsistent with the astronomical spectra. The distribution of the fitted center positions is compared to the distribution of center positions of the laboratory spectra in Fig. 3.14. Only five different laboratory spectra of non-hydrogenated ice mixtures are in the narrow parameter range defined by the observed middle component using the standard grain shapes out of a possible 228.

The variety of laboratory mixtures that are consistent with the observational peaks range from pure CO at 10 K with a CDE grain shape, a $H_2O:CO:O_2 = 1:20:60$ at 30 K for coated spheres, to $H_2O:CO:O_2:N_2:CO_2=1:50:35:15:3$ at 10 K for all the grain shapes. The latter mixture gives a reasonable center and width for all grain shapes since the dielectric function is weak. The shift and the broadening are therefore caused by the presence in the mixture of CO_2 and O_2, respectively, rather than by grain shape effects. It will be shown in Sec. 3.4.4 that the shape of the ^{13}CO band rules out the multi-component mixtures. This range in possible mixtures illustrates the degeneracy inherent in fits to the middle component. However, it also shows that the range of ice mixtures in which the carrier of the middle component is present must be very limited since most of the non-hydrogenated ice analogs are excluded, i.e. the laboratory spectra coupled with commonly used grain shape corrections show a much larger range in centers and band widths than those commensurate with the observations. This is encouraging, since it points towards a simple solution to the questions regarding the composition and structure of CO-rich ice on interstellar grain mantles.

We will proceed to show that the simplest physical model of pure CO ice is sufficient to explain all the middle components observed. Furthermore, it will be shown that in nearly all cases perfect fits are achieved using the CDE grain shape.

3.4.2 Lorentz oscillators as models for binding sites

The simplest possible physical model of the absorption of a molecule in the solid phase is that of a Lorentz oscillator. This is fundamentally a classical model but yields expressions similar to those of simple quantum mechanical models (see e.g. Gadzuk, 1987; Ziman, 1979), albeit with significant conceptual differences. Interactions with the surrounding medium may of course alter the potential energy surface of the oscillator, affecting the line shape.

In the classical picture the CO molecules are seen as a set of identical springs with mass m, corresponding to the reduced mass of the CO molecule, charge e, spring constant K and damping constant b. The last two parameters are affected by the bond of a CO molecule to the surrounding molecules, and for each configuration of a CO molecule and its nearest neighbours a unique set of K and b exists. In an amorphous ice there is a continuum of different configurations for a classical CO molecule, which when averaged over a large number of CO molecules results in a characteristic set of K and b. In the simplest model the configurations of the

CO molecules are random, resulting in a "pure de-phasing" broadening. See Appendix 3.1 for the technical argument for modeling solid state dielectric functions with Lorentz Oscillators.

The complex dielectric function for a Lorentz oscillator is:

$$\epsilon = \epsilon_0 + \frac{\omega_p^2}{\omega_0^2 - \omega^2 - i\gamma\omega}, \tag{3.2}$$

where $\omega_p^2 = e^2\mathcal{N}/m\varepsilon_0$ is the plasma frequency, $\omega_0^2 = K/m$ and $\gamma = b/m$. $\mathcal{N}$ is the number density of oscillators. Finally ϵ_0 determines the dielectric function at frequencies which are low compared to the electronic excitation frequencies. The parameter is basically the low-frequency wing of the combined dielectric functions of all the electronic transitions.

A thick slab, i.e. much thicker than a monolayer, of pure amorphous CO ice is expected to show just a single dominant environment, namely CO on CO, and the simple model should fit well to the measured optical constants. In the case of CO this is well known: the vibrational spectrum of adsorbed CO is commonly used as a probe of surfaces in the chemical literature (see e.g. Somorjai, 1994, and references therein). Sub-monolayer coverages of CO can be used to probe the underlying surface structure, physical and chemical behaviour of CO on the surface, interactions between CO and other adsorbates at the surface, and to identify the range of binding sites favorable to CO on any particular surface.

Note that dielectric functions superpose such that additional binding sites and environments can be included in the model simply by adding single Lorentz oscillators in ϵ-space. In this picture, the optical constants of more complicated ice mixtures can also be reproduced by fitting a sufficient number of Lorentz oscillators accounting for specific environments including other ice species, although the problem may quickly become too degenerate to yield useful physical information.

Naturally, this is a very simplified picture and many other effects may play a role. For instance, some hydrogenated molecules, such as H_2O, complicate the picture significantly by forming hydrogen bonds with the CO molecules, thus breaking the assumption of pure de-phasing. However, for weakly interacting environments such as that of CO interacting with itself or with N_2 or O_2, such a model may yield useful information. This is a break with the traditional view that solid state features from amorphous ices have a continuous range of shapes depending on the abundance of other species, but should be easy to verify experimentally using high resolution laboratory spectroscopy in the limit of a low concentration of contaminating molecules, which interact with CO molecules only through van der Waals bonds, such as O_2, N_2 and CO_2. In the following the term "environment" means a sum of unique sets of nearest neighbours giving rise to a sum of Lorentz oscillators. We will show that in the case of pure CO a simplified physical model can be used to fit the data.

3.4.3 Oscillator density as fitting parameter

There is a standing controversy in the literature regarding the accuracy of the determination of optical constants from laboratory measurements. Since the grain
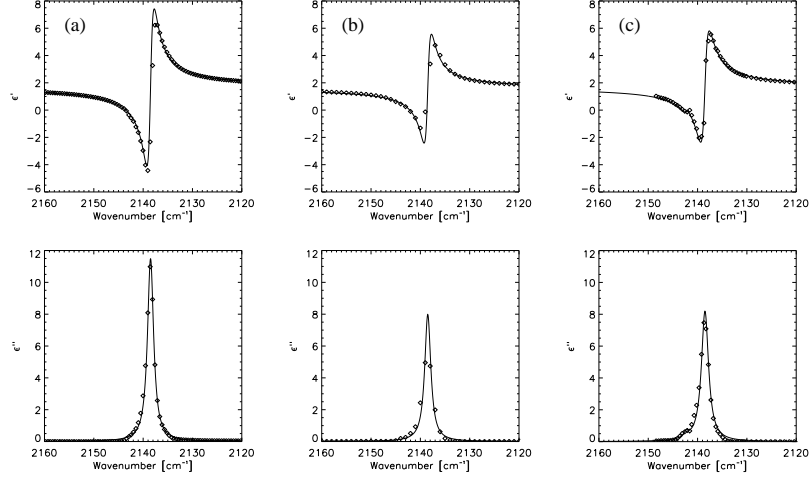
Figure 3.15: *Fit of a single Lorentz oscillator to the dielectric function of a pure CO ice at 10 K from E97 (a), Baratta & Palumbo (1998) (b) and Elsila et al. (1997) (c). The best fitting parameters are: (a): $\gamma = 1.5 \ cm^{-1}$, $\omega_{\mathrm{p}} = 195 \ cm^{-1}$ and $\epsilon_0 = 1.67$. (b): $\gamma = 1.5 \ cm^{-1}$, $\omega_{\mathrm{p}} = 160 \ cm^{-1}$ and $\epsilon_0 = 1.57$. (c): $\gamma = 1.75 \ cm^{-1}$, $\omega_{\mathrm{p}} = 175 \ cm^{-1}$ and $\epsilon_0 = 1.67$. All have $\omega_0 = 2138.5 \ cm^{-1}$ Additionally a second component has been fitted in panel (c) with parameters: $\gamma = 1.2 \ cm^{-1}$, $\omega_{\mathrm{p}} = 30 \ cm^{-1}$ and $\omega_0 = 2142.3$.*

shape correction is sensitive to small differences in optical constants, the derived band profiles of mixtures with a high concentration of CO can vary significantly when using different optical constants from the literature (e.g. E97 and Boogert et al., 2002a). This is particularly true for pure CO. The resulting differences in the dielectric functions are illustrated in Fig. 3.15, where the optical constants for pure CO from Baratta & Palumbo (1998) (hereafter BP) and Elsila et al. (1997) (hereafter EAS) have been used to calculate the dielectric functions in panels (b) and (c), respectively. The main difference between the functions is in the plasma frequency, resulting in strengths of ϵ varying by more than 20%. Also, the fits to a single Lorentz oscillator are slightly worse for the dielectric functions from BP and EAS. There is a second component clearly present in the spectrum from EAS with $\omega_0 = 2142.3 \ cm^{-1}$, which has been included in the fit. This may be a contaminant. Also, recent results and work by Collings et al. (2003) clearly shows the presence of this second peak, attributed to LO-TO splitting. Further discussion of this effect is found in Sec. 3.4.7 of this article. The width (γ) and center positions (ω_0) of the dielectric functions are very similar in all the experiments. Within the model, the only parameter which can change the plasma frequency, and thus the optical constants, is the number of oscillators per unit volume, $\mathcal{N}$. In other words, the difference between the laboratory spectra of identical mixtures can to a large extent be explained by differing ice density, differing ice porosity, or, less likely, by dilution by a relatively inactive molecule such as N_2. Uncertainties in the deter-
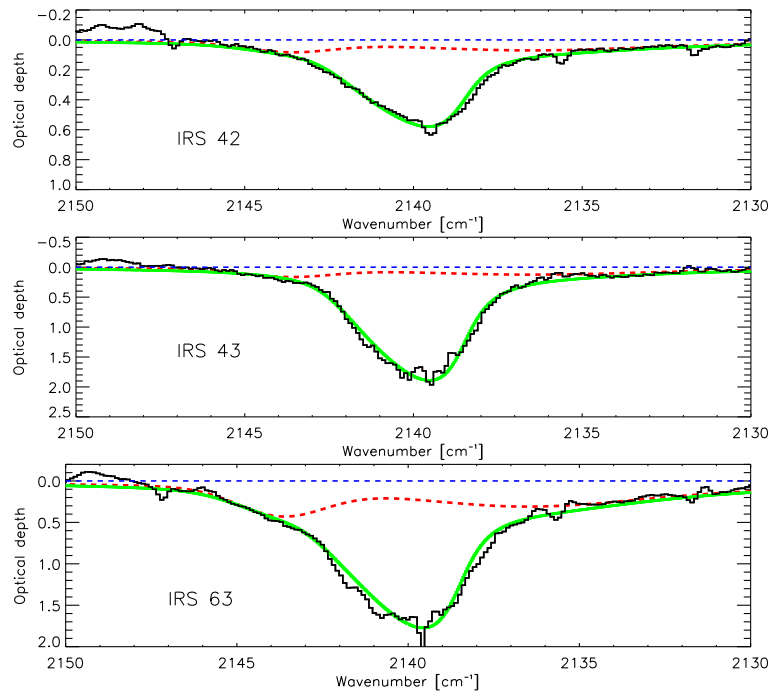
Figure 3.16: *Fit of a pure CO Lorentz oscillator model corrected for CDE grain-shape effects to the best observed spectra which are dominated by the middle component. The red and blue components have been added to the shape-corrected Lorentz oscillator as in the purely phenomenological model (cf. Table 3.3). Often, the depth of the blue component had to be lowered by up to 30% for sources with a deep middle component when using a Lorentz oscillator due to the presence of a blue wing in the CDE corrected profile. For the parameters of the adopted Lorentz oscillator the fit to the optical constants from E97 are used, except for the plasma frequency which is allowed to vary from $170 - 180\ cm^{-1}$. The dashed curve shows the sum of the red and blue components. A dashed straight line indicates the continuum level at zero optical depth.*

mination of ice thickness in lab experiments may also play a role in the differences of the optical constants obtained by different groups.

Fits using a single Lorentz oscillator as a model of the middle component to the interstellar spectra with the highest S/N ratios are shown in Figs. 3.16 and 3.17. The model uses the same phenomenological components for the red and blue components, but now adopts the Lorentz oscillator fit to the pure CO spectrum by E97. The middle component is grain-shape corrected using CDE particles. The CDE particles are used simply because they fit the data extremely well and because this model is believed to simulate irregular particles well by including a maximal range of possible shapes. The CDE particles have a specific distribution and have thus no free parameters. The actual shapes of interstellar grains are
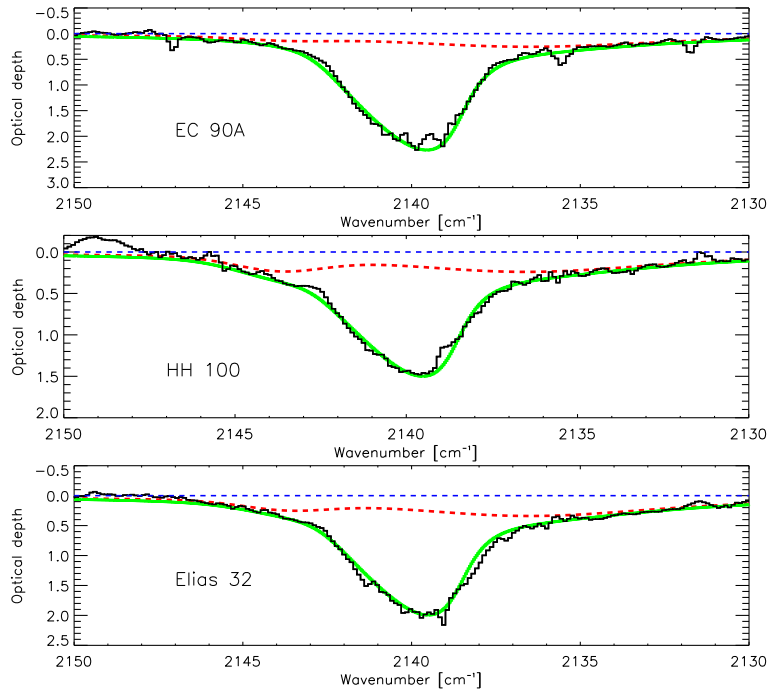
Figure 3.16: *Cont.*

expected to be entirely different. The plasma frequency is allowed to vary to account for different ice densities or for small differences in dilution. ω_p was found to vary slightly between values of 170 to 180 cm^{-1} corresponding to densities 8 to 13% smaller than the E97 laboratory ice but very similar to the densities of the BP and EAS ices. Overall the fits are excellent and often clearly an improvement over the Gaussian model. Note that the fact that the grain-shape corrected Lorentz oscillators so closely emulates Gaussian profiles indicates that the blue and middle components are ices with a high concentration of CO, thus making grain shape effects important, while the red component is likely much more dilute, since it is close to the Lorentzian profile.

It is instructive to repeat the exercise for the other three grain shapes used in the literature. Fig. 3.18 shows the CO profile for IRS 43 compared with the pure CO profile corrected for spherical grains, coated spheres and coated spheres with an MRN size distribution. Clearly none of the other Rayleigh limit grain shapes fit the observed profile. If any of these grain shapes is to be made to fit, some ice mixture is needed to broaden the profile. Alternatively, the MRN size distribution can be modified. Since the MRN distribution is a power law with exponent -3.5, it is dominated by small grains. This is reflected in the CO profile by the fact that it peaks at 2140.2 cm^{-1}; i.e. a large mantle to core volume ratio shifts the profile to the blue. If a power law grain size distribution is to fit the red wing of the observed profile, the distribution must be much shallower in order to include a
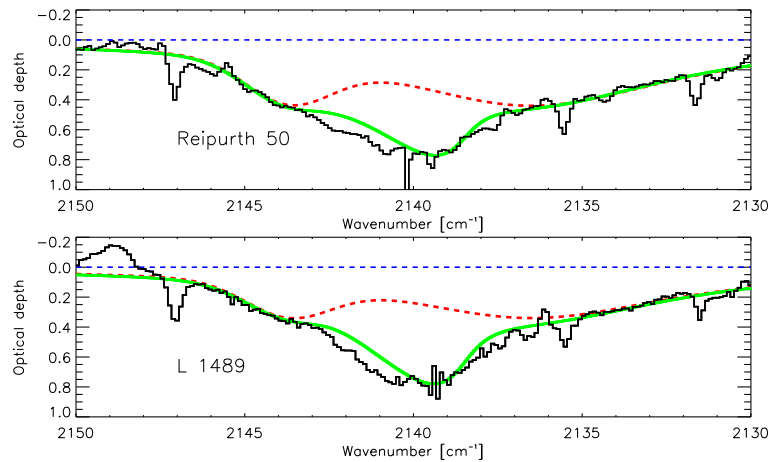
Figure 3.17: *Same as Fig. 3.16 for sources dominated by the red and blue components. For these sources a clear deviation from the pure CO model is seen between 2140 cm^{-1} and 2143 cm^{-1}.*

larger fraction of large grains. A broader shape-corrected profile can be obtained if the exponent is changed to a value closer to -1. This may be interpreted as evidence for grain growth near the young stars. However, this scenario requires that a change in profile is seen in YSO's as compared to quiescent dense clouds. Fig. 3.19 shows the observed CO profile of the well-studied background star CK 2. This is most likely a K0/G8 supergiant seen through a dense part of the Serpens molecular cloud core (Casali & Eiroa, 1996). While the CO profile towards CK2 is severely affected by absorption lines intrinsic to the star as well as being saturated, it is clear that the wings of the CO profile are consistent with the shape given by CDE grains and inconsistent with MRN grains. In conclusion, the data presented here do not provide evidence for a strong difference in grain shapes in the quiescent medium compared to lines of sight towards YSOs. The similarity between the CO profile towards CK 2 and the other observed profiles also show that the separation of a possible contribution from solid CO in quiescent foreground clouds may be very difficult using only the solid state band. Gas-phase observations of rotational lines are thus needed to estimate the foreground contribution to a CO band towards a YSO in a rigorous manner (Boogert et al., 2000b).

The excellent fit to the middle component as a single CO environment is strong evidence that the non-hydrogenated or van-der-Waals interacting component of interstellar ices is pure CO with at most a 5-10% contaminants. This percentage corresponds to the range of oscillator strengths of the pure CO dielectric function (from 170 to 180 cm^{-1}) used to fit the data. With the current lack of knowledge about the true grain shapes in the interstellar medium, it can be concluded that within the quality of the presented data, the middle component is indistinguishable from the profile of pure CO along all observed lines of sight where the middle component dominates the CO profile. Deviations are seen in sources dominated by the red component. This is most clearly evident in Reipurth 50 and L 1489 as
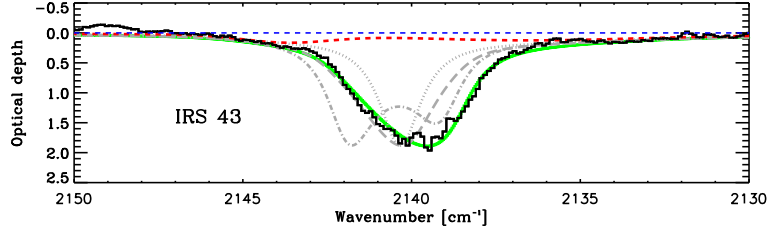
Figure 3.18: *Comparison of different grain shape corrections for a Lorentz Oscillator pure CO. Solid line: CDE; Dotted line: Identical spheres; Dash-dotted line: identical coated spheres with equal volume core and mantle; Dashed line: MRN distribution of coated spheres with a 0.01 μm mantle thickness.*
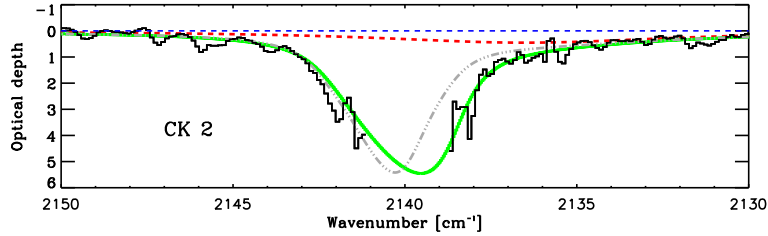

Figure 3.19: *Model profiles using a Lorentz oscillator for pure CO at 10 K corrected for CDE grains (solid curve) and MRN-distributed coated spheres (dot-dashed curve) compared to the spectrum of CK 2.*

shown in Fig. 3.17. While the pure CO component is still present, one or perhaps two new features appear around 2141 cm^{-1} and 2142 cm^{-1}. The features may also be present in IRS 63. These features have optical depths of only $0.1 - 0.2$ and may therefore be present in all spectra, but are simply swamped by the deep middle component when this dominates. The centers of these new components coincide well with the bulk of the laboratory spectra in Fig. 3.14, and may be evidence for a small contribution from mixed CO ices.

For the pure CO combined with CDE grains the column densities can be found from:

$$N_{\text{Pure,CDE}} = 6.03 \text{ cm}^{-1} \times \tau_{\max} \times A_{\text{bulk}}^{-1}, \tag{3.3}$$

where A_{bulk} is the band strength of the bulk material. The numerical factor takes into account the $\tau = 1$ band equivalent width and the fact that the grain shape effect changes the effective band strength with respect to the band strength measured in the laboratory with a factor of $0.71 = \int C_{\text{CDE}} d\hat{\nu} / \int C_{\text{slab}} d\hat{\nu}$ in this specific case. C_{CDE} and C_{slab} are the absorption coefficients for pure CO CDE grains and for a pure CO slab, respectively. In the following we use a laboratory band strength of $1.1 \times 10^{-17} \text{ cm molec}^{-1}$ (Gerakines et al., 1995).

3.4.4 ^{13}CO in IRS 51

Solid ^{13}CO is detected towards one of the sources, namely IRS 51 (Fig. 3.20). Since the isotopic ratio of ^{12}CO to ^{13}CO is expected to be between 65 and 75 in the gas phase for typical molecular cloud conditions (Langer & Penzias, 1993) and between 55 and 85 in the solid phase (Boogert et al., 2000a), ^{13}CO is highly dilute in the ice. An important consequence is that grain shape effects are unimportant and the solid ^{13}CO band therefore offers the chance to disentangle, with respect to the band profile, the effects of the ice matrix from those of the grain shape (Boogert et al., 2002a).
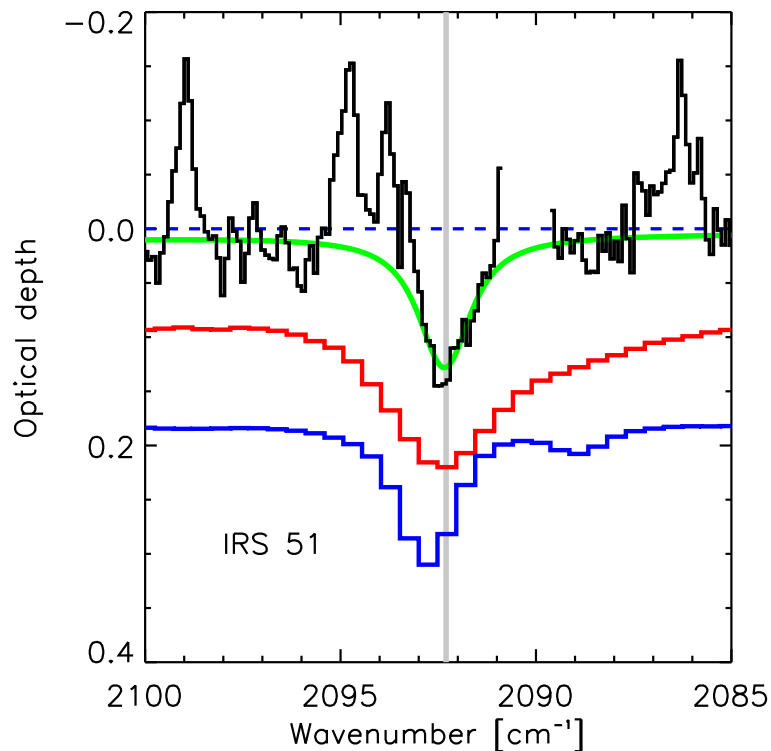
Figure 3.20: *The solid ^{13}CO band of IRS 51. The upper solid line is a Lorentz oscillator fit for a pure CO ice. The blue wing is somewhat affected by a broad CO gas phase emission line. The middle and lower curves are laboratory spectra of binary mixtures at 10 K rich (1:1) in O_2 and N_2, respectively. The vertical line indicates the center of the pure CO profile.*

For the ^{13}CO band towards IRS 51 the same procedure as for the middle component of the ^{12}CO band is repeated. A Lorentz oscillator was fitted to the dielectric function by E97. The best fitting parameters are $\omega_p = 22$ cm^{-1}, $\omega_0 = 2092.3$ cm^{-1} and $\gamma = 1.5$ cm^{-1}. Again the plasma frequency is adjusted to fit the observed band. A good fit to the interstellar profile is found with $\omega_p = 21$ cm^{-1}, although the blue wing contains flux from the $v = 2-1$ P(6) (2193.40 cm^{-1}) and the $v = 1-0$

P(12) (2194.86 cm^{-1}) emission lines from gas phase ^{12}CO. The red wing of the observed band is fully consistent with a pure CO ice. The ratio of the integrated imaginary part of the Lorentz oscillator dielectric functions gives the isotopic ratio of solid CO along the line of sight, $N(^{12}\text{CO})/N(^{13}\text{CO}) = 68 \pm 10$ for IRS 51. The uncertainty reflects the fitting uncertainty in the saturated ^{12}CO band assuming that the shape of the band is identical to the other sources. Comparisons with laboratory spectra of binary mixtures with O_2 and N_2 at 10 K from E97 are also shown in Fig. 3.20. Both laboratory mixtures give significantly worse fits to the IRS 51 spectrum, the O_2-rich mixture being too broad, and the N_2-rich mixture being shifted to the blue. Heating the O_2-rich mixture to 30 K narrows the profile, but not enough to equal the quality of the fit of that of pure CO. It may also be considered unlikely to find most of the volatile solid CO component in dense clouds at a temperatures higher than 20 K.

The results for the solid ^{13}CO band agree well with the conclusions reached by Boogert et al. (2002a) for the ^{13}CO band towards the high mass source NGC 7538 IRS9, who also found both isotopic bands of CO to be fitted well with pure CO. Furthermore, the isotopic ratio for NGC 7538 IRS9 of 71 ± 15 is remarkably similar to that found for IRS 51. Indeed, the shapes of the two ^{13}CO bands match closely, in agreement with the similarities observed among the ^{12}CO bands.

3.4.5 The red component

The red component in the interstellar CO ice profile was first assigned by Sandford et al. (1988) and Tielens et al. (1991) to CO mixed in a hydrogen-bonding "polar" mixture containing species such as H_2O or CH_3OH. The previous M-band surveys towards young embedded stars all concluded that this assignment is roughly consistent with the data. The ice mixtures found to provide the best fits in the literature (Boogert et al., 2002b; Chiar et al., 1994, 1995, 1998; Kerr et al., 1993) are almost exclusively pure H_2O-CO mixtures containing 25 or 5% CO, but with temperatures ranging from 10 to 100 K. Occasionally good fits are found with irradiated H_2O-CH_3OH mixtures. The identification of a phase of CO mixed in water ice is also indirectly supported by observations, since large columns of solid, generally amorphous, water ice are known to exist along the same lines of sight. Nonetheless, we find that the assignment of the red component to an amorphous CO-H_2O mixture presents some inconsistencies between the observations and both old (high vacuum) and new (ultra-high vacuum) laboratory results.

Laboratory spectra of CO co-deposited with water at low temperature ($T < 20$ K) show two distinct absorption peaks. One well defined peak near 2152 cm^{-1} and one generally stronger peak near 2138 cm^{-1}, although different experiments disagree somewhat on the peak position of the lower frequency peak, some placing it at $2136-2137$ cm^{-1} (Sandford et al., 1988; Schmitt et al., 1989). This shift may be related to the degree to which the CO and the water are mixed, since CO deposited on a water surface shows absorption at 2138 cm^{-1}. In recent work by (e.g. Collings et al., 2003; Devlin, 1992; Manca et al., 2001; Palumbo, 1997) strong experimental evidence is presented that the 2152 cm^{-1} peak is due to the CO bonding with the hydrogen in OH dangling groups as was suggested by e.g. Schmitt

et al. (1989). In the same picture the 2137 cm^{-1} peak is the normal CO bond site also found in pure CO but perturbed by a water ice surface. This holds in particular for CO trapped in micropores inside the amorphous water ice. Therefore the 2152 cm^{-1} feature represents the principal binding site for CO on water, the presence of which would be strong evidence for CO interacting with an OH containing species. The 2152 cm^{-1} bond is suppressed by warm-up and is known to completely disappear for $T > 80$ K. Also irradiation by UV photons or bombardment by energetic particles destroys the bonds responsible for the 2152 cm^{-1} feature. In general, warm-up of a H$_2$O-CO mixture also narrows the 2136 cm^{-1} feature and shifts it towards the red. Irradiation also shifts the feature to the red, but in contrast to pure thermal processing broadens the band slightly. All of these processing effects are irreversible. Therefore the search for the 2152 cm^{-1} feature is essential because it has the potential to not only uniquely confirm the association of the red component with OH-bearing species, but also to provide a sensitive temperature and processing indicator.

None of our interstellar spectra show any evidence of the 2152 cm^{-1} OH-CO bond. The lower limits on the ratio between the optical depth of the red component and the 2152 cm^{-1} feature for the best quality spectra are shown in Fig. 3.21. They are compared to the temperature-dependent ratios from the laboratory spectra by Sandford et al. (1988) and Schmitt et al. (1989). Assuming that the laboratory spectra used are suitable as interstellar ice analogs, the limits on 8 sources are good enough to exclude ice temperatures below 60 K while an additional 6 sources can exclude ice temperatures below 40 K. However, the profiles for ice mixtures at temperatures higher than 60 K have FWHM of only ~ 7 cm^{-1}, making them inconsistent with the broader profiles observed along all lines of sight. It can be concluded that the available laboratory spectra in general exclude the low temperature non-processed hydrogenated ices, otherwise traditionally found to be consistent with interstellar spectra, due to the absence of CO in a OH bonding site (the 2152 cm^{-1} feature). Alternatively, the interstellar ices may in general be strongly irradiated, but this requires an explanation why no other signatures of irradiation are seen along many lines of sight, such as OCN$^-$, aliphatics, etc. Strong irradiation may also be inconsistent with the strength of the typical UV-field in a dark cloud, since UV photons can only be formed as a secondary effect to cosmic ray hits due to extinction except at cloud surfaces.

A significant problem in the interpretation of the red component is thus revealed. On the one hand, there is clearly evidence in the data for the presence of a CO component embedded in the water ice and for migration of a pure CO component into a porous water ice (Sec. 3.3.6). The shape of the red component, a high efficiency of CO migration and the general shape of water ice bands towards low-mass YSOs all suggest that most of the water ice column has a fairly low temperature (Boogert et al., 2000b; Thi, 2002). On the other hand the absence of the 2152 cm^{-1} feature seems to exclude this. It is a challenge for laboratory studies to explore how the CO-OH bonds can be avoided or efficiently destroyed under interstellar conditions. Possible explanations may include the destruction of CO-OH bonds on interstellar time scales ($> 10^3$ years). Also, the formation of water molecules on grain surfaces may produce an ice structure different from
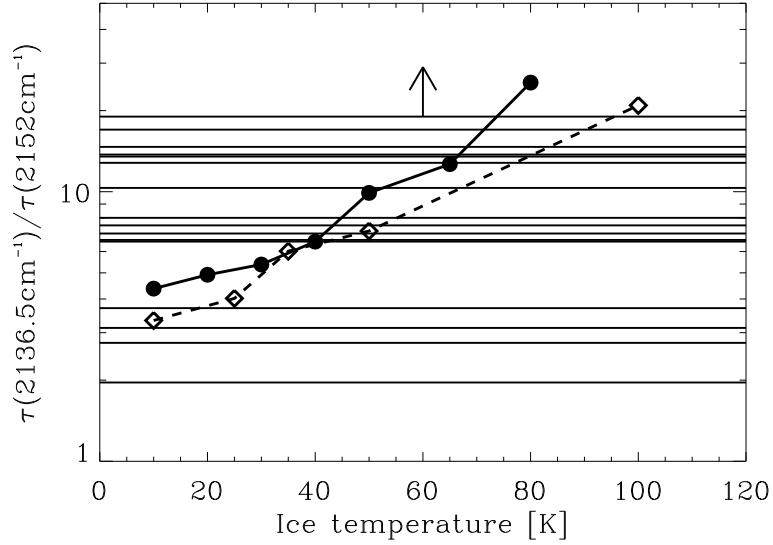
Figure 3.21: *Lower limits on the ratio between the red component at 2136.5 cm^{-1} and the 2152 cm^{-1} OH-CO bond for the highest quality interstellar spectra. The horizontal lines indicate the limits while the curves show the expected ratios from co-deposited mixtures of H$_2$O and CO. Solid line: H$_2$O:CO = 20:1 (Sandford et al., 1988). Dashed line: H$_2$O:CO = 4:1 (Schmitt et al., 1989)*

structures obtained by deposition. Finally, the possibility that the red component is not due to CO interacting with water should not be ruled out, although it seems unlikely given the ubiquitous presence of water ice in grain mantles.

For the red component, assuming grain shape effects are negligible, the column densities can be found from:

$$N_{\rm rc} = 16.0 \ {\rm cm}^{-1} \times \tau_{\rm max} \times A_{\rm rc}^{-1}, \tag{3.4}$$

where $A_{\rm rc}$ is the band strength of the bulk material. It assumed that the CO concentration small so grain shape effects can be ignored. The numerical factor is then the equivalent width of a $\tau = 1$ band. In the following a band strength for a water-rich mixture of $A = 1.1 \times 10^{-17}$ cm molec^{-1} is used (Gerakines et al., 1995).

3.4.6 The blue component

Since the blue component was only identified recently in the high resolution Keck-NIRSPEC spectrum of L1489 IR by Boogert et al. (2002b), the only available statistics are from our work. In the present sample, it is found that the component is particularly prominent as a distinct shoulder in the profile in L1489 IR and in Reipurth 50. The feature is detected as a well-defined shoulder in many of the other sources such as HH 100, Elias 32, SVS 4-9 and IRS 63, but has a smaller ratio with the middle component.

Boogert et al. (2002b) suggest that the blue component can be identified with CO mixed in a CO_2-rich ice ($CO_2/CO> 1$) or a mixture with less CO_2 but with significant amounts of O_2 and N_2 present. While reasonable fits can be obtained with a suitable CO_2-containing laboratory mixture, we will argue in the following sections that another candidate explanation exists, namely the longitudinal optical (LO) component from pure crystalline CO, which appears when the background infrared source is polarised. The presence of this component can be independently tested by measuring the linear polarisation fraction at 4.7 µm.

3.4.7 LO-TO splitting in crystalline α-CO?
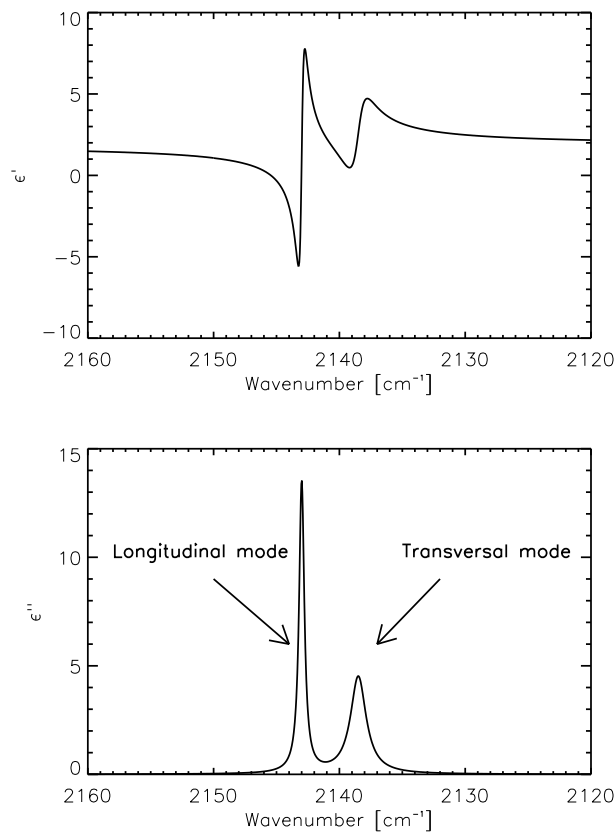
Figure 3.22: *The adopted model of the complex dielectric function of α-CO for p-polarised light.*

Laboratory spectroscopy of multi-layered crystalline CO (α-CO) using a p-polarised (light polarised parallel to the plane of incidence) infrared source shows a splitting of the CO-stretching vibration mode (Chang et al., 1988; Collings et al., 2003). The splitting is due to vibrations perpendicular and parallel to the ice surface which are generally referred to as the longitudinal optical (LO) and the transversal op-

Table 3.5: *Polarisation fractions assuming LO-TO splitting*

Source	$P_{4.7}$ [%]	$P^d_{2.2,\text{max}}$ [%]
L 1489	41	70[a]
Reipurth 50	57	60[b]
HH 100 IR	9	–
IRS 63	18	–
Elias 32	7	–
SVS 4-9	23	–
CK 1A	< 10	5[c]
CK 1B	< 10	5[c]

[a] Whitney et al. (1997)

[b] Casali (1991)

[c] Sogawa et al. (1997)

[d] Observed value

tical (TO) modes, respectively. In this article model parameters for LO-TO split CO are derived using the laboratory work of Chang et al. (1988), unless otherwise stated. For thin ice layers ($\lesssim 30$ mono-layers), the two modes show very narrow profiles. According to Chang et al. (1988), the LO and TO modes have widths of 0.25 cm^{-1} and 0.85 cm^{-1}, respectively. The LO mode disappears for a single monolayer. For thicker layers ($\gtrsim 100$ monolayers), the TO mode exhibits a profile very similar to the profile seen in unpolarised light, i.e. $\omega_0 = 2138.5$ cm^{-1} and FWHM $= 2\gamma = 1.5$ cm^{-1}. The LO mode gives for thick layers a strong very narrow and blue-shifted profile with $\omega_0 = 2143$ cm^{-1} and $2\gamma = 0.5$ cm^{-1}. Here $\epsilon_0 = 1.84$ is adopted as given in Zumofen (1978). Unpolarised light will produce a single peak at 2138.5 cm^{-1} very similar to that seen for amorphous pure CO ice. It is assumed that the dielectric functions for α-CO and amorphous CO are identical when subjected to unpolarised light.

The dielectric function of α-CO for p-polarised light is therefore modeled by two Lorentz oscillators (Chang et al., 1988). The plasma frequencies of the two modes are assumed to be identical. A value of $\omega_\text{p} = 120$ cm^{-1} is found to reproduce the strength of both modes in the laboratory spectrum of Chang et al. (1988). This value is allowed to vary slightly to account for uncertainties in the determination of the sample thickness. The LO-TO splitting model is corrected for grain-shape effects using the same CDE grains as for the middle component. After correcting for grain shape, $\omega_\text{p} = 140$ cm^{-1} gives a significantly better fit to all the astronomical spectra. The difference compared to the laboratory data is considerable, also since a crystalline ice in space is not expected to have a different oscillator density than the laboratory sample. Further laboratory experiments are needed to confirm if a discrepancy indeed is present.

The necessary linear polarisation fraction at 4.7 μm to explain the blue compo-

nent with the LO mode is found through:

$$C_{\text{total}} = C_{\text{unpolarised}} + \frac{P_{4.7}}{1 - P_{4.7}}[\beta C_{\text{LT,p}} + (1 - \beta)C_{\text{LT,s}}], \tag{3.5}$$

where $P_{4.7}$ is the polarisation fraction at 4.7 µm while $C_{\text{unpolarised}}$, $C_{\text{LT,p}}$ and $C_{\text{LT,s}}$ are the absorption cross sections for unpolarised, p-polarised and s-polarised light, respectively. β is a factor accounting for the fraction of the light seen as being "p-polarised" by the CO molecules on a grain surface. In general, $\beta = 1/2$ for randomly oriented particles, which can be realised by volume-integrating the projection on the plane of the incoming polarised light of the surface normal vector. If the grains are aligned along magnetic field lines, β can deviate considerably from $1/2$, but will never exceed unity. The CO ice is assumed to be entirely crystalline and the absorbing grains are assumed to be randomly oriented. It is important not to confuse the absorbing grains with the background grains producing the scattered and polarised light, since their properties may be different.
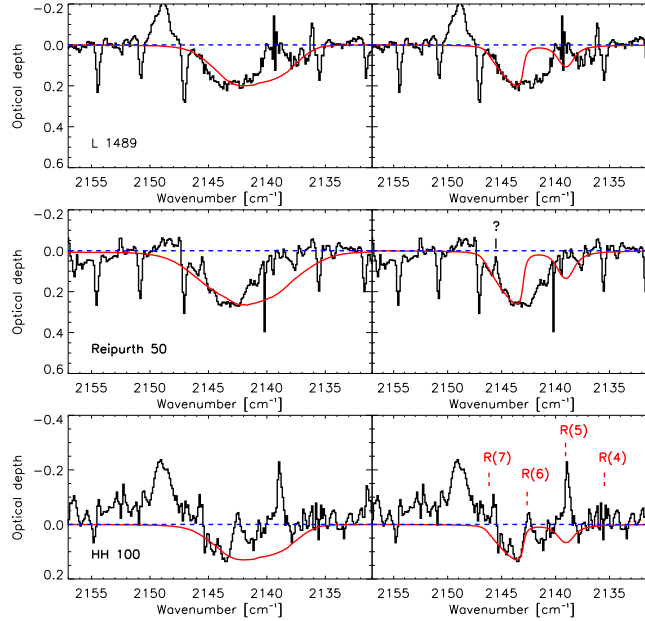
Figure 3.23: *Spectra of sources with a clearly defined blue component. The Lorentz oscillator model for the middle component and the phenomenological red component have been subtracted. The plots on the left show the spectra compared to the grain-shape corrected laboratory spectrum of $N_2:O_2:CO_2:CO=1:5:0.5:1$ at 12 K by EAS. The plots on the right show the grain shape corrected LO-TO splitting model as described in the main text. All grain shape corrections use CDE grains. Positions of the gas-phase ^{12}CO v=1-0 (solid lines) and v=2-1 (dashed lines) ro-vibrational transitions are also indicated, when present.*

The model fits are shown in Fig. 3.23 where they are compared to the CO_2-rich laboratory spectrum proposed by Boogert et al. (2002b) and EAS to fit the blue
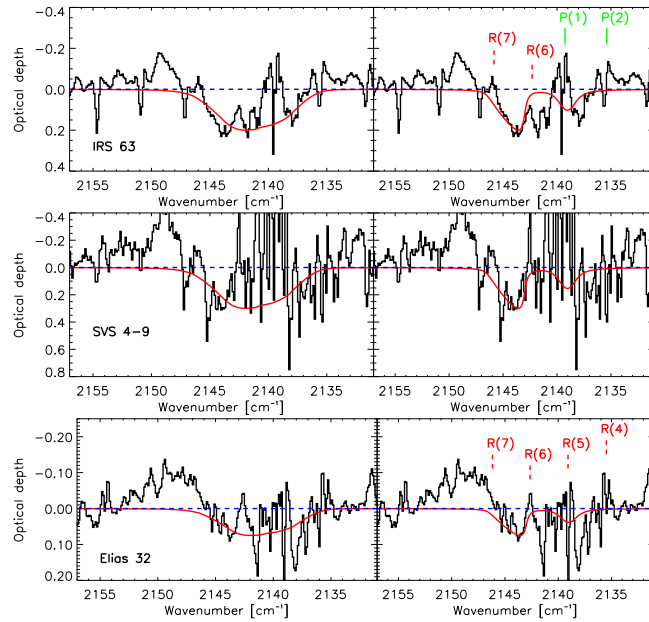
Figure 3.23: *Cont'd*

component, in particular in the case of L 1489. The derived polarisation fractions are given in Table 3.5. For L 1489 and Reipurth 50 the CO_2 laboratory profile indeed gives a good fit to the blue wing of the residual. For the other sources the fit is worse since the residual feature seems to be a factor of 2-3 narrower than the laboratory profile, although this may be an effect of line emission from hot CO gas as indicated in Fig. 3.23. In no case does the laboratory mixture give a good fit to the red side. It may be possible to construct a more complex ice mixture, which fits better. Also a better fit to the red side can be obtained by subtracting a middle component of slightly smaller optical depth. However, since the slope of the blue wing is similar in all the sources, the exact same complicated mixture is required along all lines of sight, which seems very unlikely.

On the other hand, the extremely narrow LO mode profile accurately reproduces the blue wing in the residual for all the sources. Taking into account the line emission from CO gas which clearly fills in the red side of the band in all sources but L 1489 and Reipurth 50, it is seen that also the LO-TO splitting scenario has problems reproducing the red wing. In L 1489 and Reipurth 50, excess absorption is clearly seen at 2141 and $2142 \, \mathrm{cm^{-1}}$, as previously mentioned. Nevertheless, the polarisation scenario has several advantages over the CO_2-rich mixture scenario. First, since the polarisation fraction at 4.7 μm is predicted, an independent test is available. L 1489 and Reipurth 50 need very high polarisation fractions ($> 50\%$) to explain the blue component. However, these two sources also have some of the highest K-band polarisation fractions known in YSOs, as is indicated in Table 3.5. It is expected that the linear polarisation fraction decreases with increasing wave-

length if more of the light received originates directly from the emitting source rather than being scattered. In these sources, the polarisation fraction is seen to decrease from the H to the K-band and the maximum polarisation fraction occurs offset from the mid-infrared position (Casali, 1991; Whitney et al., 1997). It is not known if this behavior in general continues to 4.7 μm. If the grains are small and the emitting source is obscured at 4.7 μm e.g. by a circumstellar disk, the polarisation fraction can be largely independent of wavelength up to 5 μm. Although few observations of polarisation fractions have been made at longer wavelengths than 2.2 μm, some protoplanetary nebulae have been found to show this behaviour, such as the Egg nebula, which has a constant linear polarisation fraction of 50% from 2.2 to 4.5 μm, thus requiring grain sizes of less than ~ 1 μm (Kastner et al., 2002). Also, the polarisation fraction at 4.7 μm for W 33A is known (Chrysostomou et al., 1996). The measured value of 10-13% is consistent with an upper limit of 15% from the decomposition of the ISO-SWS spectrum. Curves of constant polarisation fraction have been drawn in Fig. 3.12, showing that the majority of the sources in the sample will require polarisation fractions of less than 30%.

The main problem in the determination of the polarisation fraction from the CO profile are the systematic uncertainties introduced by the assumptions on the fits of the middle and red components as well as the assumptions regarding the dielectric function of LO-TO split α-CO, especially concerning the width and strength of the LO component.

All the sources are thus consistent with a LO-TO splitting scenario, but the result must be confirmed by imaging polarimetry at 4.7 μm as well as further laboratory experiments using polarised light and high resolution spectrometers. It will have important consequences for the understanding of the processes governing the freeze-out of CO in the circumstellar medium if the blue component, and indeed also the middle component, is carried by crystalline CO. Note that the formation of crystalline CO can occur at low temperatures, depending on deposition rate and the adsorbing surface and is not necessarily a sign of processing of the ice (Collings et al., 2003).

3.5 Discussion

3.5.1 Implications for the evolution and processing of CO-rich ices

The most intriguing lesson learned from the presented data set is that the fundamental structure of the CO ice on grain mantles seems to be practically identical along all observed lines of sight. It is well-established that the absorption profile of solid CO is sensitive to the conditions under which it is formed. This is an observation which suggests that the CO ices are formed under similar conditions regardless of the macroscopic context of the circumstellar medium or that the CO ice profile is invariant to differences which may exist in composition and grain shape distributions.

It is well known that CO can efficiently freeze out on a given grain when it passes through a region of a dense cloud with the temperature and density most

suited for the formation of solid CO. In addition, an efficient method of desorption at low temperature must exist, since CO is found in the gas phase in abundances even in the densest and coldest clouds (e.g. Bergin et al., 2001; Lada et al., 1994). An important desorption mechanism seems to be via the release of chemical energy through reactions with radicals produced by a cosmic ray induced UV field (Shen et al., 2003), although other mechanisms connected with cosmic ray particles may contribute. At the same time ambient UV photons may only play a role on the surface of the cloud due to extinction. A given grain may also experience that all or parts of the ice mantle are evaporated and refrozen several times on the evolutionary pathway from dense cloud to protostellar envelope to circumstellar disk.

In the light of this active processing which is expected to take place for any grain mantle, it is highly surprising that we see almost no change in the fundamental three profiles of solid CO for different lines of sight. The observational constraints presented here are thus that any processing, be it chemical or physical, must leave the profiles of the three components invariant but may change the relative intensities. Typical lines of sight have 60-90% of the solid CO in a pure or nearly pure form. Models must be able to explain why this component of the CO has not experienced any kind of mixing with other species neither during formation nor as a result of subsequent processing. The results presented here thus seem to be consistent with a layered structure of the ices, which at least separate the CO ice from other species. Furthermore, the association of the red component with a simple H_2O-rich ice mixture is problematic. If the red component is indeed associated with H_2O, it must be explained why it has the same profile for the quiescent medium (e.g. CK 2), low mass YSOs (e.g. Elias 32), low mass YSOs in high mass star forming regions (e.g. TPSC 78), circumstellar disks (CRBR 2422.8) and high mass stars with abundant methanol (e.g. W 33A). Similar to the case for the middle component, this is unexpected since the profile of the red component should vary with the different temperatures and the different abundances of secondary species known to be associated with the water ice, such as methanol and ammonia, in the varity of circumstellar and interstellar regions surveyed. These differences in temperatures, ice structure and composition are observed through clear variations of the 3.08 μm H_2O band and should be reflected in the shape of the red component as well.

The implication is that solid CO seems to take part in little observable chemical processing around young stellar objects. Only the two sources L 1489 IRS and Reipurth 50 show some evidence for additional environments to the CO molecules through the excess absorption at 2141-2142 cm^{-1} and even here the environments is not likely to have a very high column density compared to the pure CO ice, since the features are so shallow ($\tau \sim 0.2$). Chemical processing may still take place, but the products of any chemical reactions involving CO must be efficiently removed from the environment of the remaining CO.

At the same time the variations in relative intensities of the three different components are consistent with physical processing affecting the total CO band profile, such as the evaporation of the volatile pure middle CO component prior to a hydrogen-bonding red component as a result of thermal processing. This is sup-

ported by the observation that the red component is detected along every line of sight with solid CO. The presence of an exclusion region in Fig. 3.10 may also support the mixing of pure CO into the water ice component as discussed in Sec. 3.3.6.

3.5.2 Is the grain shape constrained?

Even though the astronomical spectra can be so well fitted with the simple physical model presented here, it is a genuine worry that this is simply due to a degeneracy similar to that which haunts the mix-and-match approach. It is not possible to exclude a different combination of dielectric function and grain-shape model. It is, however, far easier to theoretically explain the common presence of pure CO rather than some specific and complicated mixture. Perhaps the most significant evidence for the applicability of a model using irregular grains simulated by a CDE shape distribution, is the evidence given when applying the same combination of pure CO and grain shape correction to other features. In particular it is shown by Boogert et al. (2002b) and in this work that the stretching vibration profile ^{13}CO along the line of sight towards two YSOs (one high mass and one low mass) is also consistent with pure CO independently of the grain shape. Furthermore, we have shown that the blue component, which is possibly the LO component of crystalline CO, has a shape which is consistent with CDE grains as well.

Thus, under the assumption that the optical constants of the middle component are known, a strong constraint on the grain shape is given. The used CDE grains is not a realistic model for interstellar grains. The CDE model assumes grains of solid ice and includes grain shapes like thin needles and disks, which are not likely to be formed. However, they are known to simulate irregular grains well (Bohren & Huffman, 1983) and thus provide a simple mathematical expression for this purpose. One possible scenario is that the pure CO exists as small irregular clumps on top or inside the water ice mantles. This may unify the observational constraints given by the CO band with the constraints on the icy grain size distribution given by the 3.08 μm water band (Dartois et al., 2002). However, detailed calculations of the grain shape effects of simulated interstellar grains using for instance fractal models (Fogel & Leung, 1997) are necessary to confirm the conjecture that CDE grains are appropriate for an irregularly shaped CO ice mantle. To further refine the adopted grain shape correction, additional solid state features from other species must be included. Ideally, it must be demanded that all observed solid state features are consistent with the same grain shape correction. However, since solid CO supplies one of the simplest and most easily observable bands, it likely provides the best single constraint. Other features which can constrain the grain shape correction further include the CO_2 stretching vibration band at 4.27 μm and the CO_2 bending mode at 15.2 μm. Also, having shown that a simple formula for the absorption cross section can reproduce the observed middle components, a convenient template is provided against which more detailed models of grain shapes can be tested.

3.5.3 Strategies for comparison with solid CO laboratory data

The presented data provide new challenges for laboratory studies of CO-rich ice mantles and some technical requirements become evident. The spectral features distinguishing the solid CO profiles of different sources show structures with widths less than 1 cm^{-1} and much of the modeling requires high quality laboratory spectra to investigate e.g. the structure of LO-TO split crystalline CO, which can have widths as small as 0.2 cm^{-1}. Accurate determinations of optical constants require laboratory spectra which are fully resolved. Thus, to match the present resolution of astronomical spectra, it is essential for the further study of interstellar solid CO to have laboratory data with a spectral resolving power of at least 0.1 cm^{-1}.

The accurate astronomical CO ice profiles encourage a change of strategy when comparing observed solid state profiles to laboratory data. As mentioned in Sec. 3.3.1 a mix-and-match approach is often employed to analyse the observed CO ice profiles. However, due to the many parameters governing a given laboratory simulation (abundances of mixture constituents, deposition and annealing temperatures, irradiation parameters and the details of the laboratory setup) and given the low spectral resolution of the available laboratory spectra, degeneracies are introduced when trying to constrain the compositions of CO-rich ices in space using a mix-and-match approach. As has been shown in (e.g. Boogert et al., 2002b; Dartois et al., 2002) and this work, both the quality and quantity of astronomical near to mid-infrared spectroscopy is now sufficient that more advanced physical models can be applied to the shape of the observed solid state features. In particular, this requires on the laboratory side high resolution optical constants, but also detailed experimental and theoretical studies of the microscopic structure of simple ices under interstellar conditions. On the astrophysical side, it is evident that solid state features in general also probe non-chemical phenomena in addition to the chemistry such as grain shape, size distributions and the overall temperature and density structure of the interstellar, circumstellar and disk material, which contain dust. The macroscopic properties of the objects observed are thus inseparable from the chemical properties of the ice mantles and must be modeled concurrently. Ideally, a single dust model including grain shapes and sizes, physical and chemical structure of the grain mantles and a macroscopic structure of the material along a given line of sight should be used to ensure consistency between the interpretations of different solid state features.

3.6 Conclusions and future work

Medium resolution M-band spectroscopy of a large sample of low mass young stellar objects has been used to explore the line profiles of the 4.67 μm stretching vibration mode of solid CO. A simple phenomenological three-component decomposition reveals a remarkable similarity of the structure of the CO stretching vibration mode at 2140 cm^{-1} between all observed lines of sight. A simple physical model is presented, which can reproduce the shape of all profiles to a high degree of accuracy.

- The phenomenological decomposition of the profile is found to provide good fits for all observed sources. The decomposition uses three different components: a red Lorentzian profile centered on 2136.5 cm^{-1}, a middle Gaussian profile centered on 2139.9 cm^{-1} and a blue Gaussian profile centered on 2143.7 cm^{-1}. Also the widths of the three components are kept constant such that only the relative intensities are varied between the sources. This approach reduces the information contained in a single line of sight to three linear parameters.

- In 30 of the 39 sources a broad and shallow absorption band is detected centered in the spectral range 2165–2180 cm^{-1}. The central optical depth of the band is found to correlate with the optical depth of the red component of the CO ice band for low mass YSOs only. Higher mass sources tend to show excess absorption at 2165 cm^{-1}. We propose that in addition to the traditional XCN band a second weak absorber centered at 2175 cm^{-1} is present. Furthermore, due to the correlation with the red CO component, the 2175 cm^{-1} band may be due to CO in a new, unidentified binding site.

- A simple physical model of the dielectric functions of the CO ice using Lorentz oscillators is described. It is shown that the middle component of the CO ice can be entirely explained along all lines of sight by modeling pure CO with a single Lorentz oscillator and grain-shape correcting the profile with a continuous distribution of ellipsoids (CDE). We suggest, that the CDE particles may work so well, because they simulate irregular grain surfaces or small irregularly shaped CO clumps on top of the water ice mantle. The same model suggests that the different optical constants of pure CO obtained from laboratory experiments vary only due to a varying oscillator density (or porosity) of the ice. A variation of ice porosity in the lab can be caused by slightly different experimental setups. The observed middle components show no direct evidence for the presence of contaminating species such as N_2, O_2 and CO_2 mixed with the carrier of the van-der-Waals interacting component and their concentration is likely less than 10%.

- The blue component can be explained by the LO mode of pure α-CO, which appears when the background source is linearly polarised, although it cannot be ruled out that the component is carried by a CO_2-rich ice. If the blue component is due to the LO mode of crystalline CO, the polarisation fraction at 4.7 μm is predicted in a number of sources. The derived polarisation fractions seem to correlate well with measured K-band polarisation fractions from the literature. The distribution of the relative contributions of the middle and blue components support the polarisation scenario. An important implication of LO-TO split CO is that a large fraction of the pure interstellar CO ice must be crystalline. This would put strong constraints on the processes governing the formation and structure of solid CO in space.

- The red component does not fit well with any simple H_2O-rich laboratory mixture due to the total absence of the 2152 cm^{-1} feature, which is due to CO-OH bonds. Although thermal and energetic processing tend to destroy

the CO-OH bonds, it also irreversibly changes the shape of the red component. Since CO adsorbed on many types of surfaces can produce a profile similar to the red component, it is suggested that alternative candidates which can explain the correlation with the $2175 \, \text{cm}^{-1}$ are tested. Conversely, statistics of the relative contributions of the middle and red components support a scenario where pure CO migrates into a porous water ice upon warmup. This scenario also predicts a strong $2152 \, \text{cm}^{-1}$ feature. There is thus a significant discrepancy between the data and all interpretations of the red component, which may require additional laboratory studies to solve.

A number of observations and laboratory experiments are necessary to both confirm and to elaborate on the results presented here. Further modeling will also significantly improve the understanding of solid state features of simple interstellar ices.

- Modeling of the expected ice mantle structure using existing dynamical models of collapsing protostars are necessary to theoretically understand the degree of mixing of the principal ice species which can be expected to exist at different stages of the star formation process. Useful output from such a model would include the detailed composition of the ice as a function of mantle depth for a given grain. Clearly, such a model depends on the physical and chemical processes governing the adsorption of ice on surfaces, the surface chemistry of the grain, but also on the time the grain spends in different physical environments (density and temperature) during its lifetime.

- Calculations of 'realistic' grain shape effects are required to explore which types of irregular grain surfaces can produce a grain shape correction similar to CDE particles.

- UHV laboratory spectroscopy with resolving powers of at least $0.1 \, \text{cm}^{-1}$ is needed to confirm the adopted dielectric functions for LO-TO split α-CO, to derive optical constants for other relevant CO-rich ices with narrow absorption profiles and to further explore the effect of polarised light on astrophysical ices.

- Future work should also include comparisons of other solid state bands of sources in the same sample such as H_2O and CO_2 with the results presented in this work. A physical model of the protostellar envelopes surrounding the sources using gas phase studies of rotational lines is required to fully understand the context of the observed ices and to separate the possible contribution from foreground material.

Acknowledgements

Appendix 3.1: Solid state line shapes

We review here the physical argument for using Lorentz oscillators as a first order approximation to the dielectric functions of simple solid state species. The formalism presented is mostly following Gadzuk (1987).

Common for both gas-phase and solid state lines is that any line shape from a spectroscopic transition is fundamentally the Fourier transform of the auto-correlation function of the relevant time dependent physical variable, $q(t)$.

$$I(\omega) = \int_\infty^\infty \exp(-i\omega(t-t_0))\langle q(t_0)q^*(t-t_0)\rangle dt. \tag{3.6}$$

This can be conveniently expressed with the Fourier transform $Q(\omega) = F(q(t), \omega)$, via the convolution theorem by using that the auto-correlation function is the convolution of $q(t)$ with itself:

$$
\begin{aligned}
I(\omega) &= F(F^{-1}(F(q, \omega) \times F^*(q, \omega))) \\
&= Q(\omega) \times Q(\omega)^*.
\end{aligned}
\tag{3.7}
$$

The relevant solution for the pure harmonic oscillator is:

$$q(t) = q_0 \exp(i\omega_0 t - \eta t), \tag{3.8}$$

where ω_0 is the frequency of the oscillator and η is the dampening factor determined by the finite decay time of the transition modeled by the oscillator.

It is well known that this solution, when inserted into eq. 3.7 yields a Lorentzian line profile, which collapses into a delta function when the oscillator is not damped, i.e. $\eta = 0$. Any model specific for solid state applications must take the interaction of the oscillator with a background surface into account. A picture which is often used, is that the oscillator interacts via elastic collisions with a thermally fluctuating background of atoms or molecules. Every elastic collision will change the phase of the oscillator with a random phase shift. Such a phase shift destroys the correlation between the oscillator coordinate before and after the collision. If the collisions are random, but occur with a certain probability, an exponential correlation decay is introduced and the correlation function in eq. 3.7 is modulated with a factor $\exp(-t/\tau_c)$, where τ_c is the average lifetime of the oscillator before a collision. It is straightforward to show that such a scenario will again result in a Lorentzian line shape broadened by $1/\tau_c$.

The effect is called de-phasing and is an often used concept in vibrational spectroscopy. Naturally higher order effects may produce more complex line shapes,

of which the best known examples include *non-homogenous* broadening caused by non-random intermolecular distances. E.g. low surface coverage is known to have profound effects on the profile of CO adsorbed on metals (Somorjai, 1994). However, more advanced models may still be result in basic Lorentzian profiles modified with frequency-dependent width functions as in Fano (1961) and Kubo (1969). We conclude that the use of harmonic oscillators and Lorentzian profiles provide a physically sound *starting point* for the theoretical study of the structure of interstellar ices using simple molecules such as CO as environmental probes.

Appendix 3.2: Notes on individual sources

3.6.1 Ophiuchus

IRS 43 is the closest source to the edge-on disk CRBR2422.8-3423 (Thi et al., 2002). It has a reasonably deep ice band and shows broad ro-vibrational lines in emission from hot CO gas.

GSS 30 IRS1 is associated with a large well-studied reflection nebulosity. Almost no CO ice is detected along the line of sight towards this source although it is located in the most embedded region of the ρ Ophiuchi clouds according to the extinction map by Cambrésy (1999) ($A_V > 10$). The M-band spectrum of this source is distinguished from other sources by showing very strong ro-vibrational lines in emission from gaseous CO (Pontoppidan et al., 2002).

3.6.2 Serpens

EC 90 also known as CK 1 or SVS 20 is a $1.6''$ binary young star, known to show signs of outflow activity (Huard et al., 1997). The CO ice band has previously been observed at low resolution by Chiar et al. (1994), but without resolving the binary. Solid CO_2 ($\tau = 2.6$) at 4.27 μm has been detected by Gürtler et al. (1996). We obtained well separated spectra of both components showing deep CO ice in both sources as well as cold CO gas. EC 90B additionally shows hot CO gas phase lines blueshifted by ~ 100 km s^{-1} showing that the outflow activity is probably associated with this component. The depth of the CO bands are $\tau = 2.1$ and $\tau = 1.2$ for EC 90A and EC 90B north, respectively. This shows that the distribution of CO ice around young stars can vary significantly on physical scales of a few hundred AU.

SVS 4-5 and 9: SVS 4 is a dense cluster of YSOs near the Serpens cloud core. The cluster is so dense, that it has often been confused with a single source. It was first resolved by Eiroa & Casali (1989), who counted 11 bright sources in the cluster. Our acquisition image obtained under exceptional seeing conditions (see Fig. 3.24) confirms the number of sources and shows that no fainter sources are present to a limit of $M_{4\,\mu m} = 11$. Low resolution M-band spectra of the two brightest 2 μm sources have been previously obtained by Chiar et al. (1994) who
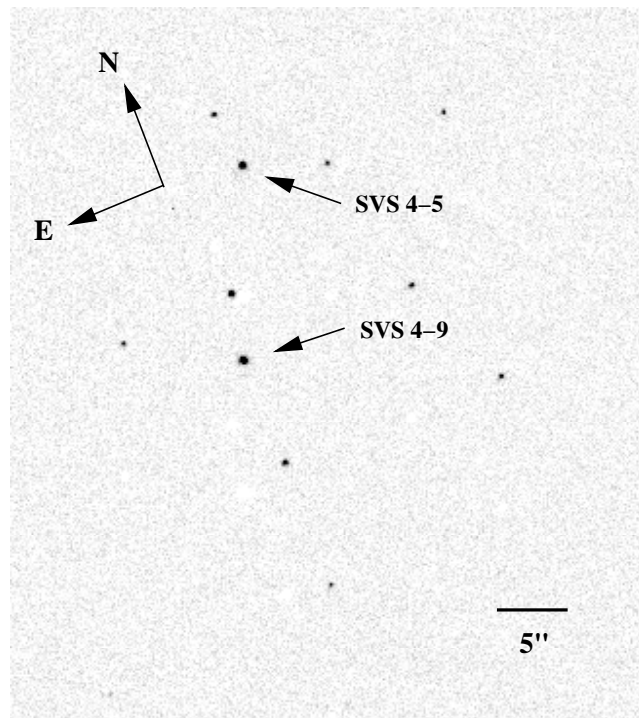
Figure 3.24: *4 μm acquisition imaging of the SVS 4 cluster of young stellar objects in Serpens indicating the location of the two observed sources. The seeing is measured to* 1.7 pixels $= 0''25$.

observed SVS 4-9 and SVS 4-10, $5''$ to the north. We obtained simultaneous spectra of the two brightest 4 μm sources as indicated in Fig. 3.24, the southern source, SVS 4-9, being the same as observed by Chiar et al. (1994) while the northern source, SVS 4-5, is new.

Deep CO ice is detected in both sources. The northern source has a typical narrow CO band, while the ice in the southern source shows a much broader feature consistent with the spectrum from the literature.

3.6.3 Chameleon

These are the first ground-based observations of ices in the molecular cloud complex in Chameleon. The observations are difficult due to the extremely southern location of the cloud ($\delta \sim -77°$). Consequently the sources never rise above an airmass of 1.7 as seen from Paranal, which makes proper correction for telluric features difficult. Additionally, gas phase observations are near impossible since the velocity shift compared to the telluric lines will be very small.
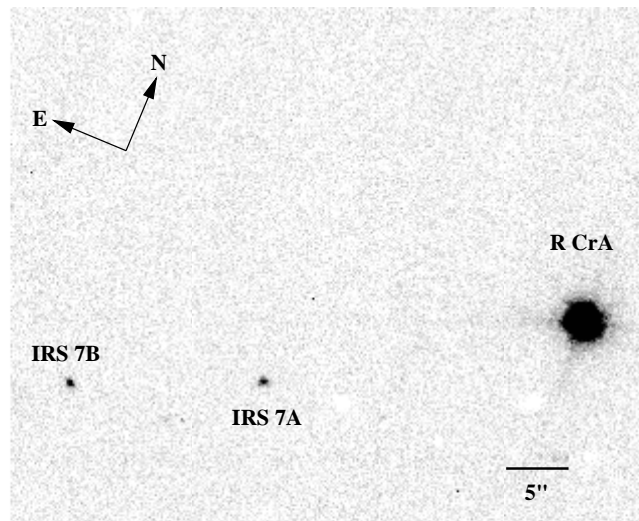
Figure 3.25: *Mnb image of the region around RCrA IRS 7 with the sources A and B indicated. Neither IRS 7A nor B is detected at 3.21 μm due to the presence of a deep water band. IRS 7B is detected in the K-band as a compact, but resolved reflection nebula.The positions of the two sources are IRS 7A: $\alpha = 19\ 01\ 55.16$, $\delta = -36\ 57\ 20.9$ and IRS 7B: $\alpha = 19\ 01\ 56.25$, $\delta = -36\ 57\ 26.9$, J2000.*

Cha INa 2 (source 1 in Table 2 of Persi et al. (1999)) is the only source with near-infrared excess detected by ISOCAM in the Chameleon I North a cloud. It has a class I SED and is surrounded by a small reflection nebula. It is estimated that the source is only extinct by 17 magnitudes (Persi et al., 1999). The source may be creating the large CO outflow observed in the area. This is one of the few sources which has a CO ice profile showing only a contribution from the red component.

3.6.4 Corona Australis

RCrA IRS 7 A and B There is some confusion in the literature regarding the identification of IRS 7 in the CrA cloud. At 2 and 6 cm the cloud is dominated by a strong binary radio source with a separation of $14''2$ (Brown, 1987). It has been suggested that the two radio sources represents a strong bipolar outflow, since no obvious near-infrared counterparts to the radio sources were known. We detect two bright point sources at 4.8 μm located at the positions of the radio sources, and can therefore confirm that it is unlikely that the radio emission is from a bipolar outflow from a single source. This was also found by Wilking et al. (1997) who imaged the source at 10 μm and detected IRS 7A, but not IRS 7B, perhaps indicating that IRS 7B has a very deep 9.7 μm silicate absorption feature. 2-5 μm spectra of IRS 7 was obtained by Tanaka et al. (1994), but it is unclear which source was observed due to the confusing K-band field. A narrow band M VLT-ISAAC image obtained at a seeing of $0''35$ is shown in Fig. 3.25.

3.6.5 Orion

TPSC 1 and TPSC 78   are two extremely red sources located in the trapezium cluster within 2′of the BN/KL region, with $K - L > 6.1$ and 4.85, respectively Lada et al. (2000). Their M-band spectra show very broad CO ice bands with the narrow component almost entirely missing as well as strong gas phase absorption. Also evident in both sources is strong absorption in the CN stretch region around 4.62 μm. The ices are likely to have been affected by the close proximity to young high mass stars.

Reipurth 50 IRS   is an intermediate-mass source with a large associated reflection nebula similar to that of Cha IRN, GSS 30 IRS 1 or L 1489. The source and the VLT-ISAAC spectroscopy is described in detail in Dartois et al. (2003).

Bibliography

Baratta, G. A. & Palumbo, M. E. 1998, J.Opt.Soc.Am, 15, 3076

Bergin, E. A., Ciardi, D. R., Lada, C. J., Alves, J., & Lada, E. A. 2001, ApJ, 557, 209

Bohren, C. F. & Huffman, D. R. 1983, Absorption and scattering of light by small particles
 (Wiley-Interscience)

Bontemps, S., André, P., Kaas, A. A., et al. 2001, A&A, 372, 173

Boogert, A. C. A., Blake, G. A., & Tielens, A. G. G. M. 2002a, ApJ, 577, 271

Boogert, A. C. A., Ehrenfreund, P., Gerakines, P. A., et al. 2000a, A&A, 353, 349

Boogert, A. C. A., Hogerheijde, M. R., & Blake, G. A. 2002b, ApJ, 568, 761

Boogert, A. C. A., Tielens, A., Ceccarelli, C., et al. 2000b, A&A, 360, 683

Brown, A. 1987, ApJ, 322, L31

Cambrésy, L. 1999, A&A, 345, 965

Casali, M. M. 1991, MNRAS, 248, 229

Casali, M. M. & Eiroa, C. 1996, A&A, 306, 427

Chang, H.-C., Richardson, H. H., & Ewing, G. E. 1988, J. Chem. Phys., 89, 7561

Chen, H., Grenfell, T. G., Myers, P. C., & Hughes, J. D. 1997, ApJ, 478, 295

Chen, H., Myers, P. C., Ladd, E. F., & Wood, D. O. S. 1995, ApJ, 445, 377

Chiar, J. E., Adamsom, A. J., Kerr, T. H., & Whittet, D. C. B. 1994, ApJ, 426, 240

Chiar, J. E., Adamson, A. J., Kerr, J., & Whittet, D. C. B. 1995, ApJ, 455, 234

Chiar, J. E., Gerakines, P. A., Whittet, D. C. B., et al. 1998, ApJ, 498, 716

Chrysostomou, A., Hough, J. H., Whittet, D. C. B., et al. 1996, ApJ, 465, L61

Collings, M. P., Dever, J. W., Fraser, H. J., McCoustra, M. R. S., & Williams, D. A. 2003, ApJ,
 583, 1058

Dartois, E., d'Hendecourt, L., Thi, W., Pontoppidan, K. M., & van Dishoeck, E. F. 2002,
 A&A, 394, 1057

Dartois, E., Thi, W.-F., Pontoppidan, K. M., et al. 2003, A&A, submitted

Devlin, J. P. 1992, J. Phys. Chem., 96, 6185

Ehrenfreund, P., Boogert, A. C. A., Gerakines, P. A., Tielens, A. G. G. M., & van Dishoeck,
 E. F. 1997, A&A, 328, 649

Eiroa, C. & Casali, M. M. 1989, A&A, 223, 17

Elsila, J., Allamandola, L. J., & Sandford, S. A. 1997, ApJ, 479, 818

Evans, N. J. 2003, PASP, in press

Fano, U. 1961, Phys. Rev., 124, 1866

Fogel, M. E. & Leung, C. M. 1997, ApJ, 501, 175

Gadzuk, J. W. 1987, in Vibrational spectroscopy of molecules on surfaces (Plenum Press), 49

Gerakines, P. A., Schutte, W. A., Greenberg, J. M., & van Dishoeck, E. F. 1995, A&A, 296, 810

Gillett, F. C. & Forrest, W. J. 1973, ApJ, 179, 483

Gürtler, J., Henning, T., Kömpe, C., et al. 1996, A&A, 315, L189

Hagen, W., Allamandola, L. J., & Greenberg, J. M. 1979, Ap&SS, 65, 215

Huard, T. L., Weintraub, D. A., & Kastner, J. H. 1997, MNRAS, 290, 598

Hudson, R. L., Moore, M. H., & Gerakines, P. A. 2001, ApJ, 550, 1140

Kastner, J. H., Jingquiang, L., Siebenmorgen, R., & Weintraub, D. A. 2002, AJ, 123, 2658

Keane, J. V., Tielens, A. G. G. M., Boogert, A. C. A., Schutte, W. A., & Whittet, D. C. B. 2001, A&A, 376, 254

Kenyon, S. J., Calvet, N., & Hartmann, L. 1993, ApJ, 414, 676

Kerr, T. H., Adamson, A. J., & Whittet, D. C. B. 1993, MNRAS, 262, 1047

Kubo, R. 1969, Adv. Chem. Phys., 15, 101

Lacy, J. H., Baas, F., Allamandola, L. J., et al. 1984, ApJ, 276, 533

Lada, C. J., Lada, E. A., Clemens, D. P., & Bally, J. 1994, ApJ, 429, 694

Lada, C. J., Muench, A. A., Haisch Jr., K. E., et al. 2000, AJ, 120, 3162

Langer, W. D. & Penzias, A. A. 1993, ApJ, 408

Liseau, R., Lorenzetti, D., Nisini, B., Spinoglio, L., & Moneti, A. 1992, A&A, 265, 577

Manca, C., Martin, C., Allouche, A., & Roubin, P. 2001, J. Phys. Chem. B, 105, 12861

Mathis, J. S., Rumpl, W., & Nordsieck, K. H. 1977, ApJ, 217, 425

Novozamsky, J. H., Schutte, W. A., & Keane, J. V. 2001, A&A, 379, 588

Palumbo, M. E. 1997, J. Phys. Chem., 101, 4298

Pendleton, Y. J., Tielens, A. G. G. M., Tokunaga, A. T., & Bernstein, M. P. 1999, ApJ, 513, 294

Persi, P., Marenzi, A. R., Gómez, M., & Olofsson, G. 2001, A&A, 907

Persi, P., Marenzi, A. R., Kaas, A. A., et al. 1999, AJ, 117, 439

Pontoppidan, K. M., Schöier, F. L., van Dishoeck, E. F., & Dartois, E. 2002, A&A, 393, 585

Sandford, S. A. & Allamandola, L. J. 1988, Icarus, 76, 201

Sandford, S. A., Allamandola, L. J., Tielens, A. G. G. M., & Valero, G. J. 1988, ApJ, 329, 498

Schmitt, B., Greenberg, J. M., & Grim, R. J. A. 1989, ApJL, 340, L33

Schutte, W. A. & Greenberg, J. M. 1997, A&A, 317, L43

Shen, C. J., Greenberg, J. M., Schutte, W. A., & van Dishoeck, E. F. 2003, A&A, submitted

Sogawa, H., Tamura, M., Gatley, I., & Merril, K. M. 1997, AJ, 113, 1057

Soifer, B. T., Puetter, R. C., Russel, R. W., et al. 1979, ApJ, 232, L53

Somorjai, G. A. 1994, Introduction to surface chemistry and analysis (Wiley and sons)

Tanaka, M., Nagata, T., Sato, S., & Yamamoto, T. 1994, ApJ, 430, 779

Teixeira, T. C., Emerson, J. P., & Palumbo, M. E. 1998, A&A, 330, 711

Thi, W.-F. 2002, PhD thesis, Leiden Observatory

Thi, W.-F., Pontoppidan, K. M., van Dishoeck, E. F., Dartois, E., & d'Hendecourt, L. 2002, A&A, 394, 27

Tielens, A. G. G. M. & Hagen, W. 1982, A&A, 114, 245

Tielens, A. G. G. M., Tokunaga, A. T., Geballe, T., & Baas, F. 1991, ApJ, 382, 523

van Broekhuizen, F., Schutte, W. A., & Fraser, H. 2003, A&A, in prep

Vandenbussche, B., Ehrenfreund, P., Boogert, A. C. A., et al. 1999, A&A, 346, L57

Whitney, B. A., Kenyon, S. J., & Gomez, M. 1997, ApJ, 485, 703

Wilking, B. A., Lada, C. J., & Young, E. T. 1989, ApJ, 340, 823

Wilking, B. A., McCoughrean, M. J., Burton, M. G., et al. 1997, AJ, 114, 2029

Wilking, B. A., Taylor, K. N. R., & Storey, J. W. V. 1986, AJ, 92, 103

Willner, S. P., Gillet, F. C., Herter, T. L., et al. 1982, ApJ, 253, 174

Ziman, J. M. 1979, Principles of the Theory of Solids, 2nd edn. (Cambridge University Press)

Zumofen, G. 1978, J. Chem. Phys., 68, 3747

Chapter 4

Mapping ices in protostellar environments on 1000 AU scales

Methanol-rich ice in the envelope of Serpens SMM 4

Abstract

We present VLT-ISAAC L-band spectroscopy toward 10 stars in SVS 4, a $30'' \times 45''$ dense cluster of pre-main sequence stars deeply embedded in the Serpens star forming cloud. The ISAAC spectra are combined with archival imaging from UKIRT and ISOCAM to derive accurate extinctions toward the SVS 4 stars. The data are then used to construct a spatial map of the distribution of ice in front of the cluster stars with an average angular resolution of $6''$ or 1500 AU, three orders of magnitude better than previous maps. We show that water ice is present throughout the region and confirm the presence of methanol ice with an abundance of up to 25% relative to water. It is shown that methanol ice maintains a very high abundance relative to H_2 throughout SVS 4, but drops by at least an order of magnitude only $75''$ away from SVS 4. The maps indicate that some of the lines of sight toward the SVS 4 stars pass through the outer envelope of the class 0 protostar SMM 4. The abundance of water ice relative to the refractory dust component shows a sudden increase by 90% to $(1.7 \pm 0.2) \times 10^{-4}$ relative to H_2 at a distance of 5000 AU to the center of SMM 4. The water ice abundance outside the jump remains constant at $(9 \pm 1) \times 10^{-5}$. We suggest that this is an indication of a significantly enhanced ice formation efficiency in the envelopes of protostars. The depletion of volatile molecules in the envelope of SMM 4 is discussed. In particular, it is found that up to 2/3 of the depleted CO is converted into CO_2 and CH_3OH in the ice. Therefore, only 1/3 of the CO originally frozen out will return to the gas phase as CO upon warmup. [1] [2]

4.1 Introduction

In the last decade, it has become increasingly clear that the interaction between molecular gas and ice mantles on dust grains in dense clouds significantly affects

the overall chemistry of the cloud as well as the way molecules are observed. The chemistry of a dense cloud is influenced by the presence of ices through reactions taking place on the surfaces of dust grains and by changing the composition of the gas when ice species are desorbed through heating or energetic processing (Aikawa et al., 2003). Additionally, molecules may be removed from the gas-phase by freezing out onto dust grains in the early phases of star formation (e.g. Jørgensen et al., 2002). Many observational studies have attested to the high abundance of a large range of molecular ice species in dark clouds and in star forming regions in particular (e.g. Boogert & Ehrenfreund, 2004; Gibb et al., 2004; van Dishoeck et al., 2003). Since interstellar ice can only be observed in absorption toward an infrared source, most of these observational studies have concentrated on ices along single, isolated lines of sight. Large variations in the abundances of some ice species have been observed in different regions, but the lack of spatial information has often made any interpretation difficult. Examples of ice species with strongly varying abundances relative to water ice include methanol ice (Dartois et al., 1999; Pontoppidan et al., 2003a), OCN^- ice (Gibb et al., 2004; Pendleton et al., 1999) and CO ice (Pontoppidan et al., 2003b). Other abundant ice species are found to have a fairly constant abundance relative to water ice, such as CO_2 (Gerakines et al., 1999). This shows that the composition of interstellar ice depends on the physical conditions under which it formed. Thus, for a complete study of the chemical evolution of interstellar ice, spatial information as well as detailed information on the physical environment in which it is found are needed. Infrared spectrometers are now sensitive enough to record spectra along lines of sight toward closely spaced infrared sources, which can be young stars or background stars. This opens the possibility of directly obtaining spatial information on the distribution of interstellar ices. For example, Murakawa et al. (2000) constructed a water ice map of the Taurus molecular cloud using bright background stars. The resulting spatial resolution of this study was $\sim$1 line of sight per 100 square arcminutes. In this chapter we present high angular resolution (1 line of sight per 0.02 square arcminutes) observations of the distribution of ices in a small region of the Serpens star forming cloud centered on the cluster SVS 4.

SVS 4 is a small but dense cluster of low- to intermediate mass ($L = 1 - 50\,L_\odot$) pre-main sequence stars located in the south-eastern core of the Serpens molecular cloud. It was first studied by Eiroa & Casali (1989), who found it to be one of the densest YSO clusters known with 11 stars within a region only 12 000 AU across, corresponding to a stellar density of $\sim 5 \times 10^4\,M_\odot\,pc^{-3}$. One of the cluster members, SVS 4-9/EC 95, is the brightest X-ray source in Serpens and is probably a very young intermediate mass star with abnormal coronal activity (Preibisch, 2003). The center of the cluster is located only 30″ or 7500 AU from the deeply embedded class 0 protostar, SMM 4 (e.g. Hogerheijde et al., 1999). Lines of sight toward the stars in the SVS 4 cluster may therefore intersect part of the outer envelope of SMM 4. This system thus provides a unique opportunity to directly probe the amount of freeze-out near deeply embedded young stellar objects. Detailed millimeter studies of pre-stellar cores (e.g. Bergin et al., 2002; Caselli et al., 1999; Tafalla et al., 2004) and protostars (e.g. Jørgensen et al., 2004) indicate that a significant fraction of the gas-phase molecules ($\gtrsim$ 90% of the condensible species)

is depleted onto grains in the cold parts of the envelopes where the timescales for freeze-out are shorter than the age of the core. For the case of protostellar envelopes, Jørgensen et al. propose a 'drop' abundance structure where the gas-phase abundances are relatively high in the low density outermost envelope and then drop abruptly to a very low value at the radius where freeze-out becomes effective. In the inner warm regions of the envelope, the ices evaporate resulting in high gas-phase abundances. Our observational ice maps can test such abundance structures directly.

Pontoppidan et al. (2003a) presented low-resolution L-band spectra toward two of the SVS 4 cluster members, SVS 4-5 and SVS 4-9, and found that the ices in front of these two stars contain a very high abundance of methanol ice of up to 25% compared to water. This was the first detection of methanol ice outside of high-mass star forming regions and is among the highest abundances observed. Previous searches for methanol ice in low-mass star forming regions have only provided strict upper limits to the abundance of methanol down to a few % relative to water ice (Chiar et al., 1996). The reason for this large variation in the methanol ice abundance is currently not understood. Recent laboratory experiments have shown that methanol can be formed in dense clouds through successive hydrogenation of CO at 10-20 K on the surfaces of dust grains (Watanabe et al., 2003). It is found that the formation of methanol ice along this route depends primarily on the abundance of atomic hydrogen, the thickness of the ice mantle and the temperature of the ice, with the most efficient formation of methanol at 15 K. Thus, a variation in these parameters could be related to the observed differences in methanol ice abundance. Alternatively, bombardment with energetic protons has also been found to produce moderate yields of methanol in $CO:H_2O$ ice mixtures (Hudson & Moore, 1999). The study of the relation of interstellar methanol ice to the cloud environment in which it is found therefore provides direct constraints on the formation mechanism of this important molecule. Due to the high stellar density, the proximity to SMM 4 and the very high methanol ice abundance of the SVS 4 cluster, it presents an excellent case for studying the distribution of methanol-rich interstellar ice on small angular scales in a protostellar environments.

In this chapter we present low-resolution L-band spectra of 10 SVS 4 stars obtained with the ISAAC spectrometer on the Very Large Telescope (VLT) at Paranal in Chile. Additionally, we use archival data from the Infrared Space Observatory (ISO) and the United Kingdom Infrared Telescope (UKIRT) to further constrain the environment. We use the spectra to produce a detailed map of the distribution of water and methanol ice in the SVS 4 region with a spatial resolution of $6'' = 1500 \, \text{AU}$. The corresponding line of sight density is one per 0.02 square arcminutes, which is more than three orders of magnitude higher than previous ice maps.

This chapter is organised as follows: §4.2 describes the observations from ISAAC as well as archival data used. §4.3 shows how the basic observational parameters have been derived. §4.4 interprets the relation to the SMM 4 envelope and §4.5 discusses the distribution of ices in the observed region.

4.2 Observations and archival data

L-band spectra of 10 sources in the SVS 4 cluster were obtained using the ISAAC spectrometer mounted on UT 1 of the VLT on the nights of July 8–9, 2003. The low resolution grating and the $0\overset{''}{.}6$ slit were used, yielding a resolving power of $\lambda/\Delta\lambda \sim 600$ and an instantaneous wavelength coverage from 2.84–4.15 μm. Typical on-source integration times were $\sim$40 minutes per pointing. Additionally, the two brightest sources, SVS 4-5 and SVS 4-9, were observed in one setting centered on the CH-stretching mode of solid methanol at 3.53 μm using the medium resolution grating with a resolving power of $\lambda/\Delta\lambda \sim 3300$. The spectra were reduced using IDL following the procedure described in Pontoppidan et al. (2003b). The spectra were ratioed by the early-type standard stars, BS 6629 (A0V) and BS 7236 (B9V) to remove telluric absorption lines.

A 4.07 μm image was obtained by co-adding 8 acquisition images from the spectroscopic observations and was flux calibrated relative to the acquisition image of the standard star BS 7348 (B8V). The 4 μm flux of the standard star was estimated by extrapolating the V-band magnitude of 3.95 to 4 μm using blackbody colours, yielding $M_{4\,\mu\mathrm{m}} = 4.15$. The spectra were then scaled to the 4.07 μm photometric points. We estimate the accuracy of the photometry to be better than 0.1 mag. Standard stars of spectral type A or B are known to have photospheric hydrogen lines in absorption. This may result in excess line emission in the ratioed spectra. The two standard stars show the presence of the Brα line at the 7% level relative to the continuum while other hydrogen lines have strengths of $< 5\%$. The Brα line was not detected in any of the SVS 4 spectra and any residual emission lines are due to the standard stars. Since the hydrogen lines do not affect the ice bands, no attempt to correct for them was made.

J- H- and K-band imaging from UFTI at the United Kingdom Infrared Telescope (UKIRT) were extracted from the UKIRT archive, and ISOCAM 6.7 and 14.3 μm imaging as well as a CVF field centered on SVS 4 were extracted from the ISO archive[3]. The near-infrared images were flux calibrated using bright 2MASS stars in the field. Standard aperture photometry was performed using $1.5''$ apertures. The absolute photometry was found to be better than 0.1 mag when comparing to 2MASS. The ISOCAM data were reduced using the CIA reduction package version DEC01. Because the SVS 4 sources are partially blended at the ISO-CAM resolution, the raster maps were resampled to a finer sampling by a factor of two. ISOCAM fluxes were then derived from the broad-band images by fitting a PSF derived from an isolated source in the field to source positions taken from the 4.07 μm ISAAC image. The ISOCAM images where then flux calibrated using conversion factors of $2.32\,\mathrm{adu\,g^{-1}\,s^{-1}\,mJy^{-1}}$ and $1.96\,\mathrm{adu\,g^{-1}\,s^{-1}\,mJy^{-1}}$ for LW2 and LW3, respectively (Blommaert et al., 2000), where adu is the Analog to Digital Unit, and g is the gain. Any colour corrections to the broad band ISO-CAM fluxes were found to be less than 2%. CVF spectra were extracted using $3\,\mathrm{pixels}\times3\,\mathrm{pixels}=18''\times18''$ apertures.

---

[3]Based on observations with ISO, an ESA project with instruments funded by ESA Member States (especially the PI countries: France, Germany, the Netherlands and the United Kingdom.) and with the participation of ISAS and NASA.

4.3 Derivation of observed physical parameters

4.3.1 Distance to the Serpens molecular cloud

There is some controversy in the literature regarding the distance to the Serpens cloud. Distance estimates based on accurate photometry of a few stars ($\sim$10) range from 250 pc (Chavarria-K. et al., 1988) to 400 pc (Chiar, 1997; Hogerheijde et al., 1999). However, accurate photometric surveys of larger samples of stars seem to converge on the smaller distance of ~ 250 pc. Straizys et al. (1996) find a distance of 259 ± 37 pc using 105 stars. This result is supported by a preliminary distance estimate of 220-270 pc using 2MASS photometry of a similarly sized sample (Knude et al., in prep). In this chapter all distance-dependent quantities are scaled to a distance of 250 pc.

4.3.2 Determination of extinction and water band continuum

In order to study the distribution of ices toward the SVS 4 cluster, accurate optical depths of the water bands as well as column densities of the refractory dust component must be determined. The optical depths of the water bands depend sensitively on the continuum chosen. However, since the blue wing of the water band is outside of the atmospheric L-band window, the determination of a continuum will always have some degree of uncertainty. One solution is to use a K-band spectrum to define an empirical continuum (e.g. Murakawa et al., 2000). Unfortunately, only photometric JHK points are available for the SVS 4 stars. However, as will be shown in this section, most of the sources in SVS 4 have almost no infrared excess. This allows reasonably accurate modeling of the continua using Kurucz stellar atmosphere models. Furthermore, a simultaneous determination of the extinction toward each source can be derived with confidence.

Since the effective temperatures of low-mass pre-main sequence stars are quite insensitive to their masses (Siess et al., 2000), Kurucz models with a low $\log g$ and $T_{\mathrm{eff}} = 3500 - 4500$ K can be used as a rough model of the photospheric emission. In the case of SVS 4-9 and SVS 4-10, the effective temperatures have been determined spectroscopically by Preibisch (1999). Any infrared excess is modeled by a single blackbody of $T = 500 - 1500$ K or by a disk model from Dullemond et al. (2001) if the excess is large. The observed SED of each source was de-reddened to fit a Kurucz model at the J, H and K points and a blackbody or disk model was added to fit any infrared excess at longer wavelengths as well as the 3.8-4.15 μm slope of the L-band spectra. In cases where a strong infrared excess would also affect the near-infrared points, the extinction and infrared excess contribution were iteratively corrected until a fit was found, which reproduced both the photometric points and the slope of the L band spectra. This approach was chosen to provide a realistic continuum at 3 μm rather than to yield an unambiguous excess model. The fits to sources with a strong excess are therefore degenerate to some extent. However, due to the very high absolute values for the extinction ($A_J > 5$) the determination of water ice optical depths and extinction was found to be very insensitive within the allowed parameter space, and the uncertainties given on the derived quantities reflect the fitting degeneracy.
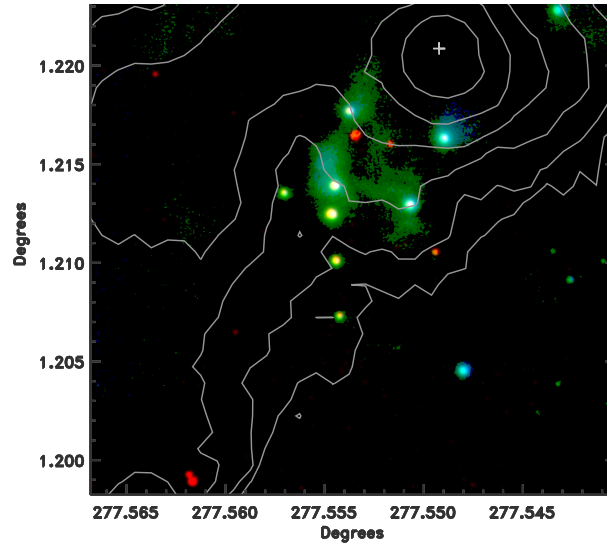
Figure 4.1: *J, H, 4 μm colour composite of SVS 4. The contours show the 850 μm SCUBA map by Davis et al. (1999). The cross indicates the central position of SMM 4.*
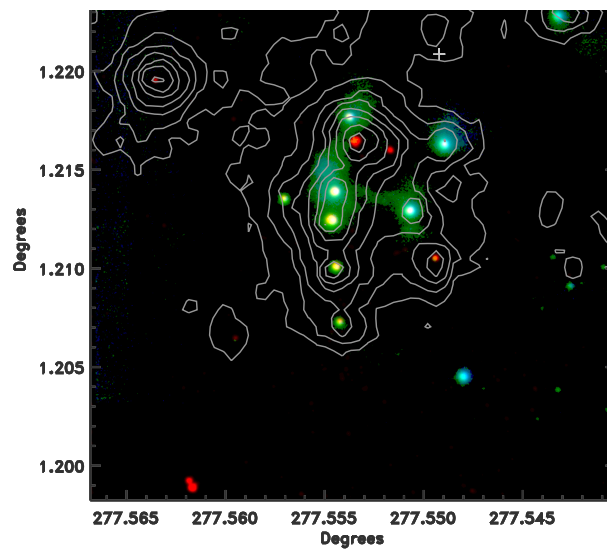

Figure 4.2: *The SVS 4 J, H, 4 μm colour composite overlaid with ISOCAM 6.7 μm contours.*
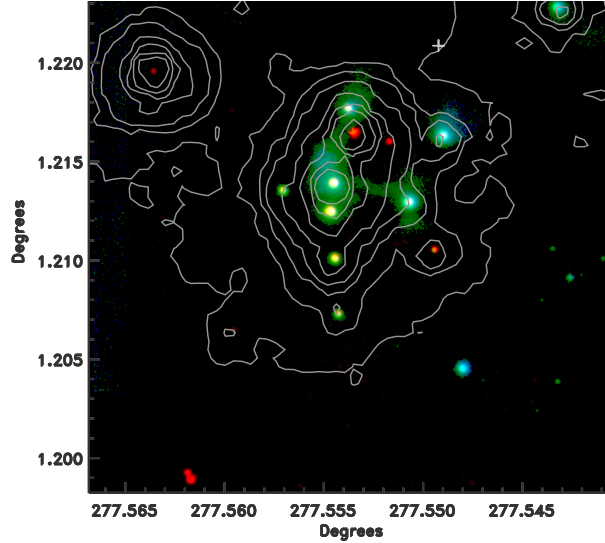
Figure 4.3: *The SVS 4 $J, H, 4\,\mu$m colour composite overlaid with ISOCAM 14.7 μm contours.*

The extinction law at near-infrared wavelengths is well described by a power law, $A_\lambda/A_J = (\lambda/1.25\,\mu\text{m})^\alpha$, where $\alpha = 1.6 - 2.0$ (Cardelli et al., 1989; Martin & Whittet, 1990). A high value of α has been found to best describe dust in some dense molecular clouds (e.g. Lutz et al., 1996; Martin & Whittet, 1990). A low value for the power-law index of 1.6 was attempted, but this was found to give extinction-corrected 2–5 μm fluxes, which were too steep to correspond to a black-body or Kurucz model for stars with no infrared excess when the $(J - H)$ colours were used to determine the extinction. In particular, an extinction law index of at least 1.85 was required to simultaneously fit all spectral and photometric points of sources like SVS 4-3, SVS 4-5 and SVS 4-9. A higher index could also be used since this would simply create a small infrared excess. Here, we adopt the minimum value of $\alpha = 1.85$. In the mid-infrared range, the empirical extinction law toward the galactic center by Lutz et al. (1996) is used. This is consistent with the ISOCAM extinction law for Serpens ($A_{\text{LW2}} = 0.41 A_K$ and $A_{\text{LW3}} = 0.36 A_K$) derived by Kaas et al. (2004). The resulting SEDs and water bands are shown in Figs. 4.4, 4.5 and 4.6. The corresponding fitting parameters are shown in Table 4.2. The extinctions are given in terms of the extinction in the J-band, A_J, to avoid making unneces-sary assumptions about shape of the extinction law in the optical wavebands by extrapolating to A_V.

It is seen that the extinction toward SVS 4 is in general very high ($A_J = 5 - 25$), roughly corresponding an A_V of up to 100 mag. Most of the sources exhibit very little infrared excess shortwards of 6 μm with the exceptions of SVS 4-6 and SVS 4-10. This results in a fairly accurate absolute determination of A_J with an un-certainty dominated by the chosen extinction law rather than the accuracy of the photometry or, in most cases, the SED model assumptions. We estimate a relative

uncertainty on A_J of 5%. A different extinction law may cause systematic effects larger than this. The bolometric luminosities of the stars can then be estimated by integrating over the fitted Kurucz models. The derived stellar parameters are included in Table 4.2. It should be cautioned that the effective temperatures of the stars are not well constrained using photometric points and should ideally be determined by high resolution near-infrared spectroscopy. The derived luminosities thus depend sensitively on the assumption that the stars are indeed pre-main sequence stars. As a consistency check the stellar ages and masses have been derived using the evolutionary tracks of Siess et al. (2000). These are also given in Table 4.2, but are associated with large uncertainties except in the cases of SVS 4-9 and SVS 4-10, which have spectroscopically determined spectral types.

In order to convert optical depth and extinction to column density, the relations $N_{H_2O}/\tau_{H_2O} = 1.56 \times 10^{18}\,\mathrm{cm}^{-2}$ (Pontoppidan et al., 2003a) and $N_H/A_J = 5.6 \times 10^{21}\,\mathrm{cm}^{-2}\,\mathrm{mag}^{-1}$ (Vuong et al., 2003) are used. The water ice column density conversion uses a band strength of $2 \times 10^{-16}\,\mathrm{cm}\,\mathrm{molec}^{-1}$ (Gerakines et al., 1995).

4.3.3 Derivation of the extinction and water ice optical depth toward SVS 4-12

The determination of the extinction and water optical depth toward SVS 4-12 must be discussed in detail, since this source is not detected in the J- and H- band images from UKIRT and since the water ice band is heavily saturated. Only a K-band point, the 3.8-4.2 μm spectral slope and an uncertain 6.7 μm ISOCAM point are available for the extinction determination. In principle, the lack of near-infrared photometric points prevents an accurate determination of extinction if the source has a significant infrared excess. However, an extinction of $A_J = 26$ mag gives a good fit to a Rayleigh-Jeans slope of a stellar spectrum, without any infrared excess (see Fig. 4.6). The presence of any excess will result in a smaller extinction, since the dereddened SED in that case will be shallower. Therefore, the derived extinction is a conservative upper limit. However, the simultaneous good fit of the K-band point and the slope of the ISAAC spectrum indicates that SVS 4-12 has a naked photospheric SED at least to wavelengths of 4 μm, although the current data do not allow us to rule out the possibility that SVS 4-12 has some minor infrared excess at longer wavelengths.

The optical depth of the water ice band toward SVS 4-12 is determined by scaling the water band from SVS 4-9 to the SVS 4-12 red wing. In general, all the water ice bands observed toward the SVS 4 sources have very similar shapes, i.e. one water band can generally be scaled to fit well with another at the 10% level. The best fit of $\tau_{H_2O} = 8 \pm 1$ for SVS 4-12 using the water band of SVS 4-9 is shown in Fig. 4.7. This value does not change significantly if other water bands from SVS 4 are used. Thus if the extinction is overestimated due to an infrared excess in SVS 4-12, the measured abundance of water ice relative to the dust column density will be a strict lower limit.

Table 4.1: *Flux densities and astrometry of SVS 4 sources*

Source	RA (J2000)	DEC (J2000)	1.250 μm	1.635 μm	2.159 μm	4 μm	6.7 μm	14.3 μm
SVS 4-2	18:29:56.58	+01:12:59.4	1.8 ± 0.2	8.5 ± 0.9	16.4 ± 1.0	19 ± 2	10 ± 2	19 ± 4
SVS 4-3	18:29:56.70	+01:12:39.0	–	0.4 ± 0.1	1.6 ± 0.2	28 ± 3	16 ± 4	17 ± 3
SVS 4-4	18:29:57.00	+01:12:47.6	1.5 ± 0.2	10.5 ± 1	24.5 ± 2	35 ± 4	15 ± 4	15 ± 3
SVS 4-5	18:29:57.63	+01:13:00.2	–	0.03 ± 0.01	2.9 ± 0.3	130 ± 10	242 ± 50	494 ± 100
SVS 4-6	18:29:57.69	+01:13:04.4	0.5 ± 0.1	3 ± 0.3	10.3 ± 1.0	38 ± 4	40 ± 6	84 ± 20
SVS 4-7	18:29:57.84	+01:12:27.8	0.015 ± 0.005	0.6 ± 0.1	4.3 ± 0.4	15 ± 2	7 ± 2	7 ± 2
SVS 4-8	18:29:57.88	+01:12:37.7	0.04 ± 0.01	1.8 ± 0.2	14.4 ± 1	56 ± 6	51 ± 10	56 ± 10
SVS 4-9 (EC 95)	18:29:57.92	+01:12:46.0	0.21 ± 0.05	9.7 ± 1.0	68.6 ± 7.0	155 ± 15	147 ± 30	89 ± 20
SVS 4-10 (EC 92)	18:29:57.88	+01:12:51.1	0.6 ± 0.1	9.9 ± 1.0	41.4 ± 4.0	111 ± 11	152 ± 40	700 ± 70
SVS 4-12	18:29:57.22	+01:12:58.4	–	–	0.2 ± 0.02	26 ± 3	24 ± 5	–

All flux densities are given in units of mJy.
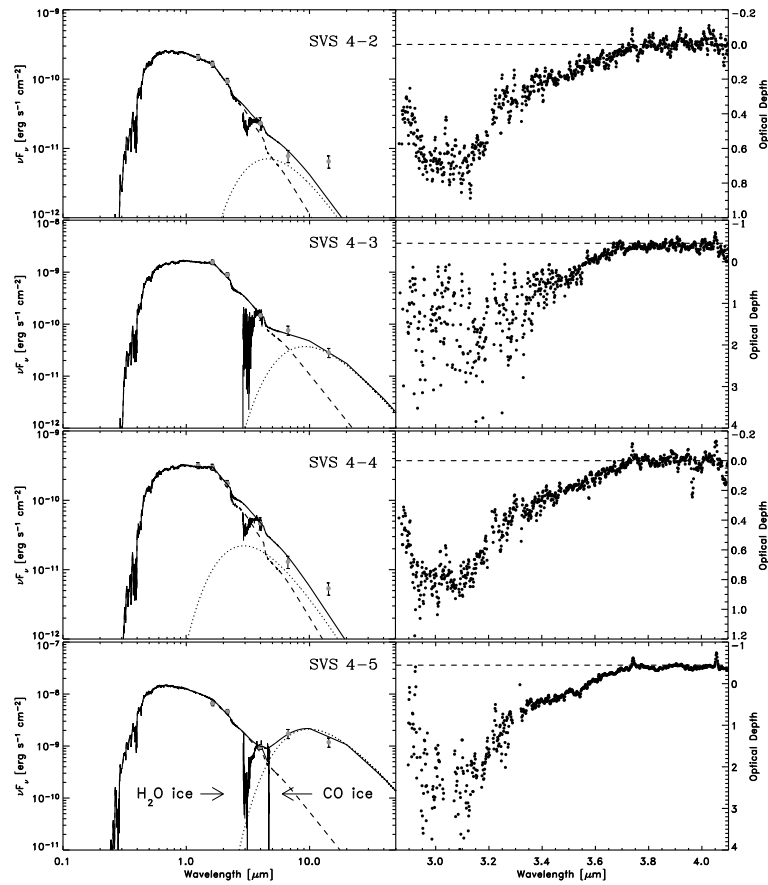
Figure 4.4: *The spectral energy distributions of the SVS 4 stars, which were used to define a continuum for the water bands. The extracted water ice bands are shown next to each SED on an optical depth scale. On the left, the dashed lines show the Kurucz stellar atmosphere model, the dotted line shows the added infrared excess and the full line is the sum of the two contributions.*
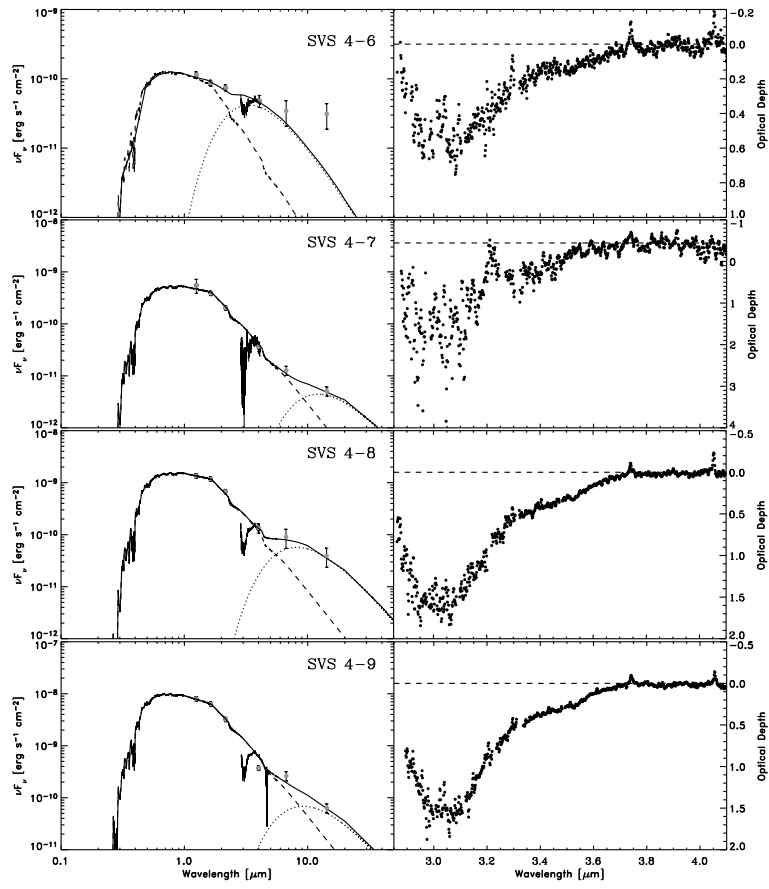
Figure 4.5: *Continued from Fig. 4.4.*
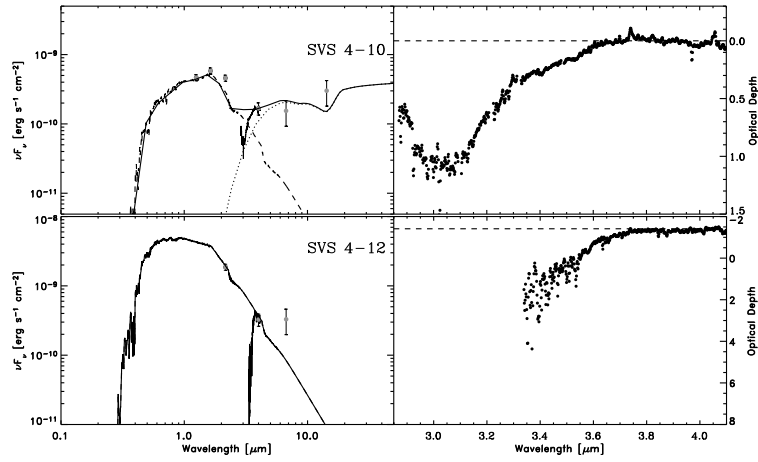
Figure 4.6: *Continued from Fig. 4.5.*
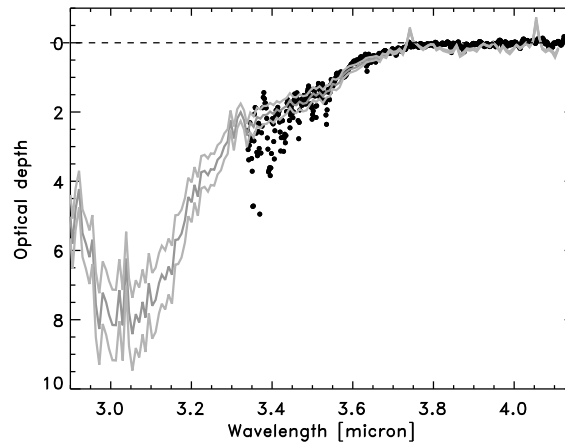
Figure 4.7: *Determination of the optical depth of the water ice band toward SVS 4-12. The dots show the parts of the SVS 4-12 L-band spectrum which are detected with more than 5σ. The curves are the spectrum of SVS 4-9 scaled to optical depths of 7, 8 and 9 to indicate the allowed range of depths of the SVS 4-12 water ice band.*

Table 4.2: *Physical parameters for SVS 4 sources*

Source	L_{bol} [L$_\odot$]	T_{eff} [K]	stellar mass [M$_\odot$]	Age [Myr]	A_J^a [mag]	τ_{H_2O}	N_{H_2O} [10^{18} cm^{-2}]	H$_2$O ice abundance $\times 10^{-5}$ w.r.t. H$_2$
SVS 4-2	0.7	4750	1.5	17	4.2	0.7 ± 0.1	1.1 ± 0.2	9.3 ± 1.4
SVS 4-3*	4.9	4250	1.0	0.5	18.0	3.5 ± 0.5	5.5 ± 0.8	10.9 ± 1.6
SVS 4-4	0.9	4250	1.0	3	4.9	0.85 ± 0.1	1.3 ± 0.2	9.7 ± 1.2
SVS 4-5	38	4500	3.5	0.3	21.0	3.5 ± 0.3	5.5 ± 0.5	8.6 ± 0.8
SVS 4-6	0.4	4750	0.8	42	4.9	0.7 ± 0.1	1.1 ± 0.2	9.1 ± 1.4
SVS 4-7	1.5	4500	1.3	3	10.5	2.0 ± 0.3	3.1 ± 0.5	10.6 ± 1.8
SVS 4-8	4.6	4500	1.4	0.8	10.8	1.7 ± 0.2	2.7 ± 0.3	8.8 ± 1.2
SVS 4-9	27	4750	3.5	0.4	10.5	1.6 ± 0.1	2.5 ± 0.2	8.5 ± 0.8
SVS 4-10	1.2	3750	0.5	0.8	6.2	1.1 ± 0.1	1.7 ± 0.2	9.9 ± 1.2
SVS 4-12*	28	5000	3.5	0.5	26	8 ± 1	12.5 ± 2.0	17.2 ± 2.4

^{a} Estimated relative uncertainty of 5%.

* Not detected in J, making the derived spectral type and age uncertain.

4.4 Relation to the envelope of SMM 4

The projected distances of the individual SVS 4 stars to the central submillimeter position of SMM 4 are 15-40″, corresponding to 3 750 - 10 000 AU at a distance of 250 pc. SMM 4 is also associated with a large scale molecular outflow oriented NW-SE. Consequently, the projected south-eastern lobe of the outflow passes through the SVS 4 region. Therefore, there is a possibility that the lines of sight toward some SVS 4 stars may probe the outer envelope of SMM 4 and/or material which has been processed by shocks created by the outflow.

It is therefore an important issue to determine the depth of the SVS 4 cluster relative to the envelope and outflow of SMM 4. Clearly, much of SVS 4 share the line of sight with the SMM 4 envelope as seen in Fig. 4.1. However, it is not clear whether the SVS 4 stars are situated in front of, inside, or behind the envelope of SMM 4. Only the two last scenarios allow for a study of the ices in the envelope of a class 0 protostar since the ice absorption bands do not probe what lies behind the individual SVS 4 stars. The last scenario would require the presence of a second dense cloud in front of SVS 4, which can produce the ice absorption and extinction corresponding to H_2 column densities of up to $7 \times 10^{22}\,\mathrm{cm}^{-2}$ for SVS 4-5 and SVS 4-12. The Serpens cloud was mapped in a range of optically thin molecular lines by Olmi & Testi (2002) who found a column density through the SVS 4 region of $6 \times 10^{22}\,\mathrm{cm}^{-2}$ within a large beam of $\sim 50''$. However, this column density was measured using $C^{18}O$, a molecule known to be partially frozen out at low temperatures and high densities. The direct measurement of the CO ice abundance discussed in Sec. 4.5.3 shows that the gas-to-solid ratio of CO is 2-5 toward SVS 4, assuming a total abundance of CO of 2×10^{-4}. However, if the CH_3OH and CO_2 ices have been chemically formed from hydrogenation and oxidation of CO molecules, the fraction of CO molecules directly observed to be removed from the gas-phase increases by more than 50% (see §4.5). Taking the freeze-out into account, the H_2 column densities may increase to $12 \times 10^{22}\,\mathrm{cm}^{-3}$ in the most extreme case. The observed column densities can therefore not completely rule out the presence of a dense cloud containing SVS 4 and the observed ices, which is unrelated to SMM 4. A high resolution map ($\sim 20''$) of the $C^{18}O$ (2-1) line by White et al. (1995) shows that SVS 4 is located on the edge of the molecular ridge of the south-eastern clump in Serpens, but shows no evidence of a separate, extended clump of dense gas with very high column density associated with SVS 4. Additionally, the $C^{18}O$ line has a single gaussian shape with a $FWHM$ of $\sim 2\,\mathrm{km\,s}^{-1}$ in the direction of SMM 4, indicating that no other large scale velocity component is present. It will be assumed that SVS 4 is not associated with a foreground cloud, although it should be noted that this issue is not fully resolved.

To decide whether SVS 4 can be placed behind or significantly inside the envelope of SMM 4, a physical model for the envelope was calculated using the procedure described in Jørgensen et al. (2002). The model was fitted to the SCUBA 850 μm map by Davis et al. (1999) and the ISO-LWS spectrum extracted by Larsson et al. (2000). The resulting model has a power law density profile with index -1.6 and an outer radius of slightly less than 10 000 AU where the temperature drops to 9 K. The total luminosity is 11 $L_\odot$, the density at 1000 AU is $5 \times 10^6\,\mathrm{cm}^{-3}$ and
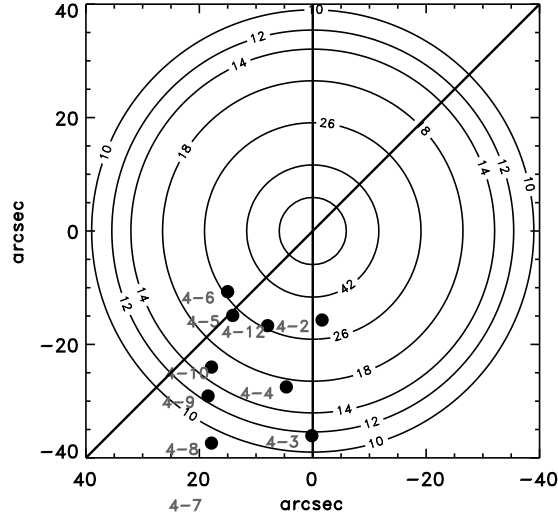
Figure 4.8: *Contours showing the projected extinction in the J-band through the model envelope of SMM 4 compared to the positions of the SVS 4 lines of sight. The solid lines indicate the range of observed position angles of the outflow associated with SMM 4.*

the total mass is $5.8\,M_\odot$. These values are largely consistent with earlier simple models by Hogerheijde et al. (1999).

The projected extinction through the envelope of SMM 4 calculated from the model density profile is shown in Fig. 4.8. Clearly, the extinction through the SMM 4 envelope is too high for all the SVS 4 stars to lie entirely behind the SMM 4 envelope. However, SVS 4-5 and SVS 4-12, which both have measured extinctions of $A_J \sim 25$ mag, lie very close to the $A_J = 26$ contour. This places them effectively behind the envelope if all the extinction is caused by SMM 4. Conversely, SVS 4-2 and SVS 4-6 must in any case lie in the frontal part of the envelope because their measured extinctions are much less than those predicted by the SMM 4 model. It is interesting to note that this behaviour is expected if SVS 4 is a roughly spherical cluster directly embedded into the envelope of SMM 4. In other words, since the angular extent of the cluster is similar to the depth of the envelope ($\sim 10\,000\,\text{AU}$), it is expected that some sources lie in front of the envelope and some behind. This geometry is thus consistent with the drastic variation of extinction from source to source on very small angular scales.

4.5 The distribution of ice toward SVS 4

4.5.1 Constructing an ice map

Once the ice column densities and infrared extinctions are determined, maps can be constructed showing the spatial distribution of these quantities toward SVS 4. Some caveats apply to such maps. Since only pencil-beam lines of sight are probed, no information about the ice content of the cloud between the lines of sight can in principle be inferred. However, under the assumption that the observed lines of sight resolve any variations in ice abundance, a map can be constructed using interpolation techniques. In this work, the IDL 2-dimensional kriging interpolation algorithm is used.

The creation of an ice map is similar to the construction of extinction maps of dark clouds using background stars (e.g. Alves et al., 2001). Due to sensitivity limitations, background stars can often not be used to obtain ice maps of high spatial resolution. In this chapter, a densely packed collection of stars embedded in the molecular cloud rather than background stars are used, and consequently great care has to be taken in interpreting the resulting distribution of ice. One problem concerns the interpretation of differences in column densities, since embedded stars are likely to probe different depths through the cloud. This problem will not affect maps of abundances of the ice relative to extinction or other ice species. The second caveat concerns the interaction of the embedded stars with the ice in their immediate surroundings. We will show in the following section that this is unlikely to cause problems for stars of low luminosity ($L \sim 1\,L_\odot$). Conversely, maps can be used to study the interaction of individual embedded stars with local ice.

4.5.2 Water ice

The water ice map

Maps of the water ice column density, extinction and water ice abundance toward SVS 4 are shown in Fig. 4.5.2. The water ice abundance map is simply the ratio between the water ice column density map and the extinction map. It thus shows the line of sight averaged abundance of water ice relative to the refractory dust component or H_2 column density in front of the SVS 4 stars. It can be seen that the extinction and the column density of water ice vary with factors of 5 and 10, respectively, on angular scales of only $\sim 10''$. The largest extinction and water ice column density are observed toward SVS 4-12. The abundance of water ice relative to molecular hydrogen is also seen to peak sharply toward SVS 4-12 by a factor of 1.9. Within the framework of the envelope model of SMM 4, the line of sight toward SVS 4-12 passes through a gas density of $4 \times 10^5\,\mathrm{cm}^{-3}$ and a temperature of 11 K. Furthermore, the abundance rises slightly in the south-western part of the cluster, parallel to the dense ridge in the south-eastern Serpens core seen in molecular gas (White et al., 1995).

The relation between the infrared extinction and the water column density is show in Fig. 4.10. The derivative of this relation basically measures the water ice abundance as a function of depth into the cloud. Note the important distinction to

the absolute line of sight abundance, which is simply the ratio of ice column density to H_2 column density. The derivative of the abundance relation is a measure of the *local* ice abundance averaged over the angular dimension of the observed cloud. An absolute abundance is an average over local abundances and does for example not remove any contribution from bare grains along the line of sight. The absolute ice abundance can thus be seen as a lower limit to the local ice abundance.

The lines of sight toward the SVS 4 sources exhibit a linear relation or constant water ice abundance between $A_J = 5 - 25$ except for the line of sight toward SVS 4-12, which is over-abundant in water ice by a factor of 1.9 relative to the other SVS 4 sources. The best-fitting least-squares line for SVS 4 between $A_J = 4 - 25$ and excluding SVS 4-12 is:

$$\tau_{H_2O} = (0.07 \pm 0.09) + (0.15 \pm 0.01) \times A_J \qquad (4.1)$$

The slope of the derived relation corresponds to a local abundance of water ice relative to H_2 of $(9\pm1)\times10^{-5}$. Extrapolating the linear relation to small extinctions yields a negative intercept with the A_J axis of -0.5 ± 0.6. However, the negative intercept is not statistically significant and the relation could also pass through the origin. Note that a negative intercept with the A_J axis, if significant, translates into the presence of water ice without a refractory dust component. This is an unlikely scenario, and more plausible explanations of a negative threshold would be that a systematic error plays a role or that the relation is no longer linear for small A_J. Significantly, the SVS 4 sources seem to exclude a positive threshold for the water ice in the $\tau_{H_2O} - A_J$-relation of $A_J \sim 1$ such as found in general for molecular clouds (e.g. Whittet et al., 1988) and for Serpens in particular (Eiroa & Hodapp, 1989). The two sources SVS 4-3 and SVS 4-7 have a slightly, but significantly, higher water ice abundance compared to the best fitting line of about 20%. These two sources are responsible for the higher water abundance in the south-western part of SVS 4 as seen in Fig. 4.5.2.

For comparison, lines of sight toward three other young stellar sources from the south-eastern clump in Serpens (EC 90A+B and EC82), unrelated to SVS 4, have also been plotted in Fig. 4.10. These objects were observed and analysed using the same approach as for the SVS 4 sources. It is found that the other Serpens sources are systematically and significantly under-abundant in water ice compared to SVS 4 and result in a relation with a small, but positive intercept with the A_J axis of $A_J = 0.4 \pm 1.3$. This is roughly consistent with previous determinations of the water ice–extinction relation for Serpens (Eiroa & Hodapp, 1989), but also consistent with the relation passing through the origin. This may be an indication of a higher degree of ice evaporation near these sources or a lower ice formation efficiency outside the densest parts of the Serpens core.

The corresponding relation for the Taurus molecular cloud of $\tau_{H_2O} = 0.072 \times (A_V - 3.2)$ is included in Fig. 4.10 (Whittet et al., 2001). The dense cloud extinction law derived by these authors in Taurus, $A_V = rE_{J-K}$ with $r = 5.3$, was used to convert the optical extinction to A_J, giving $\tau_{H_2O} = 0.24 \times (A_J + 0.95)$. The conversion is relevant for extinctions above the ice threshold. The water ice relation for Taurus was determined using sources with $A_V < 26$, roughly corresponding to $A_J \lesssim 7.5$. It is seen to be consistent with the SVS 4 points out to $A_J \sim 6$, but de-
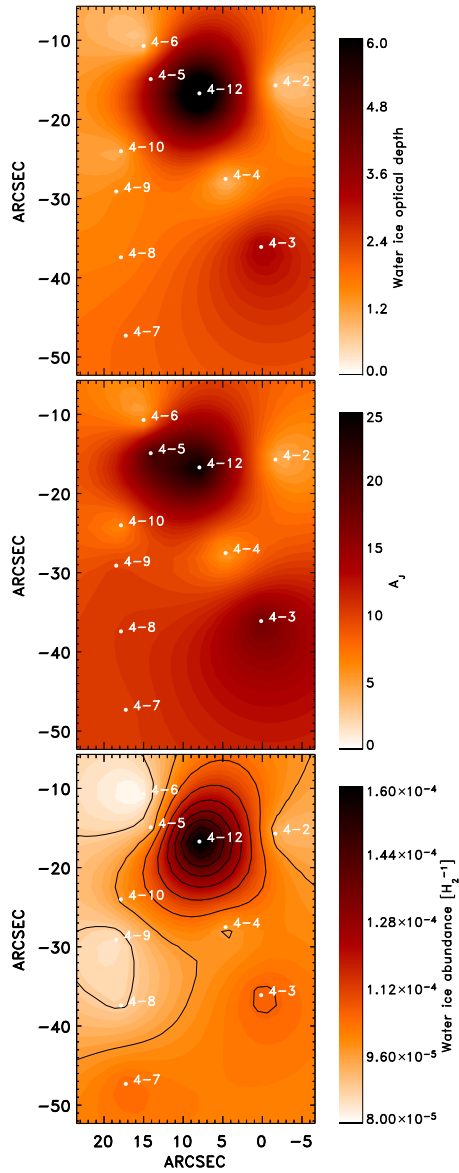
Figure 4.9: *Top: Map of the water ice optical depth toward SVS 4. Middle: Map of A_J of the same region. Bottom: Map of the abundance of water ice relative to H_2. Filled circles indicate the positions of the measured sight-lines. SMM 4 is centered on (0,0).*
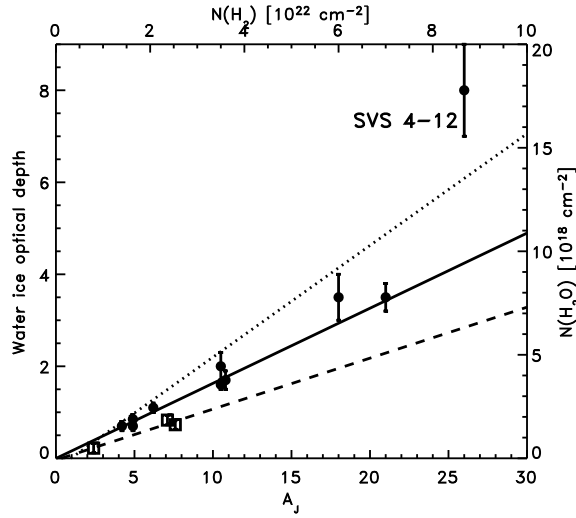
Figure 4.10: *Relation between extinction and water ice column density for the SVS 4 sources (filled circles) and the 3 unrelated Serpens YSOs, EC 90A+B and EC 82 (open squares). The solid line indicates the best-fitting line through the SVS 4 points, excluding SVS 4-12. The dashed line is the best-fitting line through the three comparison Serpens sources and the dotted line is the relation measured for the Taurus cloud by Whittet et al. (2001) (see text).*

viates significantly from the best-fitting line through the SVS 4 points. According to the Taurus relation, the water ice abundance in Taurus is 1.35×10^{-4}. In other words, assuming that the grain size distribution in SVS 4 and in Taurus are identical, the ice mantle volume must be on average 40% smaller in SVS 4 compared to Taurus in order to create the SVS 4 ice abundance. However, the abundance of water ice toward SVS 4-12 is significantly higher than that of the Taurus cloud.

A jump in the abundance of water ice in the SMM 4 envelope?

The very high abundance of water ice observed toward SVS 4-12 merits further scrutiny. Fig. 4.11 shows the observed water abundance toward each SVS 4 source as a function of the maximum density (or the minimum distance to SMM 4) probed by each line of sight. The densities and distances were calculated using the model profile of SMM 4 and the measured extinctions of the individual sources to estimate their depth in the SMM 4 envelope. SVS 4-12 is the source which probes the deepest into the envelope at a minimum distance to the center of SMM 4 of 4700 AU and a maximum density of $4.3 \times 10^5 \, \text{cm}^{-3}$. In the figure, a sharp jump in the water ice abundance is evident just below 5000 AU, while the abundance remains constant at larger distances. However, the presence of the jump depends on only one source, SVS 4-12. As discussed in Sec. 4.3.3, we regard the abundance measurement toward SVS 4-12 relative to those of the other SVS 4 sources as robust or possibly a lower limit. As discussed by Jørgensen et al. (2004), the amount

101
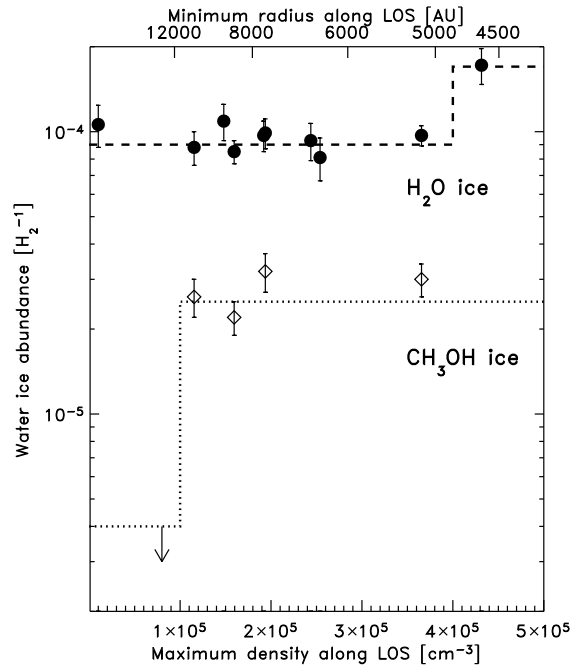
Figure 4.11: *Relation between the water and methanol ice abundances and the SMM 4 envelope model. The bottom axis indicates the maximum density encountered by each line of sight. The top axis indicates the corresponding minimum distance to the center of the SMM 4 envelope. The dashed line sketches the sharp jump in water ice abundance around 5000 AU from the center of SMM 4. The dotted line sketches the jump in methanol ice abundance observed at a radius of ~12 000 AU relative to the center of SMM 4. Outside this radius only strict upper limits on the abundance of solid methanol are available (see Sec. 4.5.4).*

of freeze-out is expected to increase significantly at the envelope radius where the density is high enough for the freeze-out timescale to become shorter than the age of the core. For a typical lifetime of $\sim 10^5$ yr, this is expected to occur at densities of a few $\times 10^5$ cm^{-3}, comparable to the density at which the jump occurs. Of particular interest is the apparent sharpness of the jump, which seems to be no more than 500 AU wide. If real, this provides strong constraints on such models and justifies further ice mapping of protostellar envelopes. Unfortunately, the data presented here only give constraints on the abundance of water ice toward SVS 4-12 and additional deep mid-infrared spectroscopy is required to study the abundance jump in other ice species.

Caveats

To test the conclusions reached by analysing the $\tau_{\text{H2O}} - A_J$-relation, sources of systematic errors should be explored. For example, a shallower infrared extinction law would result in a systematic underestimate of the extinction of up to 10%, sufficient to cause the relation to pass through the origin. However, as discussed in Sec. 4.3.2, a small index for the extinction law is not favoured. Also, this effect would influence the three comparison sources. The errors in the individual water optical depths are often larger than 10%, but systematic effects are estimated to be smaller. The dominant systematic sources of error in the optical depths are related to the adopted model for the intrinsic SED. This error can be estimated by comparing the shape of the water ice band for sources with and without a large infrared excess. In Figs. 4.4, 4.5 and 4.6 it is seen that all water ice bands have similar shapes regardless of the shape of the background source SED. This is a clear indication that the derived optical depth is reasonably model independent.

Finally, it can be expected that the stars heat the dust in their immediate vicinity to temperatures high enough to evaporate water ice. The question is if this dusty, but ice-free region is large enough to significantly affect the observations. A zone of dust with no ice mantles around each star would create a threshold in the $\tau_{\text{H}_2\text{O}} - A_J$-relation. We used a 1-dimensional radiative transfer model of a $50\,L_\odot$ star embedded in a cloud of constant density, calculated using the DUSTY code (Ivezić et al., 1999), to estimate the threshold created by the radiation of the star. These models show that the temperature rises above an assumed water sublimation temperature of 90 K only within a radius of 300 AU. For a star of $1\,L_\odot$, the sublimation temperature is reached at 50 AU. The contribution to the extinction from bare grains is then $A_J \simeq 0.7$ mag for the most luminous stars in SVS 4 and $A_J \simeq 0.1$ for the least luminous stars. Correcting for this contribution using the calculated luminosity of each star brings the $\tau_{\text{H}_2\text{O}} - A_J$-relation slightly closer to the Taurus relation.

No line of sight is expected to pass through the ice evaporation zones from any of the other stars. If the density around the stars is increasing inwards, i.e., if each star in SVS 4 is associated with a remnant envelope, the column density of warm, bare grains and thus the ice threshold will increase. Conversely, this scenario is unlikely since no significant ice threshold has been observed. A full map of CO ice toward the SVS 4 stars will be much more sensitive to moderate heating of the envelope material due to the higher volatility of CO ice. The limited CO ice observations toward SVS 4 sources described in Sec. 4.5.3 do indicate that a significant fraction of the dust in the region presently has temperatures of $\sim$ 20 K, in agreement with moderate heating of the cloud and no significant density gradients near the SVS 4 stars.

4.5.3 CO ice

An additional constraint on the temperature of the ice can be found from high resolution spectroscopy of CO ice in the stretching vibration mode around $2139\,\text{cm}^{-1} = 4.67\,\mu$m. Laboratory experiments by Collings et al. (2003) indicate that a layer of pure CO ice will partly migrate into an underlying layer of porous water ice

upon warmup. The different types of CO ice can be distinguished by the shapes of their corresponding spectral profiles (Tielens et al., 1991). Pontoppidan et al. (2003b) suggested that the relative column densities of the pure CO ice band at $2139.9\,\mathrm{cm}^{-1}$ and of CO ice trapped in water ice at $2136.5\,\mathrm{cm}^{-1}$ are a sensitive indicator of the thermal history as well as current temperature of interstellar ice due to the migration effect. In this scenario, a strong band of pure CO ice indicates the presence of ice with temperatures less than $\sim 20\,\mathrm{K}$, while a strong band of water-rich CO indicates that a significant amount of ice at some point in time has been heated to temperatures higher than $20\,\mathrm{K}$.

Three of the SVS 4 stars have been observed in CO ice (see Table 4.3). The spectrum of SVS 4-10 by Chiar et al. (1994) is not of high enough quality to extract quantitative information about column densities of different CO ice components, although a rough estimate is given in Table 4.3. The observed total line of sight column densities of CO ice in SVS 4-5 and SVS 4-9 are $2.7 \times 10^{18}\,\mathrm{cm}^{-2}$ and $2.5 \times 10^{18}\,\mathrm{cm}^{-2}$, respectively. However, since SVS 4-5 has an extinction in the J-band of 22.8 magnitudes, while SVS 4-9 has an extinction of 10.5, the total line of sight CO abundance for SVS 4-9 (8.5×10^{-5}) is twice that of SVS 4-5. Interestingly, the line of sight abundances of pure CO toward SVS 4-5 and 9 are almost identical at 3×10^{-5}, while a factor of almost four distinguishes the abundances of CO in water. The estimated column density of pure CO toward SVS 4-10 from Chiar et al. (1994) is consistent with a constant local abundance of pure CO in SVS 4.

Although it is not possible to identify any unambiguous relationship using only two points, some interesting suggestions can be made. Clearly, the amount of water-embedded CO ice on a grain varies significantly through the cloud. This stands in sharp contrast to the pure CO ice, which seems to have a constant local abundance, based on three sources. This is difficult to explain from simple migration of CO from the pure form to the water-embedded form upon warmup, but also does not conform to a scenario where the water-embedded CO has formed together with the water mantle. In the case of efficient migration, a large component of CO in water should be reflected by a correspondingly smaller component of pure CO. In the simultaneous formation case, the water-embedded CO might be expected to show a constant local abundance. Instead, the CO ice abundances may point to a more complex thermal history of the cloud material. A constant local abundance of pure CO might indicate recent freeze-out, while the abundances of water-embedded CO could indicate thermal processing of an earlier CO layer. Also, a processing scenario other than heating which drastically changes the water-rich CO abundance could easily change the abundances of other ice species, such as methanol and CO_2. This is not observed to the same degree as for CO (see Secs. 4.5.4 and 4.5.5) In this picture, the early thermal processing might have been caused by the formation of the SVS 4 cluster, while the recent freeze-out of CO might be related to the formation of SMM 4. Alternatively, the CO ice bands may show processing from interaction of the SMM 4 outflow with the envelope material. A complete map of SVS 4 in CO ice will be needed to explore this question further.

Table 4.3: *CO ice observations toward SVS 4 sources*

Source	N(Pure CO) [10^{18} cm^{-2}]	N(CO in water) [10^{18} cm^{-2}]	Abundance (pure CO) [10^{-5}] w.r.t. H$_2$	Abundance (CO in water) [10^{-5}] w.r.t. H$_2$	Reference
SVS 4-5	1.8 ± 0.4	0.9 ± 0.1	2.8 ± 0.7	1.4 ± 0.2	a
SVS 4-9	0.9 ± 0.15	1.6 ± 0.1	3.1 ± 0.6	5.4 ± 0.6	a
SVS 4-10	0.4 ± 0.2	1.0 ± 0.5	3 ± 2	6 ± 3	b

References: a) Pontoppidan et al. (2003a), b) Chiar et al. (1994)

Table 4.4: *CH₃OH ice observations toward SVS 4 sources*

Source	N(CH₃OH) [$10^{18}\,\mathrm{cm}^{-2}$]	Abundance [10^{-5}] w.r.t. H_2
SVS 4-5	1.9 ± 0.2	3.0 ± 0.4
SVS 4-8	0.80 ± 0.08	2.6 ± 0.4
SVS 4-9	0.64 ± 0.06	2.2 ± 0.3
SVS 4-10	0.56 ± 0.06	3.2 ± 0.5

4.5.4 Methanol ice

Abundance

One of the primary objectives of mapping ices toward SVS 4 was to explore the large excess of methanol ice known to be present in this region. Fig. 4.12 shows the spectra of the four lines of sight from which a high-quality $3.53\,\mu$m methanol band could be extracted. The remaining lines of sight do not have sufficient signal-to-noise ratios to allow a meaningful estimate of the column density of solid methanol. In Fig. 4.13 the relation between extinction and the column density of methanol ice is shown. The best-fitting line to the $\tau_{\mathrm{CH_3OH}} - A_J$-relation is:

$$\tau_{\mathrm{CH_3OH}} = 0.06 \pm 0.11 + (0.07 \pm 0.01) \times A_J. \tag{4.2}$$

The relation gives a local abundance of methanol ice of $(2.5 \pm 0.4) \times 10^{-5}$ relative to H_2. The measured threshold value is consistent with 0 mag and may therefore be identical to the water ice threshold. There is a significant scatter in the relation, which is not seen for the water ice band for the same four sources. The methanol abundances in SVS 4-5 and SVS 4-10, both of which are located in the northern part of SVS 4, are slightly higher than for SVS 4-8 and SVS 4-9. For comparison, strong upper limits on the methanol abundance for EC 90 A and B are shown in Fig. 4.13. In absolute terms, the upper limits for these sources are $3 - 4 \times 10^{-6}$. This large difference between SVS 4 and EC 90 is particularly interesting since EC 90 is located only $75''$ north of SVS 4-5. Therefore, the methanol ice must reside in a region no more than 2 arcminutes in extent. This region contains only SVS 4, and the outflow and envelope of SMM 4. There are thus strong indications that the high efficiency of methanol formation in the ice mantles in SVS 4 is related to the protostellar envelope of SMM 4.

Methanol band profile

The detected methanol bands toward SVS 4 sources are indistinguishable within the noise. In order to maximise the signal-to-noise, a weighted average of the four detected methanol bands has been calculated. The resulting $3.53\,\mu$m methanol band profile is shown in Fig. 4.14 where it is compared to an ISAAC spectrum of the well-studied methanol band toward the massive YSO W 33A (e.g. Dartois et al., 1999). While the methanol bands from SVS 4 are similar in shape to that of W 33A, they almost completely lack the so-called $3.47\,\mu$m band, which is prominent
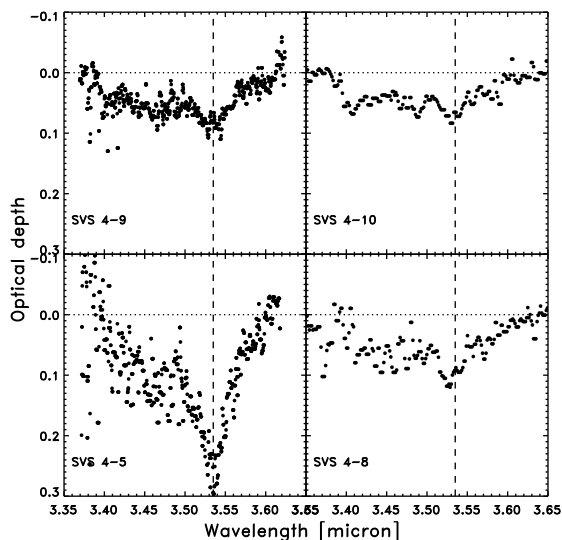
Figure 4.12: *The four lines of sight in SVS 4 where a spectrum of good quality of the 3.53 μm CH$_3$OH band could be extracted. All spectra are depicted on the same optical depth scale. The spectra of SVS 4-5 and 9 are new medium resolution (R=3300) observations; the other two spectra are taken using the low resolution mode of ISAAC yielding a resolving power of R=600. The vertical dashed line indicates 3.535 μm.*

toward W 33A. A laboratory spectrum of a mixture of H$_2$O:CO$_2$:CH$_3$OH=1:1:1 ices deposited at 10 K from Ehrenfreund et al. (1999) is compared to the SVS 4 methanol band. The main band at 3.53 μm is seen to be well matched by the laboratory profile in position and width. The secondary bands at 3.32–3.42 μm are in general harder to match with a laboratory spectrum. This may be due to an uncertain continuum determination in the blue wing of the band, since most of the SVS 4 sources are very faint below 3.35 μm. However, even the brightest source, SVS 4-9, shows no sign of excess absorption below 3.35 μm. Some substructure absorption bands may be seen at 3.40 and 3.47 μm, the last of which is discussed in more detail in Sec. 4.5.6.

4.5.5 CO$_2$ ice

Abundant CO$_2$ ice has been observed toward SVS 4 using ISOCAM-CVF (Alexander et al., 2003). Unfortunately, many of the SVS 4 sources are blended in the CVF images, especially at the longer wavelengths, and accurate decompositions are very difficult due to the spatial undersampling of the detector. However, our ISOCAM photometry of the high resolution broad-band imaging shows that a few sources dominate the flux at 14.3 μm. For instance, SVS 4-5 is 6 times brighter than
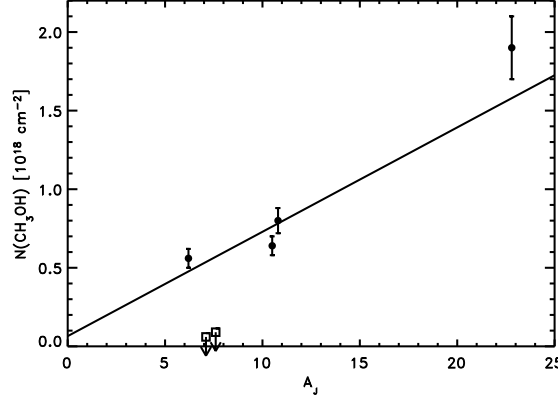
Figure 4.13: *Relation between extinction and methanol ice column density for SVS 4. Filled circles indicate SVS 4 sources, while open squares are upper limits for the unrelated Serpens YSOs EC 90 A+B. The solid line is the best-fitting line through the SVS 4 points.*

SVS 4-6 with which it is blended. Similarly, SVS 4-10 is 8 times brighter than SVS 4-9. In principle, the optical depth of an absorption band toward two blended sources will depend on the ratio of continuum fluxes as well as on the absolute optical depths of the two lines of sight. In particular, the depths of optically thick bands may be significantly underestimated by filling-in from another line of sight. The observed optical depth of an ice band, τ_{obs}, from two blended sources, S_1 and S_2, is given by:

$$\exp(-\tau_{\mathrm{obs}}) = \exp(-\tau_1)[1 + 1/R]^{-1} + \exp(-\tau_2)[1 + R]^{-1}, \qquad (4.3)$$

where R is the ratio of the continuum flux level of S_1 to the continuum flux level of S_2. The filling-in effect is most severe if the two sources are equally bright ($R = 1$) and one source has an optically thick ice band ($\tau > 1$). For instance, the observed optical depth will never exceed $\ln(2) \simeq 0.7$ if the ice band is not present in one of the blended, equally bright sources. Therefore, if the CO_2 ice bands are not optically thick, it should be possible to use the ISOCAM spectra of the two bright sources to estimate reasonably accurate optical depths.

The observed optical depths of the SVS 4-5/6 blend and the SVS 4-9/10 blend are 0.5 and 0.25, respectively. In the extreme and unlikely scenario that SVS 4-6 and SVS 4-9 have no CO_2 ice bands, the optical depths of SVS 4-5 and SVS 4-10 would be corrected to 0.61 and 0.29, respectively. Conversely, if the fainter sources have a very deep ice band, the actual optical depths would be corrected to as little as 0.35 and 0.13. Since the extinction of SVS 4-5 is 5 times higher than the extinction of SVS 4-6, a large correction is expected for this line of sight due to filling-in from SVS 4-6. A smaller correction is expected for SVS 4-10, since the second source has an extinction which is only 1.7 times higher. Assuming that the local CO_2 abundances for the blended sources are identical, the most likely CO_2 ice optical
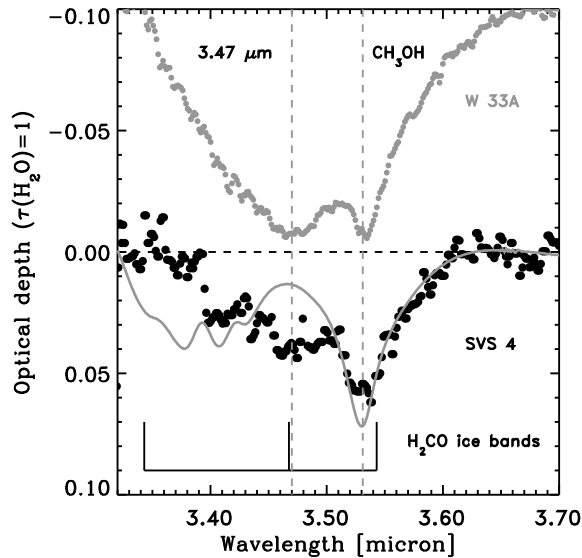
Figure 4.14: *Weighted average of the observed methanol bands from SVS 4-5, 4-8, 4-9 and 4-10 (black dots) compared to an ISAAC spectrum of the same region toward the massive YSO W 33A (grey dots). The solid line is a laboratory spectrum of a H_2O:CO_2:CH_3OH=1:1:1 mixture at 10 K. The bands from solid H_2CO which may be superposed on the main methanol band around 3.53 μm are indicated.*

depths for SVS 4-5 and SVS 4-10 are then 0.60 and 0.23, corresponding to absolute abundances of 2.0×10^{-5} and 3.5×10^{-5}, respectively. Although more uncertain, the CVF spectrum of SVS 4-8 gives a CO_2 ice abundance of 2×10^{-5}. There are thus some indications of a slightly varying CO_2 ice abundance across SVS 4. It is interesting to note that the two sources with the lowest absolute abundance of CO_2 ice are the same sources with the highest absolute abundance of methanol ice. Although not conclusive, this may indicate a competition between the formation of CO_2 and CH_3OH from CO through oxidation and hydrogenation, respectively.

4.5.6 Presence of formaldehyde?

The abundance of formaldehyde (H_2CO) ice in star forming regions has been a much debated issue. If the methanol ice has been formed through successive hydrogenation of CO, a significant abundance of formaldehyde is expected in the ice (Watanabe et al., 2003). Lines of sight toward massive young stars have been found to have fairly small abundances of formaldehyde of at most 5% relative to water (Dartois et al., 1999; Keane et al., 2001). H_2CO has several strong bands, but they all suffer from blending with other strong features. The most isolated band is the ν_4 mode at 3.47 μm. There is a sharp band at this position which is common when methanol ice is abundant. However, the corresponding ν_1 band of

H_2CO at 3.54 μm would create a significant shoulder on the red side of the 3.53 μm methanol band, which is not clearly observed in SVS 4 (see Fig. 4.14). This is the same conclusion reached for other sources by Dartois et al. (1999). Formaldehyde ice has its strongest bands centered at 5.8 μm and 6.69 μm. These bands are unfortunately blended with the 6.0 μm water ice band and the 6.85 μm band, which has still not been unambiguously identified. In Fig. 4.15 the ISOCAM CVF spectrum of the 5-8 μm region toward the SVS 4-5/6 blend is shown to explore whether a significant abundance of formaldehyde is consistent with the shape of the ice bands in this region. The SVS 4-5 line of sight has the deepest ice bands as well as the highest signal-to-noise in the CVF pointing. The ice bands are compared to laboratory spectra of pure water ice and pure formaldehyde ice at 10 K. The two laboratory spectra have been convolved to the resolution of the CVF spectrum and scaled to optical depths of 3.5 and 0.1 of the 3.1 μm water band and the 3.47 μm formaldehyde band, respectively. This corresponds to an abundance of formaldehyde ice of 1×10^{-5} or about 10% relative to water ice, using a band strength of 0.96×10^{17} cm molec^{-1} (Schutte et al., 1993) for the 5.8 μm band. The CVF resolution significantly under-resolves the two formaldehyde bands, so a spectrum of higher resolution will significantly enhance the contrast of the formaldehyde to the underlying 6.0 and 6.85 μm bands.
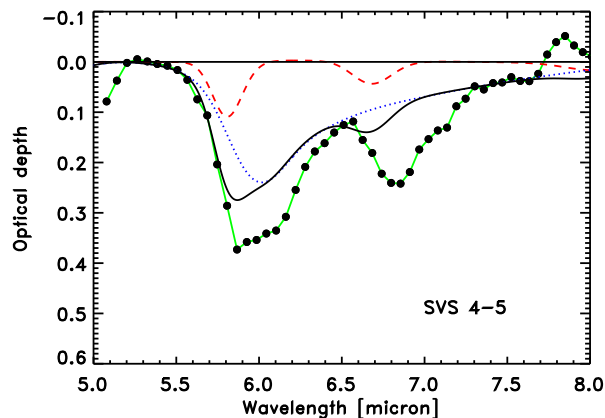
Figure 4.15: *ISOCAM CVF spectrum of the 5-8 μm region of the SVS 4-5/6 blend. The curves are laboratory spectra of pure water ice (dotted line) and pure H_2CO ice (dashed line). Both spectra have been convolved to a resolving power of R=35 to match the CVF spectrum. The water band has been scaled to match the 3.1 μm band observed with ISAAC toward SVS 4-5. The H_2CO band has been scaled to the depth of the 3.47 μm band. The solid line is the sum of the two laboratory spectra.*

It is found that the water ice band cannot account for the entire 6.0 μm band, but falls short by about 50%. This is a well-known problem and probably indicates that one or more additional carriers contribute to the band. Typically, it is found

Table 4.5: *Summary of ice abundances in the outer envelope of SMM 4*

Species	Abundance w.r.t. H_2O	Abundance $\times 10^{-5}$ w.r.t. H_2
H_2O	1	$9 - 17$
CH_3OH	0.28	3
Pure CO	0.3	3
CO in water	0.1-0.6	$1 - 5$
CO_2	0.2	$2.0 - 3.5$
H_2CO	$\lesssim 0.05$	$\lesssim 0.5$
XCN	< 0.003	$< 0.02^a$

[a] Pontoppidan et al. (2003b)

that the 6.0 μm band is twice as deep as it should be when comparing to the 3.1 μm band (Gibb & Whittet, 2002). The reason that a slightly smaller discrepancy is found here may be due to veiling by SVS 4-6. According to Eq. 4.3 a blended source with a shallow ice band a factor of 10 fainter than the primary source will change the optical depth from an observed 0.37 to an intrinsic 0.42. The presence of a formaldehyde component indeed gives a better match to the blue wing of the 6.0 μm band. However, the 6.69 μm band does not seem consistent with the shape of the 6.85 μm band. We conclude that while the spectra toward the SVS 4 stars are not consistent with a high abundance of formaldehyde, an abundance of $\sim 5\%$ relative to water ice is possible. Higher resolution spectroscopy in the 5–8 μm region is required to convincingly detect formaldehyde ice.

4.5.7 Interaction of the outflow with the ice

SMM 4 is associated with a large bipolar outflow. Estimates of the position angle of the outflow range between $180°$ (Hogerheijde et al., 1999) and $135°$ (Garay et al., 2000). The south-eastern outflow lobe is red-shifted, while the north-western lobe is blue-shifted. An outflow is expected to evaporate at least part of the ice mantles through shock-induced sputtering.

Observations of rotational lines of gaseous methanol have shown that the gas-phase abundance of methanol in the SE lobe is enhanced by a factor of 40 relative to typical abundances in quiescent molecular gas of $CO/CH_3OH = 3 \times 10^{-5}$, while the abundance in the NW lobe is enhanced by a factor of 330 (Garay et al., 2000). It is common to see such enhanced abundances in the gas phase of methanol toward bipolar outflow sources. The most favourite interpretation is that the methanol originates in icy mantles, which have been shock-evaporated by the outflow. However, it is important to note that the peak column density of gas-phase methanol toward the SE lobe of SMM 4 is only 1.4×10^{15} cm^{-2}, which translates to a gas-to-solid ratio for methanol of $\sim 2 \times 10^{-3}$. Consequently, even in lines of sight with strong gas-phase enhancement, the vast majority of the methanol molecules

remain as ice in the grain mantles. It is shown in Sec. 4.5.4 that the abundance of methanol ice is enhanced by an order of magnitude in the SMM 4 outflow region. If the grain mantles in the specific case of the SMM 4 outflow were to have a typical abundance of methanol of less than a few percent relative to water ice rather than the observed 25%, the line of sight gas-phase enhancement of methanol would be less than a factor of 4. In this case, it is doubtful that the outflow would have been recognised as having an enhanced gas-phase methanol abundance. Extrapolating this result to other protostellar outflows with strongly enhanced gas-phase methanol abundances could indicate that the ice-phase methanol abundance is commonly enhanced in protostellar envelopes. In most chemistry models, the ice mantles are assumed to form during the pre- and protostellar stages, either by direct freeze-out of molecules from the gas (e.g., CO) or grain-surface chemistry of accreted species (e.g., H_2O from accreted O). (Bergin et al., 1998) proposed an alternative scheme in which ice mantles form in the wake of low-velocity shocks due to the outflow impacting on the envelope. At the high shock temperature, most of the gas-phase oxygen is driven into H_2O, resulting in very high H_2O ice abundances if all of this H_2O freezes out before it is chemically altered into other species in the cold post-shock gas. Such a scenario could be tested by comparing high-resolution maps of gas-phase H_2O with ice maps of stars behind outflow lobes such as presented here.

4.5.8 Absolute ice abundances and gas-phase depletion

The abundances relative to H_2 of the different ice species observed in the outer envelope of SMM 4 are summarised in Table 4.5. The species constitute all of the most abundant products of surface oxygen chemistry according to current ice mantle models. It is therefore of interest to consider the abundances in relation to the gas phase components of the protostellar envelope and surrounding dense cloud. For instance, since the abundance of chemical products believed to originate in CO frozen out from the gas is very high, a considerable amount of the CO will be bound in the form of other molecules once the ice is returned into the gas phase upon warm-up. This will to some extent invalidate gas phase abundances determined relative to CO even in warm gas. In other words, contrary to the gas phase, CO is a chemically active molecule in the solid phase. Toward SVS 4, the abundance of molecules formed from CO (CO_2, CH_3OH, H_2CO) is up to 7×10^{-5}. This is up to 2 times as much as the CO ice remaining in the grain mantles. Therefore, in some cases, only 1/3 of the CO originally frozen out is returned to the gas phase as CO. The total abundance of frozen-out CO molecules, including those which have hydrogenated or oxidised to other molecules is up to 1.4×10^{-4} relative to H_2, corresponding to a high depletion from the gas-phase.

Another interesting number to mention is the total abundance of oxygen observed in the ice. For SVS 4, it is as much as 2.7×10^{-4} with respect to H_2 and perhaps as much as 3.5×10^{-4} toward SVS 4-12. In comparison, the gas phase abundance of atomic oxygen in the diffuse interstellar medium within $500\,pc$ of the Sun is $O/H = (3.19 \pm 0.14) \times 10^{-4}$ (Meyer et al., 1998). Thus, about half of the available oxygen is bound in ice in the dense parts of the Serpens core. A

similar conclusion holds for carbon. The ice abundance and composition may therefore be expected to vary considerably in regions with significantly different abundances of heavy elements. One example may be in star-forming regions in the Large Magellanic Cloud, which is known to have a sub-solar abundance of heavy elements.

4.6 Conclusions

We have presented VLT-ISAAC L-band spectroscopy of most of the stars in SVS 4, a dense cluster of low-mass YSOs located near the class 0 protostar, SMM 4. These observations have been coupled with archival data from ISO and UKIRT to produce a detailed view on the distribution of ices in the immediate environment of a very young protostar. The main conclusions are:

- It is shown that SVS 4 is likely located inside the south-eastern part of the outer envelope of SMM 4. The cluster members are distributed evenly throughout the envelope such that the lines of sight toward some stars probe the entire depth of the envelope. This is in particular true for SVS 4-12.

- A $30'' \times 45''$ map of the water ice abundance with a spatial resolution of $6''$ has been constructed. It shows that water ice is distributed throughout the SVS 4 cluster with an abundance of $9 \pm 1 \times 10^{-5}$ relative to molecular hydrogen. The abundance of water ice rises sharply to at least 1.7×10^{-4} toward SVS 4-12, which is the line of sight probing closest to the center of SMM 4. The ice along this line of sight accounts for up to 50% of the available oxygen in the interstellar medium. This is a clear indication of an enhanced efficiency of ice formation in the inner parts of protostellar envelopes.

- Along with the water ice, methanol ice is present in SVS 4 with a fairly constant high local abundance of $2.5 \pm 0.4 \times 10^{-5}$ or 28% relative to water ice. The methanol ice is confined to SVS 4, and the upper limit to the methanol ice abundance just $75'' = 19\,000\,\mathrm{AU}$ away from the center of SVS 4 is $< 3 \times 10^{-6}$ or $< 5\%$ relative to water ice. This testifies to a strongly enhanced efficiency of the formation of solid methanol in the envelope of SMM 4.

- Other ice species show normal abundances relative to water ice. There is, however, tentative evidence for a varying abundance of CO_2 ice across SVS 4.

- Mapping of ices at a spatial resolution comparable to that of gas-phase emission observations is now possible with current instrumentation on 8 m class telescopes. Due to the fortunate alignment of a dense cluster of young stars with a protostellar envelope it was possible to achieve the high spatial resolution of $6''$. However, a spatial resolution of $30 - 60''$ is possible in the more general case.

- Maps of the abundances of H_2O, CH_3OH and CO ices relative to the column density of refractory dust or H_2 are potentially powerful probes of the physical history of molecular cores. Further ice mapping is essential to explore

the possibilities of using ice as a physical probe. Additionally, it is important to couple maps of ices with corresponding gas-phase maps and models of the density and temperature of the dust to obtain a complete picture of the chemistry in particular of the saturated species. Indeed, about half of all molecules apart from H_2 not bound in refractory dust is in the form of a chemically active ice for most of the lifetime of a dense core. The Spitzer Space Telescope allows mapping at higher sensitivities in ice species not observable from the ground, such as CO_2 and CH_4.

Acknowledgements

Bibliography

Aikawa, Y., Ohashi, N., & Herbst, E. 2003, ApJ, 593, 906

Alexander, R. D., Casali, M. M., André, P., Persi, P., & Eiroa, C. 2003, A&A, 401, 613

Alves, J. F., Lada, C. J., & Lada, E. A. 2001, Nature, 409, 159

Bergin, E. A., Alves, J., Huard, T., & Lada, C. J. 2002, ApJL, 570, L101

Bergin, E. A., Neufeld, D. A., & Melnick, G. J. 1998, ApJ, 499, 777

Blommaert, J. A. D. L., Metcalfe, L., Altieri, B., et al. 2000, Experimental Astronomy, 10, 241

Boogert, A. C. A. & Ehrenfreund, P. 2004, ASP Conf. Ser., 309, 547

Cardelli, J. A., Clayton, G. C., & Mathis, J. S. 1989, ApJ, 345, 245

Caselli, P., Walmsley, C. M., Tafalla, M., Dore, L., & Myers, P. C. 1999, ApJL, 523, L165

Chavarria-K., C., de Lara, E., Finkenzeller, U., Mendoza, E. E., & Ocegueda, J. 1988, A&A, 197, 151

Chiar, J. E. 1997, Ph.D. Thesis

Chiar, J. E., Adamson, A. J., Kerr, T. H., & Whittet, D. C. B. 1994, ApJ, 426, 240

Chiar, J. E., Adamson, A. J., & Whittet, D. C. B. 1996, ApJ, 472, 665

Collings, M. P., Dever, J. W., Fraser, H. J., McCoustra, M. R. S., & Williams, D. A. 2003, ApJ, 583, 1058

Dartois, E., Schutte, W., Geballe, T. R., et al. 1999, A&A, 342, L32

Davis, C. J., Matthews, H. E., Ray, T. P., Dent, W. R. F., & Richer, J. S. 1999, MNRAS, 309, 141

Dullemond, C. P., Dominik, C., & Natta, A. 2001, ApJ, 560, 957

Ehrenfreund, P., Kerkhof, O., Schutte, W. A., et al. 1999, A&A, 350, 240

Eiroa, C. & Casali, M. M. 1989, A&A, 223, L17

Eiroa, C. & Hodapp, K.-W. 1989, A&A, 210, 345

Garay, G., Mardones, D., Rodríguez, L. F., Caselli, P., & Bourke, T. L. 2000, A&A, 358, 593

Gerakines, P. A., Schutte, W. A., Greenberg, J. M., & van Dishoeck, E. F. 1995, A&A, 296, 810

Gerakines, P. A., Whittet, D. C. B., Ehrenfreund, P., et al. 1999, ApJ, 522, 357

Gibb, E. L. & Whittet, D. C. B. 2002, ApJL, 566, L113

Gibb, E. L., Whittet, D. C. B., Boogert, A. C. A., & Tielens, A. G. G. M. 2004, ApJS, 151, 35

Hogerheijde, M. R., van Dishoeck, E. F., Salverda, J. M., & Blake, G. A. 1999, ApJ, 513, 350

Hudson, R. L. & Moore, M. H. 1999, Icarus, 140, 451

Ivezić, Z., Nenkova, M., & Elitzur, M. 1999, User's manual for DUSTY (astro-ph/9910475)

Jørgensen, J. K., Schöier, F. L., & van Dishoeck, E. F. 2002, A&A, 389, 908

—. 2004, A&A, 416, 603

Kaas, A. A., Olofsson, G., Bontemps, S., et al. 2004, A&A, accepted

Keane, J. V., Tielens, A. G. G. M., Boogert, A. C. A., Schutte, W. A., & Whittet, D. C. B. 2001, A&A, 376, 254

Larsson, B., Liseau, R., Men'shchikov, A. B., et al. 2000, A&A, 363, 253

Lutz, D., Feuchtgruber, H., Genzel, R., et al. 1996, A&A, 315, L269

Martin, P. G. & Whittet, D. C. B. 1990, ApJ, 357, 113

Meyer, D. M., Jura, M., & Cardelli, J. A. 1998, ApJ, 493, 222

Murakawa, K., Tamura, M., & Nagata, T. 2000, ApJS, 128, 603

Olmi, L. & Testi, L. 2002, A&A, 392, 1053

Pendleton, Y. J., Tielens, A. G. G. M., Tokunaga, A. T., & Bernstein, M. P. 1999, ApJ, 513, 294

Pontoppidan, K. M., Dartois, E., van Dishoeck, E. F., Thi, W.-F., & d'Hendecourt, L. 2003a, A&A, 404, L17

Pontoppidan, K. M., Fraser, H., Dartois, E., et al. 2003b, A&A, 408, 981

Preibisch, T. 1999, A&A, 345, 583

—. 2003, A&A, 410, 951

Schutte, W. A., Allamandola, L. J., & Sandford, S. A. 1993, Icarus, 104, 118

Siess, L., Dufour, E., & Forestini, M. 2000, A&A, 358, 593

Straizys, V., Cernis, K., & Bartasiute, S. 1996, Baltic Astronomy, 5, 125

Tafalla, M., Myers, P. C., Caselli, P., & Walmsley, C. M. 2004, A&A, 416, 191

Tielens, A. G. G. M., Tokunaga, A. T., Geballe, T. R., & Baas, F. 1991, ApJ, 381, 181

van Dishoeck, E. F., Dartois, E., Pontoppidan, K. M., et al. 2003, The Messenger, 113, 49

Vuong, M. H., Montmerle, T., Grosso, N., et al. 2003, A&A, 408, 581

Watanabe, N., Shiraki, T., & Kouchi, A. 2003, ApJL, 588, L121

White, G. J., Casali, M. M., & Eiroa, C. 1995, A&A, 298, 594

Whittet, D. C. B., Bode, M. F., Longmore, A. J., et al. 1988, MNRAS, 233, 321

Whittet, D. C. B., Gerakines, P. A., Hough, J. H., & Shenoy, S. S. 2001, ApJ, 547, 872

Chapter 5

Ices in the edge-on disk CRBR 2422.8-3423

Spitzer spectroscopy and Monte Carlo radiative transfer modelling

Abstract

We present 5.2-37.2 μm spectroscopy of the edge-on circumstellar disk CRBR 2422.8-3423 obtained using the InfraRed Spectrograph (IRS) of the Spitzer Space Telescope. The IRS spectrum is combined with ground-based 3-5 μm spectroscopy to obtain a complete inventory of solid state material present along the line of sight toward the source. Archival JHK_s imaging as well as 350 μm CSO mapping, 850 μm SCUBA mapping and 3 mm OVRO interferometry is used to obtain a set of spectro-photometric data covering 1.2–3000 μm. The ices observed toward CRBR 2422.8-3423 are compared to archival ISOCAM-CVF 5-16 μm ice spectra of other nearby sources within 2′. We model the object with a 2D axisymmetric (effectively 3D) Monte Carlo radiative transfer code using all the available observations to constrain the source geometry and dust composition. In particular, the location of the observed ices in the disk and envelope material is included in the model. It is found that the model disk, assuming a standard flaring structure, is too warm to contain the very large observed column density of pure CO ice, but possibly up to 50% of the water, CO_2 and minor ice species. In particular the 6.85 μm band, possibly due to NH_4^+, exhibits a prominent red wing, indicating a significant contribution from warm ice in the disk. The shape of the CO_2 bending mode suggests interaction with up to 20% of the CO ice. It is argued that the pure CO ice is located in the dense core Oph-F in front of the source seen in the submillimetre imaging, with the CO gas in the core highly depleted. A radial map of Oph-F in CO and CO_2 ice shows that the depletion of CO from the gas-phase increases sharply toward the center of the core where CRBR 2422.8-3423 is located, providing the first direct evidence for increasing CO freeze-out with increasing density in a prestellar core. Up to 50% of the CO ice embedded in water or CO_2 ice (up to 20% of the total amount of CO) may still be located in the disk, assuming constant abundances of these types of CO ice throughout the system. Discrepancies among the strength of different water ice bands are discussed. Specifically, the observed water ice libration band located at 11–13 μm is significantly weaker than that of the model. The model is used to predict which circumstances are

most favourable for direct observations of ices in edge-on circumstellar disks. Ice bands will in general be deepest for inclinations similar to the disk opening angle, i.e. $\sim 70°$, except for very tenuous disks. The ratios between different ice bands are found to vary by up to an order of magnitude depending on disk inclination due to radiative transfer effects caused by the 2D structure of the disk. Ratios between ice bands of the same species can therefore be used to constrain the location of the ices in a circumstellar disk. [1]

5.1 Introduction

It has been realised in the last decade that circumstellar disks surrounding young low-mass stars are a common occurrence. Along with the discovery of a large number of extra-solar planets orbiting older stars, significant observational evidence exist indicating that planets and planetesimals are forming in circumstellar disks within 10^6 years. Understanding the chemical structure and evolution of the molecular material of circumstellar disks is crucial because it determines the initial conditions for the composition of planets. This is especially important for the study of icy bodies in the Solar system, such as comets and Kuiper belt objects.

A range of recent modelling and observational results indicate that the abundances of molecular gases in circumstellar disks around young low-mass stars are significantly lower than in general molecular clouds, including species such as CO, HCN and HCO^+ (Dutrey et al., 1997; Thi et al., 2004; van Zadelhoff et al., 2001). Although both photodissociation in the surface layer and freeze-out onto dust grains may contribute to the depletion, it is believed that freeze-out dominates in the disk mid-plane. Some chemical models also suggest that a unique ice chemistry, different from that of dark molecular clouds, may exist in circumstellar disks (Aikawa et al., 1997). In particular, these authors predict a large abundance of CO_2 ice in typical circumstellar disks.

Directly observing ices in circumstellar disks is challenging. The primary reason is that cold ices can only be observed via absorption bands in the mid-infrared wavelength regime and therefore require the presence of a bright infrared source behind the icy material. The best candidates for observations of ices in disks are circumstellar disks viewed close to edge-on, where the sight-line toward the inner bright regions passes through the disk mid-plane, which presumably is abundant in ice. A possible exception to this may be a binary young star, in which the sight-line toward one component pass through a disk surrounding the other. This may be the case for the T Tau binary (Beck et al., 2001; Hogerheijde et al., 1997), but binarity in this scenario may significantly complicate the structure of disks in the system through dynamical and radiative interaction. Circumstellar disks viewed at very high inclination ($\gtrsim 75°$) become very faint at mid-infrared wavelengths due to the large optical depth through the disk mid-plane. The effect this may have on observable ice absorption bands is not clear, but observations of ices in

---

[1] K. M. Pontoppidan, C. P. Dullemond, E. F. van Dishoeck, G. A. Blake, A.C.A. Boogert, N. J. Evans II, J. E. Kessler-Silacci and F. Lahuis, ApJ, in preparation. The radial CO ice map of the Oph-F core will be published separately.

this case may not probe deep into the disk mid-plane. The sensitivities of ground-based 8m class telescopes and the Spitzer Space Telescope are now high enough to directly observe ices in a range of Solar system-sized edge-on disks as faint as 10 mJy in the mid-infrared.

In this chapter we present a 5.2-37.2 μm spectrum of the edge-on disk CRBR 2422.8-3423 obtained with the Spitzer Space Telescope (Werner et al., 2004). CRBR 2422.8-3423 is located in the direction of the dense core Rho Oph-F in the Ophiuchus molecular cloud complex (Motte et al., 1998). The core contains a number of other young stars as well as two prestellar condensations. The brightest submillimetre point source in the core is IRS 43, located 27″ to the north-east of CRBR 2422.8-3423. Near-infrared imaging has shown CRBR 2422.8-3423 to be a compact (1.5″) bipolar nebula, characteristic of a disk viewed close to edge-on. The south-eastern lobe is a factor of 11 times fainter than the north-western lobe in the K-band (Brandner et al., 2000), showing that the disk has an inclination of $\sim 70°$ (Thi et al., 2002). The disk is unusually bright in the mid-infrared for an edge-on disk, making it an excellent target for infrared spectroscopy of ices.

Previous studies of ices in disks have focussed on the absorption band of solid CO at 4.67 μm observed toward isolated disks. These include Elias 18 (Shuping et al., 2001), L 1489 IR (Boogert et al., 2002) and CRBR 2422.8-3423 (Thi et al., 2002). Of these sources, the most inclined disk is that of CRBR 2422.8-3423, as evidenced in the near-infrared imaging of Brandner et al. (2000). Spitzer spectra have also been presented toward L1489 IR and DG Tau B (Watson et al., 2004). Common for all sources is the very red (increasing flux with wavelength) near-infrared colours indicating the presence of significant amounts of foreground or envelope material; an isolated edge-on disk is expected to have near-infrared colours that are much less red due to the dominance of scattering. The CO ice profiles along the three lines of sight are quite different, the first two being broad, indicating that much of the CO is embedded in a water-rich ice, while CRBR 2422.8-3423 is dominated by very deep absorption from largely pure CO ice (Pontoppidan et al., 2003). So far, only circumstantial evidence has been presented arguing for the location of the CO ice in the disks rather than in envelope/foreground material. A key point in the observational study of ices in circumstellar disks is therefore to separate the contribution to the total ice bands of the disk from the contribution of any cold foreground or remnant envelope material.

This chapter will show that detailed radiative transfer modelling of high resolution near-infrared and/or millimetre imaging combined with high-quality mid-infrared spectroscopy can yield significant new information on the location and environment of ices. We use CRBR 2422.8-3423 as a case study, but emphasise that the method can easily be applied to other edge-on disks, using sensitive Spitzer-IRS spectroscopy. This chapter is organised as follows: In §5.2, the observational data of CRBR 2422.8-3423 and the surrounding cloud are presented. §5.3 discusses the solid state absorption features detected in the infrared spectra. The radiative transfer model used for CRBR 2422.8-3423 is presented in §5.4. §5.5 discusses the distribution of ices in the CRBR 2422.8-3423 disk and the Oph-F core and §5.6 summarises predictions of the model regarding observations of ices in other edge-on disks.

119

5.2 Observations

Observations of CRBR 2422.8-3423 at wavelengths from 1.2 μm to 3 mm have been assembled using both new and archival data. JHK_s imaging by the Infrared Spectrometer and Array Camera (ISAAC) mounted on UT1-Antu of the Very Large Telescope (VLT) has been extracted from the public ESO archive[2]. L- and M-band spectroscopy has been obtained using the Long Wavelength spectroscopic mode of ISAAC; the M-band spectrum was discussed in (Thi et al., 2002) [3], but we present a new observation of the ^{13}CO ice band centered at 4.78 μm. Spitzer 5.2-37.2 μm spectroscopy was taken as part of the 'From Molecular Cores to Planet-forming Disks' (c2d) legacy programme (Evans et al., 2003). A 350 μm image was obtained with the Submillimetre High Angular Resolution Camera II (SHARC-II) at the Caltech Submillimeter Observatory (CSO), and a SCUBA 850 μm map obtained with the James Clerk Maxwell Telescope (JCMT) was extracted from the 'COMPLETE survey of star-forming regions'[4]. Finally, a 5-16 μm spectral image obtained with the set of Circular Variable Filters on the Infrared Space Observatory (ISOCAM-CVF) was extracted from the public ISO archive[5]. The spectral image contains a number of sources in the Oph-F region and provides a useful comparison for the ice bands observed toward CRBR 2422.8-3423.

5.2.1 Mid-infrared spectroscopy

5.2-37.2 μm spectroscopy was obtained with the Infrared Spectrograph (IRS) aboard the Spitzer Space Telescope on March 25, 2004 using the short-low (SL) module in the 5.2-14.5 μm range with a spectral resolving power of $R = \lambda/\Delta\lambda \sim 100$, the short-high (SH) module at 9.9-19.6 μm and the long-high (LH) module at 18.7-37.2 μm with a resolving power of ~ 600. The archival AOR key is 0009346048 for PROGID 172. Total exposure times were 28 s, 244 s and 484 s in the SL, SH and LH modules, respectively. The spectra were extracted from the pipeline (version S9.5.0) images using our c2d reduction software. The short-low spectra were extracted from pipeline products that were not corrected for stray light. The background in the SL modules was determined by fitting a Gaussian with an additive bias to the spectrum at each point along the dispersion direction. Special care was taken to match the orders of the SH and LH echelle spectra and remove the many bad pixels of the LH module. All modules were scaled to the flux level of the shortest wavelength SL2 module. The final spectrum was smoothed with a 2-pixel box-car function. It is should be stressed, however, that the present level of data reduction is likely to be improved significantly in the near future, especially in terms of the shape of solid state features.

---

[2]The VLT-ISAAC images were obtained at Paranal, Chile as part of the observing programme 63.I-0691(A).

[3]The VLT-ISAAC spectroscopy was obtained at Paranal, Chile as part of the observing programmes 164.I-0605(A) and 71.C-0338(A)

[4]See http://cfa-www.harvard.edu/COMPLETE/

[5]In part based on observations with ISO, an ESA project with instruments funded by ESA Member States (especially the PI countries: France, Germany, the Netherlands and the United Kingdom.) and with the participation of ISAS and NASA.

The L-band spectrum was obtained with ISAAC on the night of May 2, 2002 using the low-resolution mode and the $0\rlap{.}''6$ slit, yielding a resolving power of $R = 600$. The $R = 5000$ M-band setting centered on the $4.67\,\mu$m band of solid CO is dicussed in Thi et al. (2002). An additional M-band setting was obtained on May 8, 2003 of the $4.78\,\mu$m band of solid ^{13}CO with the $0\rlap{.}''3$ slit yielding $R = 10\,000$. The ISAAC spectra were reduced following the procedure described in Pontoppidan et al. (2003).

The ISOCAM-CVF image (AOR key 29601813) of the Oph-F core was reduced using the CAM Interactive Analysis (CIA) package ver. DEC01 [6]. Spectra with $R = 35$ were extracted from the 3×3 pixels$=18''$ centered on IRS 42, IRS 43 and IRS 44, all located within $90''$ of the center of the Oph-F core. The data were first presented by Alexander et al. (2003).

5.2.2 (Sub)millimetre imaging

An $850\,\mu$m SCUBA map of the region was extracted from the 'COMPLETE survey of star forming regions'. Additionally, a $350\,\mu$m map was obtained with SHARC-II on the CSO. Both maps are shown in Fig. 5.1 overplotted on the VLT-ISAAC K-band image of the region. It is evident from the thermal dust emission that CRBR 2422.8-3423 is situated close to several embedded sources, at least in projection. IRS 43 is the brightest submillimetre source in the map, although the emission peak is shifted to the west by almost $10''$ in both maps. A significant extended source corresponding to the prestellar core Oph-F MM2 (Motte et al., 1998), is evident to the north-west of CRBR 2422.8-3423. No obvious submillimetre point source is associated with CRBR 2422.8-3423, although some emission is present slightly offset to the NW. It is a priori not clear whether the observed dust emission is due to emission from the edge-on disk, blended with extended emission or due to remnant envelope material surrounding CRBR 2422.8-3423. The offset emission from IRS 43 and CRBR 2422.8-3423 could indicate pointing errors. However, the offsets are similar in both the CSO and SCUBA maps. Additionally, IRS 44, IRS 46 and GY 262 have $850\,\mu$m point source emission, whose positions closely coincide with the infrared sources.

The disk is not detected at $3\,$mm with the Owens Valley millimetre interferometer with a 3σ upper limit of $3\,$mJy ($7''$ synthesised beam). This upper limit to the amount of compact millimetre emission from the region is sufficient to indicate that the submillimetre emission is largely due to the core Oph-F MM2 together with possible extended remnant envelope material and not directly related to the disk.

5.3 Inventory of ices

The full 2.85–$37.2\,\mu$m spectrum toward CRBR 2422.8-3423 is shown in Fig. 5.2. There are two holes in the spectral coverage at 4.15–$4.55\,\mu$m and 4.9–$5.2\,\mu$m. The

---

[6]The ISOCAM data presented in this chapter were analysed using "CIA", a joint development by the ESA Astrophysics division and the ISOCAM Consortium. The ISOCAM Consortium is led by the ISOCAM PI. C. Cesarsky.
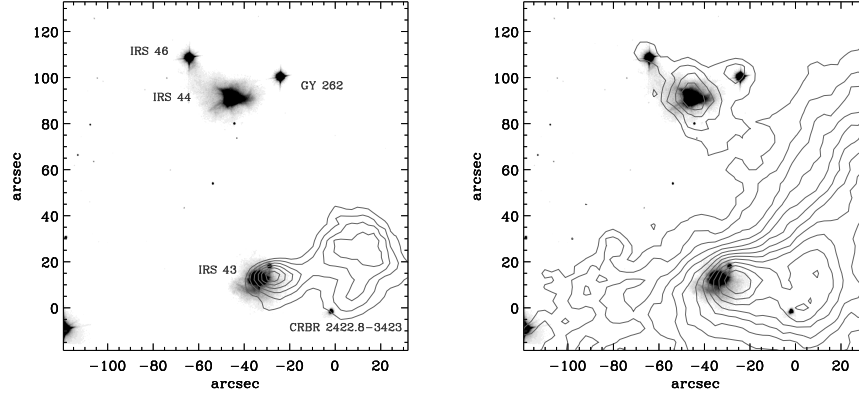
Figure 5.1: *Left panel: CSO 350 μm map of the CRBR 2422.8-3423 region overlaid on the ISAAC K_s-band image. Contours start at 1.0 Jy beam^{-1} and increase in steps of 2.0 Jy beam^{-1}. Right panel: SCUBA 850 μm map from the COMPLETE survey. Contours start at 0.05 Jy beam^{-1} and increase in steps of 0.05 Jy beam^{-1}. North is up and east is to the left.*

first interval contains the CO_2 stretching mode, which probably has a depth comparable to that of the CO stretching band at 4.67 μm toward this source. The second interval is mostly observable from the ground, but was not included in the ISAAC observations and is not expected to contain any strong solid state features.

The spectrum is dominated by absorption bands due to silicates and ices along the line of sight. The strongest bands are those due to CO, H_2O and CO_2, but also several weaker bands are detected. Specifically, the 6.85 μm band, which still lacks an unambiguous identification, is prominent. In the following, the mid-infrared spectral features are discussed in order of increasing wavelength. Table 5.1 summarises the abundances of the different ice species.

5.3.1 L-band (2.85–4.15 μm)

The L-band spectrum shows a moderately deep 3.08 μm water ice band. The band is not saturated and therefore has a well-determined optical depth of 2.3 ± 0.3. The 3.54 μm band due to the C–H stretch of solid methanol (CH_3OH) is not detected with an upper limit to the optical depth of 0.05, corresponding to an abundance relative to water ice of at most 10%. Similarly, the unidentified '3.47 μm feature', possibly due to NH_3–H_2O complexes (Dartois et al., 2002), is not detected. However, the limits on the abundances are not very strict owing to the moderate water ice column density and the low flux levels of the L-band spectrum. Finally, there is no detection of hydrogen recombination lines such as Brα at 4.07 μm, possibly due to veiling by a strong near-infrared excess.
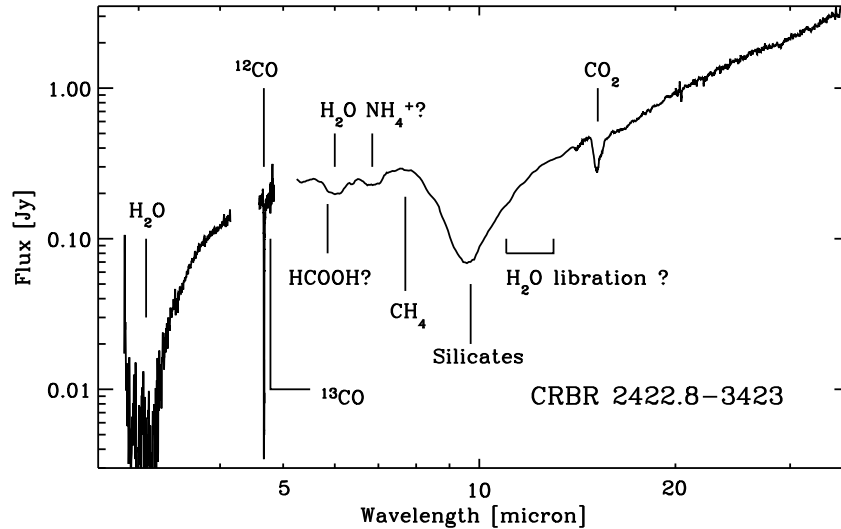
Figure 5.2: *Combined VLT-ISAAC and Spitzer-IRS spectrum of CRBR 2422.8-3423. Detected solid state bands are marked. The water ice libration band at 11-13 μm is largely missing (see text).*

5.3.2 M-band (4.55–4.90 μm)

The M-band spectrum shows an extremely deep CO ice band at 4.67 μm as well as narrow absorption lines from low-J ro-vibrational transitions of gaseous CO (Pontoppidan et al., 2003; Thi et al., 2002). In general, the shape of the main ^{12}CO ice band observed in dense clouds can be decomposed into three components with a fundamental set of centers and widths (Pontoppidan et al., 2003), such that all observed ^{12}CO ice bands can be well-fitted by only varying the relative intensities of the bands. The three-component decomposition is shown in Fig. 5.4. The CO ice band is dominated by the middle' component at 2139.9 cm^{-1}, likely due to mostly pure CO. The 'red' CO ice component at 2136.5 cm^{-1}, probably due to CO in a water-rich environment is detected with an optical depth of 10% of that of pure CO. The contribution of the 'blue' component centered on 2143.7 cm^{-1} is negligible toward CRBR 2422.8-3423. This component is not unambiguously identified, but has been associated with CO mixed with CO$_2$ (Boogert et al., 2002) or with the longitudinal optical mode of crystalline CO, which appears when the background source is polarised (Pontoppidan et al., 2003). The dominance of the 2139.9 cm^{-1} component corresponds to about 80% of the CO molecules being in a mostly pure environment.

The ^{13}CO band at 4.78 μm is clearly detected with an optical depth of 0.17 ± 0.03. This is only the third object for which ^{13}CO ice is found, and clearly testifies to the exceptionally large solid CO column density. In Fig. 5.3, the band is compared with laboratory spectroscopy from the Leiden database (Ehrenfreund et al., 1996).
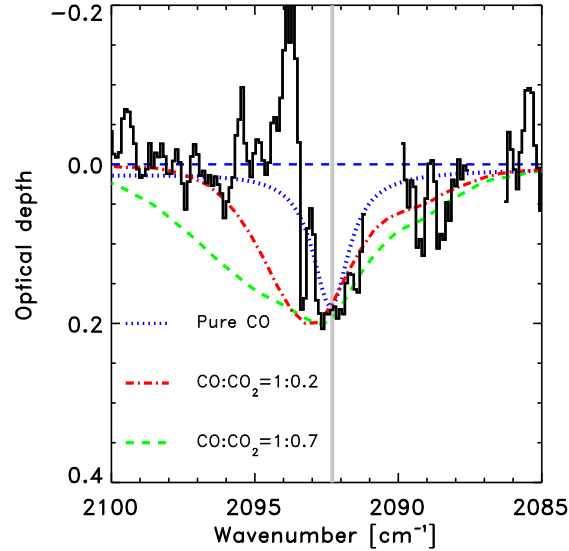
Figure 5.3: *The ^{13}CO ice band observed toward CRBR 2422.8-3423 with VLT-ISAAC. The dotted curve is pure CO at 10 K, the dashed and dashed-dotted curves are $CO:CO_2=1:0.7$ and $CO:CO_2=1:0.21$, both at 30 K. The difference in temperature of the laboratory spectra is not significant. Regions strongly affected by residuals from telluric lines have been removed from the spectrum.*

The ^{13}CO band is useful for determining the molecular environment of the CO ice. This is due to the insensitivity of this band to the grain shape effects that dominate the ^{12}CO ice band. Pure CO produces a narrow, Lorentzian ^{13}CO band centered on $2092\,cm^{-1}$, while relatively small contamination (at least 10-20%) from other molecules tends to broaden the band significantly. The presence of telluric CO gas phase lines on either side of the ^{13}CO ice band, however, complicates the profile analysis. Visual inspection of Fig. 5.3 indicates that the ^{13}CO band may be slightly broader than what is expected for pure CO. Assuming pure CO results in a $^{12}CO/^{13}CO$ ratio of 45 ± 15. This is somewhat lower than the value of 70 derived for other sources (Boogert et al., 2002; Pontoppidan et al., 2003). A broader ^{13}CO ice band will result in a larger column density of ^{13}CO and therefore an even lower isotopic ratio.

5.3.3 The 5–12 μm region

The short-low region of the Spitzer spectrum, covering 5.2-14.5 μm, contains clear detections of the enigmatic 6.0/6.85 μm solid-state line complex as well as the 9.7 μm silicate band. The silicate absorption band has an optical depth of 1.4-1.8, depending on how the continuum is defined, giving a high ratio to the water ice optical depth of $\tau_{H_2O}/\tau_{Silicate} \sim 1.4$. This is often seen for embedded sources
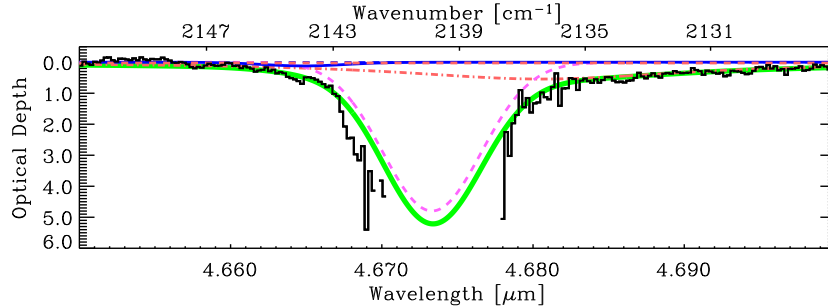
Figure 5.4: *The ^{12}CO ice band observed toward CRBR 2422.8-3423 with VLT-ISAAC. The curves indicate the three-component decomposition of Pontoppidan et al. (2003)*

and may indicate that the silicate band has been partially filled in by emission (Alexander et al., 2003).

Fig. 5.5 shows the 5-8 μm region of the CRBR 2422.8-3423 Spitzer spectrum on an optical depth scale. Laboratory spectra (e.g. Schutte et al., 1999, 1996) as well as observed ISO spectra of IRS 43 and the massive young star Mon R2 IRS 3 are used for comparison. The continuum is a 2nd order polynomial chosen to pass through the 5.3-5.5 and the 14.8-14.9 μm regions. There is some uncertainty involved in choosing a continuum in this way, but the shapes of the bands are not affected, even if their total optical depths may be uncertain up to $\sim 20\%$. The spectrum shows a prominent 6.0 μm feature, which is partly due to water ice. A laboratory spectrum of pure water ice deposited at 10 K and scaled to the 3.08 μm band is compared to the observed spectrum. It is seen that the red wing of the 6.0 μm water band can be fitted, while the main laboratory band can account for only 60% of the total observed band depth. This is very common and most likely indicates that other ice species contribute significantly to the 6.0 μm band (Keane et al., 2001), although radiative transfer effects can also cause a similar effect (see §5.6). A significant blue shoulder to the 6.0 μm band is detected at 5.85 μm. This shoulder has been found in other sources, both high mass (Keane et al., 2001) and low-mass (chapter 4). Plausible candidates include both formaldehyde (H_2CO) and formic acid (HCOOH). In this case, HCOOH provides the best fit, both because pure H_2CO is centered at 5.82 μm, which is too blue for the observed spectrum, and because the 3.47 μm band of H_2CO is not detected. A secure identification is however not possible at the present signal-to-noise and level of data reduction. The HCOOH band shown in Fig. 5.5 corresponds to an abundance relative to water ice of 2.4%.

A narrow absorption feature is seen at 6.35 μm. A sharp feature at this wavelength has not been observed for other sources. The band is possibly an instrumental artifact, although no obvious problems are seen in the pipeline spectroscopic images. Furthermore, the pipeline extraction software also produces an absorption band at this wavelength comparable to that obtained with our own

extraction. However, we regard the detection of this band as tentative. A possible identification can be the formate ion (HCOO$^-$), which has a strong band centered around 6.33 μm. The presence of HCOO$^-$ is possible, given the presence of HCOOH, since it can be produced by acid-base reactions between for instance HCOOH and NH$_3$. Only 0.4% of HCOO$^-$ relative to water ice is required to produce a similar band. Another possible explanation is that an emission band due to polycyclic aromatic hydrocarbons (PAHs) is present at 6.2 μm, thereby creating the illusion of an absorption band at 6.35 μm. The spectral resolution is too low to distinguish between these possibilities. Finally, solid O$_2$ has a very weak band at 6.45 μm. However, the depth of the observed band requires an extremely high column density of $> 10^{19}\,\mathrm{cm}^{-2}$ corresponding to an abundance of 2.5×10^{-3} for the largest band strength measured of $1 \times 10^{-19}\,\mathrm{cm\,molec}^{-1}$ (Ehrenfreund et al., 1992). The band strength of the O$_2$ band has been measured to be 1–2 orders of magnitude smaller, depending on ice composition (Vandenbussche et al., 1999).

CRBR 2422.8-3423 shows a prominent 6.85 μm band. The carrier of this band remains unknown, although a significant number of candidates have been tested. Substantial arguments have been given in favour of NH$_4^+$ (Schutte & Khanna, 2003, and references therein). A significant concern for a charged carrier of such a strong band is the lack of observed counter-ions, but Schutte & Khanna (2003) argue that the counter-ions may be distributed among a range of carriers, rendering any single ionic species unobservable. Keane et al. (2001) noted the presence of two components to the 6.85 μm band through an empirical decomposition of the band for a sample of high-mass stars. In Fig. 5.5 the 5-8 μm spectrum of CRBR 2422.8-3423 is compared to laboratory spectra as well as the ISOCAM-CVF spectrum of IRS 43 and the ISO-SWS spectrum of the massive young star Mon R2 IRS 3 from Keane et al. (2001). Mon R2 IRS 3 is included here, because this source has the most extreme red-shifted 6.85 μm band observed. The 6.0/6.85 μm band complexes toward CRBR 2422.8-3423 and IRS 43 have by chance almost identical optical depths, while the spectrum of Mon R2 IRS 3 has been scaled by a factor of 0.7. The main difference is the complete lack of the red shoulder of the 6.85 μm band toward IRS 43 as compared to CRBR 2422.8-3423. This difference may be of considerable significance. The Mon R2 IRS 3 spectrum is seen to provide a very good fit to the red part of the CRBR 2422.8-3423 6.85 μm band, which is entirely missing from the IRS 43 spectrum. A shift of the 6.85 μm component to 7.0 μm was suggested by Keane et al. (2001) to be an effect of thermal processing, meaning that the line of sight toward CRBR 2422.8-3423 contains warm ice in addition to the cold ice probed by the CO ice band. Schutte & Khanna (2003) has shown that NH$_4^+$ is shifted to the position of the reddest observed band toward Mon R2 IRS 3 at temperatures in excess of 200 K. The corresponding temperature for interstellar ice is possibly somewhat lower. The location of material at high temperatures along the line of sight toward CRBR 2422.8-3423 is discussed in terms of the radiative transfer modelling in Sec. 5.5. The abundance of NH$_4^+$ required to produce a 6.85 μm feature like that observed toward CRBR 2422.8-3423 is 10% relative to water ice, assuming a band strength of $4.0 \times 10^{-17}\,\mathrm{cm\,molec}^{-1}$ (Schutte & Khanna, 2003).

The 7.7 μm band of solid CH$_4$ is tentatively detected, but unresolved at the
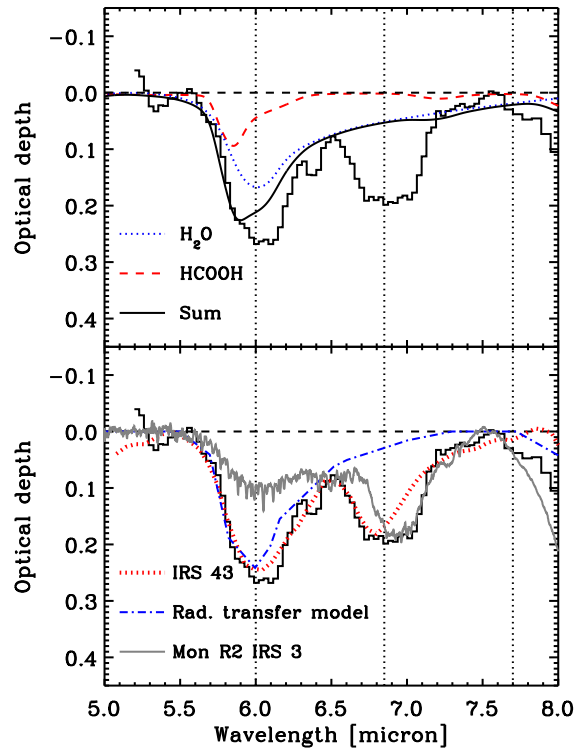
Figure 5.5: *The 5–8 μm region observed toward CRBR 2422.8-3423. Upper panel: The observed spectrum is compared to a laboratory spectrum of water ice at 10 K scaled to an optical depth of 2.3 for the 3.1 μm band (dotted curve). A laboratory spectrum of pure HCOOH at 10 K has been added to account for the blue wing of the band (dashed curve). The solid curve is the sum of the two laboratory spectra. Lower panel: The spectrum is compared to the ISOCAM-CVF spectrum of the nearby IRS 43 (dotted curve) and the ISO-SWS spectrum of Mon R2 IRS 3 from Keane et al. (2001) (solid grey curve). Note that the red shoulder of the 6.85 μm band is absent toward IRS 43 but can be well fitted by the Mon R2 IRS 3 spectrum. Three vertical dotted lines are added to guide the eye to 6.0, 6.85 μm and 7.7 μm. The IRS 43 spectrum has not been scaled to match the CRBR 2422.8-3423 spectrum, but happens to have almost the same optical depth. The dot-dashed curve is the radiative transfer model described in §5.4.*

Table 5.1: *Average abundances of ices observed toward CRBR 2422.8-3423*

	Column density 10^{18} cm^{-2}	Abun. rel. to H_2O ice	Abun. rel. to H_2 gas	band strength
H_2O	3.6	1	9×10^{-5}	2×10^{-16} [a]
CO_2	1.16	0.32	2.9×10^{-5}	1.1×10^{-17} [a]
^{12}CO pure	2.8	0.78	7×10^{-5}	1.1×10^{-17} [a]
^{12}CO in water	0.68	0.19	1.7×10^{-5}	1.1×10^{-17} [a]
NH_4^{+} [d]	0.36	0.10	9×10^{-6}	4.0×10^{-17} [e]
^{13}CO	0.06	0.017	1.5×10^{-6}	1.1×10^{-17} [a]
CH_4 [d]	0.13	0.035	3×10^{-6}	8.0×10^{-18} [b]
CH_3OH	< 0.36	< 0.10	$< 9 \times 10^{-6}$	5.3×10^{-18} [b]
$HCOOH$ [d]	0.09	0.02	2×10^{-6}	6.7×10^{-17} [c]

[a] Gerakines et al. (1995)

[b] Kerkhof et al. (1999)

[c] Schutte et al. (1999)

[d] Suggested identification (see text).

[e] Schutte & Khanna (2003)

Spitzer-IRS resolution. The silicate absorption band at 9.7 μm is largely feature-less and does not show strong evidence for the 9.35 μm 'umbrella' mode due to solid NH_3 or the 9.75 μm CO stretching mode of solid CH_3OH.

5.3.4 CO_2 15.2 μm bending mode

The short-high spectrum shows a strong band at 15.2 μm due to the bending mode of CO_2 ice. The CO_2 bending mode observed toward CRBR 2422.8-3423 is shown in Fig. 5.6 where it is compared to the laboratory spectroscopy of Ehrenfreund et al. (1996) as well as the CO_2 bending mode observed toward IRS 43. The depth of the band corresponds to an abundance of CO_2 ice relative to water ice of $N(CO_2)/N(H_2O) = 0.32$ (see Table 5.1). This is significantly higher than the typical value of 0.2 observed for high-mass stars (Gerakines et al., 1999), but is similar to abundances recently measured toward some low-mass stars (Boogert et al., 2004). Laboratory experiments have shown that the shape of the CO_2 bending mode is a sensitive tracer of ice composition and thermal history. In particular, substructure bands can determine if solid methanol is mixed with the CO_2 and if the ice has been heated (Ehrenfreund et al., 1999). The location of the CO_2 bending mode within the Spitzer high spectral resolution coverage enables a detailed study of the band shape.

Pure, partially crystalline CO_2 at 10 K is split into two narrow bands at 660 cm^{-1} (15.15 μm) and 655 cm^{-1} (15.25 μm). There is some evidence from laboratory experiments that pure, fully amorphous CO_2, which does not show this characteristic splitting of the bending mode, may be formed under certain conditions (Falk, 1987). It is possible that the amorphous form of CO_2 is formed in dense interstellar clouds. Toward CRBR 2422.8-3423, a strong, relatively narrow component is clearly present around 660 cm^{-1} (15.25 μm). Inspection of Fig. 5.6 shows that a narrow band at 655 cm^{-1} is absent, ruling out significant amounts of the pure,

partially crystalline CO_2 toward CRBR 2422.8-3423. The absence of the $655\,cm^{-1}$ band indicates that the structure of the CO_2 ice is different from that generally observed toward high-mass stars (Gerakines et al., 1999). In addition to the narrow component, the observed CO_2 band has a significant red shoulder at $647\,cm^{-1}$ ($15.45\,\mu m$), which can possibly be assigned to a CO_2–CH_3OH complex (Gerakines et al., 1999). This shoulder is most prominent for cold ices ($< 50\,K$) and when CO_2, H_2O and CH_3OH are present in the mixture in similar concentrations. A very good fit is obtained with a H_2O:CH_3OH:CO_2=1:0.6:1 mixture. The abundance of CH_3OH required by the fit is 9% relative to water ice, which is close to, but consistent with the observed upper limit of methanol ice.

The theoretical and experimental understanding of the conditions, under which different phases of solid CO_2 are formed, needs to be improved in order to explore the phase of CO_2 ice around low-mass protostars further. An alternative way to create a single narrow absorption band of CO_2 is to use a mixture with another ice species. Since a mixture with H_2O cannot produce the narrow blue component, the only other candidate known to be abundant in this source is CO. Indeed, a binary mixture with CO is found to yield an excellent fit to the rest of the band. The percentage of the total column of 'pure' CO required to be mixed with CO_2 is 20%.

The presence of a binary CO:CO_2 component is qualitatively consistent with the ^{13}CO band. Quantitatively, the best fit to the CO_2 bending mode is a mixture with CO and CO_2 in approximately equal concentration, while the ^{13}CO band is best fitted by a mixture in which CO_2 is much more dilute. Since the total ratio of CO to CO_2 along the line of sight is ~ 3, this fits well with a scenario in which a small part ($\sim 20\%$) of the CO is mixed with the CO_2, while the rest is almost pure. A binary CO:CO_2 mixture should produce a blue-shifted and broadened ^{12}CO ice band, and there is no indication of this in the observed M-band spectrum (see §5.3.2). Since the CO ice band toward CRBR 2422.8-3423 is saturated, the significance of this is not clear.

In summary, the line of sight toward CRBR 2422.8-3423 shows significant evidence for some interaction between part of the CO_2 and the CO ice components, while most of the two species remain separate. Alternatively, the narrow component of the CO_2 bending mode may be due to pure, but *amorphous* CO_2. One may speculate that the CO:CO_2 ice mixture or amorphous CO_2 ice resides in the disk material, mostly on the basis of circumstantial evidence. First, this component seems to be much less prominent toward IRS 43, although an observation of this line of sight at higher spectral resolution is required to confirm this. Second, a broadened ^{13}CO band has not previously been observed in lines of sight toward embedded sources. However, considering that CRBR 2422.8-3423 is only the third source with a ^{13}CO detection, this can hardly be considered conclusive. The relation of the CO and CO_2 ice to the disk and foreground material is discussed in the context of the Oph-F core in §5.5.2.
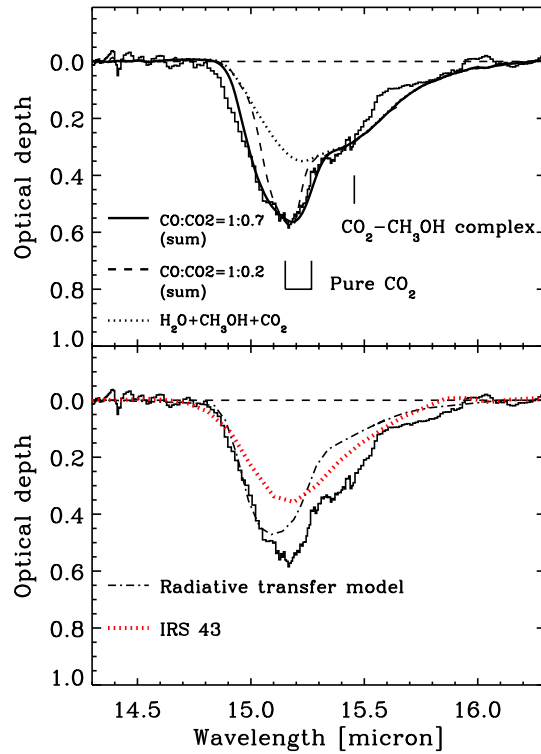
Figure 5.6: *The 15.2 μm CO_2 ice bending mode observed toward CRBR 2422.8-3422 on an optical depth scale. Upper panel: The curves show a sum of laboratory spectra of a water and methanol-rich mixture ($H_2O:CH_3OH:CO_2=1:0.6:1$ at 30 K) and a CO rich mixture. The solid curve shows a fit using $CO:CO_2=1:0.7$ at 10 K for the CO-rich mixture, while the dashed curve uses $CO:CO_2=1:0.2$ at 10 K. A continuous distribution of ellipsoid (CDE) grain model has been used to convert the optical constants to absorption coefficients. Lower panel: The dotted curve is the CO_2 band observed by ISOCAM-CVF toward IRS 43. The dot-dashed curve is the band extracted from our radiative transfer model (see §5.4). The spectral resolution of the ISOCAM spectrum is 0.4 μm at the location of the CO_2 bending mode.*

5.4 2D continuum radiative transfer

In order to better understand the location of ices in the disk and the foreground or envelope of CRBR 2422.8-3423, a 2D Monte Carlo radiative transfer model was constructed for an axisymmetric density structure. The aim was to fit the dust density structure simultaneously to the high resolution spectral energy distribution

and the near-infrared imaging. We are using the code RADMC (see Dullemond & Dominik, 2004) to calculate the temperature structure and scattering source function for a given density distribution. Spectral energy distributions and images are then calculated using the ray-tracing capabilities of the code RADICAL (Dullemond & Turolla, 2000). The Monte Carlo radiative transfer is effectively performed in full 3D, but the density structure is required to be axisymmetric. The scattering is assumed to be isotropic, although a full treatment of scattering is being developed. The effects from anisotropic scattering are typically small for wavelengths longer than $2 \, \mu$m and grains smaller than a few μm.

5.4.1 Dust model

Because it is necessary to adjust the abundances of ice species independently, a dust model must be constructed for the radiative transfer calculation to provide opacities that can reproduce the observed spectral features. Furthermore, to adequately fit the relatively narrow ice bands, a higher spectral resolution is required for the opacities than available in published tables. The adopted dust model assumes spherical silicate grains with inclusions of carbonaceous material, surrounded by a spherical ice mantle. In the diffuse medium, the silicate and carbonaceous grains are likely in separate dust populations (Draine, 2003). However, when grains coagulate in dense molecular clouds, these populations may be mixed. Thus for convenience, a single grain population is adopted here. The silicate-carbon core optical constants are calculated using Maxwell-Garnett effective medium theory (Bohren & Huffman, 1983):

$$\epsilon_{\mathrm{av}} = \epsilon_{\mathrm{mat}} \left[1 + \frac{3f(\epsilon_{\mathrm{inc}} - \epsilon_{\mathrm{mat}})/(\epsilon_{\mathrm{inc}} + 2\epsilon_{\mathrm{mat}})}{1 - f(\epsilon_{\mathrm{inc}} - \epsilon_{\mathrm{mat}})/(\epsilon_{\mathrm{inc}} + 2\epsilon_{\mathrm{mat}})} \right], \tag{5.1}$$

where ϵ_{mat} and ϵ_{inc} are the dielectric functions of the matrix (silicates) and spherical inclusions (carbon), respectively. f is the volume fraction of the inclusions. The carbon component is chosen as the inclusion, since it has the smallest volume fraction. The opacities are then obtained using the coated sphere Mie code from Bohren & Huffman (1983). A single grain size of $0.5 \, \mu$m is used, since the shape of the opacity law is mostly affected by smaller grains at the shorter wavelengths ($< 2 \, \mu$m), where little information is available due to the heavy extinction of the source. Ices are assumed to evaporate at 90 K, except CO, which evaporates at 20 K (Sandford & Allamandola, 1993). Above 90 K, only the silicate/carbon cores are left. The grains are assumed to be compact. 'Fluffy', coagulated grains are known to increase the opacity at all wavelengths resulting in a slight overestimate of the dust mass if compact grains are used (Ossenkopf & Henning, 1994).

Optical constants for the ice are taken from the Leiden database of ices (Ehrenfreund et al., 1997), those for the oxygen-rich silicates from Ossenkopf & Henning (1994), while the carbonaceous constants are from Jäger et al. (1998) for carbon clusters formed at 800 K. The choice of the carbonaceous component is the most uncertain, since few spectral diagnostics are available in dense clouds and embedded objects to guide the choice. The carbonaceous material created in the laboratory experiences a significant change in properties for pyrolisation temperatures

between 600 and 800 K, reflecting a larger contribution from graphitic material at the higher temperature. Here, the optical constants for carbon dust created at 800 K are chosen because this reproduces the observed strength of the 9.7 μm feature. The 600 K sample results in opacities that cause the 9.7 μm silicate feature to be over-estimated in the model fit to the observed spectrum, while creating very high far-infrared to millimetre opacities. The volume fraction of carbonaceous inclusions used is 0.15.

It is not possible to create a database of ice optical constants which covers even a small fraction of the parameter space of ice abundances. As a consequence, ice abundances in the mantle are varied using Eq. 5.1. As shown in §5.3, much of the CO_2 ice is embedded in water ice. Therefore, as a starting point an ice mixture of H_2O:CO_2:CO=1:0.2:0.03 at 10 K is used. The CO_2 and CO abundance is increased by adding inclusions of CO:CO_2=1:0.7. Beyond 20 μm, a revised version of the ice opacity of Warren (1984) for crystalline water ice is used, since no optical constants are available for amorphous water ice at these wavelengths. The CO_2:CO inclusions can be replaced by pure CO to test the location of this component in the disk/envelope system (see §5.5). The water ice abundance for the ice-coated dust grains is 9×10^{-5} relative to H_2, assuming an ice density of 0.6 g cm^{-3} and a gas-to-dust mass ratio of 100.

Fig. 5.7 compares the dust opacities (not including the gas mass) to those by Ossenkopf & Henning (1994) and Weingartner & Draine (2001). The calculated opacity matches fairly well that of Ossenkopf & Henning (1994) for compact bare grains (the first column of their Table 1). Their grain coagulation model produces opacities that are slightly larger at all wavelengths. The opacities show a larger variation once ice mantles are added. In particular, our higher resolution opacities include the narrow ice bands from CO and CO_2 at 4.27 and 4.67 μm. Additionally, we also find a significant contribution from the 11-13 μm water ice libration band in our opacity. Note also the presence of the 45 μm band from crystalline water ice due to the use of optical constants for higher temperature water ice at long wavelengths. The presence of this band does not affect the continuum modelling results.

5.4.2 Disk structure

The aim of the radiative transfer model is to empirically fit the dust structure of the disk, rather than to construct a self-consistent dynamical model. Basically, this means that a 'generic' disk structure is used in which the flaring angle is a free parameter, independent of the central object or the dust model. The vertical density structure is assumed to be Gaussian. A Gaussian density profile is appropriate for a vertically isothermal disk. Note, however, that the disk is not isothermal and no assumption is made concerning the temperature, which is calculated independently using the Monte Carlo code. Non-isothermal models have vertical density profiles that are similar to a Gaussian, although in the very upper layers the structure may deviate from a Gaussian (Dullemond et al., 2002). Effects such as grain settling will produce a vertical dust density profile which peaks more strongly toward the disk mid-plane. However, we are most interested in modelling the
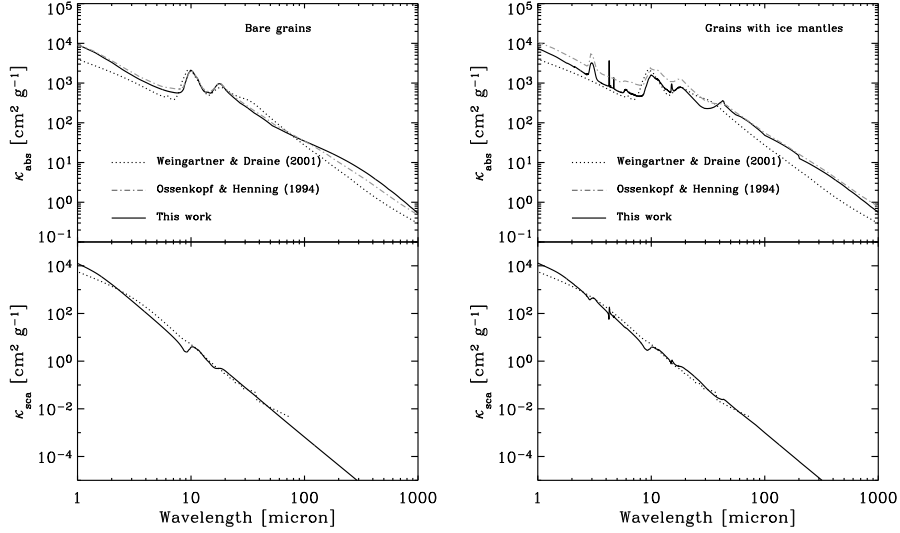
Figure 5.7: *Examples of dust mass absorption (top) and scattering (bottom) efficiencies used as input for the radiative transfer model compared to opacities from the literature. Left panels: Mass absorption and scattering coefficients for dust grains without ice. The fairly high absorption coefficients at long wavelengths are largely due to the choice of carbonaceous optical constants. Right panels: Dust mass absorption and scattering coefficients for ice-coated grains with a water ice abundance of 9×10^{-5} relative to H_2, assuming a gas-to-dust ratio of 100 and an ice density of $0.6\,g\,cm^{-3}$ (porous amorphous water ice). The opacities are relative to the mass of the refractory dust mass in order to preserve the dust-to-gas mass in a model when also ice freezes out. The opacities are compared to those of Ossenkopf & Henning (1994) for compact grains with and without a thin ice mantle and those of Weingartner & Draine (2001) appropriate for diffuse medium dust.*

structure of the disk where the optical depth at mid-infrared wavelengths is moderate, away from the densest parts of the mid-plane. A dust density profile which is strongly peaked toward the mid-plane (e.g. due to dust sedimentation) is not probed by the mid-infrared spectrum as long as the wing of the profile resembles that of a Gaussian with a larger scale height, so that the photosphere of the disk lies well above this midplane density concentration. We therefore do not include a midplane dust layer into our model. The disk density is thus modelled as a function of radius, R and height above the disk plane, Z:

$$\rho(R, Z) = \frac{\Sigma(R)}{H_p(R)\sqrt{2\pi}} \exp\left(-\frac{Z^2}{2H_p(R)^2}\right), \qquad (5.2)$$

where $\Sigma(R) = \Sigma_{\mathrm{disk}} \times (R/R_{\mathrm{disk}})^{-p}$ is the surface density and

133

$$H_p(R)/R = (H_{\text{disk}}/R_{\text{disk}}) \times (R/R_{\text{disk}})^{2/7} \qquad (5.3)$$

is the disk scale height. The flaring power of $2/7$ is that determined for a self-irradiated passive disk (Chiang & Goldreich, 1997). The parameters varied in the model are Σ_{disk}, determining the disk mass, and H_{disk} determining the disk opening angle measured at the outer edge of the disk, R_{disk}. The disk opening angle can be constrained with some degree of confidence by the near-infrared imaging. The surface density is assumed to vary with $p = 1$. The inner edge of the disk is determined by the dust sublimation temperature, here assumed to be $1700\,\text{K}$ and R_{disk} is constrained by the K-band image to $90\,\text{AU}$ (see Fig. 5.9). The surface density is not sharply truncated at the outer edge, but follows a steep power law of R^{-12} outside of R_{disk}.

The central object is assumed to be a typical pre-main sequence star with an effective temperature of $\sim 4500\,\text{K}$. The radius of 2 solar radii (corresponding to a luminosity of $1.4\,L_\odot$) is then constrained by the SED. These parameters correspond to a pre-main sequence star of age 3×10^6 years, using the evolutionary tracks of Siess et al. (2000). The model output is not very sensitive to the exact choice of temperature of the central star, only to the total luminosity. Specifically, the star could be cooler and therefore younger. An effective temperature of $4000\,\text{K}$ corresponds to an age of 10^6 years at the luminosity of CRBR 2422.8-3423.

Foreground or envelope material is added via a spherical shell of constant density. This is necessary to produce the observed high extinction toward the source. The temperature and any deviation from a constant density of the foreground material is not constrained due to the lack of far-infrared photometry. The location of the foreground material is discussed in the next section.

Finally, a puffed-up inner rim is added. The rationale behind a puffed-up inner rim is that the star over-heats an inner vertical wall of dust located at the dust sublimation temperature, causing it to expand in the vertical direction (Natta et al., 2001). This is modelled as a puffed-up scale height at the inner edge of the disk and a drop-off to a maximum radius where the flaring disk takes over. Specifically, the disk opening angle at the inner radius, R_{rim}, is increased to H_{rim}. The presence of a puffed-up inner rim makes it possible to reproduce the high mid-infrared fluxes of the source, and at the same time create a sufficiently high extinction of the central star. It is thought that a puffed-up inner rim is most prominent for disks surrounding intermediate mass stars (Dullemond et al., 2001; Natta et al., 2001), but it has also recently been found to be important for T Tauri stars (Muzerolle et al., 2003). The observed SED of CRBR 2422.8-3423 clearly requires significant excess infrared emission around $5\,\mu\text{m}$, which is hard to explain without introducing an inner rim. Also, at the inclination of CRBR 2422.8-3423, direct emission from the central star tends to dominate over scattered light from the disk surface if no inner rim is used, contrary to what is observed in the near-infrared images.

The density distribution is sampled on a polar (R,Θ) grid with a logarithmic spacing in the R-direction to ensure that all structures are properly resolved. Likewise, the spectral energy distributions are calculated using rays with impact parameters that are sampled on a logarithmic grid centered on the star. At each wavelength, the flux is determined by integrating over a predefined 'observa-

tional' aperture. The images are calculated in the following way: we arrange pixels on a regular rectangular matrix and perform a ray-tracing along the ray belonging to each pixel. However, some extra care has to be taken with this procedure. Because the pixels are equi-distant, small scale structure in the inner parts of the disk (such as the star itself) may not be resolved. This will cause an underestimate of the flux in the inner pixel of the grid. To ensure that the image reproduces the flux at all scales, including scales which are much smaller than a pixel, the following approach was taken: For each final model image, a set of three images was calculated on three different scales, all centered on the central star. The sampling chosen for the final image was 200 pixels for 1000 AU. Therefore, two images with 200 pixel sampling were calculated for the inner 10 AU and 0.1 AU. The smallest image was then resampled to a 2×2 pixel grid, which was used to replace the inner pixels in the 10 AU image. This method was then repeated for the 1000 AU image. The smallest image fully resolves the central star.

5.4.3 Best model fit

The 'best fit' density structure is shown in Fig. 5.8 corresponding to a set of parameters which reproduce the observed constraints. Fig. 5.9 compares the synthetic JHK_s composite images of the model disk to the observed image. Contours of the ISAAC images compared to the 'best fit' model are shown in Fig. 5.10, while contours showing alternative model images discussed in §5.4.4 are shown in Fig. 5.11. Figs. 5.12 and 5.13 compare the modelled and observed SED. The best-fitting parameters are summarised in Table 5.2. The table also includes estimates of the uncertainties of each model parameter due to degeneracies.

The model can in principle accommodate an arbitrary number of dust opacities, which can be made to depend on the dust temperature. This is useful for simulating the evaporation of different ices at different temperatures. For instance, a layer of solid pure CO desorbs at 20 K at densities of $\sim 10^6\,\mathrm{cm}^{-3}$, while water ice desorbs at 90 K (Sandford & Allamandola, 1993). However, the desorption temperatures are very sensitive to the structure of the ice. CO may be trapped in water ice and desorb at much higher temperatures than pure CO (Collings et al., 2003). Here we make a very simple model, assuming as a starting point that CO desorbs at 20 K, since it is known to be largely pure, while all other ice species desorb at 90 K.

The presence of several temperature dependent opacities requires that the model is iterated to obtain a self-consistent temperature structure. This was done by first calculating a model with ice-covered grains throughout the disk. The output temperature structure was then used to determine where the ices evaporate and a new model was calculated with opacities uniquely defined at the relevant locations in the disk. This was repeated until the temperature became stable within 5%. It was found that convergence is usually reached in the first few iterations.

The parameters were varied manually to obtain the best fit because computing time prohibits a calculation of a full grid. Therefore any degeneracy in the best-fitting model parameters is hard to assess in detail. However, some parameters are clearly independent. As mentioned in §5.4.2, the size of the flared disk
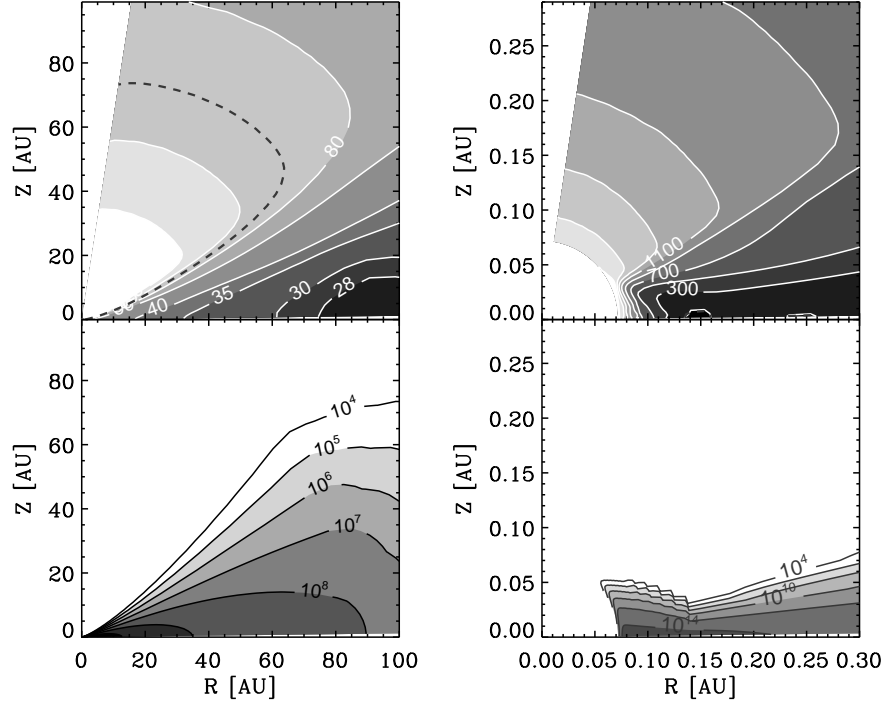
Figure 5.8: *Structure of the best-fitting model disk. The left panels show the entire disk, while the right panels show a zoom-in of the inner rim region. Upper panels: Dust temperature in Kelvin. The dashed curve indicates the ice evaporation zone at 90 K. Lower panels: H_2 density assuming a gas-to-dust ratio of 100 in units of cm^{-3}. Contours are shown in steps of 1 dex (left) and 2 dex (right).*

and the disk opening angle are constrained by the near-infrared images, as is the inclination angle. It is important to note that the disk may have a non-flared, self-shadowed component at large radii, which would not be seen in the scattered light in the near-infrared. Thus, the near-infrared images provide only a strict lower limit to the size of the disk. However, the current data cannot constrain a self-shadowed component. In particular, a flat outer disk will not contribute to the observed ice bands since the line of sight to the infrared source does not pass through such a flat disk component. Therefore only the flared part of the disk is modelled. While not unambiguously determined, the total mass of the disk is constrained by the upper limit observed at 3 mm in the OVRO interferometer to be $\lesssim 0.005\,M_\odot$. This upper limit also weakly constrains the possible mass of an outer self-shadowed disk component.

A more realistic grain size distribution may significantly affect the mass estimate of the disk (Wood et al., 2002). However, the shape of the ice bands as well
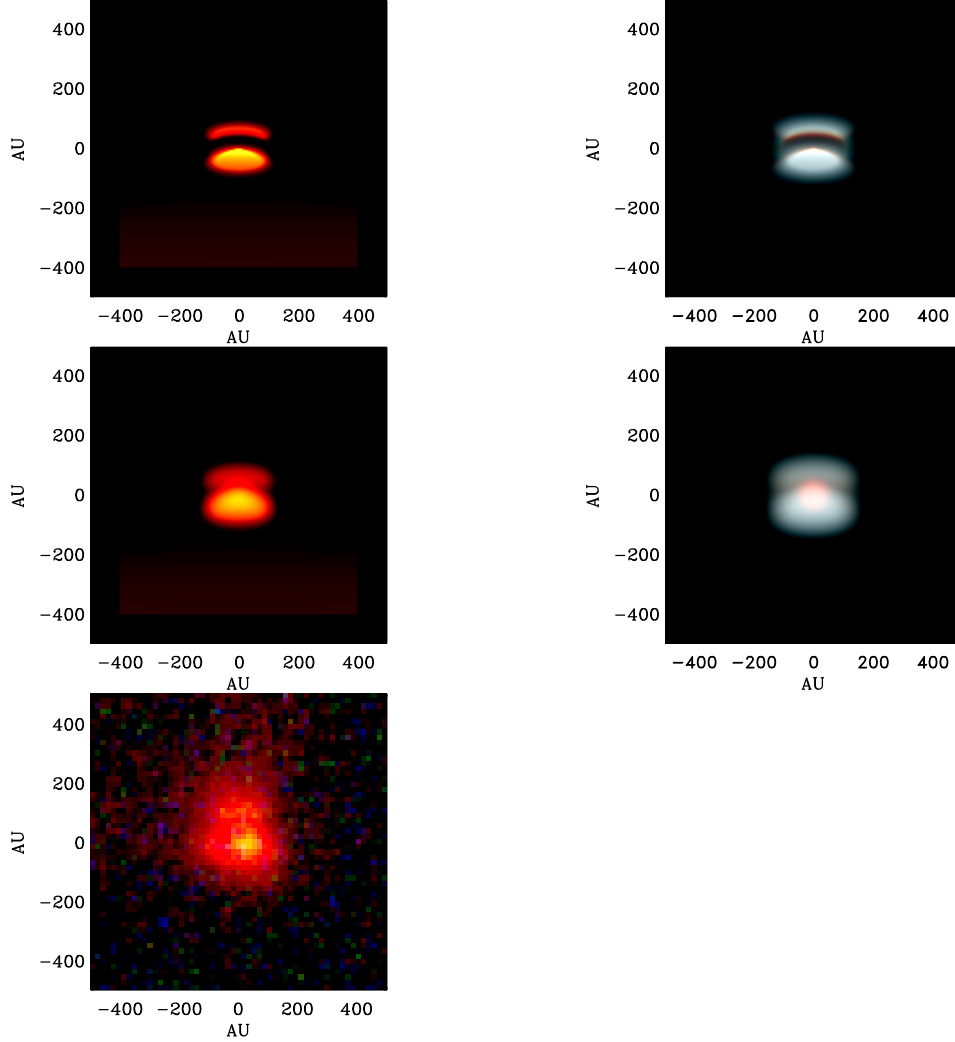
Figure 5.9: *Observed and modelled composite J (blue), H (green), K_s (red) im-ages of CRBR 2422.8-3423. The colour scale is logarithmic. The left side show the images of the disk as they appear including the foreground material, while the right side shows the images with the foreground material removed. Note that the central star and inner rim are seen as a reddened point source in the center of the disk when the foreground is removed. The images are flux calibrated to yield well-defined colours. Lower panel: VLT-ISAAC colour composite. Middle panel: JHK_s model image corresponding to the SED in Fig. 5.12. The image has been convolved with a gaussian of $FWHM = 0\rlap{.}''4$ to match the observed image. Up-per panel: As above, but without convolving with the instrumental point spread function.*
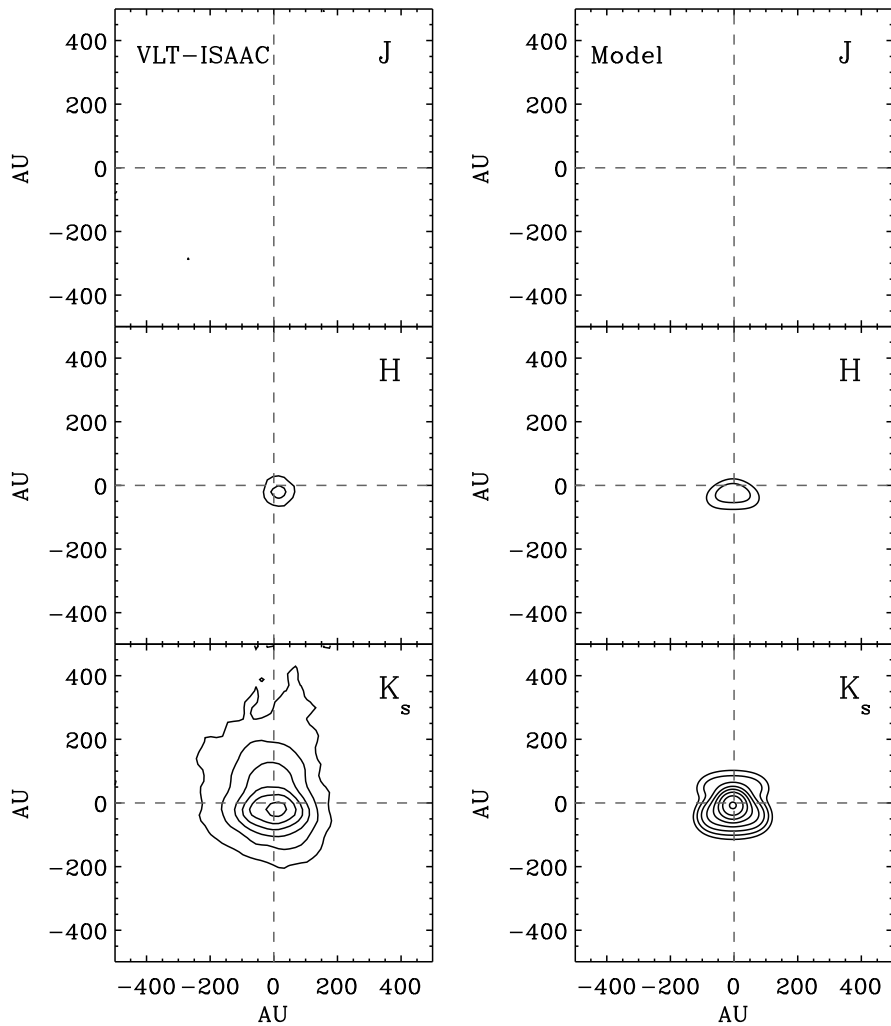
**Figure 5.10:** *Left panels: Contour plots of the VLT-ISAAC JHK_s images of CRBR 2422.8-3423. Right panels: Contour plots of the JHK_s model images for the parameters given in Table 5.2. Note that the central star is visible in the model images. The lowest contour is at 1.6×10^{-17} erg s^{-1} cm^{-2} Hz^{-1} sterad^{-1} and subsequent contours increase in steps of 0.4 dex.*
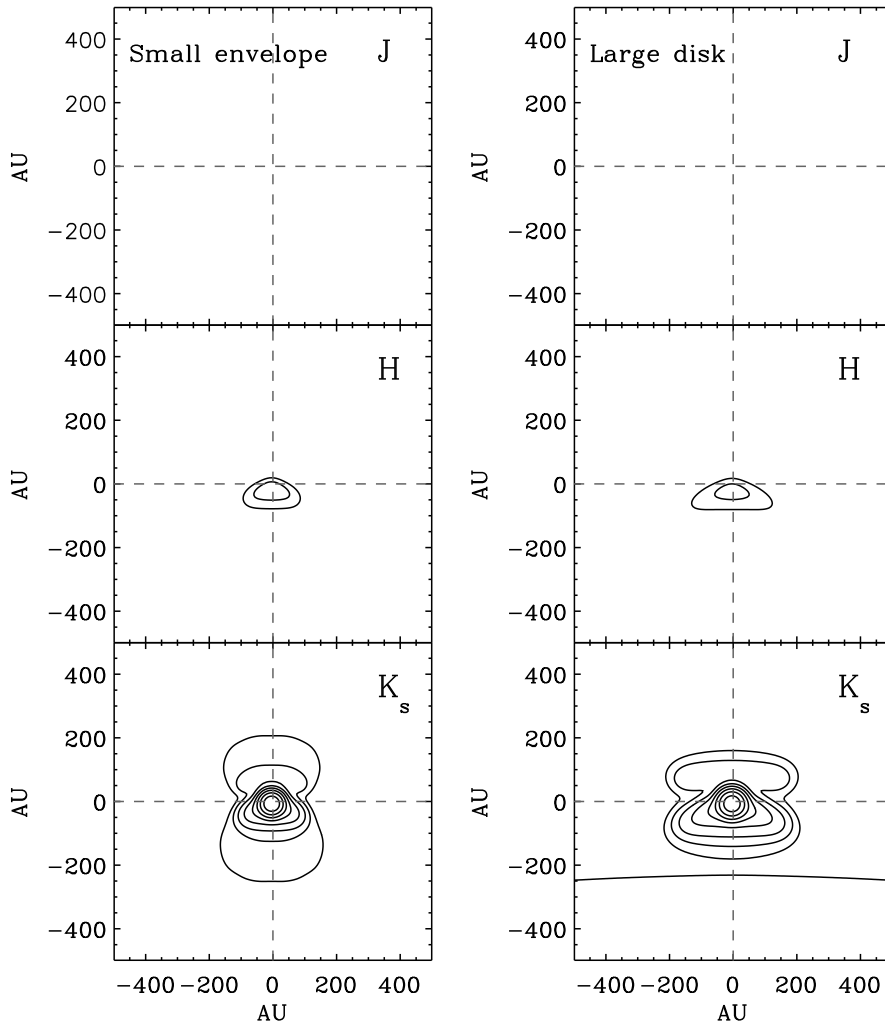
Figure 5.11: *Left panels: Contour plots of the JHK_s model images for the 'standard' model, but with a small power-law envelope added to account for the excess nebulosity seen in the ISAAC imaging. Right panels: Contour plots of the JHK_s model images for a disk with $R_{\mathrm{disk}} = 180\,AU$. The lowest contour is at $1.6 \times 10^{-17}\,erg\,s^{-1}\,cm^{-2}\,Hz^{-1}\,sterad^{-1}$ and subsequent contours increase in steps of 0.4 dex.*

as the 9.7μm silicate band indicate that the grains contributing to the absorption bands are dominated by grain sizes of 0.1–1.0 μm. This is due to the fact that scattering on grains with $2\pi a/\lambda_{\rm ice} \gg 1$, where a is the size of the grain and $\lambda_{\rm ice}$ is the wavelength of the ice band in question, will enhance the contribution to the band from the real part of the refractive index, thereby creating excess absorption on the red side of each band. This is typically seen for the 3.08 μm water ice band (see e.g. Dartois & d'Hendecourt, 2001). For CRBR 2422.8-3423, the red 'scattering wings' of the ice bands are weak at wavelengths longer than 3 μm, indicating that the contribution from grains with sizes $\gg 1$ μm is small. However, this may also simply indicate that the ice absorption is dominated by foreground material.

The most important indirect constraint on the disk structure is the high level of near to mid-infrared emission. Given the inclination angle, a high disk mass of 0.01 M$_\odot$ produces too much extinction along the line of sight to the inner disk to match the Spitzer spectrum. Even with the lower mass used in the presented model, it is found that the presence of an inner rim is essential to reproduce the shape and high flux level of the mid-infrared spectrum. Alternatively, unrealistically lowering the effective temperature of the central star to 2000 K produces a similar effect.

Another important point concerns the visibility of the central star. At an inclination of $\sim 90° \times (1 - H_{\rm disk}/R_{\rm disk})$, the inner disk and star become visible to the observer. This usually results in the star outshining the disk by orders of magnitude. This is clearly not the case for CRBR 2422.8-3423, and is the reason the source was first detected as an edge-on disk. However, the blocking of the star by the flared disk also tends to strongly suppress the mid-infrared continuum. Therefore, in order to fit both the images as well as the Spitzer spectrum, only a very narrow range of surface density profiles and consequently disk masses are possible, given an opacity. The puffed-up inner rim is vital for blocking the light from the central star sufficiently without suppressing the mid-infrared continuum, although even in our best fit model some of the stellar light can still be seen directly in excess of what is observed in the K-band. This is most clear in Fig. 5.9 where the foreground component has been removed. Here a reddened point source is visible in the center of the disk.

The column density of foreground material toward the disk is well constrained by the near-infrared colour to 2.2×10^{22} H$_2$ cm^{-2}, assuming a gas-to-dust mass ratio of 100, corresponding to an extinction in the J-band of 8 mag. If this material is placed close to CRBR 2422.8-3423, for instance in the form of a remnant envelope, a bright reflection nebulosity is created. Since no such extended reflection nebulosity is seen in the K-band imaging, the foreground material must be located at a distance of at least 1000 AU from the source. This is consistent with the line of sight passing through the Oph-F core seen in the submillimetre imaging, rather than an envelope surrounding CRBR 2422.8-3423. Alternatively, the source may already have excavated a significant cavity in its envelope. A small amount of excess nebulosity compared to the 'best fit' model within 300 AU is seen in Fig. 5.10. The possible presence of a small tenuous envelope of CRBR 2422.8-3423 is discussed in §5.4.4. The lack of bright, extended scattering nebulosity in the near-infrared imaging puts an upper limit of a few$\times 10^4$ for the density within 1000 AU

Table 5.2: *Best-fitting model parameters*

	Actual model value	Estimated range (see text)
T_*	4500 K	3500–5500 K
R_*	$2.0\,R_\odot$	1.5–$2.5\,R_\odot$
M_*	$0.8\,M_\odot$	0.2–$2.0\,M_\odot$
L_*	$1.4\,L_\odot$	1.3-$1.5\,L_\odot$
M_disk	$0.0015\,M_\odot$	0.0005–$0.005\,M_\odot$
R_disk	90 AU	80–100 AU (Only flared disk)
$H_\mathrm{disk}/R_\mathrm{disk}$	0.18	0.16–0.20
$H_\mathrm{rim}/R_\mathrm{rim}$	0.12	0.10–0.14
$R_\mathrm{in,env}$	1000 AU	$\gtrsim 1000$ AU
$R_\mathrm{out,env}$	6700 AU	$\lesssim 7000$ AU
ρ_env	$2.6 \times 10^5\,\mathrm{cm}^{-3}$	$1.3 - 3.0 \times 10^5\,\mathrm{cm}^{-3}$
Incl. angle	$69.2°$	68–$72°$
H_2O ice abundance (env.+disk)	9×10^{-5} (rel. to H_2)	$8 - 10 \times 10^{-5}$
CO ice abundance (envelope)	1.3×10^{-4} (rel. to H_2)	Assuming no CO ice in the disk

of CRBR 2422.8-3423. The density of the material producing the near-infrared extinction was constrained by fitting the submillimetre emission within an aperture of $30''$ given the column density calculated using the near-infrared colours. The arbitary method of fitting the foreground material using a spherically symmetric envelope introduces an uncertainty of a factor of at least 2 in the density. This is because the source may be located entirely behind the material producing the submillimetre emission and not in the middle, such as is assumed in the model.

5.4.4 Alternative models

In this Section, we explore the sensitivity of the model to the simultaneous constraints of SED and imaging. Specifically, an important question is whether the size of the flared disk is well-constrained by the ISAAC image. To test this, a model was calculated by assuming $R_\mathrm{disk} = 180$ AU, but fixing the remaining structural parameters of the 'standard' model given in Table 5.2. A best fit to the SED was then obtained by varying luminosity of the central star and the inclination of the system. Because the mass of the disk is kept constant the inclination needs to be higher to produce the same extinction toward the star. At the same time the fraction of warm dust in the disk decreases, requiring the luminosity to be increased to fit the mid-infrared emission. This uncertainty on the luminosity is primarily due to the lack of far-infrared photometry. The resulting image is seen in Fig. 5.11 and the SED is compared to the 'standard' model in Fig 5.14. It is seen that the SED of the large disk can still provide a good fit to the data by varying only the inclination and luminosity. However, the K_s image of the large disk clearly becomes larger than the observed image. We conclude that the size of the flared disk is constrained by the near-infrared imaging. Modelling of an outer non-flared (self-shadowed) disk is postponed to a later paper.

The ISAAC K_s image also clearly shows excess scattering emission close to the central disk (Fig. 5.10). This emission is not included in the 'standard' model. A small envelope may affect the modelled flaring properties of the disk by raising
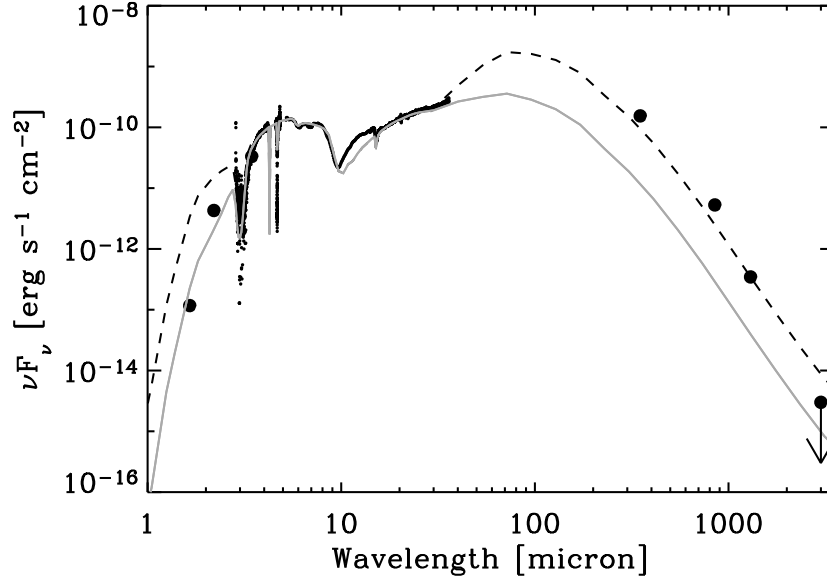
Figure 5.12: *Best fitting SED model of CRBR 2422.8-3423. The solid curve shows the model flux through an aperture of 10″, while the dashed line shows the flux through an aperture of 30″. The 350 μm, 850 μm and 1300 μm fluxes are integrated though a 30″ aperture centered on the near-infrared position of CRBR 2422.8-3423. The 1300 μm flux is taken from Motte et al. (1998).*

the scattering surface (Stapelfeldt et al., 2003). Here, we test the effect on the model image and SED of a small envelope producing excess emission. A small power-law envelope is added at radii larger than $R_{\rm disk} = 90$ AU to fit the ISAAC images. An envelope with a density power-law exponent of -1 and a gas density at $R_{\rm disk}$ of 10^4 cm^{-3} provides a reasonable fit to the excess emission in the ISAAC K_s image. Note, however, that the shape of the density profile is not strongly constrained. The influence of the small scattering envelope on the SED is seen in Fig. 5.14 to be minimal.

5.5 Where are the ices toward CRBR 2422.8-3423?

5.5.1 Ices in the model disk

The radiative transfer model of CRBR 2422.8-3423 allows the location of the ices to be studied in greater detail. In principle, the model cannot directly distinguish between ice located in the disk and ice located in foreground material. However, significant conclusions can be reached by considering the range of realistic ice abundances. Furthermore, differences in dust temperatures in the disk and fore-
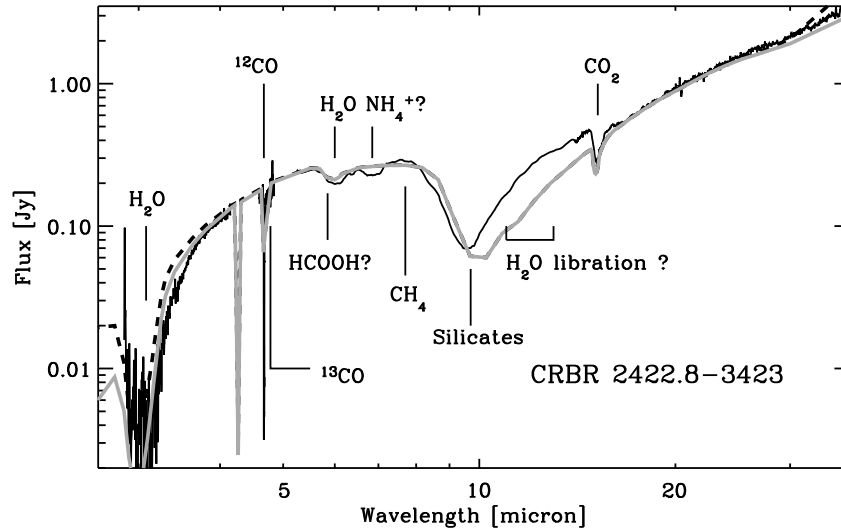
Figure 5.13: *A close-up comparison of the best-fitting model in observing apertures of $10''$ (grey curve) and $30''$ (dashed curve) with the observed infrared spectra (black curve). Note the mismatch on the red side of the $9.7\,\mu$m silicate feature due to the water libration mode in the model.*

ground put constraints on the location of the ices. Fig. 5.15 shows the SED for the disk with the foreground material removed. It is seen that significant fractions of the ice absorption lines originate in the disk material if the assumption of a constant water ice abundance of 9×10^{-5} in the disk and foreground material is correct. Quantitatively, the model disk contributes 45% of the observed water ice band for a constant ice abundance.

From Fig. 5.8 it is seen that the temperature in the model disk nowhere drops below $27\,$K. This effectively prevents any pure CO ice from being present in the model disk, since this evaporates at $\sim 20\,$K at the densities present in the disk (Sandford & Allamandola, 1993). A significant change of the disk density structure, such as 1–2 orders of magnitude denser material in the mid-plane or a significantly larger outer disk radius, is required in order to have pure CO ice in the disk. Even if CO ice is present in a dense mid-plane, it is unlikely to contribute to the observed CO ice band. This question can be explored by examining the temperature of the dust that can be probed at a wavelength of $4.67\,\mu$m. Fig. 5.16 illustrates the point for the best-fitting model disk. It shows the model optical depth of the $4.67\,\mu$m CO band as a function of desorption temperature, assuming a constant CO ice abundance for temperatures lower than the desorption temperature. The relation has been calculated by directly including a component of pure CO inclusions in the dust model for temperatures lower than the desorption temperature. Naturally, if a higher desorption temperature is assumed, a deeper CO ice band appears in the spectrum. Therefore, the contribution of ice at different tempera-

143
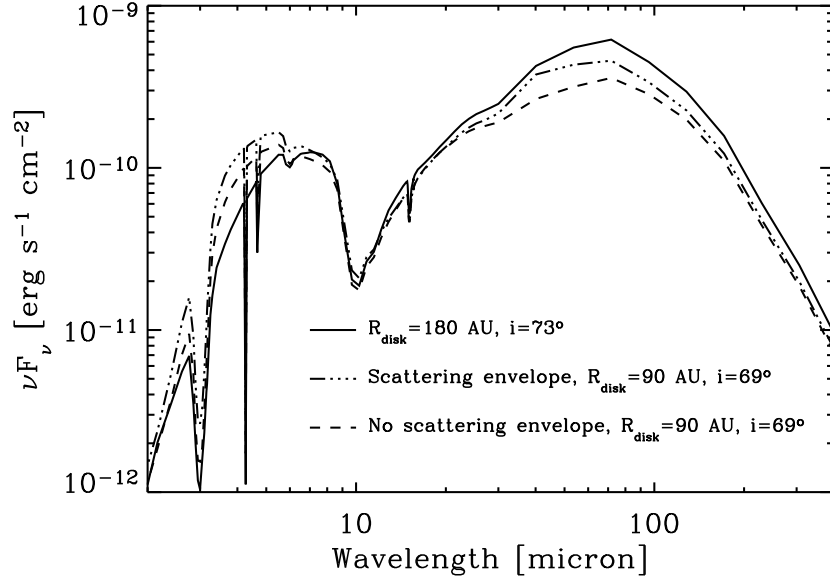
Figure 5.14: *Comparison of the SEDs of different models of CRBR 2422.8-3423. The dashed curve shows the 'standard' model fit shown in Fig. 5.12. The dash-dotted curve shows the SED if a small power-law envelope has been added to account for the excess nebulosity seen in the ISAAC images of CRBR 2422.8-3423. The solid curve shows the SED of a model with twice the disk radius of the 'standard' model (180 AU). This model has an inclination of 73° and an increased stellar luminosity of 2.9 $L_\odot$ to fit the observed SED.*

tures to an ice band centered on 4.67 μm can be read off the relation in the figure. The foreground material is seen as a sharp rise to 20 K followed by a plateau, indicating that little absorbing material is present at temperatures between 30 and 40 K. The contribution from material in the disk takes over only at temperatures above 40 K. This clearly shows that the model disk can contain no pure CO ice that will show up in the spectrum; all ice in the disk observed in the wavelength region around 5 μm must have temperatures between 40 and 90 K. This is consistent with the excitation temperature of the observed CO ro-vibrational lines of 40–60 K as determined by Thi et al. (2002). Inspection of Fig. 5.8 shows that the disk material, which contains ices contributing to the observed absorption bands, has densities of $10^6 - 10^7$ cm^{-3}. The disk must be considerably larger in order to contribute to the observed pure CO ice band. This is illustrated by plotting the CO ice band depth as a function of assumed desorption temperature of the large disk with $R_{\mathrm{disk}} = 180$ AU in Fig. 5.16. It is seen that the large disk shifts the absorbing material toward lower temperatures as expected, but only by ~ 5 K, such that the coldest dust in the disk contributing to the ice band is 35 K for the large disk.

If the CO is embedded in other less volatile ice species, such as water ice, the evaporation temperature of CO can be raised to $70\,\mathrm{K}$. However, the CO and CO_2 ice profiles indicate that at most 20% of the CO is mixed with CO_2 and another 20% with water. The remaining CO ice must reside in the cold foreground dust. The conclusion that none of the pure CO ice observed in the spectrum is present in the disk implies that the abundance of pure CO ice in the foreground must be very high, 1.1×10^{-4}, making CO the most abundant ice species in the foreground material. If the CO embedded in water ice is present in the observed average abundance of 1.7×10^{-5} (see Table 5.1) throughout the system, the CO ice abundance in the foreground may increase further to 1.27×10^{-4}. In order to determine the total depletion of gas-phase CO in the foreground, ice species formed by CO, such as CO_2 and CH_3OH, must also be included. Adding the observed average abundance of CO_2 of 2.9×10^{-5} and ignoring the relatively small contribution from CH_3OH, the total amount of CO depleted from the gas-phase is as much as 1.6×10^{-4}. For a total CO abundance of $2 - 3 \times 10^{-4}$ w.r.t. H_2, this leaves at most 1×10^{-4} for gas-phase CO, corresponding to a foreground column density of $2.2 \times 10^{18}\,\mathrm{cm}^{-2}$. This is roughly consistent with the total CO column density (foreground + background) of $\sim 5 \times 10^{18}\,\mathrm{cm}^{-2}$ derived from millimetre $C^{18}O$ data (Thi et al., 2002). We conclude that the molecular gas in the foreground cloud is highly depleted.

The assumption that all other ice species evaporate at $90\,\mathrm{K}$ used in the model is not very realistic and was adopted for simplicity. In reality, the ices considered evaporate at a range of temperatures between 20 and $100\,\mathrm{K}$, depending on species and ice composition. Fig. 5.17 shows the variation of the model ice features in the disk if an evaporation temperature of $45\,\mathrm{K}$ is assumed instead. It is seen that the ice bands become $\sim 30\%$ weaker for the lower evaporation temperature, corresponding to most of the disk ice. The implication is that all disk ice features should show significant signatures of heating above $40\,\mathrm{K}$. For CRBR 2422.8-3423 this effect may be difficult to observe due to the contribution from cold foreground ice. However, as discussed in Sec. 5.3.3, the red shoulder of the $6.85\,\mu\mathrm{m}$ band indeed provides significant evidence for the presence of warm ices along the line of sight. It is important to note that most of the disk mass has temperatures below $40\,\mathrm{K}$, but that this material is simply not probed by the ice bands due to the high optical depths in the mid-plane. This illustrates how the location of ices in circumstellar disks and probably in most low-mass protostars require a detailed axisymmetric 3D model to be adequately constrained.

In summary, we find that up to 50% of the observed band optical depths of ice species that remain in the solid state at temperatures above $40\,\mathrm{K}$, may be due to disk ice. This includes water, CO_2 ices and CO embedded in water ice. The observed pure CO ice is most likely located entirely in the Oph-F core.

5.5.2 CO and CO_2 ice maps of the Oph-F core

In order to gain additional insight into the nature of the ices observed toward CRBR 2422.8-3423, ice abundances toward other sources in the Oph-F core have been extracted. High quality $3\text{-}16\,\mu\mathrm{m}$ spectra are available for 4 additional sources
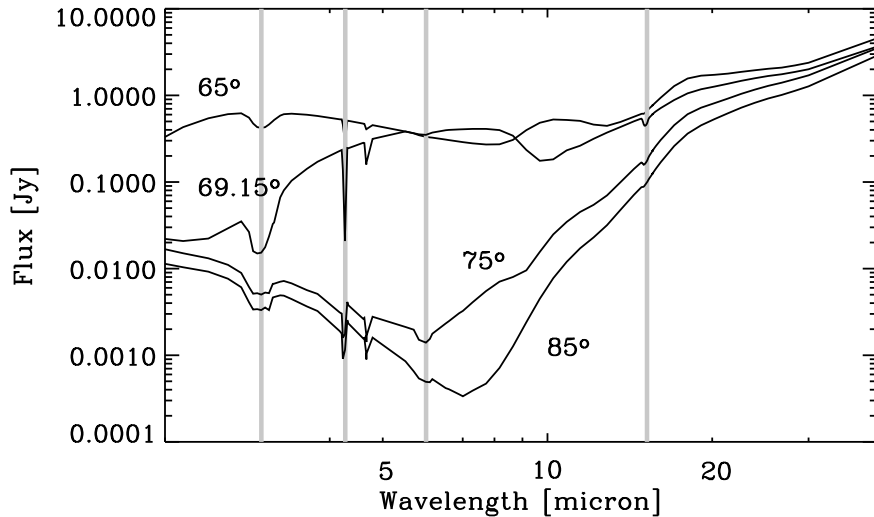
Figure 5.15: *Models showing the effect of inclination on the ice bands. The models are the best-fitting CRBR 2422.8-3423 model, only with the foreground cloud removed. The inclinations shown are from top to bottom: $65°$, $69.15°$, $75°$ and $85°$. Note the significant changes in line ratios, especially between the $3.08\,\mu m$ and the $6.0\,\mu m$ water ice bands. The vertical lines indicate the position of the $3.08\,\mu m$ water stretching mode, the $4.27\,\mu m$ CO_2 stretching mode, the $6.0\,\mu m$ water bending mode and the $15.2\,\mu m$ CO_2 bending mode.*

within a radius of $15\,000\,AU$ from the center of the core defined to be that of the prestellar core Oph-F MM2 ($\alpha=16^h27\,24.3$, $\delta=-24°40\,35$, J2000) (Motte et al., 1998). The 3–5 μm spectra have been extracted from the VLT-ISAAC survey by Pontoppidan et al. (2003); van Dishoeck et al. (2003), while the 5–16 μm spectra are extracted from the ISOCAM-CVF image of the core. This yields CO and CO_2 ice abundances relative to H_2O ice as a function of distance to the center of the core. The radial map is shown in Fig. 5.18. It is seen that the abundances of pure CO, water-rich CO and CO_2 all increase toward the center of the core. This behaviour is expected for CO freezing out from the gas-phase at high densities. Assuming a constant water ice abundance of 9×10^{-5} relative to H_2 in accordance with the model of the CRBR 2422.8-3423 line of sight, the average abundance of pure CO ice is seen to rise from 4.5×10^{-6} to 7.0×10^{-5}, and the total CO and CO_2 abundances from 2.3×10^{-5} to 12×10^{-5}. This corresponds to a total CO depletion ranging from 12% to 60%, assuming an initial CO gas-phase abundance of 2×10^{-4}.

Since the young stars that are used to estimate ice abundances in the core material are possibly embedded in the core, some caveats apply. Heating of the core material may desorb CO ice within a radius of a few hundred AU of each source, depending on the luminosity. However, since the projected size of the core is $30\,000\,AU$, desorption is likely to play only a minor role.
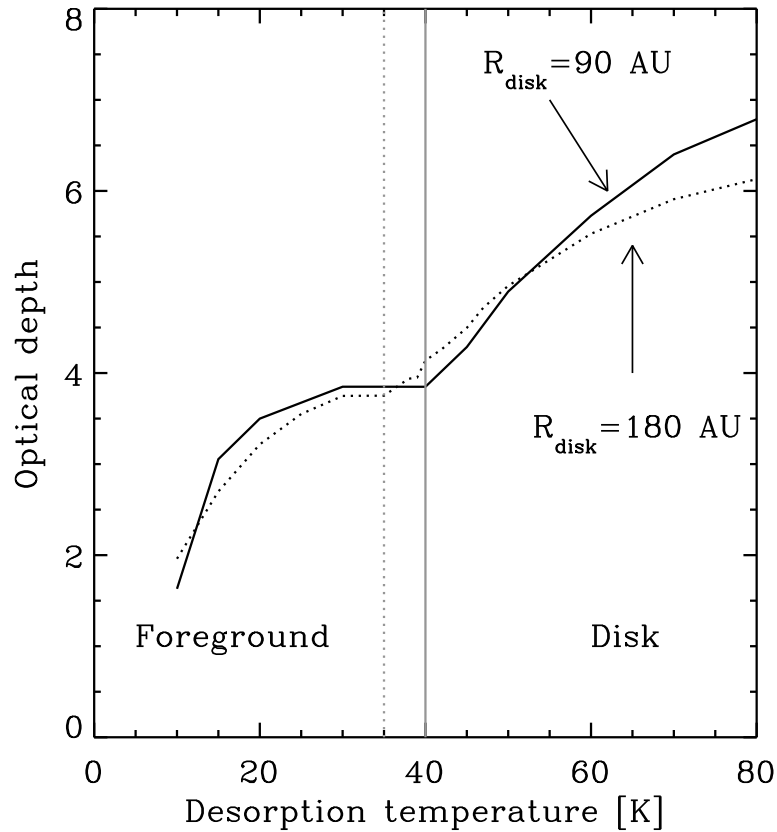
Figure 5.16: *Optical depth of the 4.67 μm band of CO for the CRBR 2422.8-3423 model as a function of (assumed) desorption temperature. The abundance is arbitrarily assumed to be constant at 9×10^{-5} whenever the temperature is below the desorption temperature. Both the 'standard' model (solid curve) of Table 5.2 and the model with $R_{\mathrm{disk}} = 180$ AU (dotted curve) are shown. The vertical solid and dotted lines indicate the separation between contributions from the foreground material and from the disk material for the 90 AU and 180 AU disks, respectively.*

The radial map constitutes the first direct observation of the freeze-out of CO on dust grains in a prestellar core previously inferred indirectly from observations of millimetre lines of molecules (Caselli et al., 1999; Tafalla et al., 2004). Additionally the observed increase in CO_2 ice abundance toward the center is the first quantitative observational evidence of the formation of CO_2 from CO on the surfaces of dust grains. The map gives significant credence to the conclusion reached using the model of CRBR 2422.8-3423 that the observed CO ice is dominated by highly depleted foreground material.

147
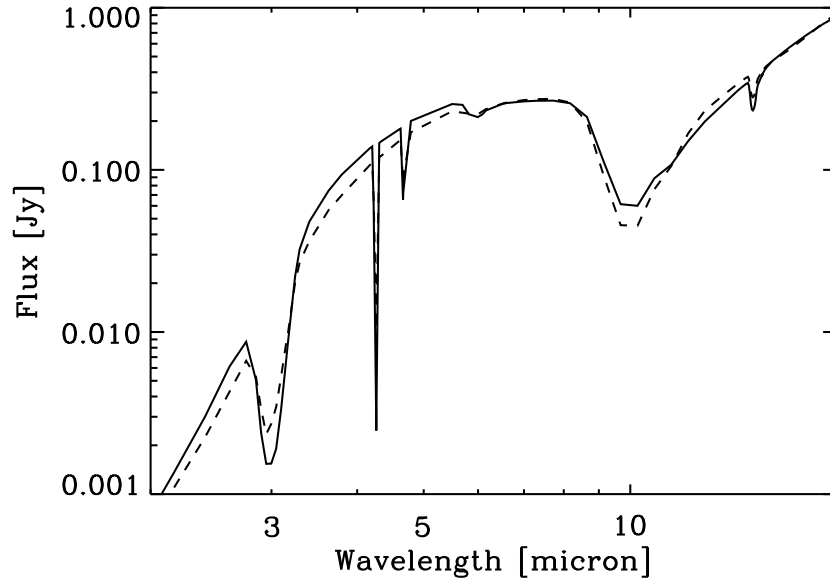
Figure 5.17: *Comparison of a model assuming that the ice evaporation temperature is $T_{evap} = 90\,K$ (solid curve) with a model using $T_{evap} = 45\,K$ (dashed curve). For CRBR 2422.8-3423, a significant amount of the ice has temperatures in excess of 45 K.*

5.5.3 The missing water ice librational band

In Fig. 5.12, it is evident that the red wing of the 9.7 μm silicate band is not well-fitted by the model. The model red wing is caused by the librational (hindered rotation) band of water ice. This band is centered around 12-13 μm, but the center and width are sensitive to ice composition (Hagen et al., 1983). The band strength of the water libration band is almost three times higher than the CO_2 bending mode, which is located in the same wavelength region (Gerakines et al., 1995). Combined with the higher column density of water ice, the libration band should be about 10 times stronger than the corresponding 15.2 μm CO_2 band, although it will only contribute an optical depth of 0.3-0.5 at 12 μm due to the large width of the band. Laboratory experiments find that the strength of the librational band is fairly constant under interstellar conditions (Kitta & Kraetschmer, 1983). Careful radiative transfer models of other sources compared to e.g. Spitzer-IRS spectroscopy may show if the problem is universal. Recent Spitzer-IRS spectra of the embedded low-mass star HH 46 IRS, toward which the ice bands are about twice as deep as toward CRBR 2422.8-3423, also do not show a water ice libration band as strong as expected (Boogert et al., 2004). The librational band is sensitive to the dust model, through the grain size distribution as well as the shape of the grains. It is possible that a more realistic dust model may provide a better fit the
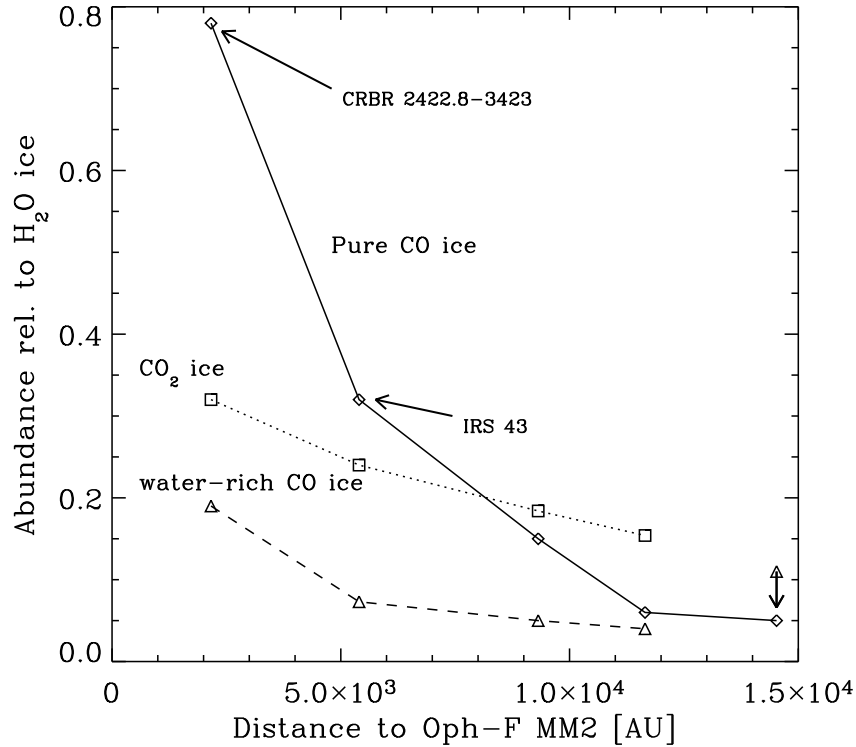
Figure 5.18: *Radial map of CO and CO$_2$ ices of the Oph-F core, which is located partly in front of CRBR 2422.8-3423. Ice abundances relative to H$_2$O ice toward young stars are plotted as functions of projected distance to the center of the core. The lines of sight toward the young stars IRS 42, IRS 43, IRS 44 and IRS 46, in addition to CRBR 2422.8-3423, are used to construct the map.*

librational water ice band.

5.6 Observing ices in other edge-on disks

Using the model for the CRBR 2422.8-3423 disk, some general predictions can be made for observations of ices in other edge-on circumstellar disks. Clearly, the presence of cold foreground material complicates any interpretation of ice bands from a disk. However, since this problem often cannot be avoided, it is interesting to explore how the ice bands intrinsic to the disk may be distinguished from those produced by foreground material.

An interesting question to explore is how the ice bands behave with varying inclination. For instance, are disks with an inclination angle close to 90° more
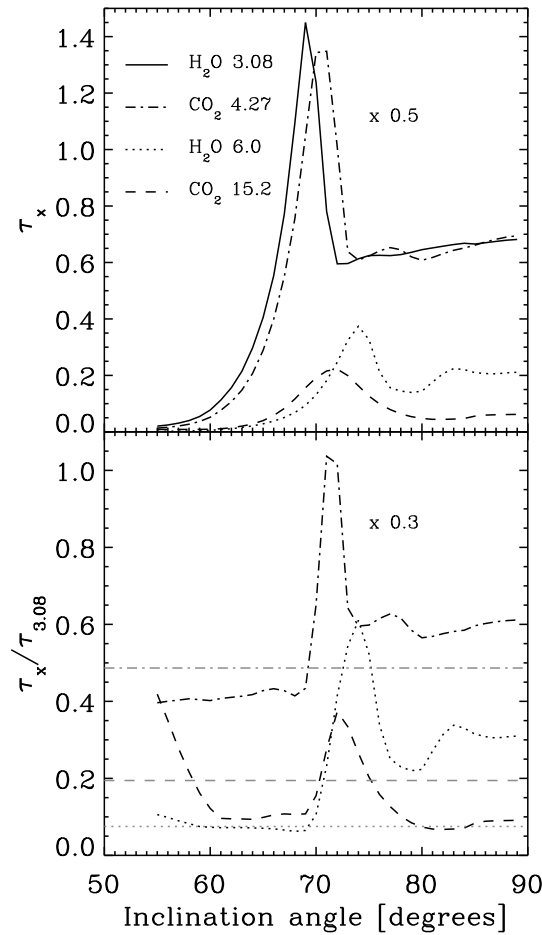
Figure 5.19: *Upper panel: Optical depths of H_2O and CO_2 ice bands as functions of disk inclination for the model of CRBR 2422.8-3423. Lower panel: Line ratios relative to the 3.08 μm water ice band. The horizontal lines indicate the ratios of the extinction coefficients of the bands, i.e. the line ratio expected to be observed in a cold foreground cloud. No foreground material has been included to clarify the effects intrinsic to the disk. The curves for the CO_2 4.27 μm band have been scaled by a factor of 0.5 (upper panel) and 0.3 (lower panel) to fit in the figure.*

favourable for observing ices than disks with lower inclination angles of 70°? In Fig. 5.15 the spectra of the best fitting model of CRBR 2422.8-3423 viewed at different inclination angles are shown. It is apparent that an inclination of 70° in fact

produces the deepest ice bands. A disk similar to CRBR 2422.8-3423 viewed very close to edge-on shows only weak intrinsic ice features. This is an effect produced by the large optical depth through the mid-plane. Disks 1–2 orders of magnitude less massive than CRBR 2422.8-3423 will have optical depths approaching unity along the mid-plane. Such an edge-on disk will have deep ice bands, if ices are present in abundance. For CRBR 2422.8-3423, the ice bands are seen in absorption only toward light scattered in the relatively tenuous disk surface.

Another observation of considerable interest is, that the ratios between different ice bands of the same species are not preserved as a function of inclination. To illustrate this quantitatively, the model optical depths of H_2O and CO_2 bands are plotted in Fig. 5.19 as functions of disk inclination. Common for all ice bands is that the optical depth peaks strongly for inclinations between 65 and 75°. For most ice bands a constant plateau is reached at higher inclination angles after the main peak. The exception here is the 15.2 μm CO_2 bending mode, which drops to a very small absorption depth at the highest inclination. Finally, the different bands are seen to peak at somewhat different inclination angles.

The model optical depths are also shown relative to the model 3.08 μm water band depth in the figure. Clearly, the line ratios of all ice bands relative to the water band change dramatically depending on inclination. Note that this is not an effect of varying ice abundances within the disk, since both H_2O and CO_2 ices are assumed to evaporate at 90 K. The effect is especially apparent for the 3.08 μm and 6.0 μm water ice bands, the ratio of which drops from ~ 10 at an inclination of 65° to ~ 0.7 at an inclination of 74°. At even higher inclination, the ratio between the two water ice bands drops to a plateau of 0.2-0.25.

Note that the varying ratios of the ice absorption bands are in this case a purely 2-dimensional effect. The 'classical' radiative transfer scenario for ice bands is material in a cold slab seen toward a background infrared point source. The important difference for observing ices in a disk is that the background source is extended relative to the absorbing material. For instance, if the infrared source is due to scattered light, the size of the background source may be comparable to the size of the flared disk. There are two mechanisms which produce the extended source in the case of a disk. The first is light from the central star and inner rim scattered in the surface layer of the disk, and the second is thermal emission from the surface layer. Inspection of Fig. 5.15 illustrates the relative importance of these two effects. For the spectrum produced by the highest inclination, a minimum in the flux is observed at $\sim 8\,\mu$m. At shorter wavelengths, scattered light dominates the spectrum, while thermal emission from the disk surface layer dominates at longer wavelengths. This means that the 15.2 μm CO_2 bending mode is always observed against a thermal source, while the rest of the main ice bands are observed toward a scattered source for a highly inclined disk. At an inclination similar to the disk opening angle, the emission from the central star and inner rim start to dominate. In this case the entire length of the disk is probed and the deepest ice bands are produced. In Fig. 5.15, it is seen that the inclination where the peak absorption of the first three ice bands (the 3.08 μm and 6.0 μm water ice bands and the 4.27 μm CO_2 ice band) occurs, increases with increasing wavelength of the band. This is, however, not true for the 15.2 μm CO_2 ice band, which peaks at a lower inclination

than the 6 μm band. This is due to the fact that the first three bands are seen toward a scattering source, while the 15.2 μm band is seen toward a thermal source with a different geometry.

Obviously, such behaviour significantly complicates the determination of accurate ice abundances in disks and other multi-dimensional scenarios. On the other hand, strongly deviating ice band ratios seen toward an edge-on disk is a strong signature that the ices are intrinsic to the disk. For the case of CRBR 2422.8-3423, no strongly deviant line ratios are observed, at least not when compared to other ice sources. In particular the ratio between the 6.0 μm and the 3.08 μm water ice bands is typical of embedded sources. It is a long-standing problem that the water ice band 6.0/3.08 ratio is up to two times higher than expected. Part of this may be explained by radiative transfer effects analogous to those identified here for edge-on disks. However, since most observed icy lines of sight exhibit this anomalous ice band ratio, the effect is unlikely to be entirely due to the presence of disk geometry. The CO_2 bending mode of CRBR 2422.8-3423 can unfortunately not be compared to the stretching mode at 4.27 μm, which is located outside the spectral coverage of Spitzer-IRS. The ratio of the two CO_2 ice bands could otherwise constitute an excellent tracer of radiative transfer effects in disks.

The fact that CRBR 2422.8-3423 has an inclination which is exactly optimal for observing ices in the disk is an interesting coincidence. Had the inclination been a few degrees higher, the mid-infrared continuum flux level would have dropped by an order of magnitude, and the ice band ratios would have deviated strongly from the norm. Another important conclusion is that pure CO ice is not expected to show up in spectra of disks with radii smaller than 100–150 AU. Any CO ice present should show clear signs of being embedded in a less volatile ice matrix, such as a dominance of the red water-rich component at 2136 cm^{-1}.

5.7 Conclusions

We have presented a full mid-infrared spectrum covering all of the strongest absorption features due to interstellar ices, except the 4.27 μm CO_2 band. By fitting an axisymmetric, but effectively 3D Monte Carlo radiative transfer model to the spectrum as well as photometric data covering 1.6-3000 μm and spatially resolved near-infrared images, we have been able to constrain the location of ices in the disk and in foreground material. The main conclusions can be summarised as follows:

- The use of an axisymmetric 3D continuum radiative transfer model to simultaneously fit a high spectral resolution SED as well as high spatial resolution imaging is a powerful tool to estimate the physical conditions of dust in a circumstellar disk. Combining the model with high resolution temperature-dependent opacities allows a detailed study of the icy material present in the disk.

- The extinction of the near-infrared emission together with sub-millimetre imaging indicate that a dense and cold foreground component containing a

significant part of the observed ices is present. Specifically, the line of sight toward CRBR 2422.8-3423 passes through the dense core Oph-F that may be pre-protostellar.

- If a constant ice abundance for all ice species apart from CO is assumed throughout the disk and foreground material for temperatures below 90 K, up to 50% of the water and CO_2 ice reside in the disk. The 6.85 μm feature shows signatures of strong thermal processing, indicating that a similar fraction of the carrier, which is possibly NH_4^+, also resides in the disk. The shape of the 6.85 μm band is arguably the strongest evidence for the presence of ices in the disk.

- None of the pure CO ice observed toward CRBR 2422.8-3423 can be located in the model disk because the temperature in the model is too high. The presence of a colder self-shadowed disk at larger radii is not ruled out, but CO ice in a flat outer disk will not contribute to the observed ice band. This is because an outer disk with a component in the line of sight to the central star will also appear in scattered light. According to the disk model, only dust with temperatures of 40–90 K and associated gas densities of $10^6 - 10^7 \, \mathrm{cm}^{-3}$ can contribute to the observed ice bands. Up to 20% of the CO ice is trapped in water ice and can survive in the disk together with an additional 20% trapped in CO_2 ice. For a constant abundance of these types of CO ice throughout the disk and envelope, at most 20% of the observed total amount of solid CO originates in the disk. In general, pure CO ice should only be observed in large quantities in disks surrounding low-mass stars if the disks have radii much larger than ~ 150 AU. Indeed, Thi et al. (2002) concluded that most of the CO ice is located in the disk, based on a larger model disk. Excluding the presence of pure CO ice in the disk required the detailed 3D modelling presented here. It should be emphasised that the new Spitzer observations indicate that warm rather than cold ices are indeed present in the disk.

- The model does not provide a good fit to the red wing of the 9.7 μm silicate band. The discrepancy is due to the absence of the strong librational band of water ice centered at 12-13 μm. We are unable to explain the absence of the band since laboratory experiments indicate that the strength does not change appreciably under interstellar conditions.

- The infrared source against which ice bands are observed is extended for an edge-on disk due to scattering at wavelengths shorter than $\sim 7 \, \mu$m and due to thermal emission from the disk surface layer at longer wavelengths. This results in ice band ratios which are not equal to the corresponding band ratios of the opacity. The model indicates that the ratio between the 3.08 μm and the 6.0 μm water ice bands as well as the ratio between the 4.27 μm and the 15.2 μm CO_2 ice bands are excellent tracers of radiative transfer effects on ice bands intrinsic to an edge-on disk. Ratios between bands of the same ice species are potentially powerful probes of the distribution of ices in disks. At the same time, anomalous ratios may be used to determine if the ices are

located in the disk as opposed to a foreground cloud. The opposite is not true, i.e. normal band ratios do not indicate that the ices are not in the disk.

- We have presented a radial map of the abundances of CO and CO_2 ices in the Oph-F core. This represents the first direct observation of increasing freeze-out of CO molecules with increasing density in a prestellar core. The abundance of CO_2 ice increases along with the CO ice, providing direct quantitative evidence that CO_2 is formed by oxidation of CO on dust grain surfaces.

Acknowledgements

Bibliography

Aikawa, Y., Umebayashi, T., Nakano, T., & Miyama, S. M. 1997, ApJL, 486, L51+

Alexander, R. D., Casali, M. M., André, P., Persi, P., & Eiroa, C. 2003, A&A, 401, 613

Beck, T. L., Prato, L., & Simon, M. 2001, ApJ, 551, 1031

Bohren, C. F. & Huffman, D. R. 1983, Absorption and scattering of light by small particles (New York: Wiley, 1983)

Boogert, A., Pontoppidan, K., Lahuis, F., et al. 2004, ApJ, 154, in press

Boogert, A. C. A., Hogerheijde, M. R., & Blake, G. A. 2002, ApJ, 568, 761

Brandner, W., Sheppard, S., Zinnecker, H., et al. 2000, A&A, 364, L13

Caselli, P., Walmsley, C. M., Tafalla, M., Dore, L., & Myers, P. C. 1999, ApJL, 523, L165

Chiang, E. I. & Goldreich, P. 1997, ApJ, 490, 368

Collings, M. P., Dever, J. W., Fraser, H. J., McCoustra, M. R. S., & Williams, D. A. 2003, ApJ, 583, 1058

Dartois, E. & d'Hendecourt, L. 2001, A&A, 365, 144

Dartois, E., d'Hendecourt, L., Thi, W., Pontoppidan, K. M., & van Dishoeck, E. F. 2002, A&A, 394, 1057

Draine, B. T. 2003, ARA&A, 41, 241

Dullemond, C. P. & Dominik, C. 2004, A&A, 417, 159

Dullemond, C. P., Dominik, C., & Natta, A. 2001, ApJ, 560, 957

Dullemond, C. P. & Turolla, R. 2000, A&A, 360, 1187

Dullemond, C. P., van Zadelhoff, G. J., & Natta, A. 2002, A&A, 389, 464

Dutrey, A., Guilloteau, S., & Guelin, M. 1997, A&A, 317, L55

Ehrenfreund, P., Boogert, A. C. A., Gerakines, P. A., et al. 1996, A&A, 315, L341

Ehrenfreund, P., Boogert, A. C. A., Gerakines, P. A., Tielens, A. G. G. M., & van Dishoeck, E. F. 1997, A&A, 328, 649

Ehrenfreund, P., Breukers, R., D'Hendecourt, L., & Greenberg, J. M. 1992, A&A, 260, 431

Ehrenfreund, P., Kerkhof, O., Schutte, W. A., et al. 1999, A&A, 350, 240

Evans, N. J., Allen, L. E., Blake, G. A., et al. 2003, PASP, 115, 965

Falk, M. 1987, J. Chem. Phys, 86, 560

Gerakines, P. A., Schutte, W. A., Greenberg, J. M., & van Dishoeck, E. F. 1995, A&A, 296, 810

Gerakines, P. A., Whittet, D. C. B., Ehrenfreund, P., et al. 1999, ApJ, 522, 357

Hagen, W., Greenberg, J. M., & Tielens, A. G. G. M. 1983, A&AS, 51, 389

Hogerheijde, M. R., van Langevelde, H. J., Mundy, L. G., Blake, G. A., & van Dishoeck, E. F. 1997, ApJL, 490, L99+

Jäger, C., Mutschke, H., & Henning, T. 1998, A&A, 332, 291

Keane, J. V., Tielens, A. G. G. M., Boogert, A. C. A., Schutte, W. A., & Whittet, D. C. B. 2001, A&A, 376, 254

Kerkhof, O., Schutte, W. A., & Ehrenfreund, P. 1999, A&A, 346, 990

Kitta, K. & Kraetschmer, W. 1983, A&A, 122, 105

Motte, F., Andre, P., & Neri, R. 1998, A&A, 336, 150

Muzerolle, J., Calvet, N., Hartmann, L., & D'Alessio, P. 2003, ApJL, 597, L149

Natta, A., Prusti, T., Neri, R., et al. 2001, A&A, 371, 186

Ossenkopf, V. & Henning, T. 1994, A&A, 291, 943

Pontoppidan, K. M., Fraser, H. J., Dartois, E., et al. 2003, A&A, 408, 981

Sandford, S. A. & Allamandola, L. J. 1993, ApJ, 417, 815

Schutte, W. A., Boogert, A. C. A., Tielens, A. G. G. M., et al. 1999, A&A, 343, 966

Schutte, W. A., Gerakines, P. A., Geballe, T. R., van Dishoeck, E. F., & Greenberg, J. M. 1996, A&A, 309, 633

Schutte, W. A. & Khanna, R. K. 2003, A&A, 398, 1049

Shuping, R. Y., Chiar, J. E., Snow, T. P., & Kerr, T. 2001, ApJL, 547, L161

Siess, L., Dufour, E., & Forestini, M. 2000, A&A, 358, 593

Stapelfeldt, K. R., Ménard, F., Watson, A. M., et al. 2003, ApJ, 589, 410

Tafalla, M., Myers, P. C., Caselli, P., & Walmsley, C. M. 2004, A&A, 416, 191

Thi, W. F., Pontoppidan, K. M., van Dishoeck, E. F., Dartois, E., & d'Hendecourt, L. 2002, A&A, 394, L27

Thi, W.-F., Zadelhoff, G.-J., & van Dishoeck, E. F. 2004, A&A, in press, astro

van Dishoeck, E. F., Dartois, E., Pontoppidan, K. M., et al. 2003, The Messenger, 113, 49

van Zadelhoff, G.-J., van Dishoeck, E. F., Thi, W.-F., & Blake, G. A. 2001, A&A, 377, 566

Vandenbussche, B., Ehrenfreund, P., Boogert, A. C. A., et al. 1999, A&A, 346, L57

Warren, S. G. 1984, Appl. Opt., 23, 1026

Watson, D. M., Kemper, F., Calvet, N., et al. 2004, ApJS, 154, 391

Weingartner, J. C. & Draine, B. T. 2001, ApJ, 548, 296

Werner, M. W., Gallagher, D. B., & Irace, W. R. 2004, Advances in Space Research, 34, 600

Wood, K., Wolff, M. J., Bjorkman, J. E., & Whitney, B. 2002, ApJ, 564, 887

Chapter 6

Bright CO ro-vibrational emission lines in the class I source GSS 30 IRS1

Abstract

 We present a 4.5-4.85 μm $R = 5\,000$ spectrum of the low mass class I young stellar object GSS 30 IRS1 ($L = 25$ L$_\odot$) in the ρ Ophiuchus core, observed with the infrared spectrometer (ISAAC) on the Very Large Telescope (VLT-UT1). Strong line emission from the ro-vibrational transitions of ^{12}CO and ^{13}CO is detected. In total more than 40 distinct lines are seen in the covered region. The line emission is spatially extended and detected up to $2'' = 320$ AU from the central source but is spectrally unresolved ($\Delta v < 30$ km s^{-1}). This is the first time strong emission in the fundamental ro-vibrational band from CO has been observed from an embedded young stellar object. The line fluxes were modeled using a 1-dimensional full radiative transfer code, which shows that the emission is fully consistent with a gas in LTE at a single well constrained temperature ($T = 515 \pm 5$ K). Furthermore, the ratios between lines from the two detected isotopic species of CO show that the ^{12}CO lines must be optically thick. However, this is inconsistent with the observed spatial extent of the emission, since this implies such low CO column densities that the lines are optically thin. A likely solution to the discrepancy is that the lines are emitted by a smaller more dense region and then scattered in the bipolar cavity present around the central star. This gives a rough estimate of the total molecular gas mass of $1 - 100$ M$_\oplus$ and a physical extent of $\sim 20 - 100$ AU. We propose that the most likely origin of the line emission is post-shocked gas in a dense dissociative accretion shock from the inner $10 - 50$ AU of a circumstellar disk. The presence of a shock capable of dissociating molecules in the disk will have implications for the chemical evolution of disks around young low mass stars. [1]

6.1 Introduction

The innermost 50 AU of the circumstellar environments around embedded young stellar objects is poorly constrained observationally due to the large extinction

---

[1] K. M. Pontoppidan, F. L. Schöier, E. F. van Dishoeck and E. Dartois 2002, A&A, 393, 585

through the embedding material ($A_V > 20$ mag) and the small angular size ($< 1''$) of the region. The usual molecular probes in the millimeter-submillimeter region are not effective for the temperatures ($T > 200$ K) and densities ($n_{H_2} > 10^7$ cm^{-3}) thought to be present. However, an understanding of the processes taking place in this regime is essential to obtain a complete picture of the process of accretion and the driving of outflows from low mass protostars as well as the early chemical and physical evolution of circumstellar disks.

One of the most effective probes of warm dense gas is through emission in molecular ro-vibrational transitions. The most common bands readily available from ground-based facilities are the CO overtones and H$_2$ fundamental bands around 2.2 μm (e.g. Reipurth & Aspin, 1997) and the fundamental transitions of CO in the M-band around 4.7 μm. Also emission from very hot water gas ($\sim$ 2000 K) near 2.29 μm has been reported toward a few sources (e.g. Najita et al., 2000). Since the upper levels of these transitions lie at temperatures of up to a few thousand Kelvin, they probe hot gas with temperatures between 100 and 1000 K, making them ideal to study the region of interaction between disk, protostar, accretion and outflow. With the new generation of sensitive ground-based high resolution spectrometers for the 3-5 μm region an efficient window has been opened for the detailed study of the CO ro-vibrational lines toward embedded young stellar objects (YSO). The past generation of instruments was suitable to either observe a low resolution spectrum with a fairly wide spectral range (e.g. Teixeira et al., 1998) or a high resolution echelle spectrum with a very narrow spectral range (e.g. Carr et al., 2001). The main exception are the Fourier Transform Spectroscopy (FTS) observations of Mitchell et al. (1988, 1990), who observed a number of high-mass stars in the entire M band at high spectral resolution ($R > 10^6$), but such studies are limited to the brightest objects. VLT-ISAAC has a large instantaneous spectral range in the M-band (0.237 μm), which combined with a medium resolution of $R = 5\,000 - 10\,000$ and a limiting magnitude of $M \sim 10$ allows the entire fundamental band of gaseous CO of a wide range of young stars to be observed in a short time, including low mass stars down to a few tenths of a solar mass in the nearest star-forming clouds.

The embedded stars studied so far in CO ro-vibrational bands have showed mostly lines in absorption (Boogert et al., 2002, 2000; Mitchell et al., 1990) implying that the warm CO gas is seen in front of a bright infrared continuum, produced by hot dust close to the central object. The fundamental CO lines are usually only seen in emission towards more evolved sources characterized by a class II type spectrum where a circumstellar disk is directly visible (Blake et al., 2002; Carr et al., 2001). CO overtone bandhead emission at 2 μm has been observed in emission toward a few intermediate mass pre-main sequence stars (Najita et al., 1996; Thompson, 1989) and T Tauri stars (Carr, 1989), and has been associated with hot gas ($T \sim 1\,500 - 5\,000$ K) located within a fraction of an AU in a Keplerian disk.

We present here the peculiar 4.5-4.8 μm spectrum of the illuminating source IRS1=Elias 21 of the bipolar reflection nebula GSS 30 located in the core of the ρ Ophiuchus molecular cloud at a distance of 160 pc. It has been classified as a low mass class I YSO from its spectral energy distribution (SED) (Elias, 1978;

Grasdalen et al., 1973; Wilking et al., 1989) and low bolometric luminosity ($L_{bol} = 21 - 26 \, L_\odot$, Bontemps et al., 2001; Greene et al., 1994). Extensive polarimetric studies in the H and K band of the reflection nebula have shown that the source is surrounded by a large ($\sim 2\,000$ AU) disk-like envelope and a smaller circumstellar disk of ~ 150 AU, which are inclined about $25°$ away from the plane of the sky, i.e. close to edge-on (Chrysostomou et al., 1996, 1997). The high degree of linear polarization (up to 50%) as well as the presence of circular polarization imply that the light coming from the reflection nebula must have been multiply scattered, before heading into the line of sight.

Two other sources (IRS2 and IRS3) are present toward the K-band reflection nebula (within $20''$ of IRS1). IRS2 has a class III SED and is probably a more evolved star (André & Montmerle, 1994). IRS3 has a class I SED, but is much fainter than IRS1 in the near-infrared. It has a bolometric luminosity of $0.13 \, L_\odot$, (Bontemps et al., 2001). IRS3 shows strong 6 cm emission (see Leous et al., 1991, where IRS3 is designated LFAM 1).

The presence of a molecular outflow has not been firmly established. High velocity red- and blue-shifted CO millimeter emission to the south of GSS 30 has previously been reported by Tamura et al. (1990), but since both lobes are located to the south of the infrared source, the gas is likely to be associated with the VLA 1623 jet, which is passing only $30''$ to the SW of IRS1. Using millimeter interferometric line data, Zhang et al. (1997) find evidence for a spherical expansion of the core surrounding the three sources in GSS 30. In addition, the inner region of the core seems to be cleared, which is indicative of a young outflow. This is additionally supported by the presence of variable unbound water maser emission from within $0''\!.3$ of IRS1 (Claussen et al., 1996).

6.2 Observations

The observations of GSS 30 IRS1 were carried out using the long wavelength (LW) medium resolution mode on the Infrared Spectrometer And Array Camera (ISAAC) mounted on the Very Large Telescope (VLT-UT1) at the Paranal Observatory on September 3, 2001. The detector for 3-5 μm observations is a $1K \times 1K$ Aladdin InSb array, which allows a spectral coverage of 0.237 μm per setting in the M-band with a spectral resolution of up to $R = 10\,000$. The detector resolution in the spatial direction in the spectroscopic modes is $0''\!.148$/pixel. The spectrum of this source was taken as a part of a large program to study ices and gas around young low mass stars (van Dishoeck et al., 2001).

The data were obtained under excellent photometric conditions in service mode with $\sim 0''\!.3$ infrared seeing and $\lesssim 10\%$ humidity which gave a very stable atmosphere. The frames were both chopped and nodded along the slit with a $15''$ chop throw. The $0''\!.6$ slit was used in two settings for 20 minutes per setting yielding a final signal to noise ratio on the continuum of the extracted spectrum ranging from 50 to more than 100 over a spectral range from 4.5 μm to 4.82 μm and with a spectral resolution of $R = 5\,000$.

The standard star BS6084 (B1III) was observed at air masses between 1.2 and

1.5 immediately before GSS 30 for removal of telluric features, while the source was observed at air masses between 1.5 and 2.1. Because the source was already descending at the time of observation, it was not possible to observe source and standard at the same airmass as is otherwise of importance in order to obtain a good telluric subtraction. However, due to the exceptional stability of the atmosphere through most of the night we were able to correct for the airmass difference using a simple Lambert-Beer law, which states that the depth of the atmospheric lines scales exponentially with the airmass. The final corrected spectrum turned out to be of acceptable quality in spite of the airmass difference. Our experience is that it is crucial to use a B star or an early A star as the standard because many narrow intrinsic stellar lines become visible in the 3-5 μm region for spectral resolutions better than ~ 1000 if an F or later type star is used.
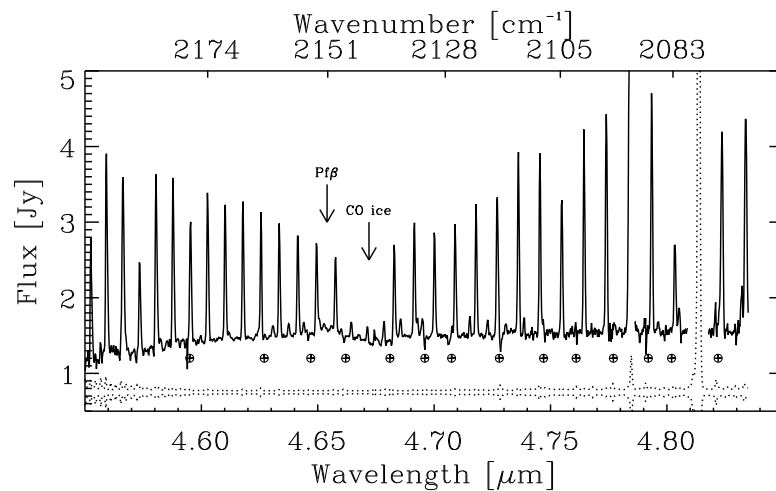
Figure 6.1: *The VLT-ISAAC M-band spectrum of GSS 30 IRS1 at $R = 5\,000$. The statistical (3σ) error is shown below the spectrum. Note that this error does not take the systematical errors introduced by variable telluric absorption into account which dominate in some parts of the spectrum. Since the peaks in the statistical error indicate deep atmospheric absorption they can be used to locate where telluric residuals might be interfering with the intrinsic spectrum. The telluric residuals which are exceeding the noise are marked with a $\oplus$ and are seen to correlate well with the peaks in statistical error.*

The spectrum was reduced with IDL routines using standard methods appropriate for chopped and nodded infrared spectroscopy. Bad pixels were removed, the frames were distortion corrected using the telluric features in a star-trace map as reference, and AB nodded pairs were subtracted to remove the long time scale differences which the chopping is not capable of removing. The spectra were extracted by integrating over a spatial width determined by the positions along the slit where the signal drops below the 3σ level. The raw spectrum was then ra-

tioed by the standard after applying an optimized shift and airmass correction. In the final spectrum, the points where telluric residuals are apparent have been removed, including the region short-wards of 4.55 μm, where atmospheric CO_2 lines render the spectrum useless. The final result is shown in Fig. 6.1.

The CO ro-vibrational lines in the spectrum are red-shifted with $\sim$ 20 km s^{-1} due to the systemic velocity of the Earth relative to the source, which means that there is a significant overlap between intrinsic CO lines and telluric absorption by CO. In spite of this, the telluric division is very good, especially when taking the unfavorable air masses of source and standard into account. A few residuals from telluric ^{12}CO absorption are visible and are marked in the final spectrum. Since the resolution of our spectra is 60 km s^{-1}, none of the features in the source are unaffected by the telluric lines. At higher resolution ($R > 20\,000$) the telluric lines may saturate, thereby forcing a division by zero when ratioing with the standard and resulting in a loss of information in the affected pixels. At sufficiently high resolution, this will not be a problem since the narrow telluric lines will often be completely offset from the intrinsic lines. However, at a resolution of 5 000, the typical telluric line has a depth which is only a fraction of the intrinsic continuum allowing a significant signal to be present in the standard spectrum even in the center of a telluric line and only very few lines are partially or completely lost due to saturated telluric lines.

By measuring the strength of the small residuals from telluric lines of species not intrinsically present in the source spectrum, the systematic uncertainty in the source lines is estimated to be less than 15%. The statistical uncertainty for the brightest lines is typically a few %, while the faintest lines are 3σ detections. The spectrum was wavelength calibrated relative to the telluric lines and flux calibrated relative to the standard star. The wavelength calibration of high resolution M band spectra is very accurate due to the large number of telluric lines, and a conservative estimate for the precision is $\sim$ 5 km s^{-1} over the entire spectrum. Indeed, the standard deviation of the line center velocities given in Table 6.1 is 4.2 km s^{-1}. Due to the difference in airmass between standard and source, we estimate the systematic uncertainty in absolute flux calibration to be $\sim$ 30%. Since the bright lines are typically most severely affected by telluric residual, all line fluxes have total uncertainties with values between 15 and 50%. The exact uncertainty for each line is difficult to estimate and we consequently adopt a value of 30% for all lines.

6.3 Results

6.3.1 Signatures of hot CO gas

It is evident that the M-band spectrum of GSS 30 is dominated by strong emission lines from the ro-vibrational (v=1–0) transitions of ^{12}CO gas. R- and P-branch lines within the observed spectral range are detected up to J=15 and J=18, respectively. The lines are all unresolved at a resolution of $R = 5\,000$, which gives an upper limit to the intrinsic line width of 30 km s^{-1}. No apparent decrease in line intensity is seen towards higher rotational quantum numbers, so observ-

ing the source in the entire M-band will clearly detect more lines. The brightest lines reach peak fluxes of more than 200% of that of the continuum. However, since none of the lines are resolved, this is only a lower limit to the peak flux. Fainter detected features include ^{13}CO v=1–0 lines as well as ^{12}CO v=2–1 lines. The fact that the observed gas has a population excited to the second vibrational level already indicates that the gas is at least warmer than a few hundred K. The ^{12}CO v=1–0 lines have intensities of order 2×10^{-13} erg s^{-1} cm^{-2}, the ^{13}CO v=1–0 and ^{12}CO v=2–1 lines being 1-2 orders of magnitude fainter. The line fluxes of all unblended lines were extracted by fitting a gaussian as well as a first order polynomial to the local continuum. After subtraction of the continuum, the fluxes were derived by integrating the spectrum in a 3σ region around the line.

The extracted fluxes of all unblended lines are given in Table 6.1. Many of the faint lines are completely blended with the bright lines, but it was still possible to extract 12 ^{13}CO v=1–0 lines and 4 ^{12}CO v=2–1 lines, which is sufficient to constrain the most important parameters of the emitting gas.

In addition to the CO emission lines, a faint 4.67 μm CO ice feature is visible. Since the feature is partly filled by the bright ^{12}CO P(1) line it is not possible to obtain a well-defined ice profile. For the same reason the affected emission line is not included in the analysis and modeling. There is also a very broad (FWHM $\sim$ 500 km s^{-1}), 4.65 μm Pfund β hydrogen recombination line visible, although with the bright CO lines superposed.

Finally the H$_2$ $0 - 0$ S(9) line is detected with an integrated line flux of $2 \pm 1 \times 10^{-14}$ erg s^{-1} cm^{-2}, signifying the presence of hot (> 1000 K) molecular hydrogen or possibly shock-excited gas.

6.3.2 Size of the emitting region

In order to determine the parameters of the line emitting gas unambiguously, the size of the emitting region must be known. The FWHM of the continuum in the spatial direction is about $0.''5$, which is consistent with the seeing throughout the observation. However, the lines appear to be spatially resolved, although most of the line flux is centered on the source. The wings of the spatial profile of each line extend up to $2''$ away from the central source along the slit. This is illustrated in Fig. 6.2, which shows the normalized average of the spatial profile of the lines, with the normalized average of the continuum profile subtracted. It is evident that the line emission is resolved and detected to a distance of more than 320 AU from the central source. There is also an indication that the northern part of line emission is stronger than the southern part, which agrees with the morphology seen in the L-band image of IRS1 shown in Fig. 6.3.

This extension suggests that the line emission is associated with the scattering nebula and is not coming directly from the central source. Since the continuum is less spatially extended than the line emission, the line emitting region appears to be spatially distinct from the continuum emitting region. Possible interpretations are that the line emission can be coming from gas present in the bipolar lobes (e.g. an outflow), from resonance scattering of continuum emission or from scattering of lines emitted closer to the star. Each of these possibilities will be discussed in

Table 6.1: *Integrated CO line fluxes toward GSS 30 IRS1*

Transition	Line flux $[10^{-13}$ erg cm^{-2} s^{-1}]	Heliocentric velocity [km s^{-1}]
^{12}CO v=1–0		
$R(0)$	1.16	-16
$R(1)$	1.27	-13
$R(2)$	1.64	-11
$R(3)$	1.74	-11
$R(4)$	1.69	-10
$R(5)$	2.08	-11
$R(6)$	2.16	-11
$R(7)$	2.49	-10
$R(8)$	2.10 [a]	-5
$R(9)$	2.78	-10
$R(10)$	3.14	-14
$R(11)$	1.46 [a]	-4
$R(12)$	3.85	-14
$R(13)$	3.42	-14
$P(2)$	1.59	-11
$P(3)$	1.58	-11
$P(4)$	1.62	-12
$P(5)$	1.73 [a]	-12
$P(6)$	1.94	-8
$P(7)$	2.76 [a]	-3
$P(8)$	2.84	-9
$P(9)$	2.42	-10
$P(10)$	2.16	-8
$P(11)$	2.95	-2
$P(12)$	3.37	-4
$P(14)$	3.40	-7
^{12}CO v=2–1		
$R(6)$	0.08	-17
$R(7)$	0.10	-12
$R(8)$	0.10	-14
$R(9)$	0.07	0
^{13}CO v=1–0		
$R(3)$	0.19	-11
$R(4)$	0.18	-11
$R(5)$	0.24	-14
$R(6)$	0.29	-11
$R(10)$	0.30	-15
$R(11)$	0.43	-14
$R(12)$	0.23	-14
$R(13)$	0.27	-10
$R(16)$	0.17 [a]	-15
$R(17)$	0.23	-3
$R(18)$	0.19	-19
$R(21)$	0.02	-15

[a] This line is severely affected by telluric residual.
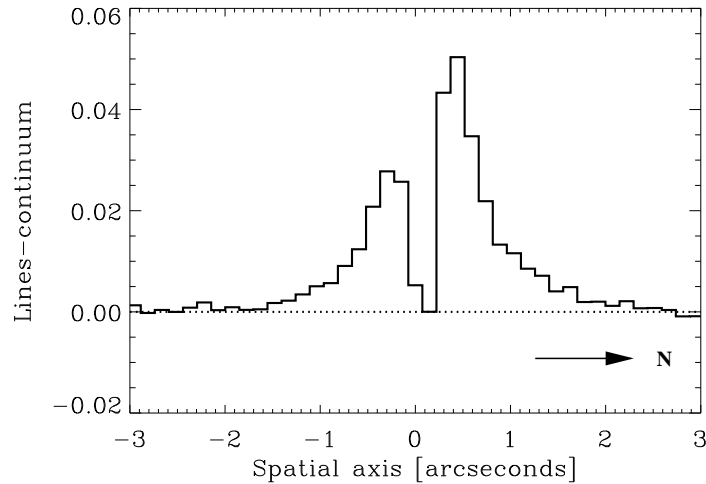
Figure 6.2: *Spatial cross section of the resolved line emission. The spatial distribution of the emission (along the slit) is shown averaged over all ^{12}CO v=1–0 lines with the continuum spatial profile subtracted. The line spatial profile was normalized to the continuum profile to show that the lines are detected over a larger region than the continuum. The direction to the north on the sky is indicated on the figure.*

detail below as the size of the emitting region depends strongly on the scenario.

6.4 Models

6.4.1 Optically thin LTE models

As a simple first approximation, the extracted line intensities were fitted with a one-temperature optically thin LTE model. The molecular data were taken from the HITRAN database (Rothman et al., 1998) and the relative line intensities were calculated directly from a Boltzmann level population distribution. The two parameters of the model, the gas kinetic temperature and the CO column density, should be well constrained in the optically thin limit. If only the ^{12}CO v=1–0 transitions are used, an optically thin model is to some extent degenerate in the two parameters. This degeneracy is due to the fact that the populations in the vibrationally excited levels are much more sensitive to temperature changes in the $400 - 800$ K range than the rotational level populations. Since lines from two species are available, the degeneracy is broken. It is reasonable to assume that the emission from both species is coming from the same mass of gas, and that the ^{12}C/^{13}C-ratio is close to 60 (e.g. Bensch et al., 2001).

This model is not able to provide a good fit to the entire line spectrum. However,
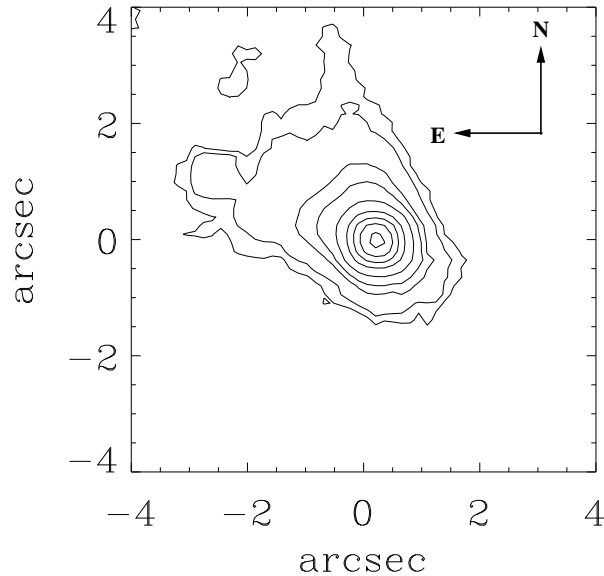
Figure 6.3: *The 3.21 μm acquisition image of the reflection nebula surrounding GSS 30 IRS1. The north-eastern lobe is clearly visible and also extended emission from the south-western lobe is resolved. The slit was centered on $(0,0)$ and directed north-south. The contours are roughly logarithmic with the lowest contour at values two orders of magnitude smaller than the highest contour.*

from Fig. 6.4 it is evident that the faint ^{13}CO v=1–0 and ^{12}CO v=2–1 lines can be simultaneously fitted with a single temperature gas in the optically thin limit. The model lines of ^{12}CO v=1–0 are however an order of magnitude too bright. Excluding the ^{12}CO v=1–0 lines from the fit yields a well-constrained temperature of 515 ± 25 K and a total ^{12}CO column density of $4 \pm 1 \times 10^{14}$ cm^{-2}. Since the fit includes lines from both CO isotopic species, we conclude that it is unlikely that the apparent discrepancy between the ^{12}CO v=1–0 and ^{13}CO v=1–0 lines is due to a deviation from the normal interstellar ratio. The simplest explanation is that the ^{12}CO v=1–0 lines are optically thick, while the rest remain optically thin. This would conveniently prevent us from seeing the whole column of ^{12}CO and could possibly lower the line intensities enough to explain the data. However, the fundamental ro-vibrational transitions of ^{12}CO do not produce optically thick lines for column densities less than $\sim 10^{17}$ cm^{-2}, which is still 250 times more than the simple model dictates. Thus the optically thin LTE model is internally inconsistent.
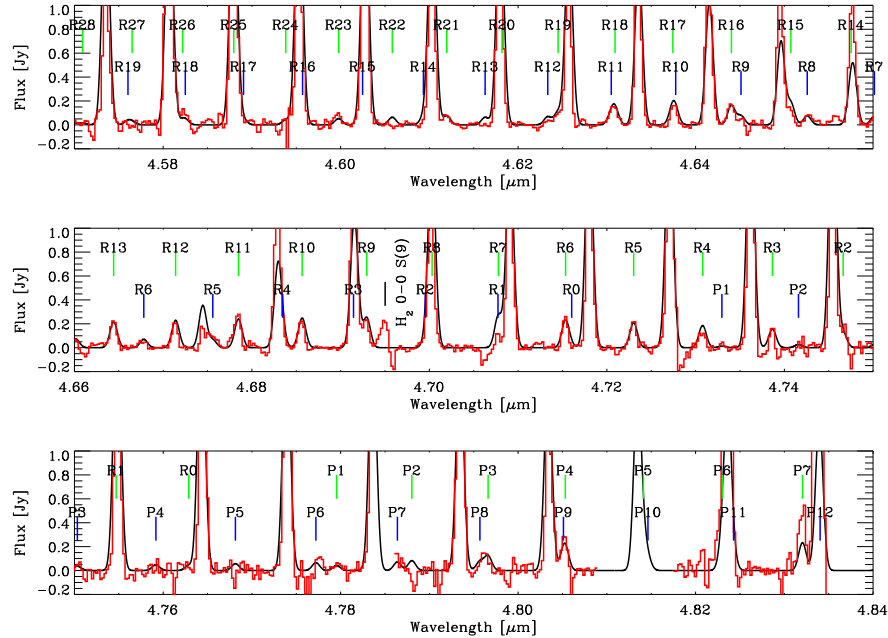
Figure 6.4: *Continuum subtracted spectrum of GSS 30 IRS1. Top row of line identifications show the ^{13}CO v=1–0 lines. Bottom row of identifications show the ^{12}CO v=2–1 lines. The data have been over-plotted with the optically thin LTE model spectrum. The model ^{12}CO v=1–0 line fluxes have been divided by a factor of 7 for clarity and to illustrate the optical depth effects.*

6.4.2 Results of the full radiative transfer model

In order to quantify the discrepancy more accurately, we computed the full radiative transfer for a single temperature static envelope in LTE. For simplicity a spherical geometry was assumed since the results are not very sensitive to geometry. The size and density of the emitting region cannot be constrained by the model, so the quantities fitted were the single gas temperature and the column density of the gas, by keeping the size fixed at the observed 4″.

Furthermore, it is assumed that the line intensity is independent of the underlying continuum. This last assumption may not be completely valid, since the CO lines could be present in absorption in the continuum before the lines from the emitting gas are superposed. The effect of this would be to lower the line peak flux with maximally the continuum flux level. Since the lines are completely unresolved, the true peak flux of the lines is higher than that observed. The observed peak flux of the ^{12}CO v=1–0 lines is 2–3 times higher than the continuum flux, so we conclude that this effect can only effectively lower the intensity of these lines with a small fraction at most. The fainter lines can be significantly suppressed by absorption in the continuum if they are optically thick, but this would only
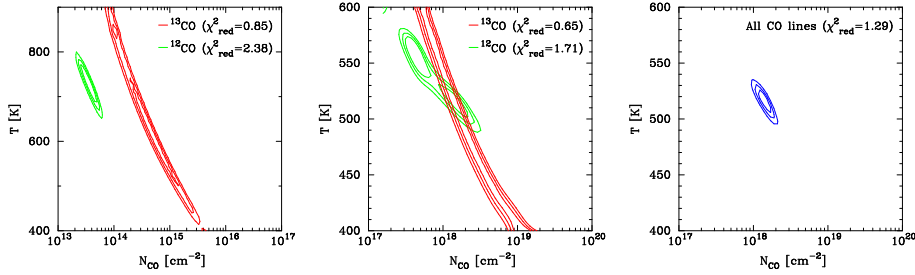
Figure 6.5: χ^2 *maps of the best fitting models. Left panel: the ^{12}CO v=1–0 and ^{12}CO v=2–1 lines plotted against the ^{13}CO v=1–0 lines without the assumption of scattering, in which case the sets of well-fitting parameters do not overlap. Middle panel: χ^2 contours for the ^{12}CO v=1–0 and ^{12}CO v=2–1 lines over-plotted by contours for the ^{13}CO v=1–0 lines, but now with a scattering factor $\epsilon = 1.4 \times 10^3$. Right panel: The weighted sum of the two χ^2 maps from the middle panel. The contours show in all the maps the 1, 2 and 3σ levels.*

increase the discrepancy between the bright and faint lines. Also, if the absorption lines are significantly broader than the superposed emission lines, the observed line intensities could be sufficiently suppressed. However, since we have no possibility of constraining this with the present data, we assume that the possible absorption lines and the emission lines have similar intrinsic widths, i.e. the contribution from absorption in the continuum is negligible. Higher resolution spectra may clarify the matter.

The ^{13}CO v=1–0 lines were first fitted independently of the ^{12}CO v=1–0 and ^{12}CO v=2–1 lines. The model confirms that the two sets of lines cannot be fitted simultaneously, although each set is consistent with a single temperature gas. There is a certain degeneracy in the two free parameters, especially in the ^{13}CO lines, and the model gives a one-dimensional family of good fits for each species. However, the two families do not overlap for the observed line intensities. Fitting the ^{12}CO v=1–0 and the ^{12}CO v=2–1 lines simultaneously yields poorer fits than fitting them separately. All the lines are in the extreme optically thin limit with typical values of $\tau \simeq 10^{-3}$ for the ^{12}CO v=1–0 lines. The discrepancy between the ^{12}CO v=1–0 and ^{12}CO v=2–1 lines may be due to non-LTE effects, reflecting that the rotational temperature $T_{\rm rot}$ and the vibrational temperature $T_{\rm vib}$ are not equal. However, non-LTE effects cannot explain why the ^{12}CO v=1–0 to ^{13}CO v=1–0 line ratios differ with almost an order of magnitude from the predictions of the simplest LTE model, since the excitation structures of different isotopic species must be almost identical.

To explain the data, we propose that all the observed line emission has been scattered by dust in the bipolar cavity seen in the near-infrared. The scattering efficiency is very low at 4.7 μm, and thus only a small fraction of the original line emission will be scattered into the line of sight. This means that the line intensities from the emitting region and consequently the column densities can reach much larger values than those previously suggested by the model. To test

this hypothesis, we adopted a factor, $\epsilon = S \times (\pi R^2)/\Omega$, which accounts for our lack of information about the true solid angle of the emitting region Ω, and the ratio of intrinsic line flux to line flux scattered into the line of sight, S. R is the observed angular radius of the emitting region, which is taken to be $R = 2''$. Absolute upper and lower bounds to the size of the emitting region are given by the natural conditions $S > 1$ and $\Omega < \pi R^2$. Decreasing the size of the emitting region will increase the column densities, but since line emission is observed far from the source, we cannot explain the entire discrepancy with a smaller emitting size. To recover the original flux it is necessary to multiply the observed values with this factor. Multiplying all observed line intensities with a sufficiently large factor will allow the ^{12}CO v=1–0 lines to become optically thick. We are able to constrain the scattering factor in the model by demanding a simultaneous fit to all the lines.

The best fitting value of the scattering factor is $\epsilon = 1.4 \times 10^3$ with a reduced χ^2 of 1.29, which gives a well-constrained single temperature LTE gas at 515 ± 5 K and $N(CO) = 1.5 \pm 0.5 \times 10^{18}$ cm^{-2}, as indicated in Table 6.2. With an extent of the emitting region of $4''$ an upper limit to the total gas mass of 200 M$_\oplus$ is found. Since the total gas mass scales with $\Omega^{0.5}$ an absolute lower limit to the mass is 1.3 M$_\oplus$ with a diameter of the emitting region of $0.19'' = 30$ AU, assuming that $S = 1$ and ignoring that line emission is observed to much larger distances from the central source. Since S must be significantly less than unity, the total mass is most likely significantly larger than the lower limit. It is not necessary to invoke any non-LTE effects to obtain a nearly perfect fit to all the observed lines and the assumption of LTE holds such that $T_{\rm rot} = T_{\rm vib}$. The χ^2 maps of the best-fitting models are shown in Fig. 6.5.

It is possible to make an estimate for an absolute lower limit to the grain size by assuming $S = 1$. In this case the scattering efficiency, $Q_{\rm sca} > \epsilon$, since it is not possible to scatter more light into the line of sight than out of it. This happens for silicate grain sizes larger than 0.2-0.3 μm (Draine, 1985; Draine & Lee, 1984). As a consequence the grains must be large, perhaps as large as 1 μm, which is expected for grain growth in dense media (Pendleton et al., 1990). On the other hand, the lower limit on the size of the scattering grains does not fit with the polarization maps of the GSS 30 nebula. Chrysostomou et al. (1996) finds that grains larger than 0.35 μm are inconsistent with the variation of linear polarization with wavelength. However, the polarization was mapped on a much larger angular scale than the size of the nebula at 4.6 μm, so the discrepancy may be explained by grain growth within a few hundred AU of the central source.

6.4.3 Other scenarios and pumping mechanisms

One way of avoiding the scattering assumption entirely may be to apply a two-temperature model to the data. In this scenario a small part of the gas close to the central source with a kinetic temperature of ~ 1000 K would be responsible for the ^{12}CO v=2–1 lines as well as part of the high J lines of the v=1–0 lines, while a massive outer component at ~ 200 K would dominate the emission in the low J lines. The scattering assumption would not be needed since the ^{12}CO v=1–0 lines require a much higher column density to create the observed line intensity

Table 6.2: *Best fitting models for GSS 30 IRS1*

Model	Lines used	T [K]	N(CO) [cm^{-2}]	Red. χ^2
Optically thin direct calculation	^{13}CO v=1–0 + ^{12}CO v=2–1	500 ± 25	$4 \pm 1 \times 10^{14}$	1.4
Full radiative transfer	^{13}CO v=1–0	degenerate	degenerate	0.85
Full radiative transfer	^{12}CO v=1–0 + ^{12}CO v=2–1	725 ± 50	$2.5 \pm 1 \times 10^{13}$	2.38
Full radiative transfer with scattering	All	515 ± 10	$1.5 \pm 0.5 \times 10^{18}$	1.29

at 200 K compared to 500 K and will thus more readily become optically thick. We applied a two-temperature model by requiring that the total column density must be the same as that determined by the single-temperature model. This is reasonable because the optical depth of the lines is given by the ratio between the ^{12}CO and ^{13}CO lines independently of ϵ and therefore must be conserved. As in the single-temperature model three parameters are varied, namely the two temperatures and the ratio of the column density between the components. In other words, ϵ is exchanged as a free parameter with a second temperature, thus keeping the number of free parameters constant.

The ^{13}CO lines can be fitted well within the two-temperature model, although the parameters are somewhat degenerate in the same way as in the single temperature model. However, it was not possible to fit the ^{12}CO lines within this scenario, with the best reduced χ^2 being of order 10. Furthermore there is a preference towards a single low temperature in the ^{12}CO lines which is inconsistent with the ^{13}CO lines. Inclusion of all lines gives no meaningful fits within the parameter space. The explanation is that it is not possible to combine the ^{12}CO v=2–1 and the ^{12}CO v=1–0 lines, since the high temperature component easily produces too much v=1–0 emission in order to fit the v=2–1 emission. We conclude that a two-temperature model is clearly inferior to the scattering model in explaining the observed line emission.

Radiative pumping by a strong infrared continuum is another possibility that needs to be considered as an alternative excitation mechanism and a way to avoid the scattering scenario by introducing non-LTE effects. This would produce a single vibrational temperature (Scoville et al., 1980). However it does not explain why the rotational and vibrational temperatures seem to be identical. Also, luminosities larger than 10^3 L$_\odot$ are required to effectively pump CO molecules to the second vibrational level or higher at distances from the central source beyond 1 AU (Scoville et al., 1980). Using the 1-dimensional Monte-Carlo radiative transfer code from Schöier (2000) illustrates the effects of radiative excitation on the line populations. The simplest possible model for radiative excitation assumes a blackbody with a luminosity $L = 25$ L$_\odot$ at the center of a single density spherical and static envelope . The blackbody temperature is taken to be the colour temperature of the continuum around 4.7 μm, determined from the M-band spectrum to 420 K. The radius used is the observed 320 AU, the gas kinetic temperature is assumed to be a power law beginning at the surface of the central source. The molecular constants are taken from Schöier et al. (2002). This leaves the gas density as the only free parameter, which basically determines the optical depth of the lines and consequently the importance of line trapping effects. The model calculations show that a density of at least $n_{H_2} \sim 10^6$ cm^{-3} is needed to reproduce the approximate flux level of the ^{12}CO v=1–0 lines. The vibrational excitation temperature is largely determined by the continuum flux level at 4.7 μm and therefore by the luminosity and to a smaller extent the temperature of the radiating source. Since the dominating mechanism for populating the v=2 level is via the v=1 level, and since both the v=2–1 and v=1–0 transitions are placed in the same narrow wavelength region, the radiative excitation rates are strongly dependent on local photon density in the 4.7 μm region. Consequently, as long as the direct route

Table 6.3: *Hydrogen recombination lines observed in GSS 30 IRS1*

Transition	Line intensity [erg cm^{-2} s^{-1}]	FWHM [km s^{-1}]	Mass loss rate [M$_\odot$ year^{-1}]
Pfβ	$1.3 \pm 0.5 \times 10^{-13}$	450 ± 50	1.7×10^{-6}
Brα	$1.6 \pm 0.2 \times 10^{-13}$	$\lesssim 500$	0.8×10^{-6}
Pfδ	$6.0 \pm 1.0 \times 10^{-14}$	$\lesssim 500$	1.8×10^{-6}

through the v=2–0 overtone transitions around 2.35 μm is not important, the vibrational level population depends on the temperature of the input radiation field only through the flux level at 4.7 μm. At the adopted luminosity, the ^{12}CO v=2–1 line fluxes are two orders of magnitude too low, reflecting an excitation temperature of 400 K. To significantly populate the second vibrational levels, a luminosity of at least 10^3 L$_\odot$ is required, in agreement with Scoville et al. (1980). Finally, the population of the rotational levels shows significant departures from a Boltzmann distribution, especially when line trapping becomes important. Altogether, this indicates that radiative pumping as an excitation mechanism in the case of GSS 30 IRS1 is unlikely.

Finally, the possibility that the lines are continuum emission which is resonance scattered in CO transitions should be considered. It is known that this takes place in the case of asymptotic giant branch stars, e.g. in the case of Mira (Ryde & Schöier, 2001). However, since this mechanism probes the scattering gas rather than the emitting medium, it will not solve the discrepancy. Also it would require that the gas at a distance of 320 AU from the central source has a single temperature of 500 K, which seems highly unlikely.

6.4.4 Hydrogen recombination lines and mass loss rate

There are a number of hydrogen recombination lines common to YSOs (Pfβ, Brα, Pfδ) present in the 3-5 μm region, which are usually taken as an indicator of accretion activity. This is particularly true in the case of low mass young stars, where the hard radiation from the boundary layer between disk and star is needed to produce the ionizing radiation, since the central star is not hot enough. Because these lines have broad wings ($3-500 \, \text{km s}^{-1}$), they are often interpreted as coming from a strong stellar wind, which may be the engine of an outflow. The possibility that the CO gas could be associated with a wind or molecular outflow should therefore be explored. If associated with a stellar wind, the lines could be formed either as cooling emission from the gas as molecules are reformed or as emission from a shock as the wind collides with the circumstellar envelope or disk. It is known that no large scale outflow is present which could be produced by any of the three stars in the cluster, but there is some evidence of an expanding core surrounding the cluster from interferometric observations of rotational ^{13}CO and C^{18}O lines (Zhang et al., 1997).

Hydrogen recombination lines emitted from a plasma moving at supersonic speeds can be modeled in the Sobolev approximation (Sobolev 1960), which is

valid when the thermal line broadening is much smaller than the wind speed. This formalism has been treated for spherical ionized winds in LTE from evolved stars in Castor (1970) and Krolik & Smith (1981), and for Herbig AeBe stars in Nisini et al. (1995). Using this formalism an ionized mass loss rate can be estimated for the star if a wind origin for the hydrogen lines is assumed. The extinction corrected line intensities for the hydrogen recombination lines observed in GSS 30 IRS1 are tabulated in Table 6.3 along with the mass loss rates derived from each line. The line ratios and the mass loss rate are not sensitive to the temperature, so a constant electron temperature of 10^4 K has been assumed. Finally, it is assumed that the central star does not shadow a significant part of the radiation from the wind. Changing the model parameters, i.e. the temperature and the size of the ionized region, with a factor of two changes the mass loss rate with a factor of two at most. The velocity structure is such that the wind starts at the surface of the star with 20 km s^{-1} and rises quickly to 450 km s^{-1} to fit the observed FWHM of the Pfβ line. The exact shape of the velocity structure is otherwise not significant for the derived mass loss rate.

We find that an ionized mass loss rate of 1.7×10^{-6} M$_\odot$ year$^{-1} = 0.6$ $M_\oplus$ year^{-1} is consistent with the two observed Pfund lines. The Brα line is too faint for this mass loss rate, which may indicate deviations from LTE. We can rule out that it is an effect from a poor extinction correction since the Brα line lies between the Pfβ and Pfδ lines in wavelength. The most serious problem with this model is likely that very little is known about the structure of winds from low mass embedded YSOs; in particular, the ionization structure will depend directly on energetic processes which are poorly understood, such as accretion activity or interactions of the circumstellar matter with strong magnetic fields. Also, if the wind is predominantly neutral, then the total mass loss rate will be much higher than the ionized mass loss rate and will become inconsistent with the non-detection of an outflow. It is possible that other mechanisms such as accretion flows must be considered for the formation of recombination lines from low mass young stars. The hydrogen lines are therefore not likely to provide any strong constraints on the emitting CO gas and a detailed discussion on the hydrogen emission is outside the scope of this chapter.

6.5 Discussion

In summary, to determine the origin of the CO gas emission it must be explained why only a single well-defined temperature is needed. Which mechanism can heat up to 100 M$_\oplus$ of gas to a unique temperature of 500 K, yet keep the intrinsic line width less than 30 km s^{-1}? Finally, why is no other similar embedded source from the literature showing the same strong CO rovibrational emission as GSS 30 IRS1?

6.5.1 Outflow?

If the warm CO gas resides in the wind/outflow component of the circumstellar environment then an estimate of the time needed to create it can be found from the

mass loss rate derived in Section 6.4.4 under the assumption that the wind is predominantly ionized. A mass between 3 and 100 $M_\oplus$ corresponds to a production time of minimally 5 years and maximally a few centuries, while the most likely time is about one century. It seems unlikely that hot, ionized material emitted over a longer period should thermalize at a single temperature. Also, an outflow origin of the line emission would produce broad wings in the lines, which is not observed. If the wind is predominantly neutral, the resulting mass loss rate would be so high that a clear outflow should have been detected.

6.5.2 Inner disk?

Another possibility is that the emission is produced by warm thermalized gas in the disk itself. Since more evolved T Tauri disks are known to exhibit similar CO emission, although with smaller intensities, it is conceivable that we are seeing an equivalent process in the case of a younger disk. A typical circumstellar disk around a low mass young star is often observed to have a mass of a few times the minimum solar nebula, i.e. $M_{disk} \sim$ a few 0.01 $M_\odot$ (André & Montmerle, 1994; Osterloh & Beckwith, 1995). The disk mass for GSS 30 IRS1 inferred by the 1.3 mm continuum emission is $M_{disk} = 0.03\ M_\odot$ (André & Montmerle, 1994). In hydrostatic equilibrium, a disk irradiated by the central star has a surface density $\Sigma \sim R^{-3/2}$ (Chiang & Goldreich, 1997). If viscous dissipation in the disk is taken into account the surface density attains a flatter R-dependency, $\Sigma \sim R^{-1}$. In both cases the accumulated disk mass reaches the observed $10 - 100\ M_\oplus$ between 2 and 10 AU from the central star. A single temperature of 515 K is however not consistent with the disk models, which prescribe a large range in temperatures with a small 1000-2000 K component within a few stellar radii to an extended 100-200 K component within a few AU of the central star. However, in no models for passive circumstellar disks is it expected that the disk exhibits a single temperature, indeed quite the contrary is the case. Furthermore, Keplerian rotation within a few AU would produce observable line broadening. The narrow lines could only be explained if we are seeing light emitted vertically from the plane of the disk before being scattered into the line of sight, effectively removing the effects of rotation.

6.5.3 Accretion shock?

A final option is that the emission lines are cooling lines from post-shocked dense gas. Vibrational H_2 emission is one of the principal tracers of low density ($n_{H_2} \lesssim 10^7$ cm^{-3}) shocked gas. As mentioned in Section 6.3.1 the (0–0) S(9) line of H_2 at 4.695 μm is seen in our M-band spectrum, while no H_2 lines are seen in the K-band spectrum of GSS 30 IRS1 by Greene & Lada (1996) although no upper limit is given. Assuming that the observed H_2 (0–0) S(9) line is thermalized at the CO temperature, the required molecular gas mass is $5\ M_\oplus$. This is assuming that the H_2 emission is seen directly and is not corrected for extinction, since the extinction is hard to estimate for embedded stars. A typical Ophiuchus extinction of $A_V = 25$ mag (Teixeira & Emerson, 1999) will increase the molecular gas mass

by a factor of 2. If the emission in the H_2 line is scattered in the same way as the CO emission all values must be multiplied by ϵ. If the H_2 emission is thermalized at 515 K and directly observed then the integrated line flux expected for the 2.12 μm (1–0) S(1) line is 7.5×10^{-13} erg cm^{-2} s^{-1}, which should be observable. If the H_2 lines are scattered into the line of sight with an efficiency of ϵ, then no H_2 lines should be visible in the M-band. Consequently, the H_2 line does not seem to be directly associated with the same gas emitting the CO lines since it is at least a factor of 10 too bright, but it may be an indication of a warmer component or the line may be pumped. Sensitive observations of H_2 lines in the K and L band are needed to unambigously determine the origin of the molecular hydrogen emission.

Neufeld & Hollenbach (1994) show that if a dense gas of $10^{7.5} < n_{H_2} < 10^{12}$ cm^{-3} is shocked, the vibrational emission from H_2 is significantly suppressed partly because the shock dissociates the H_2 molecules and partly because the reforming molecules can easily be collisionally de-excited in the dense post-shock gas. The main coolants will be rotational and vibrational lines from H_2O, OH and CO. This is valid for a wide range of shock velocities $5 < v_s < 100$ km s^{-1} as long as the shock is of jump-type. A J-shock occurs in any case for $v_s \gtrsim 30$ km s^{-1} and for smaller shock velocities if the magnetic field is weak or if the length scale over which the shock occurs is small compared to the length scale for acceleration of charged particles. Furthermore, the theoretical post-shock temperature structure gives an interesting prediction. A J-shock will dissociate the gas at the shock front. The gas then cools slowly from 10^5 K principally through the Lyα-line until CO forms at around 7000 K and $N(HI) \sim 10^{21}$ cm^{-2}. Once the CO molecules are available the gas cools quickly to about 500 K through the CO vibrational lines, where a constant temperature plateau is maintained due to the release of chemical potential energy as H_2 is formed which is balanced against the thermalized vibrational emission from molecules. The plateau occurs at an atomic hydrogen column density of $10^{21} - 10^{22}$ cm^{-2}, which in the model by Neufeld & Hollenbach (1994) corresponds to a CO column density of $3 \times 10^{17} - 3 \times 10^{18}$ cm^{-2}. It is stressed that the slower C-shock scenario was not treated in such high density models, and it may produce similar cooling lines. Further modelling is needed to exclude a slow shock. It is evident that the model values are remarkably similar to the values observed in GSS 30 IRS1 with temperature $T_{gas} = 515$ K and column density $N(CO) = 2 \times 10^{18}$ cm^{-2}. However, it is unclear why no hot $5000 - 7000$ K component in the fundamental CO band is observed, which is also expected from the shock. Also no overtone emission is seen in the K-band spectrum of Greene & Lada (1996). One plausible explanation is that the accretion activity is highly variable and that the hot component is only seen as the shock is occurring while the warm thermalized gas is seen in the post-shock medium. This would be supported by the variable water maser emission. The single observed H_2 line is not inconsistent with an accretion shock although it is too bright to be associated with a dense shocked gas and may only be an indication of a warmer less dense component.

As described in Neufeld & Hollenbach (1994), the most likely site for a dense shock in an embedded YSO is in a circumstellar disk which is accreting matter.

When infalling matter is colliding with the disk at supersonic velocities, a J-shock is expected to occur at the surface of the disk. If the accretion velocities are too low to produce a J-shock, the molecules will not be dissociated and the observed temperature plateau will not be present. The main uncertainty is if the high infall velocities required to create a dissociative shock are possible. However, infall velocities of 10 km s^{-1} within 10 AU are reasonable (Cassen & Moosman, 1981). Therefore, if the dissociative accretion shock scenario holds, the intrinsic line widths are *predicted* to be larger than or very close to 10 km s^{-1}. An accretion shock at a large distance ($\gtrsim$ 10 AU) from the central star is consistent with the observation that the line emitting region is physically separated from the continuum emitting region. A shock will not heat a large amount of dust and the continuum emission, which has a colour temperature of about 700 K, is likely to be produced by irradiated dust within 1 AU of the star.

Other observable tracers of a shock in a dense medium are the rovibrational lines from the H$_2$O ν_2 bending mode around 6 μm as well as the vibrational transitions of OH, all of which are unavailable from ground-based instruments. However, they may be detected by the upcoming Stratospheric Observatory For Infrared Astronomy (SOFIA) mission.

The possible dissociation of the molecules has important consequences for the chemistry in the inner disk. If the emission is indeed coming from an accretion shock, and if a significant amount of matter passes through the shock, it will significantly affect the models of chemical evolution of the innermost parts of disks around low mass YSOs, by evaporating ice mantles and inducing high temperature chemistry.

6.6 Summary

In this chapter, we have analyzed the 4.5-4.8 μm spectrum of the embedded young stellar object GSS 30 IRS1 in the ρ Ophiuchus core. The observed emission lines from the rovibrational transitions of CO are fitted with a simple full radiative transfer 1D model. It is found that the line emission must be scattered on a bipolar cavity in order to simultaneously account for the size of the observed emitting region, the absolute flux level of the lines and the ratio of ^{12}CO to ^{13}CO lines. In this case the emission is well fitted by a single temperature gas with $T = 515 \pm 5$ K and a column density of $N(\mathrm{CO}) = 2 \pm 0.5 \times 10^{18}$ cm^{-2}. Furthermore, assuming a two-temperature distribution of the gas does not yield satisfactory fits.

The observed emission line spectrum can be best explained by the presence of a J-shock in a dense medium, although other possible scenarios cannot be ruled out. Most likely the shock is produced by the accretion of gas onto a dense disk within a few tens of AU from the star as predicted by Neufeld & Hollenbach (1994). Only this scenario explains why a large amount of CO gas is thermalized at a single temperature of $\sim$ 500 K and why the emission lines are so narrow.

Acknowledgements

Bibliography

André, P. & Montmerle, T. 1994, ApJ, 420, 837

Bensch, F., Pak, I., Wouterloot, J. G. A., Klapper, G., & Winnewisser, G. 2001, ApJ, 562, 185

Blake, G. A., Boogert, A. C. A., & Kessler, J. 2002, ApJ, in prep

Bontemps, S., André, P., Kaas, A. A., et al. 2001, A&A, 372, 173

Boogert, A. C. A., Hogerheijde, M. R., & Blake, G. A. 2002, ApJ, 568, astro-ph/0112163

Boogert, A. C. A., Tielens, A. G. G. M., Ceccarelli, C., et al. 2000, A&A, 360, 683

Carr, J. S. 1989, ApJ, 345, 522

Carr, J. S., Mathieu, R. D., & Najita, J. R. 2001, ApJ, 551, 454

Cassen, P. & Moosman, A. 1981, Icarus, 48, 353

Castor, J. I. 1970, MNRAS, 149, 111

Chiang, E. I. & Goldreich, P. 1997, ApJ, 490, 368

Chrysostomou, A., Clark, S. G., Hough, J. H., et al. 1996, MNRAS, 278, 449

Chrysostomou, A., Ménard, F., Gledhill, T. M., et al. 1997, MNRAS, 285, 750

Claussen, M. J., Wilking, B. A., Benson, P. J., et al. 1996, ApJS, 106, 111

Draine, B. T. 1985, ApJS, 57, 587

Draine, B. T. & Lee, H. M. 1984, ApJ, 285, 89

Elias, J. H. 1978, ApJ, 224, 453

Grasdalen, G. L., Strom, K. M., & Strom, S. E. 1973, ApJ, 184, L53

Greene, T. P. & Lada, C. J. 1996, AJ, 112, 2184

Greene, T. P., Wilking, B. A., André, P., Young, E. T., & Lada, C. J. 1994, ApJ, 434, 614

Krolik, J. H. & Smith, H. A. 1981, ApJ, 249, 628

Leous, J., Feigelson, E. D., André, P., & Montmerle, T. 1991, ApJ, 379, 683

Mitchell, G. F., Allen, M., Beer, R., et al. 1988, ApJ, 327, 17

Mitchell, G. F., Maillard, J.-P., Allen, M., Beer, R., & Belcourt, K. 1990, ApJ, 363, 554

Najita, J., Carr, J. S., Glassgold, A. E., Shu, F., & Tokunaga, A. T. 1996, ApJ, 462, 919

Najita, J. R., Edwards, S., Basri, G., & Carr, J. 2000, in Protostars and Planets IV (The University of Arizona Press), 457

Neufeld, D. A. & Hollenbach, D. J. 1994, ApJ, 428, 170

Nisini, B., Milillo, A., Saraceno, P., & Vitali, F. 1995, A&A

Osterloh, M. & Beckwith, S. V. W. 1995, ApJ, 439, 288

Pendleton, Y. J., Tielens, A. G. G. M., & Werner, M. W. 1990, ApJ, 349, 107

Reipurth, B. & Aspin, C. 1997, AJ, 114, 2700

Rothman, L. S., Rinsland, C. P., Goldman, A., et al. 1998, J. Quant. Spectrosc. Radiat. Transfer, 60, 665

Ryde, N. & Schöier, F. L. 2001, ApJ, 547, 384

Schöier, F. L., Ryde, N., & Olofsson, H. 2002, A&A, accepted, astro-ph/0206078

Schöier, F. L. 2000, PhD thesis, Department of Astronomy, Stockholm University

Scoville, N. Z., Krotkov, R., & Wang, D. 1980, ApJ, 240, 929

Tamura, M., Sato, S., Suzuki, H., Kaifu, N., & Hough, J. H. 1990, ApJ, 350, 728

Teixeira, T. C. & Emerson, J. P. 1999, A&A, 351, 292

Teixeira, T. C., Emerson, J. P., & Palumbo, M. E. 1998, A&A, 330, 711

Thompson, R. I. 1989, ApJ, 344, 799

van Dishoeck, E. F., Dartois, E., Thi, W. F., et al. 2001, in The Origins of Stars and Planets, ed. J. Alves & M. McCaughrean (Springer Verlag), astro-ph/0110465

Wilking, B. A., Lada, C. J., & Young, E. T. 1989, ApJ, 340, 823

Zhang, Q., Wooten, A., & Ho, P. T. P. 1997, ApJ, 475, 713

Chapter 7

Projection of circumstellar disks on their environments

Abstract

We use a 2D Monte Carlo radiative transfer code to study the projection of large shadows by circumstellar disks around young stellar objects on surrounding reflection nebulosity. It is shown that for a wide range of parameters a small (10-100 AU) circumstellar disk can project a large (1 000-10 000 AU) dark band in the near-infrared that often resembles a massive edge-on disk. The disk shadows are divided into two basic types, depending on the distribution of the reflecting material and the resulting morphology of the shadows in the near-infrared. Two YSOs associated with bipolar nebulosity, CK 3/EC 82 illuminating the Serpens Reflection Nebula (SRN) and Ced 110 IRS 4 in the Chamaeleon I molecular cloud, are modelled in detail as disk shadows. Spectral energy distributions of the two sources are collected using both archival ISO data and new Spitzer-IRS data. A 2D model consisting of a small disk and a spherically symmetric envelope can reproduce the near-infrared images and full spectral energy distributions of the two disk shadow candidates. It is shown that the model fits can be used to constrain the geometry of the central disks due to the magnifying effect of the projection. The presence of a disk shadow may break a number of degeneracies encountered when fitting to the SED only. Specifically, the inclination, flaring properties and extinction toward the central star may be independently determined from near-infrared images of disk shadows. Constraints on the disk mass and size can be extracted from a simultaneous fit of SEDs and images. We find that the CK 3 disk must have a very low mass in opacity-producing, small ($\lesssim 10 \, \mu$m) dust grains (corresponding to a gas+dust mass of $\sim 7 \times 10^{-6} \, \mathrm{M_\odot}$) to simultaneously reproduce the very strong silicate emission features and the near-infrared edge-on morphology. Ced 110 IRS 4 requires that a roughly spherical cavity with radius $\sim 500 \, AU$ centered on the central star-disk system is carved out of the envelope to reproduce the near-infrared images. We show that in some cases the bipolar nebulosity created by a disk shadow may resemble the effect of a physical bipolar cavity where none exists. We find that a disk unresolved in near-infrared images, but casting a large disk shadow, can be modelled at a level of sophistication approaching that of an edge-on disk with resolved near-infrared images. Selection criteria are given for distinguishing disk shadows from genuine large disks. It is found that the most obvious observable difference between a disk shadow and a large optically thick disk is that the disk shadows have a compact near-infrared source near

the center of the dark band. High resolution imaging and/or polarimetry should reveal the compact source in the center of a disk shadow as an edge-on disk. Finally, it is shown that disk shadows can be used to select edge-on disks suitable for observing ices located inside the disk. [1]

7.1 Introduction

The strong near- and mid-infrared excess measured from T Tauri and Herbig Ae/Be stars is generally regarded as strong evidence that these young stars are still surrounded by remnants of the accretion disks from which they were formed. Indeed, the infrared spectral signatures from these disks agree well with those theoretically expected for such 'protoplanetary disks' (Adams et al., 1987; Chiang & Goldreich, 1997; Dominik et al., 2003; Kenyon & Hartmann, 1987). However, direct evidence for the disk-like nature of this circumstellar matter is still scarce, and some indications to the contrary are troubling. For instance, interferometric observations of Herbig Ae/Be stars in the near-infrared by Millan-Gabet et al. (2001) and Eisner et al. (2003) have shown that the sources are larger than expected for thermal emission from a disk extending all the way to the central star. Although this is possibly due to gaps in the inner disk or scattering of the near-infrared photons into the line of sight from the disk surface, it illustrates the difficulties in unambiguously determining the geometry of circumstellar material. So far, perhaps the most compelling evidence for the disk-like nature of circumstellar material within a few 100 AU of a star is given by the optical and near-infrared images of edge-on disks (Padgett et al., 1999) and spatially resolved kinematic evidence from molecular line observations (e.g. Mannings & Sargent, 1997). In these images, in particular those of Padgett et al., bright bipolar reflection nebulae feature a conspicuous 'dark lane'. This dark lane is seen whenever the disk is close to edge-on. It is due to obscuration of the bright inner regions by the dark outer parts of the disk. If a bright background illumination is present (e.g. McCaughrean & O'Dell, 1996), the silhouette of the disk clearly indicates the extent and shape of the disk itself. However, when the only illuminating source of the circumstellar matter is the central star, the disk appears as a dark lane without a clear outer edge. These images allow one to detemine the geometric thickness and the minimum radius of such disks.

There may, however, be another possibility to produce a 'dark lane' signature. Hodapp et al. (2004) suggested that the bipolar morphology of the young star ASR 41 in the NGC 1333 molecular cloud is caused by the shadow of a much smaller disk projected on an envelope reflecting the light from the central star. The general possibility of disks casting shadows much larger than their size is also clear from the models by Whitney et al. (2003).

In this paper we discuss the possibility that a circumstellar disk around a young star may commonly project a large shadow onto the matter surrounding the system to produce a broader range of morphologies of reflection nebulae than that already proposed by Hodapp et al. (2004). We have selected two young stars that

---

[1]K. M. Pontoppidan and C. P. Dullemond, to be submitted

probably cast disk shadows on associated reflection nebulosity; CK 3 of the Serpens reflection nebula and Ced 110 IRS 4 in the Chamaeleon molecular cloud, and we model them in detail using a Monte Carlo radiative transfer code.

This article is organised as follows: §7.2 defines the scenarios which are expected to produce disk shadows. §7.3 describes the imaging and spectroscopy for the two disk shadow candidates which have been collected to constrain the models. The radiative transfer model is treated in §7.4. In §7.5 and §7.6, the two disk shadow candidates and the best fitting radiative transfer models are described. Finally, selection criteria for distinguishing between genuine disk shadows and large massive edge-on disks are discussed in §7.7.

7.2 Scenarios

In this section, the basic geometry of shadows cast by circumstellar disks is explored. In particular, we divide disk shadows into two basic types, based on the distribution of circumstellar, reflecting material. Quantitative aspects of the two types are discussed in the context of specific objects in §7.5 and §7.6.

In principle, an extended shadow that is visible to an observer should be produced whenever the disk is fairly close to edge-on ($> 60°$) and enough dusty matter surrounds the star-disk system to produce scattering nebulosity in the near-infrared. Another requirement is that the disk mid-plane is optically thick to near-infrared photons. The shadow of such a disk may be arbitrarily large, depending only on the extent of the illuminated nebula and not on the actual physical extent of the disk itself. It will create a bipolar morphology, which may resemble the 'dark-lane' signature of edge-on disks seen in absorption. Typically, a 100 AU disk can thereby produce a dark lane of 10^3 to 10^4 AU in a reflection nebula of similar size. If the reflecting matter *completely surrounds* the star-disk system, the shadow will acquire a symmetric wedge-like shape. This happens because only photons emitted at angles larger than the opening angle of the disk survive to be scattered on the envelope material. The wedge-like disk is likely the most common configuration, and will be referred to as 'scenario 1'. ASR 41 was shown by Hodapp et al. (2004) to be a likely 'scenario 1' candidate.

Shadows that are not wedge-shaped can be cast if a 'screen' of matter is present close to the disk. For instance, if the disk projects its shadow onto a nearby optically thick background cloud, it will have the shape of a straight dark band, very similar to what is usually seen for edge-on disks, but much larger than the size of the disk. A similar effect is seen if the star has carved out a central cavity (spherical or cylindrical) out of its circumstellar envelope. In this case the walls of the cavity act as a screen. If the envelope is not too optically thick, then the shadow can still be seen through the envelope and produce a dark band on the sky. We refer to such screen projection shadows as 'scenario 2' cases. 'Scenario 2' shadows are characterised by cavities or unevenly distributed material. Such shadows may exhibit a range of morphologies, depending on the configuration of the screen. Clearly, many young stars are illuminating nebulosity with a complex structure. Thus, axisymmetric envelope models may not always be sufficient. For

instance, this may be the case if the reflecting material is located preferably behind or in front of the illuminating star. In principle, shadows cast on reflecting material that is not axisymmetrically distributed cannot be modelled by the code used here. However, the simple geometrical principle is illustrated in Fig. 7.1. The example shown illustrates how a background 'screen' may produce a shadow completely offset from the illuminating star-disk system. In particular, it can be seen that a non-axisymmetric distribution of material is required to produce a shadow which is significantly offset from the central compact source. An axisymmetric distribution of envelope material with an inner cavity can be visualised by adding a foreground screen to Fig. 7.1 in addition to a background screen. In this case, two shadows, symmetrically offset from the central inclined star-disk system, are produced. These cases are likely common, since a 'scenario 2' disk shadow may be created for a wide range of inclinations as indicated by Fig. 7.1.

We have identified two new candidates for circumstellar disks which project a shadow on large reflection nebulae; one for each scenario. The 'scenario 1' candidate is the area of the Serpens reflection nebula that is illuminated by the star CK 3 (also known as EC 82 or SVS 2). The 'scenario 2' candidate is IRS 4, the brightest far-infrared source in the Cederblad 110 cloud in the Chamaeleon star-forming complex. We present detailed 2D Monte Carlo radiative transfer models that can reproduce the near-infrared morphological characteristics as well as the spectral energy distributions (SEDs) of the two candidates. We show how such models aided by the presence of a disk shadow can be used to gain unique insight into the structure of circumstellar disks too small to be resolved by imaging.

7.3 Observations

We use a range of both imaging and spectroscopic data to constrain the models. Archival JHK_s images from the Infrared Spectrometer And Array Camera (ISAAC) mounted on UT1-Antu of the Very Large Telescope (VLT) at Cerro Paranal in Chile have been extracted from the VLT archive[2]. The images were taken during moderate to good seeing conditions, resulting in infrared spatial resolutions of $\sim 0\rlap{.}''7$. One pointing obtained on May 3, 2001 is of the south-eastern core of the Serpens star-forming cloud, while the other obtained on April 29, 1999 is of the Cederblad 110 region in the Chamaeleon star-forming complex. The ISAAC images were reduced following standard procedures including dark subtraction, flat field division and flux calibration relative to 2MASS sources in the field. Due to the very extended near-infrared emission in the Serpens core, the background determination is somewhat uncertain in the Serpens imaging. This may cause the surface brightness to be underestimated for faint nebulosity. No corresponding problem was detected in the Cederblad 110 image.

In addition, mid-infrared spectrophotometry from the set of Circular Variable Filters on the Infrared Space Observatory Camera (ISOCAM-CVF) of Ced 110 IRS

---

[2]Based on observations made with ESO Telescopes at Paranal Observatory under programmes 63.I-0691, 164.I-0605 and 67.C-0600.
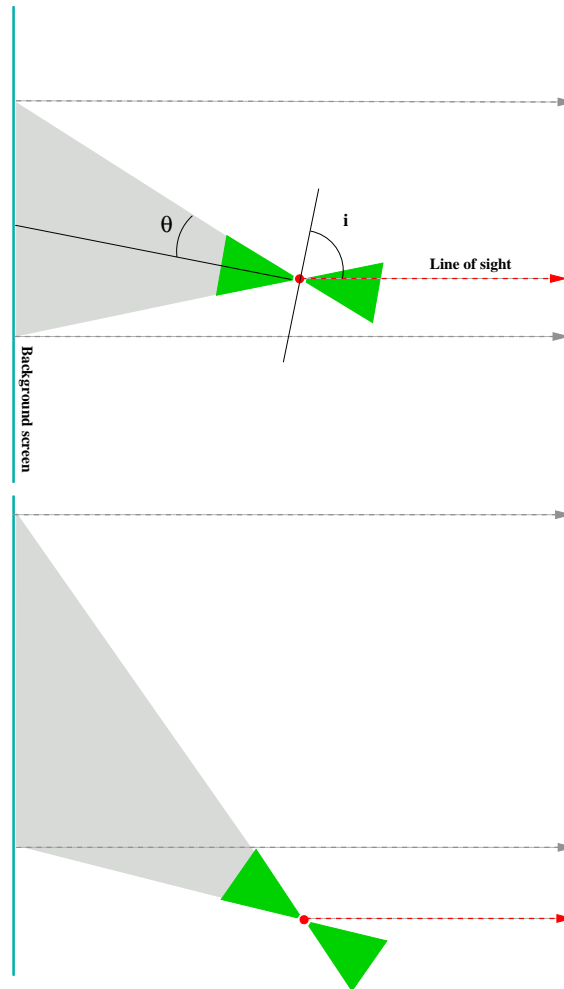
Figure 7.1: *Cartoon illustrating how a shadow completely offset from the illuminating star can be produced if the reflecting material is not distributed throughout the region surrounding the central star disk system. Note that the star is obscured only when it is offset from the shadow. The example shows the effect of material located entirely behind the illuminating source. A second shadow, offset in the opposite direction, is created if the material is located in front of the source. An axisymmetric cavity surrounding the central star-disk system conceptually creates a shadow composed of both a foreground and a background screen.*

4 was extracted from the ISO archive [3]. The ISOCAM spectral image was reduced using the Cam Interactive Analysis (CIA) package ver. DEC01 [4]. The CVF spectrum was extracted from a 3×3 pixel = $18'' \times 18''$ aperture. The spectral resolution is $\lambda/\Delta\lambda = R \sim 35$, but the spectrum as shown is smoothed to $R \sim 10$ to increase the signal-to-noise.

For CK 3, we use a a 5.2-37.2 μm spectrum obtained with the InfraRed Spectrograph (IRS) onboard the Spitzer Space Telescope as part of the 'From Molecular Cores to Protoplanetary Disks' Legacy programme (c2d) (Evans et al., 2003). The corresponding AOR key is 0009407232. The short-low module is used for the wavelength range 5.2-14.5 μm with a resolving power of 50-100, while the short-high and long-high modules are used for the ranges 9.9–19.6 μm and 18.8–37.2 μm, respectively, with a resolving power of ~ 600. The IRS spectrum was extracted from the S9.5.0 pipeline images using the extraction pipeline developed by the c2d team. The details of the IRS spectrum will be discussed in more detail in a later paper. The short-high and long-high modules have been scaled by up to 10% to match the short-low module flux. VLT-ISAAC L- and M-band spectra of CK 3 were obtained as part of a large survey of young low-mass stars (see van Dishoeck et al., 2003, and references therein). The reduction procedure of the ISAAC spectra is described in Pontoppidan et al. (2003). The spectra cover the wavelength ranges 2.85-4.2 μm and 4.55–4.90 μm in the L- and the M-band, respectively.

Near- and far-infrared photometric points were taken from the literature, specifically from Prusti et al. (1991), Hurt & Barsony (1996), Persi et al. (2001) and Lehtinen et al. (2001).

7.4 Radiative transfer models

We have modelled both 'scenario 1' and 'scenario 2' with the 2D Monte Carlo radiative transfer code RADMC (see Dullemond & Dominik, 2004). The code follows the photons in full 3D, but is restricted to an axisymmetric density structure. The same setup was also used to model the edge-on disk CRBR 2422.8-3423 (Pontoppidan et al., 2004a) (Chapter 5). Given an axisymmetric density structure, the code calculates the dust temperature and scattering source function at every geometric point in the model. Images at any wavelength can then be calculated by integrating the equation of radiative transfer along parallel lines of sight using the ray-tracing capabilities of the more general code RADICAL (Dullemond & Turolla, 2000). Model SEDs can be calculated by integrating the intensity inside synthetic 'observing' apertures at each wavelength. This is important when comparing photometric points observed using widely differing aperture sizes.

A system projecting a disk shadow is modelled using a small (~ 100 AU) disk embedded in a large dusty envelope (5 000-10 000 AU) that scatters the radiation

---

[3]In part based on observations with ISO, an ESA project with instruments funded by ESA Member States (especially the PI countries: France, Germany, the Netherlands and the United Kingdom.) and with the participation of ISAS and NASA.

[4]The ISOCAM data presented in this paper were analysed using "CIA", a joint development by the ESA Astrophysics division and the ISOCAM Consortium. The ISOCAM Consortium is led by the ISOCAM PI. C. Cesarsky.

from the central disk system. The envelope is assumed to have a radial density power law with index α_{env}. Embedded Young Stellar Objects (YSOs) are known from theoretical models of collapsing protostars (e.g. Shu, 1977) as well as from 1-dimensional radiative transfer model fits to millimetre wave emission (Jørgensen et al., 2002; Shirley et al., 2000) to have density profiles which can be approximated by a power law with a negative index of 1–2. However, we allow all power law indices in the model. This can be justified in the case of CK 3, which probably is a much more evolved source in the process of dispersing the last remnants of its envelope. Infall density profiles have also been used to model scattering in envelopes (Whitney et al., 2003).

The geometry of the model disks is given as follows:

$$\rho(R, Z) = \frac{\Sigma(R)}{H_p(R)\sqrt{2\pi}} \exp\left(-\frac{Z^2}{2H_p(R)^2}\right), \tag{7.1}$$

where $\Sigma(R) = \Sigma_{\text{disk}}(R/R_{\text{disk}})^{-p}$ is the surface density and

$$H_p(R)/R = (H_{\text{disk}}/R_{\text{disk}}) \times (R/R_{\text{disk}})^{2/7} \tag{7.2}$$

is the disk scale height. For $R < R_{\text{disk}}$, $p \sim 1$, while for $R > R_{\text{disk}}$, $p = 12$. The outer surface density profile is arbitrarily chosen to allow a smooth transition from disk to envelope. The ratio $H_{\text{disk}}/R_{\text{disk}}$ defines the disk opening angle, $\Theta_{\text{disk}} \equiv \tan^{-1}(H_{\text{disk}}/R_{\text{disk}})$. The structure of the model disk setup is described in further detail in Pontoppidan et al. (2004a) (Chapter 5). In addition to this basic disk structure, the presence of a puffed-up inner rim is allowed by increasing the disk scale height within a certain radius from the central star. The physical rationale for the presence of a puffed-up inner rim is that the disk is irradiated at an angle of 90°at the inner disk edge where the dust reaches its sublimation temperature. This causes the inner rim to attain a higher temperature and therefore a higher pressure scale height than that of a disk irradiated at a smaller angle (Dullemond et al., 2001) . The presence of a puffed-up inner rim creates an excess near-infrared flux which is often necessary to fit the observations both for intermediate mass Herbig Ae stars (Dominik et al., 2003; Natta et al., 2001) and for low mass T Tauri stars (Muzerolle et al., 2003). An additional effect of the inner rim, in the context of this work, is that it can produce additional shadowing. This may be important for CK 3 as described in §7.5.

A central spherical cavity of radius R_{cav} is carved out of the envelope. This cavity is constrained to have a radius equal to or exceeding that of the disk. No bipolar cavity is imposed, primarily because the two disk shadow candidates presented in this work do not strictly require it. Other sources may show signatures of both a bipolar cavity and a disk shadow at the same time. In the case that the cavity has a size similar to that of the disk, it has little influence on the near-infrared morphology of the shadow. A cavity much larger than the central disk produces a 'scenario 2' disk shadow by creating a screen at large distance from the central star.

A single grain size of 0.5 μm was used, since smaller grains mostly affect scattering properties at wavelengths shorter than 1 μm. The dust model is described

in detail in Pontoppidan et al. (2004a) (Chapter 5), but produces opacities similar to those for compact grains with an MRN-like size distribution by Ossenkopf & Henning (1994). Spherical silicate grains with inclusions of carbonaceous material are used. Ices are taken into account by adding an icy mantle consisting of mixed water, CO_2 and CO ices for temperatures below 90 K using an abundance of water ice of 9×10^{-5} relative to H_2. No parameter concerning the ice component was allowed to be free. The model output is sensitive to the exact choice of dust optical constants. However, to limit the number of free parameters in the model, the dust properties were fixed at a single set of optical constants. It is likely that the dust in the disk and envelope have differing optical properties due to grain growth effects and due to chemical differences (Wolf et al., 2003), however a detailed treatment of dust models is beyond the scope of this paper.

Because excessive computing time prevents the calculation of a grid of models covering the full parameter space, the fitting parameters were changed manually and the best fit evaluated by eye. It is therefore difficult to identify degeneracies in the model result. Yet, given a dust model, the main fitting parameters of disk and envelope mass, luminosity, inclination and the flaring opening angle of the disk are considered relatively robust. However, without the use of the near-infrared images, the model would be highly degenerate. Possible degeneracies will be discussed for the specific models.

7.5 CK 3

7.5.1 Observational characteristics

The Serpens reflection nebula is characterised by a bright central compact source (CK 3) surrounded by a reflection nebulosity several arcminutes in extent. The distance to Serpens was measured by Straizys et al. (1996) to 260 pc and to 220–270 pc by Knude et al., in prep. All distance dependent quantities for CK 3 are scaled to 250 pc. Near-infrared imaging polarimetry has shown CK 3 to be the illuminating source of most of the Serpens reflection nebulosity (Huard et al., 1997; Sogawa et al., 1997). The nebulosity is entirely bisected by a dark lane centered on CK 3. The angular extent of the lane is at least $35''$, which corresponds to more than 9000 AU. In the ISAAC images, the central source is extended in the H and K_s bands with deconvolved $FWHM$ of $0''5 = 125$ AU and $0''8 = 200$ AU, respectively. This may mean than the disk is resolved in the images, providing a lower limit to the physical disk size. The JHK_s colour composite image of CK 3 and the surrounding nebulosity is shown in Fig. 7.2. It is seen that the dark lane is shaped as two symmetric wedges with completely straight edges. The border between the dark lane and the nebulosity is unresolved at a spatial resolution of $\sim 0''6$. Sogawa et al. (1997) observed significant near-infrared variability of the nebulosity illuminated by CK 3 from 1991 to 1992 of up to 1 mag arcsec^{-2} in the H band. The strongest variation is observed along the dark lane. This is of particular interest to the disk shadow scenario, since the dynamical timescale of the inner disk suggested to be casting a shadow is on the order of days to years, while nebulosity at scales of 5 000–10 000 AU should have significantly longer dynamical

time scales. The implications of this for the model are further discussed in the next section.

We suggest that the dark band in the Serpens reflection nebula is a shadow of a much smaller disk surrounding CK 3. A real edge-on disk will tend to be shaped as a box with reflection nebulosity along the minor axis of the disk rather than a wedge. An example of such a disk is the Butterfly Nebula (Wolf et al., 2003). The sharpness of the edge of the dark band also resembles a shadow created by photons traveling in a straight line from the central star. A real disk may be expected to show some asymmetric structure on 10 000 AU scales. We propose that CK 3 and the associated Serpens reflection nebula are an example of a 'scenario' 1 disk shadow, i.e. a disk shadow cast into a spherically symmetric envelope.

An important question to explore is if the SED of the source as well as the near-infrared morphology can be fitted by a disk shadow model. The observed SED of CK 3 is shown in Fig. 7.3 including the 3–$5\,\mu$m VLT-ISAAC spectra and the 5.2–$37.2\,\mu$m Spitzer-IRS spectrum. The overall shape of the SED is that of a class II or flat spectrum source, typical of a young star surrounded by a disk. CK 3 is dominated in the mid-infrared by very bright emission features from silicates at 10 and $18\,\mu$m. Additionally, PAH emission features are seen at 3.3 and $6.2\,\mu$m and broad ($\sim 80\,\mathrm{km\,s^{-1}}$) ro-vibrational emission lines from warm, gaseous CO are observed around $4.7\,\mu$m, while shallow absorption bands from water and CO ices are evident at 3.08 and $4.67\,\mu$m. The shapes of the water and CO ice bands indicate that the ice is cold ($\lesssim 30\,$K). The far-infrared photometric points are taken from IRAS measurements by Hurt & Barsony (1996). Casali et al. (1993) only found an upper limit at $800\,\mu$m of 0.4 Jy. It should be cautioned that the Serpens core is a very confused region in the $60\,\mu$m IRAS beam of $1'$. The IRAS fluxes have been colour corrected to match the observed $\sim 30\,$K spectral slope with factors of 1.1 and 1.02 at 60 and $100\,\mu$m, respectively (see the IRAS explanatory supplement, Beichmann, 1985).

The wealth of emission features in the spectrum presents a challenge to a disk shadow model, since strong silicate emission is surprising from a highly inclined disk, given the expected large optical depth along the disk mid-plane. Assuming the silicate emission is coming from the inner 10 AU of the disk, the features can be explained only if the disk is optically thin to $10\,\mu$m photons along the line of sight. This requires the disk to be very tenuous, at least in small dust grains. Significant mass may be hidden in large, millimetre-sized dust grains, which are not probed in the mid-infrared. However, to create the near-infrared shadow, the disk must be optically thick to 1-$2\,\mu$m photons along the same line of sight. This puts severe constraints on the model disk structure, and in particular on the small grain dust mass.

7.5.2 Model of CK 3

The best-fitting parameters of the CK 3 model are given in Table 7.1 and the model temperature and density structure are shown in Fig. 7.4. The resulting model JHK_s colour composite is compared to the observed colour composite in Fig. 7.2.

Following the hypothesis that CK 3 is a 'scenario 1' disk shadow, the object is
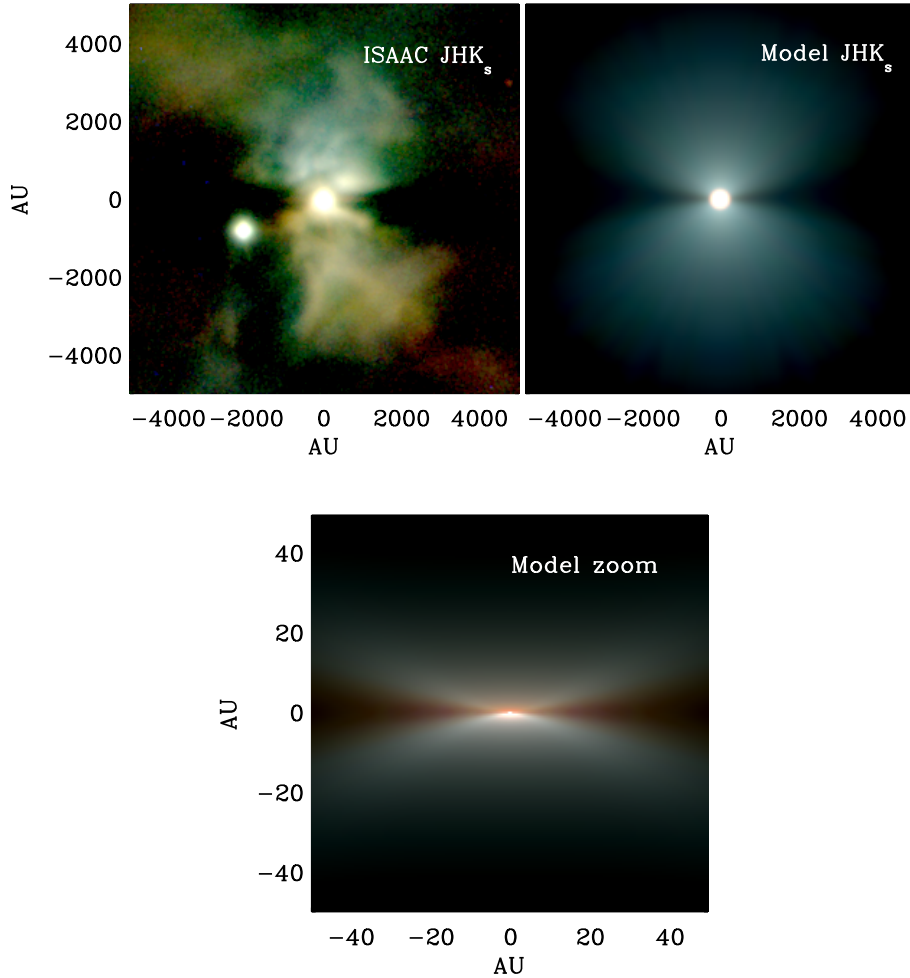
Figure 7.2: JHK_s *colour composites of the VLT-ISAAC images and the model of CK 3. All images have been constructed by assigning* $\log_{10}(F_{2.16\,\mu m})$, $\log_{10}(F_{1.6\,\mu m})$ *and* $\log_{10}(F_{1.25\,\mu m})$ *to the red, green and blue colour channels, respectively. The full colour images will be available in the published paper. Left panel: Observed ISAAC JHK_s colour composite. The observed image has been rotated by 47° east of north. Right panel: The best-fitting model of CK 3. The model has been convolved with a Gaussian with a $FWHM$ of $0.7''$ to match the observed image quality. Bottom panel: Zoomed-in view of the physical disk of the model on a 100 AU scale. The images are aligned with north pointing up and east to the left.*

modelled as a disk surrounded by an envelope extending inwards to the outer disk edge. The sudden increase in flux at wavelengths longer than $40\,\mu$m as evidenced by the SED (Fig. 7.3) indicates that the amount of warm dust in the envelope is small. This in turn requires a very flat density profile of the envelope. A
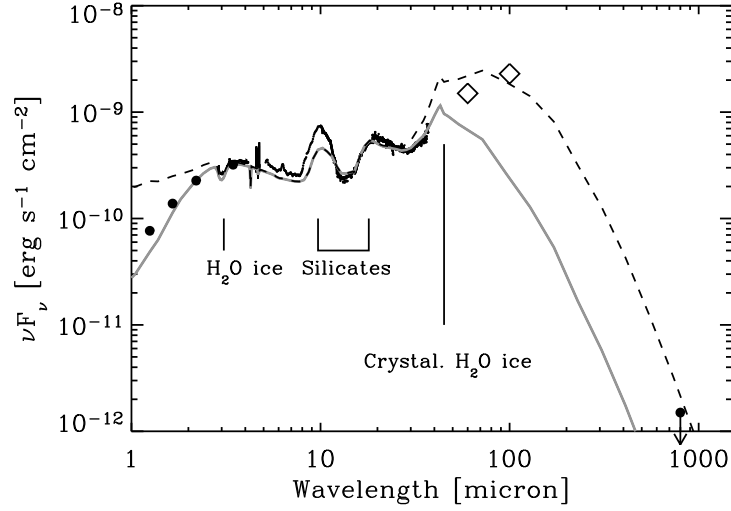
Figure 7.3: *The model fit to the observed SED of CK 3. The solid curve is the SED measured through an aperture of 5″, while the dashed curve is the SED measured through a 60″ aperture to match the IRAS photometric points (indicated by diamonds).*

Table 7.1: *Model parameters for the two disk shadow candidates*

	CK 3/EC 82	Ced 110 IRS4
$M_{\mathrm{disk}}[M_\odot]$	7.5×10^{-6}	3.5×10^{-5}
$M_{\mathrm{env}}[M_\odot]$	0.20	0.12
R_{cav} [AU]	140	530
$L_{\mathrm{bol}}[L_\odot]$	9.9	0.4
R_{env} [AU]	6000	4000
Incl. angle	77°	72°
T_{star} [K]	6500	4800
$M_{\mathrm{star}}[M_\odot]$	2.1	0.5
R_{disk} [AU]	140	35
α_{env}	-0.05	-1.5
$H_{\mathrm{disk}}/R_{\mathrm{disk}}$	0.3	0.28
$H_{\mathrm{rim}}/R_{\mathrm{rim}}$	0.07	0.29
p	0.8	1.0

nearly constant envelope density provides the best fit to the far-infrared SED and the extended emission seen in the near-infrared images (Fig. 7.2). The model fit to the near-infrared nebulosity is shown in quantitative terms in Fig. 7.5, where a cross section along the minor axis of the system is shown for each near-infrared band and in Fig. 7.6, which compares contours of modelled and observed images. It is seen that the reflection nebulosity contains a significant amount of clumpy structure at radii larger than $\sim 1000\,\mathrm{AU}$ which the model does not take into account. However, the power law envelope provides a reasonable fit to the underlying structure. The clumpy envelope structure is likely to affect the far-infrared SED by increasing the fraction of cold dust. Such structure cannot be accurately modelled by the current axisymmetric model setup, but may explain the relatively poor fit to the IRAS photometric points. The best-fitting envelope has a column density to the disk of $N(H_2) = 4 \times 10^{21}\,\mathrm{cm}^{-2}$ corresponding to an extinction of $A_J = 1.4\,\mathrm{mag}$. This is consistent with the observed column density in the 3.08 μm water ice band (Pontoppidan et al., 2004b), assuming an ice abundance of 9×10^{-5} relative to H_2.

The disk itself is modelled with $R_{\mathrm{disk}} = 140\,\mathrm{AU}$ and an outer scale height of $H_{\mathrm{disk}}/R_{\mathrm{disk}} = 0.3$. The physical property probed by the observed disk shadow opening angle is the angle relative to the disk plane at which the disk becomes optically thick to near-infrared photons. This depends on the vertical structure of the dust in the disk, the disk opening angle Θ_{disk} as well as the surface density profile $\Sigma(R)$ of the disk. The observed wedge-angle also depends on the disk inclination, getting smaller at lower inclinations. The edges of the shadow are only straight for high inclinations of more than $\sim 75°$. This effectively constrains the inclination to $> 75°$. At very high inclinations the near-infrared colours of the central source become too red, such that the best fit of the inclination is $77°$. The wedge shadow disappears completely for inclinations less than $90° - \Theta_{\mathrm{disk}}$. This means that a 'scenario 1' shadow is observed only when the line of sight to the central star passes through the disk. If the disk has a high optical depth then the star is fully obscured. For intermediate optical depths, which are still high enough to cast a shadow but low enough to allow some starlight to penetrate the disk, the star may still be seen through the disk. In the case of CK 3, the SED of the source can be fitted with a face-on disk and only the presence of a disk shadow fixes the inclination.

Therefore, in order to produce the bright silicate emission features (see Fig. 7.3) and at the same time maintain that the line of sight to the central star passes through the disk as given by the presence of a disk shadow, the extinction toward the inner parts of the disk must be very low. At the same time, the 1-2 μm optical depth must be higher than unity in order to cast the shadow. The assumed density structure in the disk (Eq. 7.1) then produces a very low total disk mass. Note, however, that the mass refers only to the mass in small dust grains. Effects such as dust growth or settling may produce similar effects for a more massive disk if most of the dust grains have grown to sizes $\gg 10\,\mu$m. Large dust grains tend to settle into the disk mid-plane (Dubrulle et al., 1995). Such 'pebble-sized' grains are not probed by the infrared observations. Yet, the strength of the silicate emission features indicates that grains much larger than $\sim 1\,\mu$m do not contribute to the
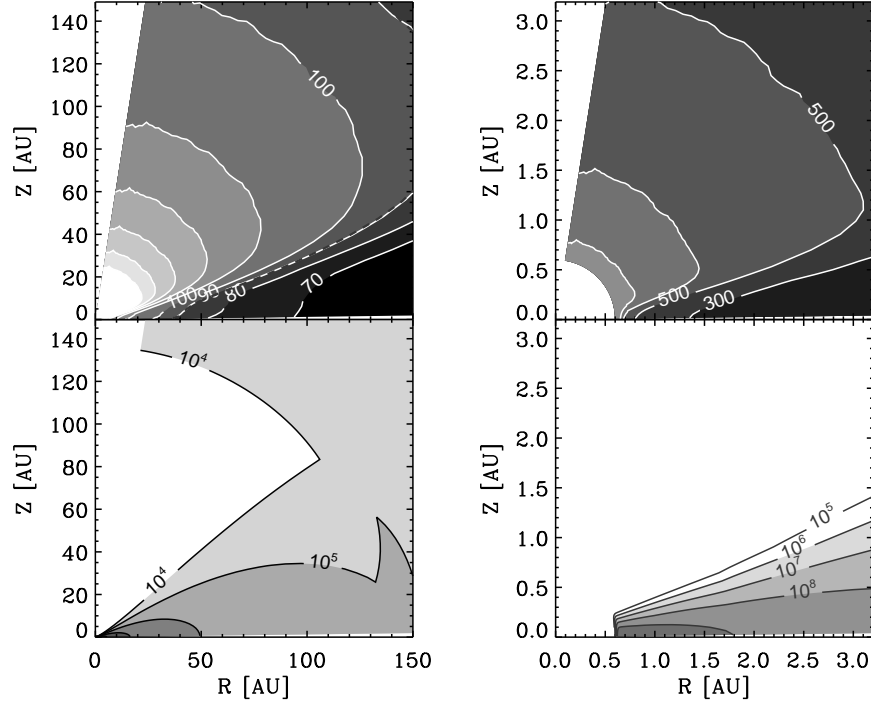
Figure 7.4: *Temperature and density structure of the CK 3 model. The top panels show the temperature in units of Kelvin and the lower panels show the density in units of cm^{-3}. The left panels show the entire disk, while the right panels show the inner parts of the disk.*

mid-infrared opacity of the warm dust. A dust grain size distribution dominated by larger (1–10 μm) grains suppress solid state features van Boekel et al. (2003). This means that if the disk has a dust mass much larger than that of the model, the average grain size distribution in the disk must be highly bimodal. For lack of observational constraints our model disks contain only small (0.5 μm) grains. But an additional population of very large (>cm) grains, perhaps even containing most of the total dust mass, may be assumed to reside in the midplane without having any effect on the resulting model images or SEDs. The best fit is obtained for a disk mass of 7.5×10^{-6} M$_\odot$, assuming a gas-to-dust ratio of 100 and 0.5 μm grains. This creates bright silicate emission features as well as a disk shadow. A more massive disk with a mid-plane that is optically thick at all mid-infrared wavelengths is able to produce at most 1/3 of the observed silicate line-to-continuum ratio, even when observed face-on. The unusual strength of the emission features is therefore strong evidence for a very tenuous, almost optically thin disk. The disk mid-plane between 50-150 AU has gas densities of $10^5 - 10^6$ cm^{-3} (Fig. 7.4). Again, if dust
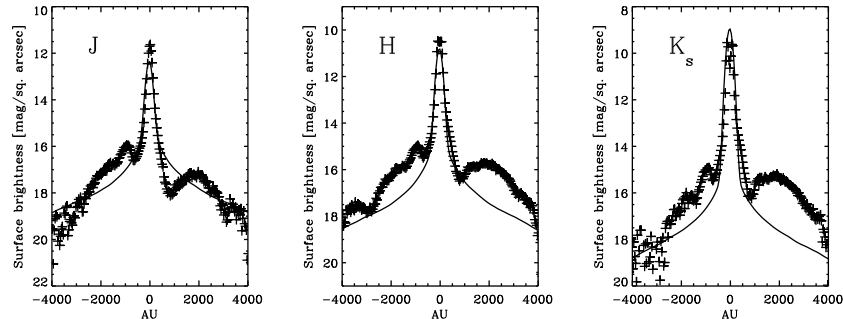
Figure 7.5: *Cross section along the minor axis of CK 3 in the different near-infrared wavebands. The curve shows the model, while the (+) symbols show the observed ISAAC surface brightness. Clumpy envelope structure not included in the model gives excess scattering at radii of $\sim 2000\,AU$.*

settling has taken place, the actual gas density in the disk may be higher. Interferometric observations of molecular gas-phase lines may answer this question. The strength of the silicate emission features as well as the depth of the shadow are dependent on the disk surface density profile. It is found that a surface density profile with $p = 0.8$ produces the strongest shadow and emission features. As a side effect of the low optical depth of the disk, the model spectrum shows strong emission from crystalline water at $45\,\mu$m, a band which unfortunately lies outside the coverage of Spitzer-IRS.

The model fit has some weaknesses, which are important to address. In the model the shadow is not completely dark because of the relatively low optical depth through the disk required by the silicate emission features. Alternatively, at high envelope densities or if large grains are present, the shadow can be filled out by multiple scattering, although this is not the case for the CK 3 model. The puffed-up inner rim may play in important role for the shadow of CK 3. Because the outer disk is so tenuous, the rim can provide a significant part of the column density producing the shadow. The shape and strength of the shadow is therefore very sensitive to the scale height of the puffed-up inner rim. In this context, it is intriguing that Sogawa et al. (1997) found the Serpens reflection nebulosity to be variable on timescales of up to a year. In this scenario, the opening angle and strength of the shadow may change dramatically accompanied by a strong variability in the 1-5 μm wavelength region of the SED. The spectral data may therefore not completely correspond to the ISAAC imaging, since the observations have been obtained at different epochs. The inner rim in the model has a temperature of 900 K in order to fit the shape of the 2-6 μm spectrum. As seen in Fig. 7.4, this corresponds to the presence of a gap in the disk with a radius of 0.6 AU. The location of the inner rim at this distance from the central star is consistent with a time scale of months for variations of the shadow produced by the inner parts of the disk. Other disk shadows may be variable on time scales ranging from days to years, depending on the size of the central dust gap. It is noted

that the observed width of the CO fundamental ro-vibrational emission lines in the ISAAC M-band spectrum of $\sim 80\,\mathrm{km\,s^{-1}}$ is consistent with gas at $\sim 1\,\mathrm{AU}$ in an edge-on disk in Keplerian rotation.

7.6 Ced 110 IRS 4

7.6.1 Observational characteristics

Ced 110 IRS 4 is a class I YSO embedded in the Cederblad 110 cloud of the Chamaeleon molecular cloud at a distance of 150 pc (Knude & Høg, 1998). The region contains a large scale outflow (Mattila et al., 1989). The source of the outflow has not been unambiguously identified, although both Ced 110 IRS 4 as well as the embedded protostar Cha MMS1 have been proposed (Reipurth et al., 1996). Recently, Lehtinen et al. (2003) determined that Ced 110 IRS 4 is a strong continuum radio source in the centimetre wavelength region and noted that this is evidence that IRS 4 is the source of the outflow. However, the outflow mapped in ^{12}CO by Prusti et al. (1991) is centered closer to the position of Cha MMS1 than that of IRS 4.

The VLT-ISAAC near-infrared image is shown in Fig. 7.7. From the near-infrared colours it is seen that the source is strongly reddened and is surrounded by a bipolar nebulosity which is intersected by a broad, dark lane (Zinnecker et al., 1999). The thickness of the lane in the north-south direction ($\sim 4.5'' = 675\,\mathrm{AU}$) relative to the width of lane ($\sim 1000\,\mathrm{AU}$) seems large for a physical disk. A compact source is seen near the center of the dark lane. The edges of the lane are sharp and unresolved at the $\sim 0.7''$ seeing of the ISAAC images. The outer edges of the reflection nebula also show a very steep decline, in particular the southern lobe. The northern lobe of the bipolar nebula is significantly more reddened than the southern lobe. The central source is observed to be extended measured relative to other stars in the field in the ISAAC H- and the K_s-bands with deconvolved $FWHM$ of 0.5''=75 AU and 0.4''=60 AU, respectively. The physical size of the reflection nebulosity of Ced 110 IRS 4 is about half that of the CK 3 nebula. The K_s-band surface brightness is similar, but the central source is clearly much more extincted. An obvious difference is the morphologies of the two dark bands; the dark band of Ced 110 IRS 4 is clearly not wedge-shaped as the band of CK 3 is.

The SED of Ced 110 IRS 4 is shown in Fig. 7.8. The source is bright at far-infrared to millimetre wavelengths as measured by ISOPHOT (Lehtinen et al., 2001), indicative of a significant amount of remnant envelope material. The SED is composed of near-infrared photometry of the central source (excluding the nebulosity), an archival ISOCAM-CVF 5-16 μm spectrum, ISOPHOT photometry at 80-200 μm as well as IRAS photometry and a 1.3 mm point from Prusti et al. (1991). The far-infrared points are very scattered and do not produce a very well-defined SED. This is probably due to source confusion as noted by Lehtinen et al. (2001). Specifically, Lehtinen et al. suggest that a previously unidentified far-infrared source designated IRS 11 is located about 30'' to the sout-east of Ced 110 IRS 4. Only the 80 μm point has the contribution from IRS 11 removed. Therefore, all photometric points which are blended are used as upper limits and the 80 μm and the 1.3 mm points are used to constrain the model. The ISOCAM spectrum shows
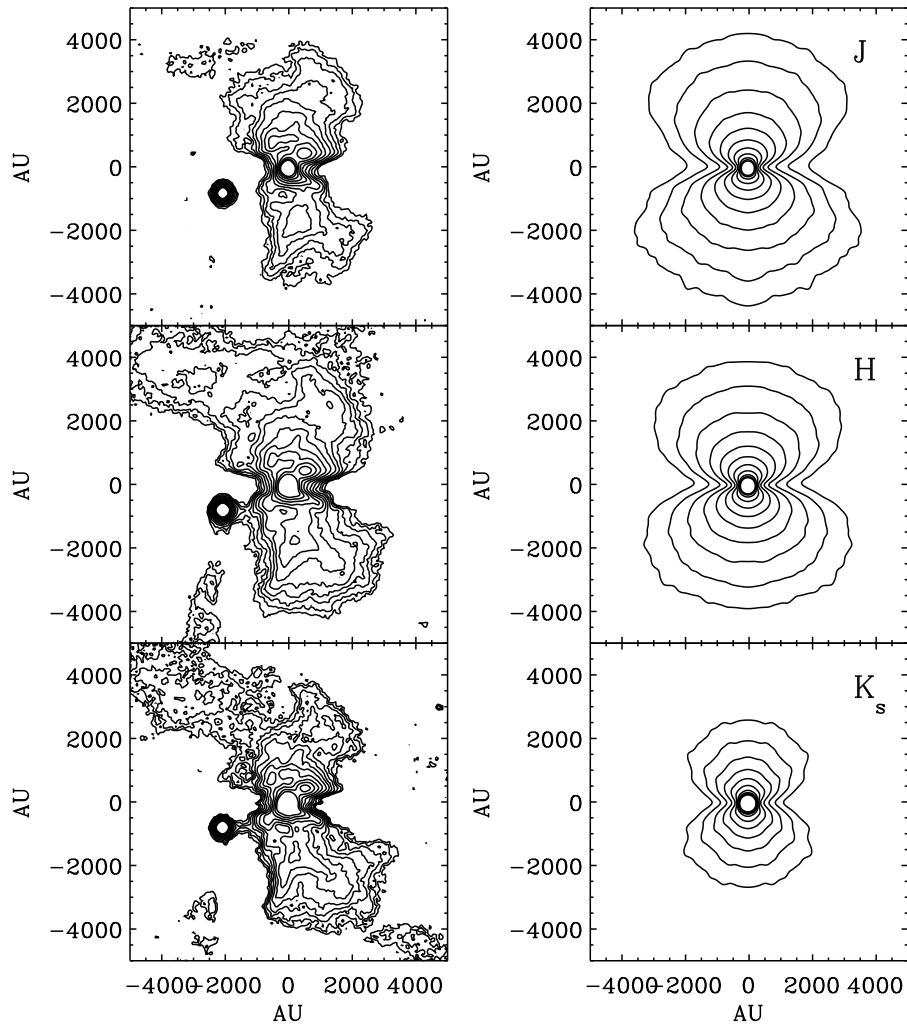
Figure 7.6: *Contours of the observed (left) and modelled (right) JHK_s band images. Model and observation are plotted on the same intensity scale. The contours are spaced logarithmically in steps of 0.2 dex with the lowest contour at $1.7 \times 10^{-17} \, erg \, s^{-1} \, cm^{-2} \, Hz^{-1} \, sterad^{-1}$. The source to the south-east of CK 3 is the unrelated star EC 86 which is probably located in the foreground of the envelope material.*

a fairly shallow silicate $9.7\,\mu$m absorption band. The low signal-to-noise of the spectrum prevents any other features to be identified.

7.6.2 Model of Ced 110 IRS 4

We suggest that the morphology of Ced 110 IRS 4 can be explained as a shadow of a small, inclined disk projected on the remnant envelope by introducing an empty *spherical* cavity with a radius of 530 AU. Note that this is not a *bipolar* cavity, often suggested to be required to produce a bipolar reflection nebulosity. Without the spherical cavity, there would still be a reflection nebulosity and a disk shadow, only the shadow would be wedge-shaped as in the case of CK 3. The presence of a spherical cavity makes the source a 'scenario 2' disk shadow. Within the radius of the spherical cavity centered on the star-disk system, the shadow will be a dark band with parallel edges. At radii larger than the cavity, the shadow will continue the wedge-like shape as in the case of a 'scenario 1' source. In essence, the scattering material will form a bipolar set of truncated cones, but without the need to invoke a bipolar cavity in which the light can be scattered. In some cases, it may be difficult to distinguish a disk shadow from a bipolar cavity observationally. However, the central compact near-infrared source is a clear signature of a projected disk shadow.

The disk shadow from Ced 110 IRS 4 can possibly be traced to very large distances, as is expected for a genuine shadow. Faint nebulosity at distances of up to 4500 AU is present, but avoids the area defined by extrapolating the observed shadow to large distances (see Fig. 7.9).

The best-fitting parameters for Ced 110 IRS 4 are given in Table 7.1 and the temperature and density structure are shown in Fig. 7.10.

The image (Fig. 7.7) and SED (Fig. 7.8) of Ced 110 IRS 4 are fitted by a relatively small central disk with $R_{\text{disk}} = 35$ AU to match the near-infrared extent of the central source. The size of the disk is well constrained assuming the model disk structure is correct, however the disk may be larger if the disk is no longer flared at radii larger than R_{disk}. The central compact object in the model is not the star itself, but only light scattered in the disk surface, as is evident in the zoomed-in image in Fig. 7.7. This is consistent with the fact that the observed central source is extended in the near-infrared ISAAC images.

The disk is surrounded by a power law envelope. The envelope is significantly more compact than the envelope of CK 3 as indicated by the red colours and extent of the reflection nebulosity, yet the total mass of the envelope necessary to reproduce the data ($0.12\,M_\odot$) is somewhat smaller for Ced 110 IRS 4 than for CK 3. The cavity required to produce the central rectangular dark band is assumed to be empty, apart from the central star-disk system. It is found that a relatively steep density profile with $\alpha = -1.5$ of the envelope is required to fit the compact reflection nebulosity. Alternatively, the envelope can be fitted by a shallower power law, which is truncated at a radius of ~ 1500 AU. The available far-infrared data do not allow a clear distinction between these two possibilities. We choose the first option because it conforms to other models of envelope material. A constraining property of the data is the relatively shallow 15–80 μm spectral slope
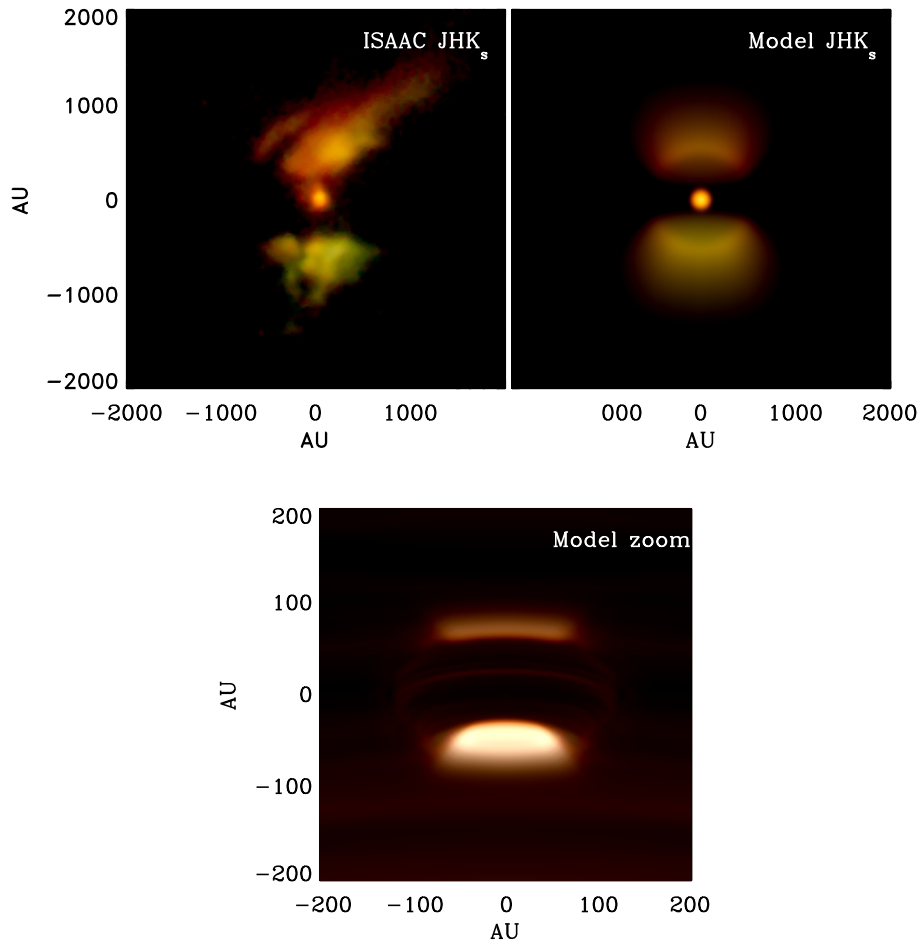
Figure 7.7: JHK_s *colour composites of the VLT-ISAAC images and the model Ced 110 IRS 4 constructed as in Fig. 7.2. The full colour images will be available in the published paper. Left panel: Observed ISAAC JHK_s image. Right panel: The model JHK_s image of CK 3 convolved with a gaussian with a $FWHM$ of $0.7''$ to match the observed image quality. Bottom panel: A zoom-in view of the physical disk of the model on a 100 AU scale. The images are aligned with north pointing up and east to the left.*
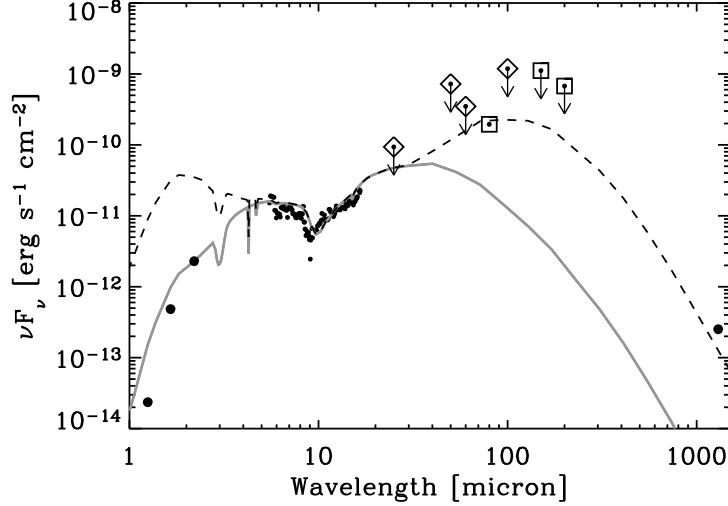
Figure 7.8: *The model fit to the observed SED of Ced 110 IRS 4. The solid curve is the model SED through a 2″ aperture, while the dashed curve is the model SED through a 50″ aperture. Upper limits indicate detections blended with nearby sources. These include 25, 60 and 100 μm IRAS points as well as 150 and 200 μm ISOPHOT points. The photometric points are taken from Prusti et al. (1991) (IRAS points indicated by diamonds) and Lehtinen et al. (2001) (ISOPHOT points indicated by squares).*

as measured by ISOCAM and ISOPHOT (see Fig. 7.8). The low $80\,\mu$m photometric point constrains both luminosity and disk mass. Increasing either in the model over-predicts the far-infrared flux at $80\,\mu$m. Decreasing the luminosity, but increasing the disk mass produces too little near to mid-infrared flux, and in particular fails to reproduce the surface brightness of the reflection nebulosity. Fitting the blended IRAS and ISOPHOT points without regard to the data at shorter wavelengths produces a significantly higher luminosity of $1.3\,L_\odot$ of the central object in agreement with Prusti et al. (1991), rather than the value of $0.4\,L_\odot$ derived using the unblended photometric points. This indicates that IRS 11 accounts for the remaining $0.9\,L_\odot$. The flat mid-infrared spectrum requires an inner rim with a large scale height given by $H_{\rm rim}/R_{\rm rim} = 0.29$. However, this model feature is not very important in terms of the shadow, since the large-scale disk produces most of the shadowing material, in contrast to the very tenuous disk of CK 3.

The total line of sight column density toward the central disk corresponds to $A_J = 3.3$ mag, which is consistent with the observed depth of the $9.7\,\mu$m silicate absorption band. The predicted $3.08\,\mu$m water ice band optical depth from the model is 0.7, of which 0.5 is due to the envelope. It is not possible to fit the very high $(J - H)$ colour of the central source of > 5 mag. Increasing the column density through the envelope creates a silicate band that is too deep, a 5–10 μm con-
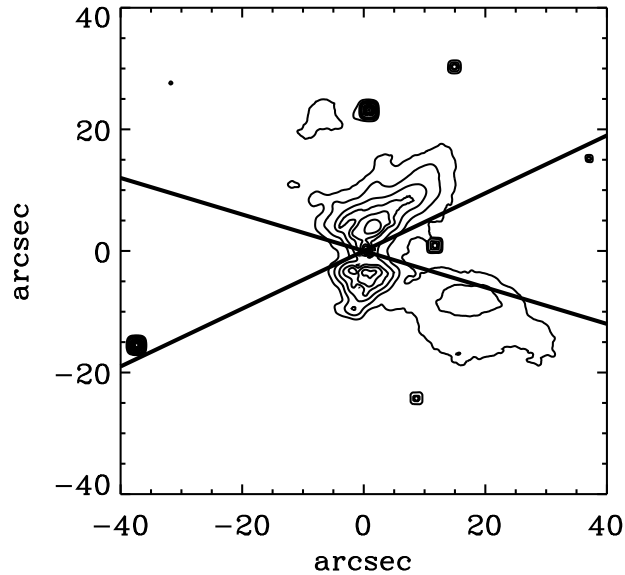
Figure 7.9: *The large scale structure of the reflection nebulosity surrounding Ced 110 IRS 4 as seen in the sum of the ISAAC JHK_s images. The lines indicate where the wedge-like shape of the shadow may be seen to large distances of up to 30″=4500 AU from the central source.*

tinuum that is too low and a bipolar nebulosity that is too extinct. This may be an indication that the dust model used is not entirely appropriate, in particular concerning the scattering properties of the disk. The colours of the bipolar nebula and the central source can possibly be reproduced by a somewhat flattened envelope, which can produce extra extinction toward the central source, while preserving the relatively low extinction toward each scattering lobe. However, this would still cause the mid-infrared extinction of the central source to be too high.

Fig. 7.11 shows a comparison of the cross section along the minor axis of the system between the model and observed near infrared images in terms of surface brightness. Contours of the separate near-infrared bands are shown in Fig. 7.12. It is seen that the higher reddening of the northern reflection lobe compared to the southern is explained by the model as a simple inclination effect. The light in the northern lobe is reflected at a smaller angle relative to the observer and therefore travels through a larger part of the envelope. The colour difference between the scattering lobes alone constrains the inclination of the system within a relatively narrow range of $70° \pm 5$. This effect is important for the envelope model, because it constrains the location of the material producing the reddening of the scattered light to the envelope rather than to a foreground component.

The size of the inner spherical cavity is determined by the position of the peaks in the reflection nebula, i.e. the width of the dark band. However, the width of
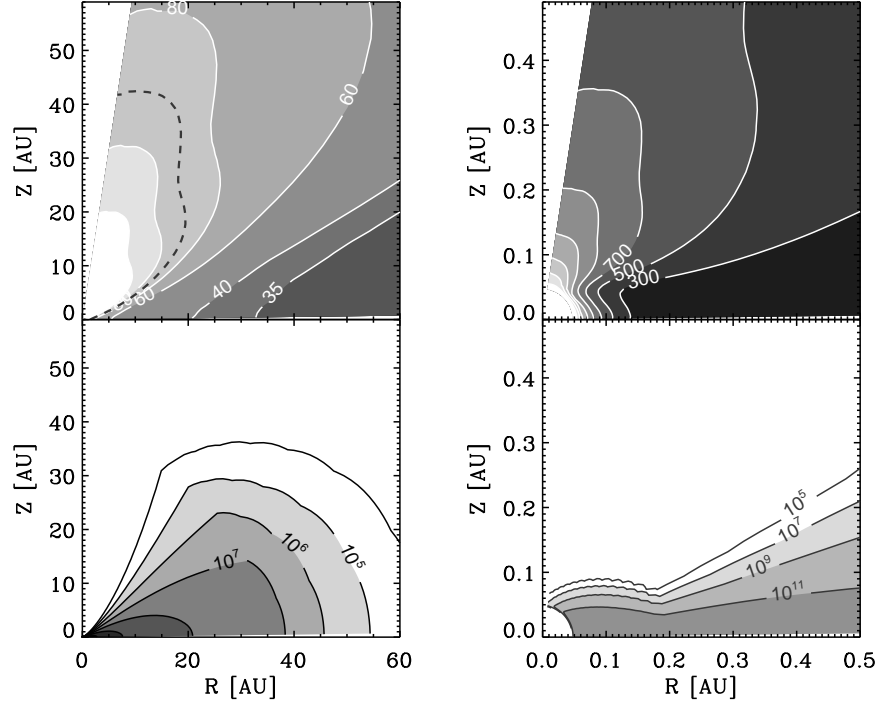
Figure 7.10: *As in Fig. 7.4, but for Ced 110 IRS 4.*

the dark band is also depending on the disk opening angle, Θ_{disk}. This means that in terms of the images, the disk opening angle and the size of the cavity are degenerate to some extent. The cavity produces a faint circle in the model due to limb brightening. It is likely that any real cavity will neither be spherical nor completely empty. Indeed some diffuse emission is seen within the dark band in the ISAAC image. Small amounts of material ($n(\mathrm{H}_2) \lesssim 10^4 \, \mathrm{cm}^{-3}$) present in the cavity or departures from spherical symmetry will tend to remove the limb brightening without affecting the shape of the shadow significantly. Significant departures from spherical symmetry of the cavity will preserve the sharp edges of the dark lane if single scattering dominates. This is a simple consequence of photons travelling in straight lines.

After constructing a model explaining the near-infrared morphology of Ced 110 IRS 4 as a disk shadow, it is important to consider whether the data can be fitted by a model without a small edge-on disk surrounding the central source. Specifically, the presence of a spherical cavity rather than a bipolar cavity may be difficult to explain from dynamical models. For instance, could the dark band be produced by a real absorbing layer of dust? It is probably possible to construct
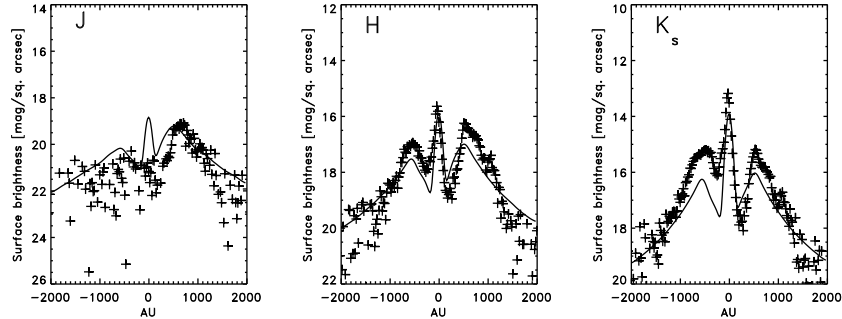
Figure 7.11: *Cross section along the minor axis of the Ced 110 IRS 4 system for the different near-infrared wavebands. The curve shows the model, while the (+) symbols show the observed ISAAC surface brightness.*

such a model consisting of a torus-like structure containing the central star. However, a central hole is needed in any case, because a large torus or disk extending all the way to the star will completely extinct the central compact source in the near-infrared images. At the same time, the circumstellar material must be dense enough to prevent any scattered light to escape from within the dark band. Alternatively, the material producing the dark band may be located at a distance of at least 2000 AU from the central star in order to suppress any reflection nebulosity. Still, the observed SED as well as the extended central object indicates that material is present close to the central star. If this material is in the shape of a disk, it must produce a shadow. It is concluded that a good explanation of the data is that a disk shadow is imprinted on the near-infrared reflection nebulosity. Ultimately, sensitive high resolution images in the far-infrared to millimetre wavelengths are needed to confirm the absence of a real flattened dusty structure, while high resolution near-infrared images will reveal if Ced 110 IRS 4 contains a small edge-on disk.

7.7 Projection versus extinction

7.7.1 The geometry of star, disk and shadow

The detailed geometrical relations between the central star, a flared disk and the morphology of the shadow are worth a closer look. Some properties are fundamental to the presence of a disk shadow. For instance for an axisymmetric distribution of circumstellar material, the presence of a well-defined dark disk shadow in general means that the central star will be obscured by the disk. This is related to the disk opening angle, Θ_{disk}. For inclinations higher than $90° - \Theta_{\mathrm{disk}}$ the central compact source consists of light reflected off the surface of the disk, the central star being obscured by the disk itself. At relatively low inclinations, disk shadows still affect the observed near-infrared morphology without showing clearly de-
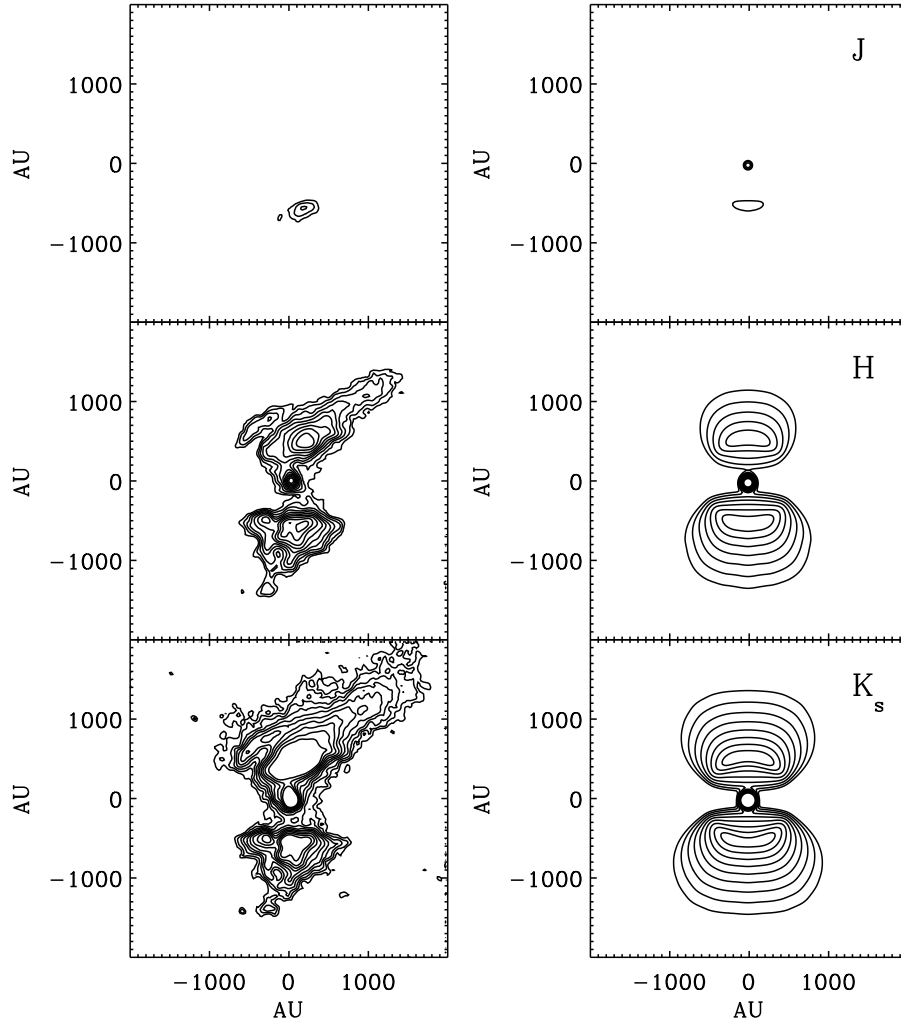
Figure 7.12: *As Fig. 7.6, but for Ced 110 IRS 4. The contours are spaced logarithmically in steps of 0.1 dex with the lowest contour at* $1.3 \times 10^{-17} \, erg \, s^{-1} \, cm^{-2} \, Hz^{-1} \, sterad^{-1}$.

fined dark bands. Fig. 7.13 shows the effects of different inclination angles of Ced 110 IRS 4. At inclinations $i < 90° - \Theta_{\mathrm{disk}}$ no dark lane is seen, but the nebulosity is still significantly elongated. This means that disk shadows can be mistaken for outflow cavities even at this inclination, but can be distinguished by the presence of a stellar source. In this case, the central star can be seen directly over the edge of the disk. If the shadow is cast on a backdrop 'screen' located entirely behind the source, a dark band will appear also for $i < 90° - \Theta_{\mathrm{disk}}$ and the central compact

source will appear outside the shadow (see Fig. 7.1). Again if the source is located outside the shadow for a backdrop screen, the central star must become visible and will outshine the scattered emission from the physical disk. The location of the central source relative to the shadow as seen in a near-infrared image is thus intimately linked to the visibility of the central star.

The strongly inter-related properties of visibility of the central star, near-infrared morphology and to a lesser degree the SED of the source means that in particular the inclination of the model system must be tightly constrained.

7.7.2 Selection criteria for disk shadows

A number of properties common to projected disk shadows can be identified from the models and compared to extinction from large disks in order to better classify any observed dark lane signatures in infrared images. In this section, we will attempt to identify useful selection criteria for disk shadows in the absence of sensitive imaging at long wavelengths.

The most important difference between dark lanes due to extinction from a large disk and the dark lanes due to projection is that the former are expected to be entirely dark while the latter will still have a bright source in the center of the system. Such a morphology is difficult to produce with a standard large disk model. For a very tenuous disk, the central star may of course be seen, such as is the case for CK 3. A very tenuous disk will produce a wedge-shaped morphology similar to a 'scenario 1' shadow, as seen in Fig. 7.2. However, the scattering lobes of a large tenuous disk will be flattened in the absence of a spherical envelope. Typically, the bright source within the dark lane is indirect stellar light which is being scattered on the disk surface into the line of sight. Much of this light may still be extincted by the envelope, such that the blueing effect of scattering is partly compensated by reddening due to extinction by the envelope material along the line of sight to the central source.

A disk shadow will for 'scenario 1' be characterised by a symmetric wedge-shaped band which covers the entire extent of the nebula illuminated by the central star. Typically, but not necessarily, the shadow will have an angular size which is much larger than what is expected from a disk. Clearly, there should be no unambiguous evidence of a physical disk *of the same size*. Conversely, a smaller edge-on disk must be present to cast the shadow. Thus, it should be possible to resolve the central object into an edge-on disk with a dark lane in high-resolution near-infrared images. Alternatively, since the light of the central compact source in the image consists exclusively of light scattered into the line of sight by grains in the disk surface layers (the direct starlight being totally obscured), it must be highly polarised to a degree that is easily observable. High resolution imaging or polarimetry of the central sources are therefore reliable methods to determine if a dark band is a disk shadow or not. For inclinations significantly higher than $90° - \Theta_{\text{disk}}$, the edge of the shadow will be straight and sharp, but for inclinations of $\lesssim 90° - \Theta_{\text{disk}}$, some curvature may be seen. For 'scenario 2', i.e. the screen shadow scenario, in which the central source is surrounded by a cavity, a dark band should be seen but with a central near-infrared compact source in the center.

202

Table 7.2: *Selection criteria for disk shadow candidates*

	Disk shadow	Large edge-on disk
Sharp edges of the dark band	typically	typically
'Wedge-like shape'	always	only for very tenuous disks
Extremely large size in the NIR (> 2000 AU)	typically	rarely
Source in the center	always	only for very tenuous disks
Variability of the dark band	possibly	very unlikely
Central source is bipolar on $\sim 1''$ scales	for $i > 90° - \Theta_{\mathrm{disk}}$	–

The presented model never produces a disk shadow without the central source being at least as bright as the reflecting material.

In some cases, significant shadowing can be produced by disk structures within a few AU of the star, such as may be the case for CK 3. Shadows produced by material located close to the central star may be highly variable on timescales as short as days. Conversely, large edge-on disks producing dark bands will have much longer timescales for variation. Thus, a variable large dark band is a clear signature of a disk shadow. The selection criteria for disk shadows are summarised in Table 7.2 and compared to bona-fide large disks.

7.8 Concluding remarks

We have argued that circumstellar disks may project large shadows onto any nebulosity illuminated by the central star, regardless of whether the scattering material is located around the star, in the background or in the foreground. The disk shadows will be most clearly recognisable if the disk is close to edge-on, but dark bands will also be present around disks with inclinations down to $\sim 70°$, and significant bipolar elongations of the nebulosity may be seen to much lower inclinations. We have presented two specific cases that fit well the selection criteria for each of the two scenarios and we have shown that all available spectroscopic and imaging data can be fitted by disk shadow models. Both candidates have very conspicuous morphologies of the near-infrared reflection nebulosity. However, many disk shadows may exist, which are more difficult to identify due to an asymmetric distribution of circumstellar material. The main objective has been to argue that a range of different observed near-infrared morphologies can be explained as large shadows cast by circumstellar disks of average size ($R_{\mathrm{disk}} \sim 100$ AU, $M_{\mathrm{disk}} \sim 10^{-6} - 10^{-2} \, M_{\odot}$). The fits to the data are not necessarily unique in every respect, although inclination and infrared extinction through the disk are well-constrained. Some parameters such as the total disk mass may change significantly if some model assumptions are changed. In particular the effect of different grain size distributions is not explored and the amount of settling of large dust grains may play a role for the derived parameters. Indeed, the very low dust mass derived for CK 3 may be taken as evidence for significant dust settling in this source.

For the two disk shadow candidates discussed here, the near-infrared images provide information which is highly complementary to fitting a model to the SED
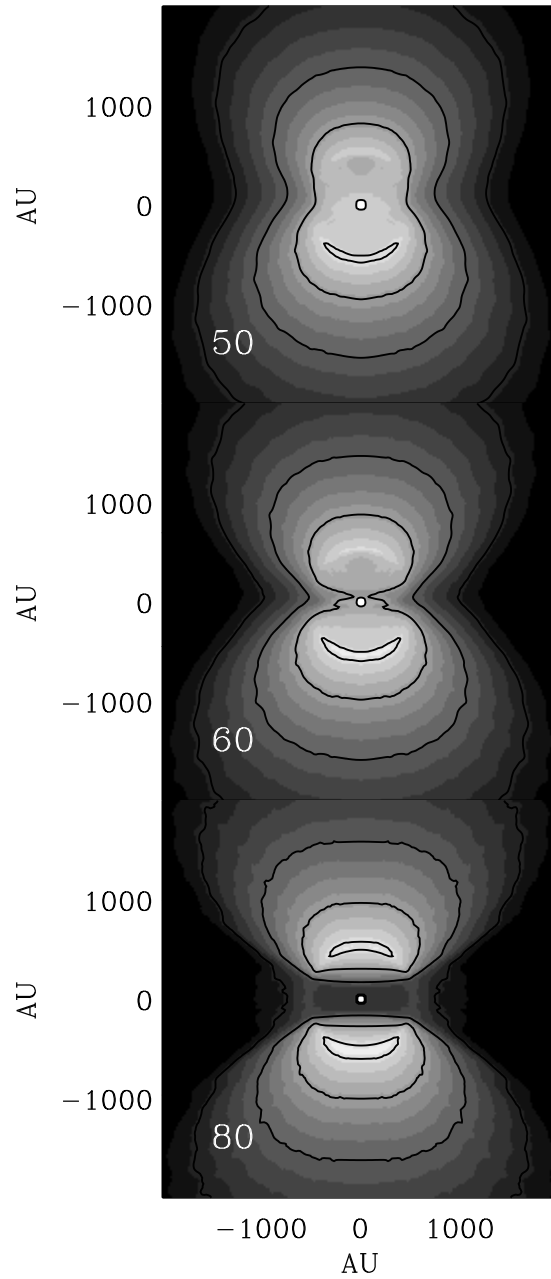
Figure 7.13: *The model of Ced 110 IRS 4 as seen at inclinations of 50, 60 and 80°. The innermost contour has a value of 10^{-16} erg s^{-1} cm^{-2} Hz^{-1} sterad^{-1} and subsequent contours decrease in steps of 0.5 dex.*

only. The presence of a disk shadow therefore may break some of the degeneracies, which haunt SED fitting. For instance, the disk shadow of CK 3 clearly shows that the system is highly inclined, while the SED alone suggests that the system is viewed close to face-on due to the emission features in the spectrum. Therefore, disk shadows unambiguously identify edge-on disk systems without the need for very high spatial resolution imaging. Furthermore, if the variability of the disk shadow of CK 3 suggested by Sogawa et al. (1997) is real, the structure and dynamics of the inner rim of the disk can be constrained in a unique way. The morphology of the shadow may in some cases constrain the distribution of envelope material. This is central to the division of disk shadows in 'scenario 1' shadows projected *into* and 'scenario 2' shadows projected *onto* the envelope material. Only a few identified edge-on disks surrounding low-mass stars are known and significantly more may be added using the signatures of disk shadows. In other words, a disk shadow source may provide modelling constraints for an unresolved disk similar to those obtained for resolved edge-on disks such as the Butterfly Nebula (Wolf et al., 2003) or HH 30 (Wood et al., 2002).

Also, edge-on disks are important for studying disk material which can only be observed in absorption, such as ices (Pontoppidan et al., 2004a; Thi et al., 2002). The possibility of identifying edge-on disks using disk shadows is interesting for observing ices in disks because such objects may be too tenuous and small to be detected through other means. Ices are expected to be abundant in the cold mid-planes of circumstellar disks. However, the very high optical depth through the mid-planes of many disks prevents the formation of ice absorption lines because the infrared continuum of the inner parts of the disk is completely obscured. Disks with a relatively low extinction through the mid-plane such as CK 3 may be excellent candidates for ice observations, yet they may be difficult to identify as edge-on disks in the absence of a disk shadow. As it turns out, the CK 3 disk optical depth along the mid-plane is so low that few ices are seen, but other disk shadow candidates may be better suited for searching for ices in disks. The disadvantage of disk shadows for ice observations is that the presence of a shadow dictates the presence of envelope material, which may contaminate the signal from disk ices.

Disk shadow scenarios may also be used to explain peculiar near-infrared morphologies. It is surprising how well a spherically symmetric envelope fits the reflection nebulosity of the two sources discussed in this paper when disk shadowing is taken into account. Specifically, no *bipolar* cavity is required for Ced 110 IRS 4, although it does require an inner *spherical* cavity to produce a dark band with parallel edges. However, it is important to note that many bipolar nebulosities still require bipolar cavities, especially for small opening angles of the bipolar nebulosity. How an inner spherical cavity is created remains an open question.

Apart from the disk shadow candidates modelled here, CK 3 of the Serpens Reflection Nebula and Ced 110 IRS 4, other examples may include some (but not all) of the bipolar nebulae in Taurus imaged by Padgett et al. (1999). In particular, IRAS 04248+2612 and CoKu Tau/1 of this sample resemble 'scenario 1' disk shadows. Other sources also show a near-infrared morphology very similar to that of Ced 110 IRS 4, i.e. a rectangular dark lane in a bipolar nebulosity with a compact source in the center. For instance, judging from the imaging of Brandner et al.

(2000), LFAM 26 (CRBR 2403.7-2948) is a good candidate for a 'scenario 2' disk shadow. Also, a recently discovered peculiar massive YSO in M17, suggested by Chini et al. (2004) to be an extremely large accretion disk of at least 100 $M_\odot$, shows many of the characteristics of a projected disk shadow of a much smaller disk. In particular, the object has a symmetric, wedge-shaped morphology extending over more than 30 000 AU and a central bright source. As such it bears strong resemblance to CK 3 and the Serpens reflection nebula. It is shown here that it is easy to produce such a morphology in terms of a disk shadow. Conversely, our radiative transfer models show that a real, massive flared disk is unlikely to produce a wedge-like shape as that seen in M 17. This object is particularly interesting since it is seen in the direction of an HII region. The presence of a disk shadow in an ionised region may indicate that parts of the cloud are shielded from ionizing photons by the disk shadow.

Acknowledgements

Bibliography

Adams, F. C., Lada, C. J., & Shu, F. H. 1987, ApJ, 312, 788

Beichmann, C. A. 1985, Infrared Astronomical Satellite (IRAS) catalogs and atlases. Explanatory supplement (Pasadena: Jet Propulsion Laboratory, 1985, edited by Beichmann, C.A.)

Brandner, W., Sheppard, S., Zinnecker, H., et al. 2000, A&A, 364, L13

Casali, M. M., Eiroa, C., & Duncan, W. D. 1993, A&A, 275, 195

Chiang, E. I. & Goldreich, P. 1997, ApJ, 490, 368

Chini, R., Hoffmeister, V., Kimeswenger, S., et al. 2004, Nature, 429, 155

Dominik, C., Dullemond, C. P., Waters, L. B. F. M., & Walch, S. 2003, A&A, 398, 607

Dubrulle, B., Morfill, G., & Sterzik, M. 1995, Icarus, 114, 237

Dullemond, C. P. & Dominik, C. 2004, A&A, 417, 159

Dullemond, C. P., Dominik, C., & Natta, A. 2001, ApJ, 560, 957

Dullemond, C. P. & Turolla, R. 2000, A&A, 360, 1187

Eisner, J. A., Lane, B. F., Akeson, R. L., Hillenbrand, L. A., & Sargent, A. I. 2003, ApJ, 588, 360

Evans, N. J., Allen, L. E., Blake, G. A., et al. 2003, PASP, 115, 965

Hodapp, K. W., Walker, C. H., Reipurth, B., et al. 2004, ApJL, 601, L79

Huard, T. L., Weintraub, D. A., & Kastner, J. H. 1997, MNRAS, 290, 598

Hurt, R. L. & Barsony, M. 1996, ApJL, 460, L45+

Jørgensen, J. K., Schöier, F. L., & van Dishoeck, E. F. 2002, A&A, 389, 908

Kenyon, S. J. & Hartmann, L. 1987, ApJ, 323, 714

Knude, J. & Høg, E. 1998, A&A, 338, 897

Lehtinen, K., Haikala, L. K., Mattila, K., & Lemke, D. 2001, A&A, 367, 311

Lehtinen, K., Harju, J., Kontinen, S., & Higdon, J. L. 2003, A&A, 401, 1017

Mannings, V. & Sargent, A. I. 1997, ApJ, 490, 792

Mattila, K., Liljestrom, T., & Toriseva, M. 1989, in Low Mass Star Formation and Pre-main Sequence Objects, 153–+

McCaughrean, M. J. & O'Dell, C. R. 1996, AJ, 111, 1977

Millan-Gabet, R., Schloerb, F. P., & Traub, W. A. 2001, ApJ, 546, 358

Muzerolle, J., Calvet, N., Hartmann, L., & D'Alessio, P. 2003, ApJL, 597, L149

Natta, A., Prusti, T., Neri, R., et al. 2001, A&A, 371, 186

Ossenkopf, V. & Henning, T. 1994, A&A, 291, 943

Padgett, D. L., Brandner, W., Stapelfeldt, K. R., et al. 1999, AJ, 117, 1490

Persi, P., Marenzi, A. R., Gómez, M., & Olofsson, G. 2001, A&A, 376, 907

Pontoppidan, K. M., Dullemond, C. P., van Dishoeck, E. F., et al. 2004a, A&A, in prep

Pontoppidan, K. M., Fraser, H. J., Dartois, E., et al. 2003, A&A, 408, 981

Pontoppidan, K. M., van Dishoeck, E. F., & Dartois, E. 2004b, A&A, in press

Prusti, T., Clark, F. O., Whittet, D. C. B., Laureijs, R. J., & Zhang, C. Y. 1991, MNRAS, 251, 303

Reipurth, B., Nyman, L.-A., & Chini, R. 1996, A&A, 314, 258

Shirley, Y. L., Evans, N. J., Rawlings, J. M. C., & Gregersen, E. M. 2000, ApJS, 131, 249

Shu, F. H. 1977, ApJ, 214, 488

Sogawa, H., Tamura, M., Gatley, I., & Merrill, K. M. 1997, AJ, 113, 1057

Straizys, V., Cernis, K., & Bartasiute, S. 1996, Baltic Astronomy, 5, 125

Thi, W. F., Pontoppidan, K. M., van Dishoeck, E. F., Dartois, E., & d'Hendecourt, L. 2002, A&A, 394, L27

van Boekel, R., Waters, L. B. F. M., Dominik, C., et al. 2003, A&A, 400, L21

van Dishoeck, E. F., Dartois, E., Pontoppidan, K. M., et al. 2003, The Messenger, 113, 49

Whitney, B. A., Wood, K., Bjorkman, J. E., & Cohen, M. 2003, ApJ, 598, 1079

Wolf, S., Padgett, D. L., & Stapelfeldt, K. R. 2003, ApJ, 588, 373

Wood, K., Wolff, M. J., Bjorkman, J. E., & Whitney, B. 2002, ApJ, 564, 887

Zinnecker, H., Krabbe, A., McCaughrean, M. J., et al. 1999, A&A, 352, L73

Nederlandse samenvatting

Oorsprong

Een ieder die opgroeit in de nabijheid van de zee, kent het staren over het eindeloze water, peinzend welke geheimen verborgen liggen in haar diepte. Dit geldt in het bijzonder voor Nederland, waar druilerige dagen zich aaneen rijgen en de overvloed aan water onvermijdelijk de vraag oproept: 'Waar kan dat vandaan komen?'

Op de middelbare school word je geleerd dat, als onderdeel van de koolstof cyclus op Aarde, water en koolstof dioxide worden omgezet in zuurstof en planten (suikers wel te verstaan) via een proces genaamd fotosynthese. Voor elk suikermolecuul dat op deze manier geproduceerd wordt zijn 6 koolstof dioxide en 6 water moleculen nodig in combinatie met zonlicht. Als bijproduct worden 6 zuurstof moleculen geproduceerd. Mensen en andere dieren ademen vervolgens de zuurstof in en eten de gevormde planten om de energie te verzamelen die in de vorm van suikers ligt opgeslagen (dit is in zekere zin het omgekeerde proces van de fotosynthese). Een snelle berekening laat zien dat, als gevolg van deze twee processen, elk water molecuul uit de oceanen op Aarde meerder malen gevormd en vernietigd moet zijn in de afgelopen 3.7 biljoen jaar waarin leven zich op Aarde heeft kunnen ontwikkelen. Voor sommigen onder ons zal dit een voldoende verklaring zijn voor het ontstaan van water op Aarde. Echter, de heersende hypothese is dat leven niet kan ontstaan in de afwezigheid van water. Waar is het oorspronkelijke water dan vandaan gekomen? Helaas is er op Aarde maar weinig bewaard gebleven van alle geologische aanwijzingen voor de oorsprong van water. Dit geldt ook voor alle planeten dichter bij de Zon. Op deze planeten heeft de intense warmte van de Zon letterlijk alle mogelijke aanwijzingen in rook op laten gaan; Venus is uitzonderlijk droog. Ook op Mercurius is het maar moeilijk voor te stellen dat water kan bestaan, hoewel er theorieën zijn dat er op de bodem van diepe kraters, dicht bij de polen waar de stralen van de Zon niet rijken, waterijs ligt.

De zoektocht naar de oorsprong van de eerste planeetchemie heeft zich daardoor natuurlijkerwijs uitgebreid naar de verderaf gelegen, donkere, koude gebieden van ons Zonnestelsel. Ons Zonnestelsel blijkt enorm rijk te zijn aan ijsdeeltjes. Zo hebben we kometen, die met tientallen per jaar de binnenste regionen van ons Zonnestelsel binnen komen. Een ander voorbeeld zijn de ringen van Saturnus. Dit is recentelijk aangetoond met behulp van de Cassini satelliet die in een baan om deze twee na grootste planeet van ons Zonnestelsel is gebracht en op die manier heeft kunnen aantonen dat de ringen van Saturnus hoofdzakelijk uit water bestaan. Ook op een groot aantal van de manen van de buitenste planeten is water aangetroffen. Op velen wordt zelfs meer water gevonden dan op Aarde.

209

Twee voorbeelden zijn Europa, de mysterieuze maan van Jupiter, en Triton, de grootste maan van Neptunus waarop vulkaanuitbarstingen in de vorm van waterijs zijn waargenomen (in plaats van uitbarstingen van gesmolten gesteente). Los hiervan bevinden zich in de buitenste regionen van ons Zonnestelsel ontelbare kleine ijsdeeltjes: de zogenaamde Kuiperbelt objecten. Het idee is dat deze deeltjes nauwelijks zijn veranderd sinds de tijd dat ons Zonnestelsel gevormd is, waardoor het waarschijnlijk is dat ze waardevolle informatie bevatten over de mogelijke oorsprong van waterijs rijke gebieden.

Stof- en Stervorming

Sterren vormen zich in zogenaamde donkere, dichte wolken die bestaan uit gas en stof. Men moet zich realiseren dat deze wolken desondanks nog steeds vele malen ijler zijn dan het beste vacuüm dat op Aarde in het laboratorium kan worden bereikt, maar wel 100-1.000.000 keer dichter dan het gemiddelde gas in de ruimte tussen de sterren. Onder bepaalde condities kan een gedeelte van zo'n wolk onder zijn eigen zwaartekracht ineenstorten en een of meerdere sterren vormen. Hierbij ontstaat een draaimoment dat leidt tot de vorming van een afgevlakte schijf die om de jonge ster roteert. In deze schijf kunnen gas en stof samenklonteren en zo planeetsystemen vormen. Het stof bestaat uit hele kleine vaste deeltjes met een diameter van 0.1-1 micrometer en draagt voor ongeveer 1% bij aan de totale massa van al het materiaal in de wolk. De stofdeeltjes bestaan hoofdzakelijk uit zuurstofrijke mineralen (silicaten). Een belangrijk, maar kleiner gedeelte bestaat uit koolstof. De koolstofdeeltjes lijken een beetje op een mengsel van sigarettenrook en microscopische diamanten! Het grootste gedeelte van dit Proefschrift zal zich echter niet concentreren op stof maar op ijs. In deze context betekent ijs vluchtige moleculen in de vaste fase. Hierbij moet niet alleen gedacht worden aan water, maar ook aan moleculen zoals koolstof monoxide (CO), koolstof dioxide (CO_2), ammonia (NH_3), methaan (CH_4), verschillende alcoholen en vele andere, soms erg giftige, stoffen.

Er is geen twijfel over mogelijk dat waterijs onlosmakelijk verbonden is met het materiaal waaruit sterren en planeten geboren worden. Tenminste, in ons eigen Melkwegstelsel. Hoe weten we dat? Licht heeft een heel specifieke interactie met verschillende materialen. In het geval van moleculaire vaste stoffen, zoals mineralen en ijs, kan licht de moleculaire bindingen laten trillen en buigen. Deze zogenaamde excitatie van een bepaalde trilling door een elektromagnetische golf absorbeert energie in een nauw golflengtegebied, waardoor een absorptieband in het spectrum wordt gevormd. Voor moleculaire vaste stoffen gebeurt dit typisch in het infrarode gebied van het spectrum (2-100 micrometer). Als zo'n vaste stof aanwezig is in een wolk in de ruimte, kan het infrarode spectrum van een ster achter deze wolk gebruikt worden om deze vaste stof te detecteren. De totale collectie van absorptie banden die op deze wijze verkregen wordt, wordt vervolgens gebruikt om de moleculaire karakteristiek van het bekeken gebied te ontrafelen. Op deze manier zie je niet zozeer gehele moleculen maar eerder de afzonderlijke bindingen in een molecuul. Bijvoorbeeld de binding tussen een waterstof en een zuurstof atoom. Deze binding geeft een absorptie band bij ongeveer 3 micrometer.

De positie van deze band is bijna onafhankelijk van het molecuul waarin de binding voorkomt. Dit betekend dat water (H_2O) en methanol (CH_3OH) een vergelijkbaar signaal rond 3 micron meter zullen geven. Een molecuul kan daardoor enkel worden aangetoond in aanwezigheid van meerdere moleculaire interacties die typisch zijn voor dat specifieke molecuul. Methanol bijvoorbeeld kan worden onderscheiden van water met behulp van de C-H strekvibratie rond 3.5 micrometer en verschillende andere absorptiebanden die worden gevormd door alle mogelijke deformaties van het molecuul. Het gedetailleerde patroon van een absorptieband helpt eveneens mee in de identificatie van een molecuul. Dit betekent dat vaste stof spectroscopie in de ruimte vaak een verwarrende bezigheid is waarbij het nodige detective werk gedaan moet worden voordat een molecuul met zekerheid geïdentificeerd kan worden.

De hypothese dat waterijs aanwezig is in de ruimte dateert uit de jaren twintig. Sindsdien is door middel van vele waarnemingen aangetoond dat waterijs inderdaad één van de meest sterke banden in dichte, donkere wolken produceert. De aanwezige hoeveelheid waterijs in dichte wolken is enorm. We weten nu dat de totale massa water ongeveer 1/10de van de totale stofmassa is. Alle andere ijs soorten samen vertegenwoordigen nog eens 2/10de van de stofmassa.

Buiten het gebied van de dichte wolk, in het zogenoemde diffuse interstellaire medium, wordt geen ijs gevonden, hoewel silicaat en koolstof deeltjes in vergelijkbare concentraties aanwezig zijn. Dit komt doordat de stofdeeltjes hoofdzakelijk gevormd worden uit het materiaal dat uitgestoten wordt wanneer een ster sterft, terwijl ijs pas gevormd wordt in het binnenste van de dichte wolken. Wanneer de wolk voldoende dichtheid heeft kunnen zuurstof en waterstof atomen samenkomen op het oppervlak van een stofdeeltje waar ze vervolgens kunnen reageren tot een water molecuul. Dit water blijft op het oppervlak zitten en vormt zo een ijslaagje. Andere soorten ijs kunnen op eenzelfde manier worden gevormd, met uitzondering van CO. CO kan enkel gevormd worden in de gasfase en wordt pas ijs doordat het vast vriest op het oppervlak van een stofdeeltje. De tijd die nodig is om ijslaagjes te vormen in de ruimte is waarschijnlijk 10.000-100.000 jaar en het is erg aannemelijk dat het water dat gevonden wordt in kometen, rond planeten, op manen en op aarde gevormd is op de manier die hierboven is beschreven.

Fig. 7.14 geeft een voorbeeld van één van de eerste, kwalitatief goede, infrarode spectra van een jonge ster, vergelijkbaar met de Zon. Deze ster is omgeven door een schijf waarin planeten zich vormen. In het spectrum zijn veel verschillende banden te zien die veroorzaakt worden door de lichtabsorptie van ijs en stofdeeltjes.

Observationele gegevens

De technische beperkingen van de apparatuur zorgen ervoor dat meerdere telescopen nodig zijn om het gehele infrarode spectrum met alle belangrijke ijs absorptiebanden van een gebied in de ruimte in beeld te brengen. De resultaten die in dit Proefschrift worden behandeld zijn voor een groot gedeelte verkregen met behulp van de Infrared Spectrometer And Array Camera (ISAAC). Dit in-
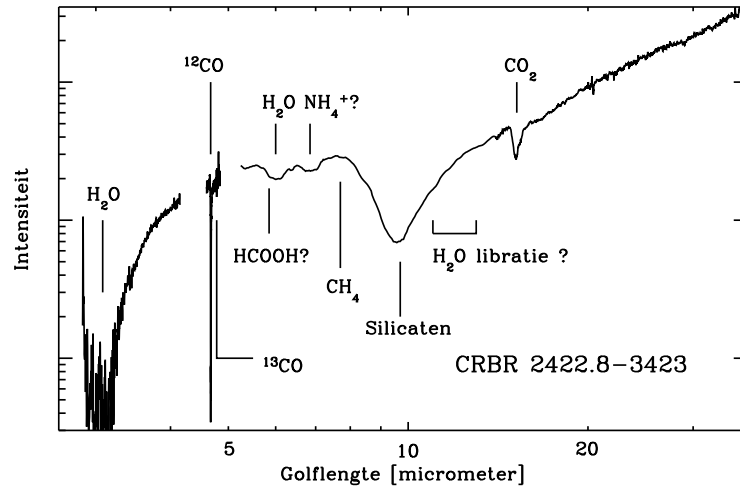
Figure 7.14: *Een gecombineerd spectrum van CRBR 2422.8-3423, verkregen met de VLT-ISAAC en de Spitzer-IRS spectrometers. Detecties van vaste stof banden zijn aangegeven, evenals de afwezigheid van de waterijs libratieband bij 11–13 micrometer (zie tekst).*

strument is geplaatst op de Very Large Telescope van de Europese Zuidelijke Sterrewacht (ESO) in de Atacama woestijn in Chili, en kan spectra van 1 tot 5 micrometer opnemen. Voor het meten van langere golflengten moet uitgeweken worden naar zogenaamde ruimtetelescopen. Hiermee kan de verstorende invloed van de Aardatmosfeer omzeild worden. Vanzelfsprekend is het geen doen om naar moleculen zoals water en koolstof dioxide te zoeken in de ruimte wanneer de aardatmosfeer, waar je doorheen kijkt, vol zit met dezelfde moleculen. In dit Proefschrift is gebruik gemaakt van twee ruimtetelescopen. In de eerste plaats waren de archiefdata, die tot 1998 verzameld zijn door de Europese Infrared Space Observatory (ISO), van belang. In augustus 2003 lanceerde NASA de laatste van de Amerikaanse Great Observatories, de Spitzer ruimtetelescoop. Enkele van de eerste resultaten die met deze telescoop zullen worden verkregen, worden met trots in dit Proefschrift gepresenteerd. De Spitzer data zijn een onderdeel van één van de zes zogenoemde legacy programma's. Elk van deze programma's is ontwikkeld om een samenhangende database te creëren van verschillen soorten objecten in de ruimte. Het legacy programma wat hier van toepassing is heet 'van moleculaire wolken naar planeetvormende schijven', en is momenteel bezig met het verzamelen van infrarode spectra van jonge sterren, hun schijven en het gebied waarin ze zich bevinden. De officiële afkorting van dit programma is c2d.

212

Dit Proefschrift

Dit Proefschrift behandelt de evolutie en het transport van ijsdeeltjes vanaf het moment dat ze gevormd worden tot het moment dat ze onderdeel gaan uitmaken van een planeetvormende schijf. Deze studie beperkt zich enkel tot jonge lage massa sterren en de wolken waarin lage massa sterren gevormd worden. Een lage massa ster is grofweg gedefiniëerd als een ster die qua massa vergelijkbaar is met de Zon op het moment dat de ster de volwassen leeftijd bereikt.

Hoofdstuk 2 presenteert de eerste detecties van methanolijs rond jonge lage massa sterren. De methanol concentratie wordt geschat op 15-20% van de aanwezige hoeveelheid water. Voorheen is methanolijs enkel gedetecteerd rond jonge sterren met een veel grotere massa dan de Zon. Het is op dit moment nog niet bekend hoe methanol in zulke hoge concentraties gevormd kan worden, maar de detectie rond lage massa sterren geeft aan dat intense ultraviolette straling, en andere energetische processen die karakteristiek zijn voor hoge massa sterren, geen noodzakelijke factoren zijn in het vormingsproces. Methanol is belangrijk als uitgangspunt voor de vorming van meer complexere moleculen in de warme, dichte gebieden vlak bij een jonge ster, de 'hot cores'. Methanol wordt ook aangetroffen in kometen, maar niet met zulke hoge concentraties als hier besproken worden.

In **Hoofdstuk 3** worden de karakteristieke patronen van interstellair koolstof monoxide (CO) in detail onderzocht. Hier wordt aangetoond dat CO moleculen kunnen worden gebruikt om de microscopische structuur van het ijs bloot te leggen. Waarnemingen van meer dan 35 jonge lage massa sterren zijn gebruikt om het gedrag van CO-ijs in de ruimte te analyseren aan de hand van het profiel van de absorptieband die wordt gevormd door de strekvibratie van de C-O driedubbele binding. Een belangrijke conclusie is dat het ijs eenzelfde soort structuur lijkt te hebben in alle verschillende bronnen waar naar is gekeken. CO lijkt overwegend puur te zijn in jong ijs. Puur wil zegen dat het niet gemixt is met andere moleculen. Een kleinere fractie van het CO-ijs is altijd gemixt met waterijs. Er is bewijs dat CO een grotere mobiliteit krijgt bij hogere temperaturen. Dit zou het mogelijk maken voor CO om in het waterijs te gaan zitten. Tevens is CO waarschijnlijk niet homogeen verdeeld over het oppervlak van de stofdeeltjes, maar bevindt het zich eerder in onregelmatige hoopjes op het oppervlak of als bubbels in het ijs. In essentie geeft de spectroscopie informatie over processen die plaats vinden op een schaal van een paar nanometer op stofdeeltjes die meer dan 500 lichtjaren ver weg liggen. Sterker gezegd, eenzelfde effect kan worden waargenomen in andere sterrenstelsels!

Hoofdstuk 4 beschrijft een nieuwe techniek waarmee de ruimtelijke distributie van interstellaire ijsdeeltjes in kaart gebracht kan worden. Omdat er een heldere ster achter een ijs-rijke wolk nodig is om interstellair ijs waar te nemen, was het tot voorkort nauwelijks mogelijk om te bepalen hoe het ijs over de ruimte verdeeld was; simpelweg omdat er niet zoveel heldere sterren aanwezig zijn. Enkel het ijs dat zich in een directe lijn voor de ster bevond kon worden bestudeerd. Recentelijk zijn de camera's en spectrometers op de grote telescopen echter zodanig gevoelig geworden dat nu ook zwakkere sterren als achtergrond lichtbron gebruikt kunnen worden. Aangezien deze sterren veel meer voorkomen dan heldere, felle sterren, kunnen sinds kort gebieden op relatief kleine schaal bekeken worden

en is het mogelijk om het gehele gebied van een wolk met een veel hogere resolutie te onderzoeken. In dit hoofdstuk wordt voor het eerst zo'n hoge resolutie plattegrond van ijs gepresenteerd. Het gaat hierbij om de buitenste schil van de stofwolk van een ineenstortende protoster. Een protoster is te vergelijken met de buik van de vrouw waarin een embryo (lees 'ster in wording') tot baby uitgroeit. Het ijs materiaal wat zich in deze stofwolk bevindt zal direct onderdeel gaan uitmaken van het planeetsysteem dat gevormd zal gaan worden. We zien dat de hoeveelheid ijs dramatisch stijgt in de binnenste regionen van de stofwolk, wat op grond van theoretische overwegingen ook verwacht kan worden.

Evenzo is het van belang om in planeetvormende schijven rond jonge sterren naar ijs te zoeken. Dit blijkt echter erg ingewikkeld. Hoewel we weten dat grote hoeveelheden ijs aanwezig zijn in ons eigen Zonnestelsel, is het onduidelijk hoe die hier terecht zijn gekomen. Een schijf wordt gevormd uit samengeklonterd materiaal, afkomstig uit de stofwolk van de protoster. In sommige gevallen kan dit gepaard gaan met hoge snelheden. Wanneer het invallende materiaal op de schijf inbeukt, is het zeer waarschijnlijk dat het aanwezige ijs verdampt. In sommige gevallen kunnen de moleculen zelfs vernietigd worden in zogenaamde dissociatieve schokgolven. Het ijs in een schijf ons dus kunnen vertellen of, en op wat voor manier, het ijs veranderd is tijdens de vorming van de disk.

Hoofdstuk 5 presenteert een van de eerste Spitzer spectra die zijn verkregen als onderdeel van het c2d legacy programma. Het object in kwestie is buitengewoon interessant omdat het hier gaat om een schijf die van opzij wordt bekeken, een zogenaamde 'schijf-op-zijn-kant'. In dit type objecten is de ster geheel verborgen in het optische gebied van het spectrum. Enkel het licht dat reflecteert van de zijkanten van de disk kan worden waargenomen. In zo'n schijf heb je de mogelijkheid om ijs in absorptie te bekijken tegen het binnenste gedeelte van de schijf doordat de ster dit gebied opwarmt waardoor het mid-infrarode straling uitzendt (200-1000°C). Zoals verwacht is er een hele hoop ijs aanwezig maar om de locatie te bepalen moest eerst een gedetailleerd model worden gemaakt. Dit model berekent de temperatuur van de schijf, en bepaalt op die manier waar het stof te warm wordt om nog ijs te kunnen bevatten. Met behulp van dit model is geconcludeerd dat ongeveer de helft van al het ijs dat gezien wordt zich in de voorgrond, dus voor de schijf, bevindt. De andere helft is waarschijnlijk wel onderdeel van de schijf.

Hoofdstuk 6 behandelt een ander bijzonder object waar mogelijk de botsing van invallend materiaal met een schijf direct kan worden waargenomen. Het object heeft uitzonderlijk sterke spectrale lijnen van warm koolstof monoxide gas van mogelijk 240°C. Deze temperatuur is typisch voor de temperatuur van het proces waarbij moleculair waterstof gevormd wordt. Dit heeft als consequentie dat de oorspronkelijke moleculen vernietigd moeten zijn toen ze in botsing kwamen met de schijf. In dit specifieke object lijken er aanwijzingen te zijn dat het ijsmateriaal significant veranderd is tijdens de vorming van de disk. De aanwijzingen zijn echter niet rechtlijnig en de eigenlijke hoeveelheid moleculen dat vernietigd is kan mogelijk maar een kleine fractie zijn.

Ter afsluiting wordt in **Hoofdstuk 7** besproken hoe de aanwezigheid van een schijf rond een ster een schaduw kan veroorzaken die veel groter kan zijn dan de

schijf zelf. Zo'n schaduw kan worden waargenomen doordat de wolk waaruit de ster zich vormde het licht van deze ster reflecteert, behalve daar waar de schaduw zich bevindt. De aanwezigheid van een schaduw helpt bij het bepalen van de structuur van de schijf wanneer de schijven te klein zijn om direct te worden waargenomen.

English summary

Origins

Anyone who grew up near an ocean knows the feeling of staring across the endless waters, wondering which secrets are hidden in the depths. Especially during the dutch rainy season one is forced to ponder the enormous amounts of water present on the Earth and inevitably, the question arises: 'Where does it all come from?'.

Elementary school teachings of the Earth's carbon cycle in which water and carbon dioxide are transformed into free molecular oxygen and plants (sugar, actually) via the process of photosynthesis states that for each sugar molecule created, 6 carbon dioxide and 6 water molecules in addition to sunlight are required and 6 oxygen molecules are produced in each reaction. The process is reverted when humans and other animals eat the plants to obtain the chemical energy contained in the sugar. A quick calculation shows that because of this process, every water molecule in the oceans of the Earth have been destroyed and reformed many times during the approximately 3.7 billion years life has existed there. To some, this may explain the origin of water. However, accepting the reasonable hypothesis that life could not have formed in the first place without the presence of water, the question transforms to where the original water came from. Unfortunately, the geological record of the origin of water on the active Earth has largely been erased. Similar to the planets closer to the Sun, signatures of a watery birth have been boiled off by the intense heat of the Solar radiation; Venus is extremely dry. It is also hard to imagine that water can exist on the Sun-scorched Mercury, although it has been suggested that water ice may exist in the bottom of deep craters near the pole, where the rays of the Sun never reach.

It is therefore natural to expand the search for the origins of the early planetary chemistry to more quiescent and cold regions of the Solar system. We know that the Solar System is awash with icy bodies. Examples include comets of which tens enter the inner Solar System each year. Recently, the Cassini spacecraft arrived to orbit Saturn, the second largest planet and is returning abundant data on the rings, which consist mostly of water ice. Many of the moons of the outer planets are much more rich in water ice than the Earth. Examples include the mysterious Europa of the Jupiter system and Triton, the largest moon of Neptune, which has vulcanos of ice instead of molten rock. Finally, in the outer reaches of the Solar System beyond the planets, there exist countless numbers of small icy bodies known as Kuiper belt objects. Many of these objects are unlikely to have changed much since the formation of the Solar System. It therefore seems clear that the regions far from the Sun carry the frozen record of a very ice-rich origin.

Dust and star formation

Stars are formed in so-called 'dense' clouds of gas and dust. These clouds are more tenuous than the best vacuum achievable in a laboratory on Earth, yet 100-1 000 000 times more dense than the average gaseous material which exists between the stars. Under certain circumstances, a part of a dense cloud may collapse under its own gravity to form one or more stars. Any initial angular momentum or rotation of the cloud fragment is transferred into a flattened rotating disk around the newly formed star. It is in this disk that dust and gas can clump together to form a planetary system. The dust consists of very small solid particles 0.1–1 μm in size and make up about 1% of the total mass of the star-forming material. Most of the dust consists of simple oxygen-rich minerals (silicates), but a considerable part is some form of carbon, which probably resembles a mix of cigarette smoke and microscopic diamonds! Much of this thesis, however, is concerned with ice. The general label of 'ice' refers to solid molecular volatiles, which includes not only water, but also carbon monoxide (CO), carbon dioxide (CO_2), ammonia (NH_3), methane (CH_4), alcohols and many other rather poisonous species.

There is no question that water ice is inseparably bound to the material of which stars and planetary systems are born, at least in our own Milky Way galaxy. How can we know this? Light interacts with all forms of matter in various ways. In the case of molecular solids, such as minerals and ice, light waves cause molecular bonds to bend and vibrate. The excitation of a given vibration by an incoming electromagnetic wave absorbs energy in a narrow range of wavelengths creating an absorption band in the spectrum, typically in the infrared (2-100 μm). If a molecular solid, including ice, is present in the form of small particles in a cloud in space, it can be detected by using an infrared spectrum of a star behind the cloud. Any solid state absorption bands detected can then be used to infer the molecular properties of the intervening material. What is seen in the spectra is typically not entire molecules, but rather individual molecular bonds in the molecules. For instance, vibrations in the bond between a hydrogen and an oxygen atom create an absorption band around 3 μm, (almost) regardless of the nature of the larger molecule. This means that both water (H_2O) as well as methanol (CH_3OH) will produce a similar signature around 3 μm. Specific molecules are identified by the presence of all the necessary molecular interactions. Methanol, for instance, can be distinguished from water by the C-H stretching band around 3.5 μm as well as several other bands produced by all the possible deformations of the methanol molecule (CH_3OH). The detailed shape of the absorption bands also aids in the identification. This means that solid state spectroscopy of dust in space is often a rather confused affair, requiring a certain amount of detective work before a definite identification can be made.

The presence of water ice in space has been hypothesised since the 1920s. Accumulated observational evidence collected since then has shown that water ice is certainly producing some of the strongest absorption bands seen in dense clouds. The amounts of water ice present in star-forming clouds are enormous. We now know that water ice makes up more than 1/10 by mass of the dust in dense clouds. Other ices add an additional 2/10 to the total budget, although water (barely) remains the single most abundant molecule in the ice.

218

Outside the dense clouds in the so-called diffuse interstellar medium, no ice is observed, while the silicate and carbon dust grains are seen in the same abundance. This is because the dust is formed primarily in dense material ejected by dying stars, while the ice is formed in dense clouds. When a cloud becomes sufficiently dense, oxygen and hydrogen can collect on the surfaces on the dust grains to combine into water molecules, which remain bound on the surface in the form of ice. Other ices are formed in a similar way, except for CO, which can be formed in the gas phase before freezing on the grain surfaces. The time scale for the formation of an ice mantle is probably only 10 000–100 000 years. It is very likely that the water present in the outer Solar System bodies as well as the water on the early Earth was formed in this way.

Fig. 7.15 shows an example of one of the first high quality infrared spectra of a solar-type young star surrounded by a planet-forming disk. The spectrum shows numerous bands due to ice and dust.
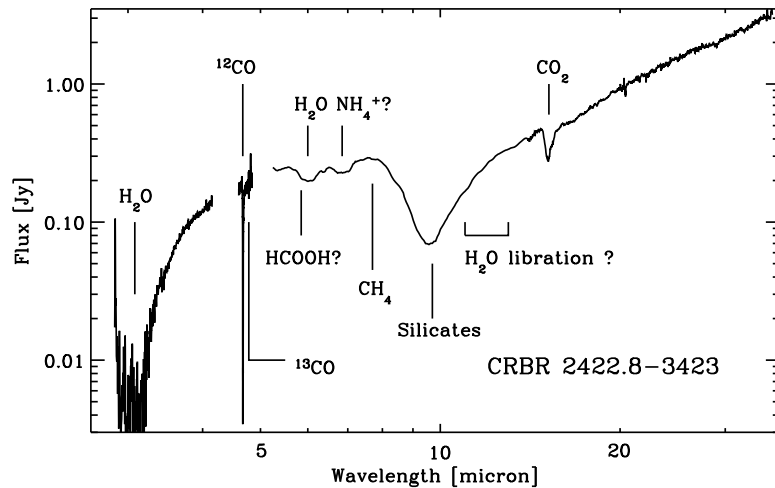

Figure 7.15: *Combined VLT-ISAAC and Spitzer-IRS spectrum of CRBR 2422.8-3423. Detected solid state bands are marked as well as the largely missing water ice libration band at 11-13 μm (see text).*

Observational data

Due to technical limitations, observations from a range of different telescopes are necessary to obtain a full infrared spectrum covering all the important ice absorption bands. The results presented in this thesis are to a large degree due to spectra obtained with the Infrared Spectrometer And Array Camera (ISAAC) mounted on the Very Large Telescope of the European Southern Observatory in the Atacama desert in Chile. This instrument is capable of measuring spectra from 1 to 5 μm. At

longer wavelengths, it has been necessary to use a telescope in space, outside the disturbing atmosphere of the Earth. Naturally, when searching for water, carbon dioxide and other such molecules in space, it is no good trying to peer through a dense atmosphere awash with these same molecules. Two space telescopes have been used. Archival data obtained by the European Infrared Space Observatory (ISO), which was operational until 1998, have been important. In August 2003, NASA launched the last of the American Great Observatories, the Spitzer Space Telescope, and some of the first results from this facility are proudly presented in this thesis. The Spitzer data used were obtained as part of one of six so-called *Legacy* programmes, each designed to provide a comprehensive database of a certain class of astronomical objects. The Legacy programme in question called 'From Molecular Cores to Protoplanetary Disks' is currently producing infrared images and spectra of young stars and their disks and environments. The official abbreviation for the programme is *c2d*.

This thesis

This thesis concerns the study of the evolution and transport of ices from their formation in dense clouds to their incorporation into a planet-forming disk. The study is limited to low-mass young stars and the clouds forming low-mass stars. A low-mass young star is roughly defined as a star which will be similar to the Sun once it has evolved to the main-sequence.

Chapter 2 presents the first detection of methanol ice around young low-mass stars. The detections of methanol correspond to a concentration of 15-25% relative to water ice. Previously solid methanol was only observed near young stars much heavier than the Sun. It is currently not well-understood how methanol can form in such quantities, but the discovery of the molecule around low-mass stars shows that intense ultra-violet light and other characteristics of high mass stars are not necessary for forming methanol. Methanol is an important molecule, because it is a necessary ingredient for forming more complex organic molecules in the warm dense regions very close to a young star, where temperatures rise high enough to evaporate ice, the so-called 'hot cores'. Methanol ice is present in Solar System comets, but not in the quantities described in this chapter.

In **Chapter 3** the nature of interstellar solid carbon monoxide (CO) is studied in detail. It is shown how the CO molecule can be used to 'see' the microscopic structure of the ice. Observations of more than 35 young stars are used to study how CO ice typically behaves in space by analysing the shape of the absorption band caused by stretching vibrations in the $C\equiv O$ triple bond. An important conclusion in this chapter is that the ice seems to have a similar structure everywhere; CO seems to be largely pure when recently formed, i.e. it is not mixed with other molecules. A smaller fraction of the CO ice is always mixed with water ice. There is evidence that the CO becomes more mobile when heated, and that it can actually move into the water ice. Also, the CO is probably not evenly distributed on the surface of the dust grains, but is rather located in irregular clumps on the surface or as inclusions in the ice. In essence, it is shown how the spectroscopy gives information on what takes place on scales of a few nanometers in dust grains lo-

cated more than 500 light years away. In fact, the same effects can be seen even in other galaxies!

A new technique, which can be used to map the spatial distribution of interstellar ices is described in **Chapter 4**. Because a bright star located behind an ice-rich cloud is required for observing interstellar ices, it has in the past been almost impossible to measure how ices are distributed in space; there are simply not so many bright stars available. Only the ice located directly in front of a star can be studied. Currently, new infrared cameras and spectrometers mounted on large telescopes have become much more sensitive than they used to be, such that fainter stars can be used as background light sources against which ices can be observed. Because faint stars are much more common than bright ones, many lines of sight toward stars behind even relatively small regions of a dense cloud can be observed. In the chapter, the first high resolution map of ices is presented. The region studied is the outer dusty envelope of a collapsing protostar, the stellar equivalent of a womb. The icy material here is what will directly be incorporated into a planetary system. It is found that the amount of ices rises dramatically in the inner regions of the protostellar envelope, as expected from simple theoretical considerations.

It is also of great interest to search for ice in planet-forming disks surrounding young stars, but doing so has proven to be quite difficult. Although we know that ices are present in great abundance in our own Solar System, it is not clear how it got there. A circumstellar disk forms by accreting material from the protostellar envelope. The material falling on the disk is believed to do so at rather high velocities in some circumstances. As the infalling material crashes onto the disk, the ice will probably evaporate, and in some cases the molecules may be completely destroyed in a 'dissociative shock'! Observing ices directly in a disk, will tell if it has been altered during the formation of the disk.

Chapter 5 presents one of the first Spitzer spectra obtained as part of the *c2d* Legacy programme. The presented object, of which the spectrum is taken, is of particular interest because it is a so-called 'edge-on disk'. The expression refers to an infant Solar System viewed almost from the side. For this type of object, the central star is completely hidden from view at at wavelengths in the optical part of the spectrum and only light reflected from the surface of the disk can be seen. An edge-on disk also provides an opportunity for directly observing ices in the disk because with this geometry the ices can be seen in absorption against the inner parts of the disk, where the star has heated the dust enough to glow in the mid-infrared (-200–1000°C). Abundant ices are indeed seen, but to properly locate them in the disk, a detailed model is constructed. The model calculates the temperatures in the disk, and in particular where the dust becomes too hot to contain ice. It is concluded that half of the ice must be located in an unrelated foreground cloud, while the other half is probably located in the disk.

Chapter 6 concerns another peculiar object, where the process of material crashing onto a circumstellar disk may be directly observed. In this source exceptionally bright lines from warm carbon monoxide gas are observed. The lines are peculiar because they can be fitted by a gas at a single temperature of 240°C. This temperature is characteristic of dense gas in the process of forming molecular hy-

drogen. If this happens, the original molecules must have been ripped apart in the collision of material falling on the disk. In this particular object, there may be signs that the icy material is altered significantly on the path from the dark cloud to the planet-forming disk. However, the evidence is not conclusive, and the amount of molecules actually destroyed may be small.

Finally, **Chapter 7** discusses how the presence of a circumstellar disk may cast a large shadow, which appears much larger than the disk itself. These shadows can be seen because the clouds out of which the star originally formed reflect light except where there is a shadow. The appearance of disk shadows helps to determine the structure of those disks, which are too small to be directly imaged.

Curriculum Vitae

I was born on November 15, 1977 in the rather smelly fishing town of Esbjerg, Denmark. The first 6 years of my life were spent just hundred meters from the beautiful, but windy Western Sea. One day in 1989 I decided to become an astronomer. I left secondary school one year short of the obligatory nine years in 1992 to attend the oldest high school in Denmark in the ancient capital of Ribe. After receiving my high school diploma in 1995, I moved to Copenhagen to study physics and mathematics at the University of Copenhagen. I achieved the degrees of Bachelor of Science in 1998 and Master of Science in October 2000 with honours. My Master's Thesis on 'The Differential Magnification of Strongly Lensed High Redshift Galaxies' was written under the supervision of Dr. Jens Knude in Copenhagen and Dr. Tommy Wiklind at the Onsala Space Observatory in Sweden. I began my PhD studies at Leiden University in November 2000 under the supervision of Prof. Dr. Ewine van Dishoeck. The purpose of the thesis work was to study young low-mass stars using infrared data from the Space Infrared Telescope Facility (SIRTF), which is now known as the Spitzer Space Telescope. I have assisted in the definition of the spectroscopic part of the Spitzer Legacy programme 'From Molecular Cores to Protoplanetery Disks' by constructing the original list of targets and analysing the first data.

During my time in Leiden, I have been on three observing trips to the Very Large Telescope in Chile and once to the Keck Observatory in Hawaii. In addition, I have prepared several service observing programmes for the VLT and for Spitzer. I have been on numerous working visits to the California Institute of Technology, the Institut d'Astrophysique Spatiale in Paris, the Max Planck Institut für Astrophysik in Munich and Stockholm Observatory. In addition to colloquia presented at these host institutes, I have given talks at international conferences in Australia, Germany, the UK, Denmark and the Netherlands. In 2001 I attended the Saas-Fee winter school in Switzerland. Until 2003, I was involved in the organisation of the International Astronomical Youth Camps (IAYC), a summer camp for young amateur astronomers.

As part of my work in Leiden, I have helped two students with their final research projects.

Acknowledgements

Before I was offered to make my PhD in Leiden, I was warned that the environment would be very competitive and that the work might be tough. Well, it was, and I am grateful for it in the end. After completing my tour of duty, I feel like joining a select group of people with common experiences of forging through a PhD in the Leiden astrochemistry group. Without the competitive, but at the same time open and nurturing environment in Leiden, I could not have written this thesis. For good or for worse, my Leidse experience has definitely made me a better scientist.

While searching for PhD positions, I had my mind set on extra-galactic star formation, gravitational lenses or other such things. I no longer remember exactly what brought me to apply for a position in astrochemistry, but I have not a for moment regretted it since. Science at high signal-to-noise is fun and dirty stuff in space is strangely appealing. Så, Kirsten, godt at du snuppede den ekstra-galaktiske stilling i Leiden før jeg kunne søge den!

Den danske klan i Leiden opstod pludseligt og forsvinder nu næsten lige så hurtigt igen. Uden jer havde jeg nok helt glemt fædrelandets fjerne kyster.

To my collaborators, who have given me invaluable inspiration: I hope we can come up with many more great ideas in the future. Helen, you opened my mind to the pristine goldmine of science that solid state astronomy is. Adding that to the moral support you have given me over the years, your presence has been invaluable. Kees, we had quite an exciting race in the end. That was some of the best fun I have had with science. My french connection, Emmanuel and Wing-Fai: we had fun on the mountain. Don't cut any cables! Vincent, your straight-forward manner was definitely what our little group needed. Good to have a fellow coffee-junkie.

Some additional friends and collaborators also deserve to be mentioned. Jackie, Adwin, Henrik, Steve, Doug and Jean-Charles: The discussions I had with you were always entertaining and educating.

Keeping me from going completely crazy was the North End club (you know who you are, and if you don't it is probably best so!). That tape recorder would have been nice. And for those of you crossing the pond: I am sure you will find your own ice cubes.

I am sure that I have had one of the most varied selections possible of office mates over the past four years. Pascale, I am sorry about your plants; it was Fredrik and Fleur who wouldn't let me water them! Fredrik (KK), who convinced me to buy a mac. I enjoyed your's and Anna's hospitality in Stockholm. Fleur, together we managed to keep the most untidy office in the astrochemistry group, but your bike really provided that extra little bit. Your translation of my dutch

summary was much appreciated. Oskar, the final addition to the office, good luck with your new baby!

Jes, den sidste øl er altid een for mange. Men hyggeligt var det. Held og lykke med at erobre Verden - Jeg håber du efterlader et lille stykke til mig.

Last but not least, I owe my mother a great deal for getting this far. She always supported and encouraged my crazy ideas of becoming a scientist. Kære mor, du har givet mig alle de rigtige forudsætninger for at skrive denne afhandling og dine kærlige tanker har altid været en stor støtte.

Zita, this thesis is all yours. Without your love and support, I would not have made it. You are my best friend who always believed in me, and I will never forget that.

Klaus Martin Pontoppidan, Leiden, August 2004